THE UNIVERSITY *of* EDINBURGH

Charge, orbital and magnetic ordering in transition metal oxides

Mark S. Senn

For the degree of Doctor of Philosophy

School of Chemistry

University of Edinburgh

January 2013

Declaration

I declare that this thesis has been composed by me alone, and that the work presented in this thesis is my own, or where it is the work of another they are duly credited. Furthermore I confirm that this work has not been submitted for any other degree or professional qualification than this doctorate. Some of the research herein has already been published as detailed in the Publications section.

Mark S. Senn

August 21st 2012

Acknowledgements

First and foremost I would like to thank my PhD supervisor Paul Attfield. Paul had the conviction that this project on the Verwey structure of magnetite would be worth the many hours of data analysis in the end, and I am grateful for his vision and support. His insight and patience when confronted with a bond angle table consisting of 56 atoms has been inspirational!

Without the hard work of Jon Wright, none of this work on the solution of the Verwey structure of magnetite would have been possible. It has been a humbling experience working with Jon – a man who I am convinced lives in reciprocal space and dreams in binary. I have learnt much, and hope I will continue to have the opportunity to learn from Jon. I am particularly indebted to Jon for the hours of his time spent integrating and reintegrating data at ID11 (ESRF) and for the reciprocal space reconstructions featured in this thesis.

I am very grateful to Ingo Loa for hours spent compiling the Wien2k code on 'Eddie' and for answering many questions on Wein2k and DFT. Without his help the work in Chapter 4 would not have been possible.

Simon Kimber has been my collaborator on the $Ba_3ARu_2O_9$ project. I would like to acknowledge Simon in particular for, synthesis of a sample of, $Ba_3NaRu_2O_9$, $Ba_3LaRu_2O_9$ and $Ba_3YRu_2O_9$, collection and analysis of the data for the charge melted phase of $Ba_3NaRu_2O_9$ (Section 6.3) and collection of magnetic susceptibility data on $Ba_3NaRu_2O_9$. I am also grateful to Simon and Adrian Hill for collection of x-ray diffraction data at ID31 on $Ba_3ARu_2O_9$ (A = Na, Nd, La, Y), and for assistance on the high pressure beamline ID09A. Thank you also to Yuichi Shimakawa and Takashi Saito of Kyoto University who allowed me to measure the $Ba_3CaRu_2O_9$ sample at Spring-8 during their diffraction experiment.

I am grateful to beamline scientists Aziz Daoud-Aladine (HRPD) and Pascal Manuel (WISH) for their support at ISIS. Michael Hanfland at ID09A (ESRF) supported us through the high pressure experiment including loading the DAC for the single crystal diffraction experiment. I would also like to thank John Evans for answering many question related to using Topas, and Simon Parsons for collecting and integrating single crystal data for $Ba_3NaRu_2O_9$ and for useful discussions on the program Twinlaws.

The Attfield group past and present have helped make this PhD so enjoyable and I am grateful for their support, friendship and for good nights out. A special thanks goes to Angel Arevalo Lopez who is always on hand and happy to help, and whose willingness to discuss all aspect of my work over a cup of tea has been a great source of motivation throughout this thesis.

I am grateful to the EPSRC and STFC for funding me on this 'Next generation facility user' PhD studentship.

On a more personal note, I would like to thank my parents, who have somehow always known that I had this thesis in me – their encouragement in all of my academic pursuits has always been greatly appreciated. And particularly, thanks to Mum who has spent many painful hours proofreading this document! Thanks also to my sister Helen and brother-in-law Ed for support and many good times out on the hills and in Edinburgh over the past few years. And last but not least, my wife Helena, who has made this time in Scotland so special and who has supported me and kept me sane during this PhD. Her enthusiasm for my work has always cheered me greatly.

Finally, I would like to thank my examiners Simon Parsons and Andrew Wills for thorough reading of this thesis and useful suggestions on how to improve it.

Publications

The following publications have been made as a result of the work carried out in this thesis:

"Charge order and three-site distortions in the Verwey structure of magnetite", M. S. Senn, J. P. Wright, and J. P. Attfield, Nature **481**, 173 (2012).

"Electronic orders in the Verwey structure of magnetite", M. S. Senn, I. Loa, J. P. Wright, and J. P. Attfield, Phys. Rev. B **85**, 125119 (2012).

"Charge Order at the Frontier between the Molecular and Solid States in $Ba_3NaRu_2O_9$", S. A. J. Kimber, M. S. Senn, S. Fratini, H. Wu, A. H. Hill, P. Manuel, J. P. Attfield, D. N. Argyriou, P. F. Henry, Phys. Rev. Lett. **108**, 217205 (2012).

The following manuscript is under review at the Journal of the Korean Physical Society:

"The Verwey phase of magnetite - a long-running mystery in magnetism", M. S. Senn, J. P. Wright, and J. P. Attfield.

Abstract

Neutron and x-ray diffraction has been used to study charge, orbital and magnetic ordering in some transition metal oxides. The long standing controversy regarding the nature of the ground state (Verwey structure) of the canonical charge ordered material magnetite (Fe_3O_4) has been resolved by x-ray single crystal diffraction studies on an almost single domain sample at 90 K. The Verwey structure is confirmed to have Cc symmetry with 56 unique sites in the asymmetric unit. Charge ordering is shown to be a useful first approximation to describe the nature of the ground state, and the conjecture that Verwey made in 1939 has finally been confirmed. However, three-site distortions which couple to the orbital ordering of the Fe^{2+} ordered states (trimerons) are shown to provide a more complete description of the low temperature structure. Trimerons explain the rather continuous distribution of the valence states observed in magnetite below T_v, anomalous shortening of Fe-Fe distances and the off-centre distortions resulting in ferroelectricity. DFT+U electronic structure calculations on the experimental coordinates support the conclusion of this crystallographic study, with the highest electron densities calculated for those Fe-Fe distances predicated to participate in the trimeron bonds.

The 6H-perovskites of the type $Ba_3ARu_2O_9$ have been reinvestigated by high resolution neutron and x-ray power diffraction. The charge ordered state of $Ba_3NaRu_2O_9$ has been characterised at 110 K (P2/c, a =5.84001(2) Å, b = 10.22197(4) Å, c = 14.48497(6) Å, β = 90.2627(3) °) and shown to consist of a structure with near integer charge ordering of $Ru^{5+}{}_2O_9$ / $Ru^{6+}{}_2O_9$ dimers. The ground state has been shown to be very sensitive to external perturbations, with a novel melting of charge ordering observed under x-ray irradiation below 40 K (C2/c, *a* =5.84470(2) Å, b = 10.17706(3) Å, c = 14.45866(5) Å, β = 90.2151(3) ° at 10 K). High pressure studies reveal that the Ru-Ru intra-dimer distance may dictate the response of the system to pressure. Empirical trends in the $Ba_3ARu_2O_9$ series of compounds have shown that change in 'chemical pressure' in these systems may be rationalised in terms of Coulomb's law. In A = La and Y the magnetic ordering is shown to be FM within the Ru_2O_9 dimers (1.4(2) μ_B and 0.5(1) μ_B, respectively per Ru), representing the first case of intra dimer FM coupling reported in a system containing face-sharing RuO_6 octahedra . The overall AFM coupling of the dimers implies an as yet unobserved breaking of the parent symmetry. In A = Nd, a complex competition between the crystal field effect of Nd^{3+} and the magnetic ordering of the Ru_2O_9 FM moments has been observed, leading first

to FM order of Nd at 25 K (1.56(7) μ_B) followed by ordering of Ru moments (0.5(1) μ_B) and a spin reorientation transition of Nd moments at 18 K. In A = Ca, the formation of a singlet ground state is observed in Ru_2O_9 rather than the expected AFM coupling and below 100 K $Ba_3CaRu_2O_9$ is diamagnetic. All five systems indicate that the Ru_2O_9 dimer is the physically significant unit in these systems when considering structural trends and the ordering of charge, spin and orbital degrees of freedom.

Table of Contents

Abbreviations

AFM – Antiferromagnetic

BVS – Bond valence sum

BZ - Brillouin zone

CO – Charge ordering

D_{BB} – Distance between two B-sites

$D_{(Ru\text{-}Ru)}$ – Distance between two Ru-sites in the same Ru_2O_9 dimer

$D_{<Ru\text{-}O>}$ – Average Ru-O bond distance in a Ru_2O_9 dimer

DAC – Diamond anvil cell

DFT – Density functional theory

DOS – Density of states

FL – Fermi level

FM – Ferromagnetic

G – Group

GGA – Generalised gradient approximation

GOF – Goodness of fit

H – External field

Irep. – Irreducible representations

JT – Jahn-Teller

k – Propagation vector

K_{max} – Maximum plane wave vector

LDA – Local density approximation

M – Induced magnetism

MG – Magnetic group

OO – Orbital ordering

OPD – Order parameter direction (distortion mode)

p – Priming of a symmetry operator

P – Polarisation

POP – Primary order parameter

$Q_{B:d\downarrow}$ - DOS of minority spin B-site in range -460 – 0 meV

Q_{JT} – Tetragonal JT mode

Q_O – Orthorhombic JT mode

Q_{Rad} – Radial breathing mode

Q_{Tot} - Total integrated charge

r_A – Ionic radii of ion A

RE – Rare earth

R_{MT} – Muffin tin sphere radius

SCF – Self-consistent field

SOP – Secondary order parameters

t – Goldschmidt tolerance factor

T_v – Verwey transition temperature

T_c – Phase transition temperature

ρ – Electron density

χ_M – Molar susceptibility

ψ – Basis vector / Basis set

Section A: Introduction

1. Properties of transition metal oxides

1.1. Structure and properties of transition metal oxides

Metal oxides form a class of materials which have a very rich chemistry and exhibit a wide range of physical properties. They behave neither as ionic solids, in which the physical properties are generally dictated by the behaviour of the cations and anions, nor as metals in which the properties are often dictated by the 'free electron gas'. Instead, they exhibit less predictable behaviour arising from the interplay between single ion effects and the band structure. These systems are commonly referred to as highly correlated electron systems. It is the precise nature of these electron-electron (or even electron-phonon) correlations which gives rise to the large range of physical properties observed in transition metal oxides. As the behaviour of the electron density dictates both the observed physical properties, and the observed structure, precise knowledge of the electron density is a key step to understanding the structural ↔ property relationship. It is, however, generally much easier to measure structure and infer the electron density by empirical methods or solution of the Schrödinger equation at an appropriate level of approximation.

It is beyond the scope of this piece of work to review transition metal oxides. The two systems which are relevant to this thesis - the spinel and the 6H-perovskite - are introduced and reviewed in the relevant chapters. Instead, in the following chapter properties and phase transitions observed in many transition metal oxides are discussed and illustrated with relevant examples.

1.1.1. Charge Ordering

The notion of charge ordering was first postulated by Winger in 1938.[1] Independently, charge ordering (CO) was proposed by Verwey in 1939 on observation of a semiconductor

to insulator transition in magnetite.[2] It is a transition in which delocalised electron density becomes localised at periodic positions of the lattice. It can occur in systems which have semi-valent cations, or cations which can undergo charge disproportionation such that $2A^{n+} \rightarrow A^{n+1} + A^{n-1}$, which reflects the stability of the n-1 and n+1 oxidation states with respect to the n oxidation state. CO transitions are typically accompanied by a metal (or semiconductor) to insulator transition as evident from resistivity measurements. Examples of charge ordering as a result of disproportionation included the perovskite $BaBiO_3$, in which Bi^{4+} disproportionates into Bi^{3+} and Bi^{5+},[3] and the A-site ordered 134-perovskite $CaCu_3Fe_4O_{12}$, in which Fe^{4+} disproportionates into Fe^{3+} and Fe^{5+}.[4] This thesis will, however, be concerned with the charge ordering of the semi-valent cation, which has recently been reviewed.[5] A summary of this review is made below, along with some more recent results.

Despite the many transition metal oxides known with semi-valent cations, only a few are observed to undergo CO transitions. With one exception ($Ba_3NaRu^{5.5+}{}_2O_9$)[6] charge ordering of the semivalent variety is restricted (within the oxides) to the first row transition metals. The manganites, in particular the A-site doped $AA'Mn_2O_6$ double perovskites form the largest family. This apparent confinement of charge ordering to the first row transition metals reflects the much reduced radial extension of the 3d orbitals with respect to the 4d and 5d orbitals, and therefore a poorer delocalisation of the electrons over the lattice.

In the half doped manganites one of two patterns of charge ordering is observed (Figure 1.1, left and centre). In two dimensions these are equivalent, consisting of a checkerboard-pattern of Mn^{3+}/Mn^{4+}. The stacking of these checkerboards out of phase leads to a rock salt-like charge order as observed in $TbBaMn_2O_6$ [7] ($Tb_{0.5}Ba_{0.5}MnO_3$) and $Y_{0.5}Ba_{0.5}MnO_3$.[8] The in-phase stacking leads to a striped ordering of charges as observed in $Pr_{0.5}Ca_{0.5}MnO_3$, and also evident in the one third doped $La_{⅓}Ca_{⅔}MnO_3$, where it leads to a 1:2 ordering of Mn^{3+}/Mn^{4+} stripes.

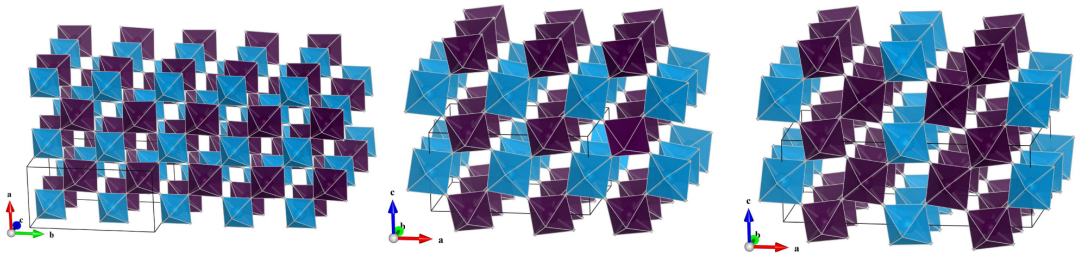

Figure 1.1: Charge ordering of the A-site doped perovskite manganites. Left, rock salt-like charge ordering of $TbBaMn_2O_6$. Centre, striped charge ordering in $Pr_{0.5}Ca_{0.5}MnO_3$. Right, 1:2 striped charge ordering in $La_{⅓}Ca_{⅔}MnO_3$. $Mn^{3+}O_6$ and $Mn^{4+}O_6$ polyhedra are shown in light blue and dark purple respectively.

Striped charge ordering is also observed in the oxygen deficient double perovskite (Figure 1.2) $TbBaFe_2O_5$,[9] $TbBaMn_2O_5$, $YBaCo_2O_5$, [10] in which the B-sites are in square pyramidal coordination. In $TbBaMn_2O_5$ the charge ordering phase is observed to be robust up to 900 K.[11] This is in contrast to the double perovskite $TbBaMn_2O_6$, which is obtained from the prior by oxygen intercalation, and undergoes its CO transition at a much lower temperature (473 K).[7] The nature of the order is also changed in $TbBaMn_2O_5$, with respect to the double perovskite with striped rather than the rock salt type order of Mn^{2+} / Mn^{3+} charges being observed.

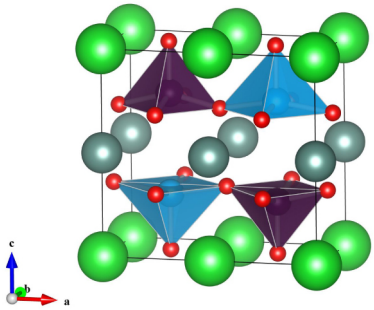

Figure 1.2: Charge ordered phase of $YBaCo_2O_5$, Co^{2+}/Co^{3+} are shown in their pyramidal coordination in light blue and dark purple respectively. Ba, Y and O ions are shown by bright green, grey and red spheres respectively.

The most complex charge ordered structure reported for any metal oxide is probably that of NaV_2O_5 (Figure 1.3), which has 8 crystallographically unique V sites below T_{CO} (34 K)[12], while above the transition all V sites are equivalent. Metal oxides containing semivalent V cations often undergo a bond dimerisation which is in competition with the charge ordering such as is observed in the spinel AlV_2O_4 (discussed in Chapter 2). In the cases of the ladder structure of NaV_2O_5 made up of edge-sharing VO_4 tetrahedra (directed along the *b*-axis, Figure 1.3), Coulombic repulsion is not minimised by the alternation of V^{4+} and V^{5+} along the ladder, but instead a $2V^{5+}$:$2V^{4+}$ modulation is observed, possibly stabilised by V^{4+} dimers formation or exchange interactions.

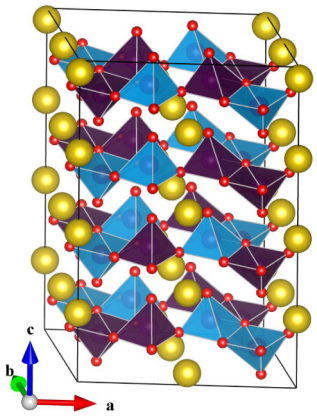

Figure 1.3: Charge ordered structure of the half ladder compound α-NaV_2O_5 expressed in the monoclinic space group A112 (C2) with a super structure of $a \times 2b \times 4b$, $\gamma \sim 107$ ° with respect to the high temperature structure. V^{5+} and V^{4+} tetrahedrally coordinated polyhedra are drawn in dark purple and light blue respectively. O and Na are shown by red and yellow spheres respectively.

Fe_2OBO_3 which has the warwickite structure has a charge ordering transition at 317 K accompanied by a semiconductor to semiconductor transition. The charge ordered structure at ~ 190 K is believed to result in a doubling of the *a*-axis and a monoclinic distortion with chains of edge-sharing Fe^{2+} and Fe^{3+} octahedra (Figure 1.4, left).[13] However, due to the nanometre scale of the charge ordered domains, reflections associated with the doubling of the *a*-axis have not been observed by powder diffraction. Single crystal diffraction has verified this axis doubling and electronic structure calculations support the proposed structure.[14] Recent resonant x-ray diffraction results suggest a charge disproportionation in the region of 0.4 – 0.8 e^-.[15]

In lutetium ferrate $LuFe_2O_4$ (Figure 1.4, right), a 2 dimensional charge ordered state is observed below 530 K as a result of the triangular lattice on which the $Fe^{2.5+}$ sites sit. [16-18] Degeneracy is lifted by exchanging e^- between the layers in close proximity (double layers) creating a dipole – the long range disorder of these dipoles in the double layers gives rise to the two dimensionality of the ordering.[16] Below 320 K, an incommensurate structure with approximate propagation vector (~ ⅓, ⅓, ⅔) is observed [16, 17] along with a spontaneous polarisation.[19] The proposed structure within the commensurate approximation, does not however, allow for spontaneous polarisation and has antiferroelectric ordering of dipoles between the layers.[20]

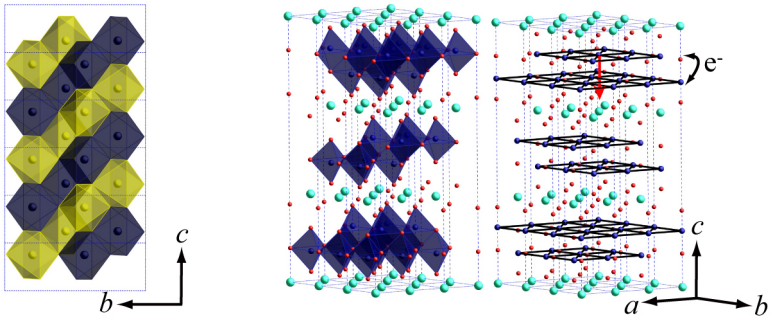

Figure 1.4: Left, charge ordered structure of Fe_2OBO_3 with Fe^{2+} and Fe^{3+} shown as blue and yellow polygons respectively. Right, the structure of $LuFe_2O_4$ with octahedral coordination of $Fe^{2.5+}$ by oxygen in the 'double layers'. The triangular lattice on which the $Fe^{2.5}$ sites is also shown, along with the electron transfer and resulting polarisation expected in the charge ordered phase (shown for one double layer only).

An important feature of all of these systems is that the observed charge order (as evidenced by bond valence sums (BVS, see Section 1.3.3)) never corresponds to integer valences. Typical charge separations, as observed by BVS, are segregations between about 30 – 60% of the expected value, with a 100% segregation never being observed.[5] Charge ordering is observed and understood in relatively few systems and is often in competition with other ground states. It is the elucidation of the structure of charge ordered phases which is one of the purposes of this piece of work.

1.1.2. Orbital Ordering

A degenerate system will distort to remove its degeneracy if it can do so by lowering its internal energy. This is the principle which, when applied to the orbital physics of transition metals, is referred to as the Jahn-Teller distortion[21] (Figure 1.5). Transition metal ions in an octahedral crystal field with d-orbital occupancies of d^1, d^2, d^4, d^5(LS), d^6(HS), d^7, d^9 are hence expected to distort stabilising fully occupied orbitals at the expense of destabilising empty or partly filled orbitals as entropy $\rightarrow$ 0. However, in the solid state there will be competing interactions (strain of the lattice, Coulombic repulsing and the orbital physics of other cations to name a few) which must be balanced with the lowering of the energy of the orbital configuration of a cation. This leads to the often complex, long range cooperative Jahn-Teller distortions which are also referred to as orbital ordering (OO). This orbital ordering must be facilitated by a distortion of the structure, in particular the shortening or lengthening of the relevant transition metal cation to oxygen bond length. Orbital order may hence be inferred by determining the structure very accurately, but other techniques such as

polarisation analysis of resonant x-ray scattering may also be employed to observe the OO directly.

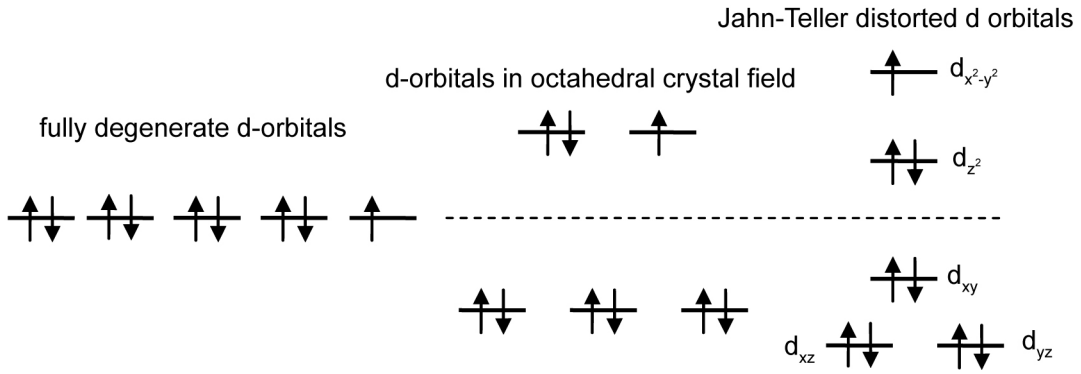

Figure 1.5: Jahn-Teller distortion for the d^9 configuration in an octahedral crystal field. The distortion corresponds to a shortening of the distance to four of the octahedrally coordinated ligands and a lengthening of two of the distances with respect to the undistorted picture.

It is convenient to describe orbital order by analogy with magnetic order (Section 1.1.3), in terms of orbitals being aligned with each other ferro (parallel) or antiferro (antiparallel) along a certain lattice direction. OO often accompanies long range CO and can be concomitant with magnetic ordering. OO has also been extensively studied in the manganite double perovskites. The CO phase of $La_{0.5}Ca_{0.5}MnO_3$ exhibits a striped orbital order that mirrors that of charge ordering, and can hence be said to have a ferro-OO along *b* (Figure 1.6, left). The OO ordering in $TbBaMn_2O_6$ (Figure 1.6, right) is markedly different on account of its rock salt-like charge ordered structure, which does not allow for ferro-OO to develop along *b*.

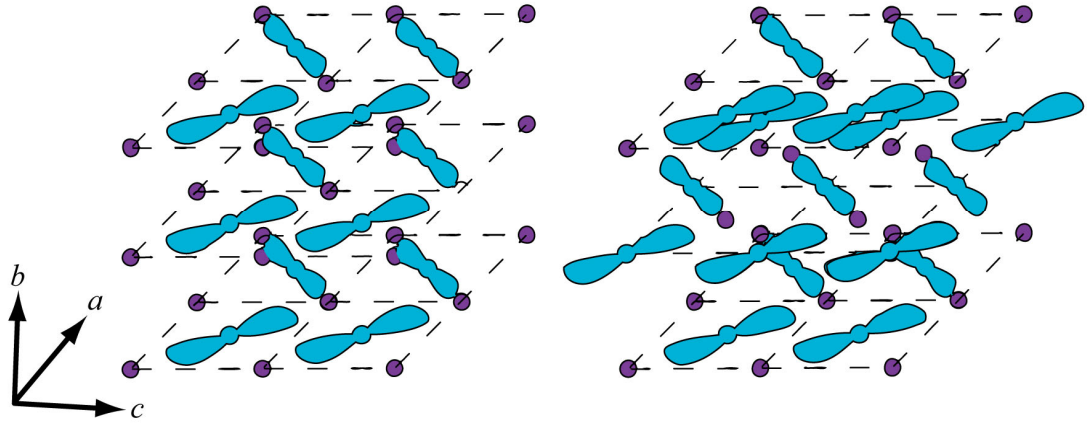

Figure 1.6: Orbital ordering in $La_{0.5}Ca_{0.5}MnO_3$ (left) and $TbBaMn_2O_6$ (right). Modified from ref. [7].

The spinels also have a particularly rich orbital physics on account of the short distances between cations in these systems, often leading to a very complex OO structure. OO in spinels is relevant to the Verwey transition in magnetite and is discussed further in Chapter 2.

1.1.3. Magnetic ordering

In order to understand the ordered magnetic states, which will be either ferro-, ferri- or antiferromagnetic, it is necessary to understand the magnetically disordered paramagnetic state. Magnetic moments arise when atoms in a sample have unpaired electrons. A site having unpaired electrons will have a magnetic moment due to its maximum spin (S) and orbital (L) angular momentum and will be dependant on the Lande g factor, as given by: [22]

$\mu_{eff} = g_J \mu_B \sqrt{(J(J+1)}$, $g_J = \frac{3}{2} + \frac{S(S+1) - L(L+1)}{2J(J+1)}$, where μ_B is the Bohr magneton.

For first row transition metal oxides, angular momentum is often quenched, that is as discussed in Section 1.1.2 the degeneracy of the d-orbitals is generally removed by crystal field splitting and Jahn-Teller distortions. This leads to the observation of the spin-only moment where J = S, and consequently the effective moment in is given as:

$\mu_{eff} = 2\mu_B \sqrt{(S(S+1)}$

For the lanthanides, where the splitting of the f-orbitals by the crystal field is often negligible, it is necessary to consider both S and L magnetic moments. Their coupling may be calculated as a perturbation to the L + S scheme using the Russell-Saunders coupling, where for f-orbitals less than half full, J = | L – S | and for those more than half full, J = | L + S |.

The incoherence of the order of the magnetic moment located at each site in a sample gives rise to the paramagnetism. The paramagnetic state is characterised by a linear dependency of the induced magnetism in a sample (M) on the magnitude of some external field (H), $M = \chi_M H$. The magnetic molar susceptibility (χ_M) is related to the magnetic moment by the application of statistical mechanics to an ensemble of spins, which are unquantised with respect to the direction in which they point (semi classical treatment), which gives Curie's law:[22]

$\chi_M = \frac{C}{T}$ where, $C = \frac{(N_A \mu_0 g_J^2 J(J+1))}{3k}$ and μ_0 is the permeability constant.[23]

χ_M^{-1} will hence tend to zero in the limit T → 0 K, corresponding to a ground state in which all spins are aligned parallel to each other. Magnetic exchange interactions will lead to the preferential parallel or antiparallel alignment of spins. The average effect of this interaction is taken account of in the Curie-Weiss law as an exchange interaction (θ) expressed as a temperature:[23]

$$\chi_M^{-1} = \frac{T - \theta}{C}$$

with θ > 0 corresponding to ferromagnetic (FM) exchange, θ < 0 corresponding to antiferromagnetic (AFM) exchange, and θ = 0 to Curie's law.

Magnetic exchange interactions were rationalised by Goodenough in terms of direct exchange and superexchange, and much of the pioneering work was done on the perovskite and spinel systems.[24, 25] Direct exchange will only occur in systems where the cations are in close proximity with each other normally, as a result of the edge or face-sharing of oxygen coordination polyhedra. It is particularly relevant to the two systems studied in this thesis, the spinel and the hexagonal perovskites, which have edge and face-sharing of octahedrally coordinated cations. Depending on the filling of the d-orbitals it will result in FM or AFM interactions (Figure 1.7, left). An often competing mechanism is the superexchange interaction (Figure 1.7, right), where magnetic exchange is facilitated by an intermediary non-magnetic anion which acts to transfer spin polarisation between the cations. Depending on the angle of exchange, FM or AFM alignment of spins will be favoured.

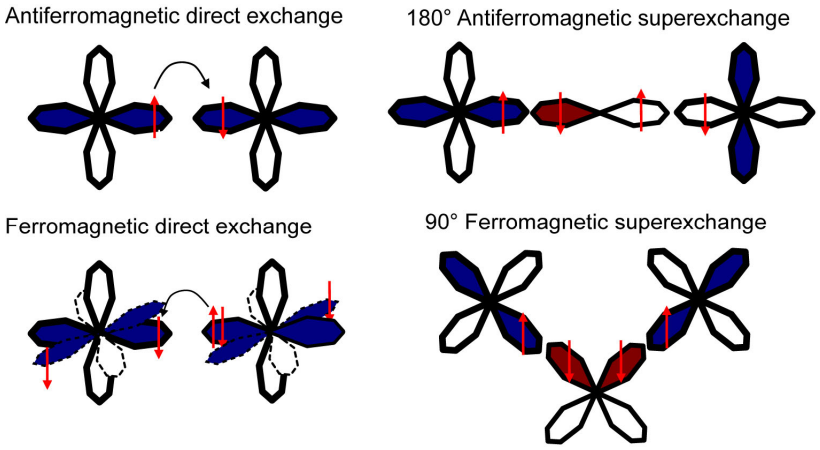

Figure 1.7: Exchange interaction in metal oxides. Cation d-orbitals are shown with blue lobes, oxygen *p*-orbitals with red lobes. All lobes are in the plane of the page, except for those drawn with dotted lines which are projected out of the page.

Some simple types of magnetic ordering often observed in the perovskites are shown in Figure 1.8. However, many magnetic structures are far more complicated, and it is non-trivial to predict the magnetic ground state for a system. It is the competing magnetic interactions along with their geometric frustration on the lattice on which they order, which gives rise to the host of complex observed magnetic structures. The magnetic ordering may not only be complex, but may also determine the ground state arrangements of the atoms.

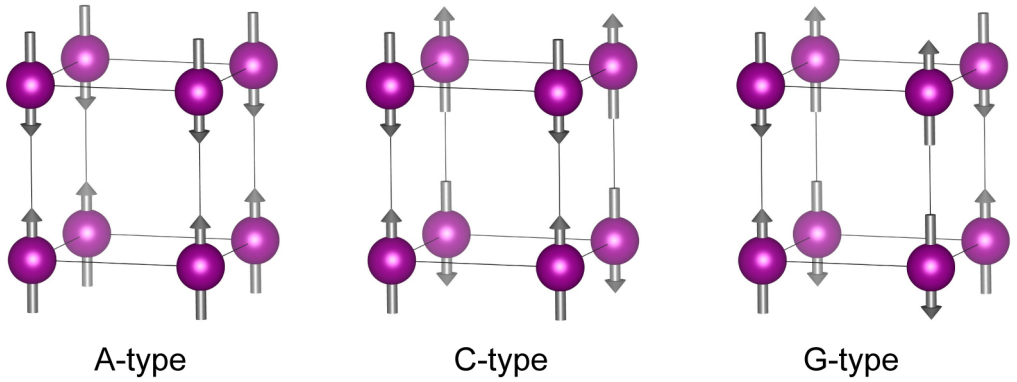

Figure 1.8: The simple types of magnetic order often observed in perovskites.[22]

1.2. Structure property relationship

1.2.1. Symmetry

Symmetry is not only a useful tool to aid in the determination of structure and magnetic structure. Its appreciation, also leads to an understanding of the allowed physical properties which can be observed in a material, as well as giving an insight into observed phase transitions.

Three dimensional structural symmetry of the solid state (that applicable to polar vectors) can be described by the translation of a unit cell, whose contents are periodically repeated along all directions of the three dimensions of the lattice. The unit cell is characterised by three lattice vectors (**a**, **b** and **c**), or often by three lattice lengths (*a*, *b* and *c*) and three angles (α, β and γ). The unit cell will belong to one of the 14 Bravais lattices which, when combined with the possible allowed point and translation elements, gives rise to 230 space

groups.[26] Thus, all crystalline matter which is said to be commensurate with respect to the period of its modulation may be characterised as having a certain set of symmetry operators. The symmetry alone, without precise knowledge of the structure (such as can normally only be obtained by detailed x-ray or neutron diffraction studies), places constraints on the expected physical properties of a sample (Neumann's principle[27]).

A case in point is ferroelectric materials, the observed phenomena in which a material may develop a spontaneous polarisation, and the direction of the polarisation may be reversed by the application of a field. In order for the development of a net dipole to be possible, the atoms within the material (assuming there are atoms of different charges) must undergo an off-centre distortion. This off-centre distortion, if it occurs cooperatively throughout the unit cell, will break the mirror symmetry perpendicular to the vector of the distortion. A structure exhibiting ferroelectric behaviour may therefore not have a space group with an inversion centre, and any structure which crystallises in a polar space group is by degrees a ferroelectric material.[28] By analogy with magnetism, a material is classed as being antiferroelectric if an off-centre distortion is countered by a distortion in an opposite direction of equal magnitude such that it cancels out any net development of a moment.

Magnetic moments do not transform as polar vectors but as axial vectors, and may be visualised as having a current loop that is perpendicular to the direction of the vector. Certain symmetry operators will hence act to reverse the direction of the current loop; this is known as a time reversal. Whether reversal occurs will depend on the direction of the axial vector relative to the symmetry operator. Magnetic space groups may hence be described by the additional consideration of a time reversal operator in order to describe all possible three dimensional magnetic ordering. If an additional time reversal is applied to a symmetry element, the element is said to be primed. This priming of symmetry operators (p) leads to additional magnetic Bravais lattices, point groups and translational symmetry elements which must be considered in constructing the three dimensional magnetic space groups. Magnetic groups (MG) are derived from a normal group (G) by considering in turn the different subgroups (g_n) of G with index two. The members of MG ({MG}) are then determined as: $\{MG\} = \{g_n\} + p[\{G\} - \{g_n\}]$. When the analysis is applied to the 230 space groups, it gives rise to the 1421 magnetic space groups (Shubnikov groups).[29] If the structural symmetry is known and the magnetic phase transition leaves the structure invariant, it is a relatively trivial task to pick a magnetic space group compatible with that of

the structural symmetry. However, magnetic ordering will often result in a breaking of the parent structural symmetry and the analysis is then no longer applicable.[29]

1.2.2. Phase transitions and Landau theory

Displacive phase transitions are characterised by a loss or breaking of symmetry with respect to a higher symmetry phase. The displacive phase transition lowers the internal energy (U) with respect to that of the high symmetry phase. As the thermodynamically stable phase is that for which the Gibbs free energy (G) is minimised, where G = U – TS + PV, the phase with lower symmetry is invariably that observed at low T and high P, and the high symmetry phase is observed at high T and low P. As G is required to be continuous across the phase transition, the two phases must coexist at a point in T. In the limit P → 0, the two phases differ only in the manner in which their G is partitioned into S and U, the high symmetry phase having higher U and hence higher S. The lowering of symmetry is hence brought about by a loss in entropy which corresponds to the "freezing out" of lattice phonons lowering U.[28]

In Landau theory, it is assumed that a single or small subset of normal modes of the lattice (frozen phonons) act as the driving force for the phase transition and may be viewed as the ordering parameter for the transition. Ordering parameters must necessarily go to zero on raising the temperature (or lowering the pressure) across a transition. They generally either do so with a discontinuity at phase transition temperature (T_c) (first order) or in a continuous manner (second order). The expansion of the free energy in terms of the order parameter as a function of temperature allows the manner in which certain physical properties vary across a phase transition to be understood. Landau theory is particularly successful for describing magnetic ordering transitions which often behave as second order phase transitions, and whose structures may often be described by a single order parameter.[28] However, more complex orderings may be described by the coupling of several order parameters. A case in point are multiferroics (Type II) in which the magnetic and structural (ferroelectric) order parameters are coupled,[30] leading to a material in which the magnetism can be controlled by the application of an electric field. Representation analysis is the tool by which order parameters are formalised.

1.2.3. Representation analysis

The coset decomposition of the space group G with respect to the propagation vector k_1 is performed such that all elements of G which transform k_1 equivalently are grouped together. Collectively the group of the generated *k* vectors is called the star of the propagation vector, with each individual *k* vector, (k_1, k_2 and so on) being referred to as arms. The coset which transforms k_1 into itself is called the little group of G (G_k).[31] In general, only representational analysis of G_k and G_{-k} (that which is related to G_k by inversion symmetry) is of interest when considering the symmetry allowed magnetic ordering, with the ordering described by the other arms of the start of k being analogous to crystal twinning which occurs at phase transitions (see Section 1.2.4). A described distortion or magnetic ordering must be self consistent under all the symmetry elements of G_K and may therefore not be transformed into itself. The description of how the (magnetic) structure transforms under each element of G_K is known as the representation. Representations may be decomposed as the sum of orthogonal irreducible representations (ireps.). An irep. hence describes the transformation of the structure under all the symmetry elements of the little group G_K.[31] The application of irreducible representation theory differs to whether it is being applied to a structural distortion or magnetic ordering.

For magnetic structures, the representation consists of the permutation representation and the axial vector representation. This representation is associated with the basis vector (ψ), which describes the magnetic moment (m_j) in the j^{th} (crystallographic) unit cell as a function of *k*, $m_j = \psi_j e^{-2\pi ik.t}$. ψ_j itself may be a sum of many basis vectors, and in a simple case could correspond to moments along *a* (ψ_1), *b* (ψ_2) and *c* (ψ_3). In fact, any choice of components of ψ_j is allowed, so long as it transforms self-consistently under the ordering irep. For ease the smallest number (n) of orthogonal ψ_n is often chosen. The final magnetic structure is hence described (in favourable cases) by a single irep. and its basis vectors, the relative ratio (or mixing) of which is determined by refinement against the magnetic scattering data.[31] Magnetic representation analysis has been implemented in the current work in FullProf studio using the program BasIreps.[32]

For structure distortions the practice is to perform the coset decomposition of G not just with respect to k_1, but also to include the experimental information of the believed (target) space group symmetry of the distorted structure in order to reduce the possible choices of ireps.

generated by the analysis. The reason for this is that the structural distortion will not be limited to the ordering of one site (such as for the magnetic ordering), but any structural distortion will couple to the whole structure requiring a large number of basis vectors to fully describe the distortion. The convention is to describe the ireps. that alone would imply the final symmetry as the primary order parameter (POP), and the other ireps. which couple to this through cooperative distortions, as secondary order parameters (SOP). The symmetry implied by an irep. is known as the kernel of the irep., and hence, kernel is the group of all symmetry operators that are mapped by an irep. onto the identity. An order parameter direction (OPD) is a subspace of an irep. which expresses a distortion (mode) of a certain symmetry.[33] For a three dimensional irep., the OPD may be one, two or three-dimensional, but the space group of the kernel of the irep. will be that implied by the most general (three dimensional) OPD. Where the target structure symmetry is unknown it is possible to perform a coset decomposition of G with respect to the propagation vector alone (space group symmetry P1), and test the resulting distortion modes against the diffraction data to ascertain the space group symmetry.[34]

The basis vector of the atomic displacement (polar vector) is handled differently to that generally used in magnetic structure refinement. Here the displacement of the atom in the the j^{th} crystallographic unit cell is dealt with by allowing each OPD which is coupled to a site to have a number of branches.[33] Each branch will describe some displacement in a crystallographic direction, which is self consistent under the symmetry of the kernel of the OPD.[33] Again, in a simple case there might be three branches corresponding to a displacement along x, y and z. The value of distortion mode analysis is that it may reveal that although the true symmetry of the structure is described by the chosen space group, the essence may be captured by relatively few distortion modes, which may lend themselves to analysis of the phase transition in terms of Landau theory. Distortion mode analysis is implemented in the current work using the web based tool ISODISPLACE[33], and direct refinement of distortion mode amplitude was performed in the program Topas[35].

1.2.4. Twinning

Twinning is most common in materials undergoing a structural phase transition from a higher symmetry to a lower symmetry space group and so is relevant to both of the results sections of this thesis. It is a natural consequence of a symmetry lowering phase transition

where the twin boundary is expected to be energetically comparable to the bulk structure.[36] It often makes the crystal structure determination by single crystal diffraction problematic, with systematic poisoning of observed reflection intensities occurring below the phase transition. It is however, not just an annoyance to be overcome during structural solution, but also reflects the degeneracy of the high temperature phase, the structural distortion often being driven by the desire to remove this degeneracy.

The analysis of twinning is formalised by coset decomposition. The maximum number of twin components for a phase **g** undergoing a transition to phase **f** can be calculated by performing the coset decomposition of the point symmetry group of **g**, **G** with respect to the point group of **f**, **F**. This coset decomposition divides the operators of **G** into sets. Each set will contain a number of operators equal to the total number of operators of **F**, and will be invariant under the operators of **F**.[37] Any operator in a given set will hence transform **f** in an invariant manner. The number of domain states (n) which could arise from the phase transition **g** → **f** is hence given by the relative ratio of the orders of the group **G** and the sub group **F**:

$$n = \frac{|G|}{|F|}$$

Any element (M) of a coset may be used to describe the possible twinning in a crystal. If the unit cell describing **f** is transformed with respect to **g** such that:

$(a_g, b_g, c_g)T = a_f, b_f, c_f$

Then the twin law which can be used to describe both the transformation of the reciprocal lattice (and hence the reflections) and the real space lattice is given as the triple product $T^{-1}MT$ (similarity transformation).[36]

Twinning is described either as merohedral or pseudo merohedral if the overlap of the reciprocal lattice of the principal and twin domain is complete or appears to be complete within some limiting resolution. In all other cases, twinning will reveal itself as reflections which cannot be indexed on integer values of the reciprocal lattice vectors, and a second orientation matrix of the twin domain with respect to the axis of the diffractometer will need to be defined so that its corresponding intensity can be integrated and assigned the appropriate reciprocal lattice vector.

1.2.5. Strain

Just as twinning is the consequence of phase transitions, so is strain, or rather a phase transition may be a consequence of an increase in strain. Strain is formally a second rank tensor. There are many different types of strain, in crystallography, micro- and macrostrain are of particular interest as detailed below.

As lattice parameters are derived with very high accuracy from powder diffraction experiments, the strain induced in these with respect to a variation in temperature or pressure is of particular interest in this current piece of work and is often the most obvious indicator of the occurrence of a transition. Strain may have two meanings; it may refer to the bulk strain of a material characterised by how the lattice parameter changes with respect to some reference value with temperature or pressure (macrostrain). However, on the microscopic level it may also refer to the variation of the lattice parameters across all of the many unit cells or domains which make up the sample (microstrain).

Formally, strain is given as:

$$e_{ij} = \frac{du_i}{dx_j},$$

a change in some displacement vector (u) with respect to the change in the position (x) of the vector. The value of e_{ij} (i, j = 1, 2, 3), will form a symmetric second rank tensor whose values will depend on the coordinate system (x_j). The choice of unit cell axis is therefore crucial in examining the macrostrain. For any unit cell there exists a set of orthogonal axes (X_1, X_2 and X_3) for which the strain responds in an approximately linear fashion. For cubic, tetragonal, orthorhombic and hexagonal unit cells, these will always be trivially related to the crystallographic axis, but for monoclinic and triclinic systems only with variable temperature / pressure data can the appropriate coordinate system which describes the fundamental mechanical response of the system to external stimuli be elucidated. [28] In other words, for monoclinic and triclinic crystal systems the principal axis may only be determined experimentally. The diagonalisation of the second rank tensor of e_{ij} gives the strain along the principal axes. In this piece of work, the web based program Pascal has been used for purpose of this analysis.[38]

Microstrain is the variance and covariance ($\sigma^2(s_{pq}, s_{uv})$) of the cosine directors of the unit cell. The (reciprocal) cosine directors of the lattice are defined as: $s_{11} = b^2c^2\sin^2\alpha$, $s_{22} = a^2c^2\sin^2\beta$, $s_{33} = a^2b^2\sin^2\gamma$, $s_{12} = abc^2(\cos\alpha\cos\beta - \cos\gamma)$, $s_{23} = a^2bc\ (\cos\beta\cos\gamma - \cos\alpha)$ and $s_{31} = ab^2c\ (\cos\gamma\cos\alpha - \cos\beta)$, where,

$$\frac{1}{d^2} = \frac{1}{V}(s_{11}h^2 + s_{22}k^2 + s_{33}l^2 + 2s_{12}hk + 2s_{23}kl + 2s_{31}lh)$$

Although the average of these values must respect the crystal symmetry (i.e. for cubic $\langle s_{11}\rangle = \langle s_{22}\rangle = \langle s_{33}\rangle$), for a given domain or grain they may deviate significantly. A large variance of the cosine directors will results in a large $\sigma^2(1/d^2)$ for a given reflection, and hence a broad Bragg peak.[39] The $\sigma^2(1/d^2)$ has the effect of introducing a $\Delta d/d$ resolution function, which is convoluted with the profile of the diffraction pattern leading to peak broadening. How this effect can be modelled in Rietveld refinement is quantified in Section 1.3.3.

1.3. Structure determination by diffraction

The purpose of this section is to describe briefly how 'the average structure' may be determined using neutron or x-ray diffraction methods.

1.3.1. Reciprocal lattice and diffraction

In real space, for diffraction to be observed, the Laue conditions must be satisfied simultaneously in all three orthogonal directions of the lattice (**a**, **b** and **c**): $\mathbf{a}(k_f - k_i) = h\times\lambda$, $\mathbf{b}(k_f - k_i) = k\times\lambda$, $\mathbf{c}(k_f - k_i) = l\times\lambda$, where k_i and k_f are the incident and scattering vector respectively and h, k, l are integers. [40] However, the abstract Bragg construction provides a more straight forward way for understanding diffraction patterns.

The coherent Bragg scattering observed from a periodic three dimensional lattice (in the kinematic limit) is given by the Fourier transformation of the lattice convolved with the function which characterises the scattering from the lattice unit cell. The Fourier transformation gives rise to the idea of the reciprocal lattice, an array of delta-like functions, which are arranged in a periodic way. The array is characterised by the reciprocal lattice vectors $\mathbf{a}^*$, $\mathbf{b}^*$ and $\mathbf{c}^*$, which are related to the lattice vectors of the unit cell by $\mathbf{a}^* = \mathbf{b} \times \mathbf{c} / V$,

b* = **a** × **c** / V and **c*** = **a** × **b** / V, where V is the real space volume and '×' is taken to represent cross product. A node exists at some distance in reciprocal (**r***) from the origin at any integer value of these reciprocal lattice vectors such that, **r*** = *h***a*** + *k***b*** + *l***c*** where *h*, *k* and *l* are the reciprocal lattice indices.[40] In real space the reciprocal lattice indices (Miller indices) may be visualised as defining a scattering plane which intercept the unit cell at spacing of **a**/*h*, **b**/*k*, **c**/*l*.

The Bragg condition, $n\lambda = 2d_{hkl}\sin\theta$ requires that the path distance (d_{hkl}) from successive planes is integer if constructive interference and diffraction is to occur. The Bragg equation may be expressed as:

$$\frac{1}{\lambda} = \frac{1}{d_{hkl}} \times \frac{1}{2\sin\theta} = \frac{r^*}{2\sin\theta}$$

This gives rise to the Ewald sphere construction (Figure 1.9, left) in which the distance from the crystal to the origin of reciprocal lattice (0 0 0) is given by the incident vector $k_i = 1/\lambda$. As the scattering process is elastic, the scattering vector k_f must also be of length $1/\lambda$. Hence k_f may be any vector on the surface of a sphere of radius $1/\lambda$. Only reciprocal lattice points cutting the surface of the sphere give rise to observable diffraction for that alignment of the crystal (reciprocal lattice) with respect to the incident beam.[36] This is equivalent to the real space Laue conditions. For a projection along a line 2θ from the incident beam, the distance from the origin of reciprocal space to the reciprocal lattice point is given as:

$$r^* = k_f - k_i = \frac{1}{\lambda} 2\sin\theta$$

Different reflections may be made to cut the surface of the sphere by rotating the crystal and hence rotating the reciprocal lattice about the beam. The construction can be used to visualise powder diffraction (Figure 1.9, centre), in which each reciprocal lattice vector will trace out a cone on the surface of a sphere with angle 2θ to the incident beam as it is rotated through all possible orientations. It also helps to visualise energy dispersive or time of flight neutron diffraction ((Figure 1.9, right) through drawing a series of concentric Ewald spheres all of which touch at the origin of reciprocal space but cut the reciprocal lattice at different points due to their differing radii. All the vectors of the reciprocal lattice intercepting any one of the surfaces of these spheres will now be observed simultaneously as diffraction spots.[40] Lorenz corrections can also be understood under this frame-work, in which reciprocal lattice points close to the origin will intercept the Ewald sphere for a longer period of time than those which are further from the origin.[36]

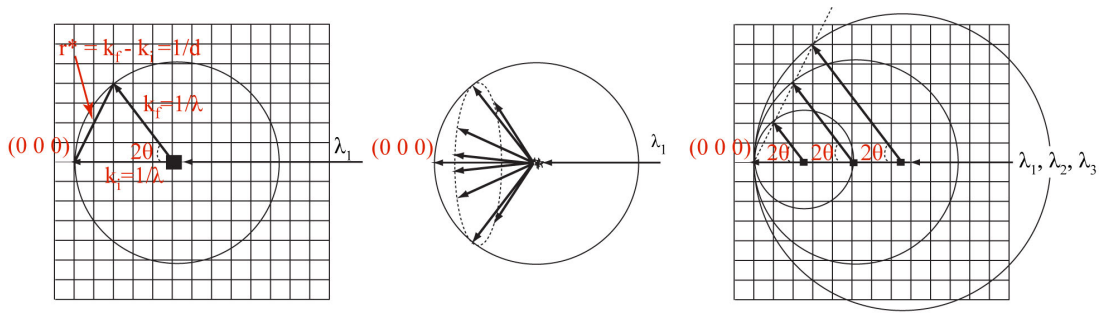

Figure 1.9: The Ewald sphere construction. Left, single crystal diffraction at constant wavelength λ_1. Centre, the effect of averaging over all possible orientations of a single crystal is to project the reciprocal lattice point onto a cone (dotted line) in three dimensions. Right, single crystal diffraction at three wavelengths. Three scattering vectors which simultaneously satisfy the Bragg condition for diffraction at θ ° are shown. The dotted line indicates the projection along reciprocal space for continuous wavelength diffraction which will satisfy the Bragg condition at θ °.

1.3.2. Structure factors

The unit cell may not just consist of a single atom at its origin, but could contain many atoms of different types. To ascertain if these atoms constitute extra periodicity in the lattice, and therefore a sparser reciprocal lattice in certain directions, a phase factor is used which determines if an atom (at fractional coordinates x_i, y_i and z_i) occurs at half a lattice spacing $d_{hkl}/2$. However, the scattering density of the two atoms may not be the same and therefore each atom must be multiplied by its corresponding scattering density function (f_i) to give the structure factor equation:

$$F_{hkl} = \sum_i f_i \exp(2\pi i(hx_i + ky_i + lz_i))$$

The scattering function f_i is different for sites with different atoms on it, and has a different form depending both on the incident radiation and the nature of the scattering density. For the scattering of x-rays by the electron density of atoms, f_i has a strong $\sin\theta/\lambda$ dependency as shown in Figure 1.10. The form factors have been characterised for all elements and their maximum at $\sin\theta/\lambda = 0$ varies in a predictable fashion with Z. For the scattering of neutrons by a nuclei, f_i is characterised by a coherent scattering length b_i, that have been determined experimentally for most stable isotopes[41] and have no $\sin\theta/\lambda$ dependency. They do not vary monotonically with Z, and this can prove to be a useful complementary property to x-ray scattering, where light elements give a weak contribution to the overall diffraction pattern. Additionally, the fact that the form factor does not fall off rapidly with $\sin\theta/\lambda$ enables a more accurate determination of the thermal parameters.

The scattering of neutrons from unpaired electrons of an atom has a rather similar form factor as that of the scattering of x-rays by electron density. However, an unpaired electron has an associated magnetic moment. If this moment is ordered there will be a strong anisotropy of the scattering, with only the component of the moment perpendicular to scattering vector giving rise to diffraction intensity. This in itself is a useful property and aids in the determination of the direction of moments in magnetic structures.[42]

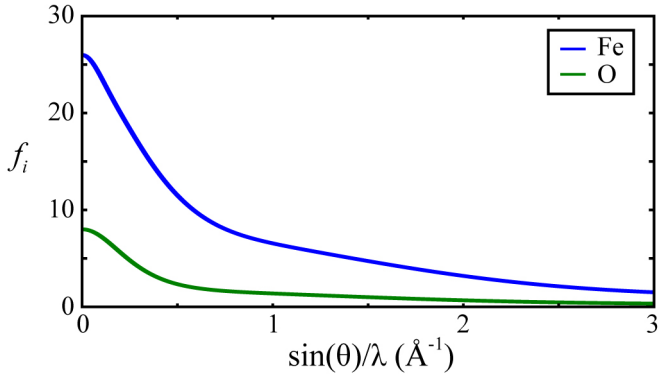

Figure 1.10: Form factor for the scattering of incident x-rays by the electron density of Fe and O atoms as a function of resolution. Figure plotted using values in ref. [43].

The form factor is not complete without taken into account the effects of the vibration motion of the atoms (smearing out of the scattering electron density), which has a strong angular dependency. The correction which must be applied to each form factor is given as $\exp(-B\sin^2\theta/\lambda)$, where B is to be determined experimentally and may be assigned a different value for each symmetry unique atom in the structure and may vary anisotropically with respect to the lattice directions. Fractional occupancy and site disorder will also act to modify the scattering function.

1.3.3. Analysis of diffraction data

Where the structure is not known a priori, structural solution must be attempted, this is equivalent to reconstructing the phases in the structure factor equation for which only the amplitudes are known. Experimentally, diffraction spots which have an intensity related to the F_{hkl} are observed. The process of calculating the reciprocal lattice vectors and hence assigning the observed reflection spots to reciprocal lattice vectors (*hkl*s) is called indexing. In single crystal diffraction experiments it is normal practice after this stage to integrate all reflection intensity and to produce a file which is a list of reciprocal lattice vectors with their

corresponding intensities and estimated standard uncertainties. The task of indexing in single crystal x-ray diffraction experiments is often trivial (for a computer) provided sufficient reflections have been observed. If the entire reciprocal lattice has been measured in some resolution ($\sin\theta/\lambda$) shell, gaps in the lattice will correspond to translational symmetry elements being present in the structure. Additionally, the symmetry of the reciprocal lattice (considering also the intensities) will correspond to the Laue group of the unit cell. The knowledge of the symmetry of the structure normally places sufficient constraints on the phase factors of the atoms, that they may be reconstructed from one of a selection of algorithms providing sufficient data (amplitudes) has been measured. The initial guess at the phases may then be improved by least squares refinement.

In the present work, where relatively subtle phase transitions are being studied, a good initial guess of the crystal structure and hence the structure factors is already known and so these first steps are not required. Instead, symmetry is systematically lowered and broken by moving atoms off high symmetry sites to generate new models. Models may then be improved by performing least square refinement of the structure factors against the experimental observed intensities. As the distortions are subtle it is often necessary to test many different models and evaluate the quality of fit at the end of refinements.

For powder diffraction data the standard approach is not to extract the intensities of the reflections, many of which are convoluted with each other, but instead to reconstruct the diffraction profile using the Rietveld method,[44] and then perform a least square refinement minimising the difference with the experimental profile. Although this method avoids the lengthy data reduction stage, the rather time consuming process of reconstructing the diffraction profile at each least squares cycle means that it is a process only suited for a reasonably powerful computer, and hence it did not gain popularity until the late 1970's. The Rietveld method has been very successfully implemented in refining structures where single crystals of sufficient size are not available, or where phase transitions introduce twinning which is problematic to model in the single crystal diffraction data sets. However, the high correlations of peak intensities, particularly at high resolution, place an intrinsic limit on the number of peaks which can be meaningfully resolved for a powder sample and hence a limit on the complexity of a structure which may be solved by this approach.

The main computationally demanding task in Rietveld refinement is the convolution of the (model) reciprocal lattice with the diffraction profile function. Computationally this is

achieved by a number of Fourier transforms (FTs). The profile peak function will be that of the instrument function convoluted with that of the sample. The sample peak shape is in principle derived from the FTs of the real space crystal lattice. If the lattice may be viewed as being approximately infinite, then the FT is just a delta function as discussed. If, however, the lattice has a finite size, its FT is an array of Lorentzian functions whose FWHM are characteristic of the particle size and vary as a function of 1/cosθ. The samples studied in this work were frequently observed to exhibit peak broadening due to microstrain which has a tanθ dependency.[45] Where the strain is anisotropic and dependent on the direction of the lattice, the contribution to peak broadening may be modelled as:

$\Gamma_A = [\sigma^2(M_{hkl})]^{1/2} \frac{\tan\theta}{M_{hkl}}$ in radians,[39]

where $M_{hkl} = s_{11}h^2 + s_{22}k^2 + s_{33}l^2 + 2s_{12}hk + 2s_{23}kl + 2s_{13}hl$, and its variance can be shown to reduce to:

$$\sigma^2(M_{hkl}) = \sum_{HKL} S_{HKL} h^H k^K l^L \text{ , for H+K+L = 4}$$

Where, for example, S_{400}, H = 4, K = 0, L = 0 corresponds to $\sigma^2(s_{11}, s_{11})$ the variance of the s_{11} defining the lattice, and S_{202}, H = 2, K = 0, L = 2 corresponds to $\sigma^2(s_{11},s_{33})$ the covariance of s_{11} and s_{33}.[39]

All other contributions to the diffraction profile must also be modelled during the reconstruction, these include scale factors of the main phase and any impurity phase, a function to describe the background form incoherent or diffuse scattering, Lorenz-polarisation corrections, and any absorption corrections. Each refined parameter should ideally have a physical meaning, which should refine to a sensible value and lead to a significant improvement in the fit.

During a refinement it is desirable to have a means of evaluating how well the model is fitting the data. The Goodness-of-fit (GOF) attempts to quantify how well the model fits the data with respect to the difference between observed (Y_{obs}) and calculated (Y_{calc}) data, and the number of variables (m) and data points (n) used in the fit, and is given as:

$$GOF = \chi^2 = \left[\frac{\sum_{i=1}^{n} w(|Y^2_{obs,i}| - |Y^2_{cals,i}|)}{n-m} \right]^{1/2}$$

For correctly weighted data (*w*), which contains only random noise, GOF should equal unity if the model is correct. Values in excess of this indicate some systematic error in the model. Values less than one may indicate that the model is being over fit or the weighting of the observations is wrong. The crystallographic figures of merit for powder diffraction are R pattern (R_{wp}) and R weighted pattern (R_{wp}):[45]

$$R_p = \frac{\sum_{i=1}^{n} \left| Y_{obs,i} - Y_{calc,i} \right|}{\sum_{i=1}^{n} Y_{obs,i}}, \qquad R_{wp} = \sqrt{\frac{\sum_{i=1}^{n} w_i \left(Y_{obs,i} - Y_{calc,i} \right)^2}{\sum_{i=1}^{n} w_i Y_{obs,i}^2}}$$

For single crystal experiment Y_{obs} / Y_{cal} may be taken as I_{obs} / I_{calc}, where I is the observed intensity of an integrated reflection, in which cases the R-factor are referred to as R_1 and wR_2 respectively.

It is often possible to achieve an acceptable value of R and GOF but for the model to be incomplete. It is hence also necessary to scrutinise the reconstructed profile fit to the data in Rietveld refinement, or the fit of individual reflections or classes of reflection to the data for single crystal refinements. Significance testing may be required to ascertain if the data is being over fit, R-free refinements to see if the model is fitting noise in the data, and Fourier difference maps should be scrutinised to see if there are any systematic errors.

Once a structure has been refined, the resulting list of atomic coordinates needs to be interpreted to ascertain the physical meaning, and to check that they are physically meaningful. This could involve calculation of bond length, angles and torsions, converting the coordinates into normal modes of either the lattice (such as discussed in Section 1.2.3) or of the coordination polyhedra. The coordinates may also be used as a starting point for an electronic structure calculation (as to be discussed in Section 1.4). Bond valence sums[46] provide a quick empirical method for assessing oxidation states of metal centres based on the proximity of coordinating anions. For an atom *i*, the valance state V_i is given as:

$$V_i = \sum \left(\frac{R_{ij} - d_{ij}}{B} \right),$$

where R_{ij} is a constant of the cation-ion pair in the coordination sphere at a bonding distance of d_{ij}, B is a constant often taken to be 0.37 Å, and the cation-anion pair constants R_{ij} are

well established and have been determined from crystal structures in which there is no ambiguity about the cation valance states.[47]

1.3.4. Instrumentation and production of radiation

In this work, neutron powder diffraction data measured at the neutron spallation source ISIS (at the Rutherford Appleton Laboratory) has been used, and single crystal and powder diffraction data has been collected at the synchrotron sources ESRF and Spring-8. The concept behind the production of neutron and x-rays at these sources is reviewed here, and a few important features of some of the beamlines used are highlighted.

The neutron spallation source at ISIS consists of a pulsed proton accelerator and two target stations (TS1 and TS2). The particle accelerator operates at 50 Hz. Four out of five pulses are sent to TS1 where they hit a tungsten target, and one in five pulses is directed to TS2 at another tungsten target. The result is to excite the nuclei of the metal targets, resulting in the emission of high energy neutrons. These neutrons have wavelengths that are too short to be of much use for diffraction and they must therefore be moderated. The composition, temperature, and distance of the moderator from the diffraction experiment is tailored to suit the needs of the experimental station. Either way, the neutrons will transfer their thermal energy to the moderator as they leak out towards the beamlines. Those that arrive first at the experimental station, will be the ones with highest energy and hence the shortest wavelength. Timing circuits allow the wavelength of each neutron to be measured, as the distance from the moderator to the point at which they are detected is known.

For magnetic diffraction, where long d-spacings are of interest, relatively long wavelength radiation is required. At WISH,[48] TS2 this is achieved by using a liquid methane moderator (subsequently upgraded to solid methane). The much slower operational frequency of TS2 also lends itself well to WISH, where this makes so called frame overlap much less of a problem than at TS1. Frame overlap is where the slowest neutrons leaking out of the moderator overlap with the fastest neutrons of the next pulse. This is avoided by using a Fermi-chopper, which defines the start and end of the pulse and hence limits the shortest and longest wavelength, which may be used in a diffraction experiment. In WISH, due to the aforementioned time between pulses, the Fermi choppers may operate at a relatively high

frequency before frame overlap becomes an issue. At HRPD,[49] TS1 where the flight path between moderator and diffractometer is very long (~100 m), frame overlap is a considerable problem. Here an additional chopper must be used which operates at a fraction (n) of the target station frequency and hence selection only every 1/n pulses from the moderator.

A long flight path is used in HRPD to improve the resolution of the instrument. In general the resolution function for a time of flight diffractometer is,

$$\frac{\Delta d}{d} = \left(\left(\frac{\Delta t}{t} \right)^2 + \left(\frac{\Delta L}{L} \right)^2 + (\Delta\theta \cot\theta)^2 \right)^{1/2},$$

so $\Delta L/L$ is minimised by having a long flight path and $\Delta\theta\cot\theta$ may be minimised by positioning the detector bank (at θ) as close to the back scattering geometry as feasibly possible. One can however, not control $\Delta t/t$, which will increase as lower d-spacings are being measured, (higher resolution) and has some fundamental uncertainty due to the lifetime broadening of the neutrons in the moderator. This said, in general, time of flight powder diffractometers perform substantially better than fixed wavelength diffractometers at low d-spacing ($d < 0.7$ Å).

X-rays are produced at synchrotrons by accelerating electrons or positrons close to the speed of light around a ring, which is under an ultra high vacuum. The ring is normally topped up by a smaller storage ring which itself is injected by a linear accelerator. In the main ring the electrons are accelerated in bunches by the application of a radiofrequency (the RF cavity). The trajectory of the electrons must be changed in order to bend them round the path of the RF cavity; this is achieved by so called bending magnets. This change in momentum of the electron as they are bent round the ring causes them to radiate a white spectrum of light, which is horizontally polarised in the plane of the ring, and is highly focused. The focusing is a consequence of the relativistic effects which demands that in the observer (experimentalist) time frame the electrons appear to be even more bunched together than they are with respect to the electron frame. The x-ray beam is extracted onto a beamline typically via a beryllium window, and is directed through various optics to achieve further monochromation and focusing (for single crystal diffraction only, ID11). In all beamlines used in this work a double Si(111) monochromator has been used in conjunction with a bending mirror, to suppress the generation of the 3λ wavelength.

In practice, most synchrotrons are not rings but polygons. The straight sections allow for insertion devises called undulators to be used, which consist of an adjacent array of magnets which change their magnetic dipole direction at regular intervals (20-30mm). This causes the electrons passing through them to undulate rapidly back and forward. At each peak and trough of an undulation, radiation is emitted which sums together to give a far more intense beam than can typically be extracted from a bending magnet. The distribution of the radiated wavelengths may be tuned by changing the distance between the adjacent array of magnets (the undulators gap) producing a maximum in the λ distribution at the desired experimental wavelength. Insertion devices are used at ID11[50] and ID31,[51] ESRF but at BM19-BL2,[52] Spring8 a bending magnet is used making it easier to change the wavelength by simply scanning the monochromator.

At ID31 where high resolution powder diffraction is the research focus, it is common to use analyser crystals between the sample and detector, allowing the scattering corresponding only to the zero momentum transfer scattering vector to be selected. This has the effect of increasing the resolution in 2θ and greatly decreasing the observed background. The BM19-BL2 diffractometer is designed with absolute intensity in mind, and here an image plate, which covers about 0 – 70 ° 2θ at the standard sample detector distance is used. For single crystal x-ray diffraction at ID11, where resolution in 2θ is less important, a CCD camera is used with an appropriately selected phosphor depending on the incident wavelength.

1.4. Electronic Structure

A description of how electronic structure calculations have been implemented in this piece of work is given in this section. The discussion broadly follows the excellent summary made in ref. [53].

1.4.1. The Born-Oppenheimer approximation

The time independent Schrödinger equation allows the energy (eigenstates, E) of the wave function (Ψ) describing the structure to be written down in terms of a Hamiltonian (H) of the system, $E\Psi = H\Psi$. The problem arises in trying to solve the equation, that the form of the Hamiltonian is dependent on the structure and hence the eigenstates. No progress can be made in solving for E without at least a reasonable first estimate of H. H ($= T_n + T_e + V_{nn} +$

$V_{ee} + V_{ne}$) consists of two terms which describe the kinetic energy of nuclei and the kinetic energy of the electrons, and three terms which describe Coulomb interaction between nuclei, electrons, and with each other. Progress can only be made in the solution of this apparently intractable many body problem by making several approximations. The first is the Born-Oppenheimer approximation where the motion of the nuclei is assumed to be fixed with respect to the electrons.[54] The electrons may now be taken to be in instantaneous equilibrium with the nuclei, leaving $H = T_e + V_{ee} + V_{ext}$ where V_{ext} is the potential energy of the electrons in the potential of the nuclei, which is now modelled as an external potential. T_e and V_{ee} are universal to any system containing electrons, and V_{ext} will vary depending on the composition and structure.

1.4.2. Density functional theory

The one-to-one correspondence of electron density (ρ) with V_{ext} is the corner stone of density functional theory (DFT), which is the most widely implemented method in solid state electronic structure calculations. However, it is not just a useful tool which leads to a tractable approximation to the Schrödinger equation, it is fundamentally significant that if the electron density is determined, the structure (V_{ext}) is also uniquely determined. Or from an experimentalist view point, if the structure is determined, the ground state electron density is uniquely determined. The theorems relating to DFT were developed by Hohenberg and Kohn[55] which expresses the Hamiltonian in terms of the electron density as:

$$H[\rho] = F_{HK}[\rho] + \int \rho(\vec{r}) V_{ext}(\vec{r}) d\vec{r}$$ (second Honhenberg-Kohn Theorem),

where $F_{HK}[\rho]$ is the Hohenberg-Kohn density functional given as; $F_{HK}[\rho] = \langle\Psi|T_e+V_e|\Psi\rangle$. This in itself is not very useful, but the Kohn-Sham equations allow F_{HK} to be rewritten as, $F_{HK} = E_H + V_{xc}$ where E_H is the solution to the non-interacting one electron Hatree equations, and V_{xc} is the exchange and correlation potential. The energy functional is hence,
$H_{KS}[\rho] = T_0[\rho] + V_H[\rho] + V_{xc}[\rho] + V_{ext}[p]$, and the corresponding Hamiltonian for this functional is, $H_{KS} = T_0 + V_H + V_{xc} + V_{ext}$. That is, the Hamiltonian in now reduced to the kinetic and potential energy of classical non-interacting electron gas ($T_0 + V_H$) which is subject to two external potentials, one due to the nuclei (V_{ext}) and the other due to the exchange and correlation (V_{xc}).[56] The Kohn and Sham equations must now be solved, $H_{KS}\varphi_i = \varepsilon_i\varphi_i$, and the electron density may then be calculated from φ_i, the single particle wave functions. As V_{xc} and V_{ext} are still dependent on the electron density a good initial guess of

the structure is still required, and then φ_i may be solved for in an iterative self-consistent manner, with the improved value of the calculated electron density being used to redetermine V_{xc} and V_{ext} at each cycle. As the description stands so far, within the Born-Oppenheimer approximation the solution presented by DFT is exact; however, the calculation of V_{xc} is non-trivial and requires the introduction of a second approximation which is described in the next section.

1.4.3. Exchange correlation

The problem of the exact form of V_{xc}, which by its very nature cannot be accounted for by single electron equations, is tackled by analogy with a homogeneous electron gas, for which the exchange correlation energies have be calculated and tabulated for a range of different densities. In the local density approximation (LDA) some infinitesimally small volume having a constant electron density is assigned the exchange correlation energies of the corresponding homogeneous electron gas of the same density. In a similar manner local spin-density approximation (LSDA) is used for a system in which electron spin (spin polarisation) must be considered.[53]

A more sophisticated approach to solving the problem of the exchange correlation energy is to consider that V_{xc} in a given volume element of the system is dependent not only on the electron density but also on its gradient with neighbouring volume elements. This approach is referred to as the generalised gradient approximation (GGA). This introduces some flexibility into the manner in which V_{xc} is parameterised, and this has lead to many semi-empirical parameterisations of the GGA. However, a popular parameterisation of GGA made by Perdew, Bruke and Ernzerhof, (GGA-PBE) which performs well for a large range of systems is made only in terms of fundamental constants.[57] GGA-PBE is the method used in the present work for approximating the exchange correlation energy.

The Hubbard band model is required to explain the existence of Mott insulators. That is, it explains materials that are insulators due to electron-electron correlations alone. It is characterised by an exchange energy accounting for the tunnelling of electrons between sites of the lattice, and an on-site Coulombic interaction term between the electrons in orbital states of a site.[58] Increasing the value of U has the effect of lowering the energy of the filled states with respect to the empty states, and hence eventually will give rise to an opening up

of a band gap, inducing an insulating state.[59] When the Hubbard model is implemented in DFT (DFT+U), the exchange and onsite Coulombic repulsion values must be chosen with care and should be justifiable in the context of values which yield good agreement with experimental data in other systems. DFT+U provides the most successful framework for calculating electronic structure of metal oxides systems, and is the approach used in Chapter 4.

1.4.4. Basis function

In order to be able to solve ε_i (the eigenvalues), the nature of φ_m (the wave function) still needs to be known. Again, the precise form of the wave function is not known but it may be written as a sum of known function:

$$\varphi_m = \sum_{p=1}^{P} c_p^m \varphi_b ,$$

where P is the size of the basis set and c_p are the coefficients of φ_b which characterises the nature of the basis function. The problem is thus reduced to finding the values of c_p. A sufficiently large value of P will always lead to a good approximation of φ_m, but will often render the calculation too computationally demanding. The key to the solution of the problem is to choose an efficient φ_b which approximate φ_m well with only a small value of P.

In this present work the augmented plane wave + local orbital (APW+lo) approach for approximating φ_m has been used. The APW contribution is given by two parts. The first part is a spherical harmonic type function (atomic orbital like) which describes φ_m in the region close to the atom. This region is often referred to as the muffin tin (MT) sphere, the remainder of the volume not within the various MT of the nuclei in the system is referred to as the interstitial region, and is characterised by plane waves (Bloch wave-like functions). The spherical harmonic functions efficiently describe the MT region and their expansion is analogous to the atomic orbital of a free ion. However, a comparatively larger plane wave basis set is required to accurately describe the interstitial region close to the MT sphere. It is therefore of interest to pick a MT radius (R_{MT}) as large as possible in order to reduce the size of the interstitial region. This is often done such that the R_{MT} of the various nuclei in the system are touching and then these values are reduced by a small percentage (< 5%). The basis set of the plane wave of the interstitial region is controlled by the largest reciprocal

lattice vector (K_{Max}) for which a plane wave is calculated and is often quoted as the dimensionless value $R_{MT}K_{Max}$, where the R_{MT} of the smallest MT sphere in the system has been chosen. The spherical harmonic type functions used in the MT spheres requires that a fixed energy is used to describe the eigenvalues (which has been determined by the initial guess), which can lead to a poor description of the eigenfunctions (seeing as the energy is not yet determined), and additional basis functions, corresponding local orbitals, are hence used which allow for a more accurate description of φ_m within the MT.[53]

Section B: The Verwey structure of Magnetite

2. Introduction to spinels and the Verwey transition

2.1. Spinels and magnetite

The spinel structure was first solved in 1915.[60] Formally the mineral spinel is $MgAl_2O_4$ but it is taken to refer to the large number of oxides XY_2O_4 which crystallise in the same crystal structure. In the normal spinel structure (Figure 2.1 (a)), the Y cations are octahedrally coordinated by oxygen and are twice as prevalent as the X cations which are tetrahedrally coordinated (The A-sites). The spinel is said to be inverse if the A-sites are occupied by Y cations and consequentially the B-sites by a mixture of X and Y cations. However, in reality many derivatives in which $X \neq Y$ exhibit chemical disorder between the two cations making them less suitable systems for the study of electronic and magnetic ordering phenomena.

The aristotypical space group of the spinel is the same as that for the pyrochlore structure, $Fd\bar{3}m$ and indeed the B-sites form their own corner-sharing tetrahedral lattice (Figure 2.1 (c)). This corner-sharing lattice has infinite chains running along the cubic <1 1 0> directions, with each B-site sharing 2 oxygens in common (edge-sharing of octahedra) with an adjacent B-site in the chain (Figure 2.1 (d)). Each B-site is intersected by three such chains and so has six short nearest neighbour B-sites. These intersecting chains also draw out a kagomé lattice as illustrated in Figure 2.1 (d). It is the interactions along these chains which is responsible for many of the observed magnetic and electronic properties in spinels as discussed below.

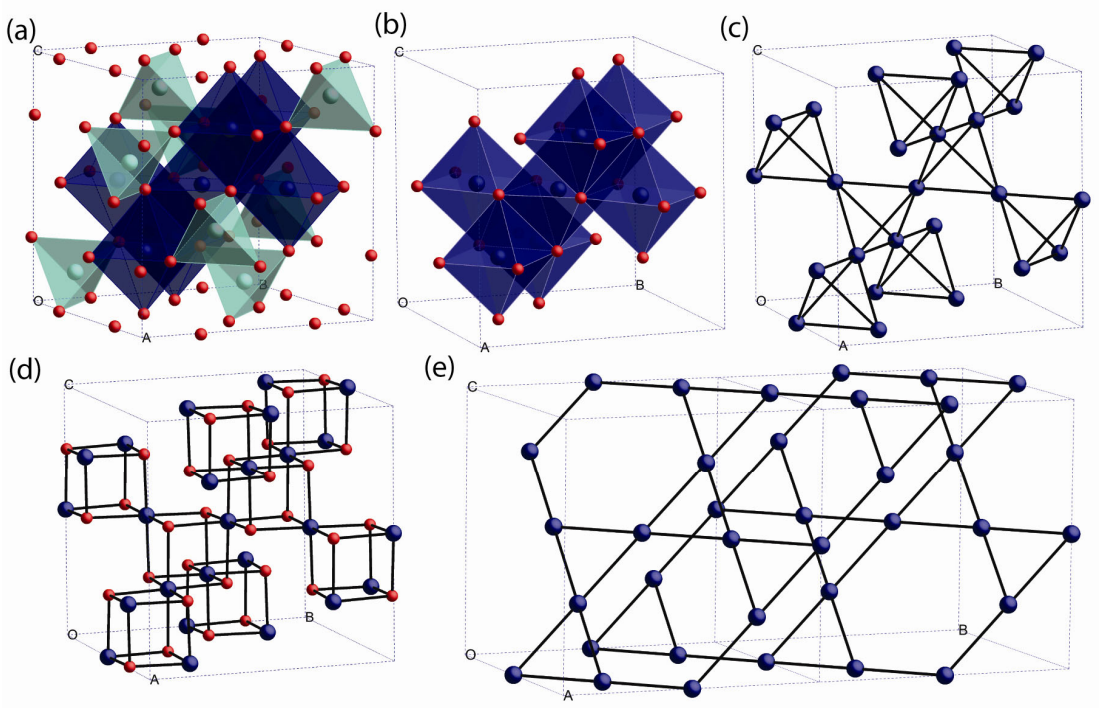

Figure 2.1: a) The cubic structure of spinel showing tetrahedrally coordinated A-sites and octahedrally coordinated B–sites in a cubic close packed lattice of oxygen anions, b) The octahedral coordination of the B-site by oxygen, c) the corner-sharing tetrahedral pyrochlore lattice of the B-site cations in which every cation is connected to six nearest neighbours in infinite chains that propagate through the crystal structure, d) Fe_4O_4 cubes, each B-site is part of two cubes but each oxygen is only part of one cube and is coordinated to three B-sites and one A-site (not shown), e) The kagomé planes of the pyrochlore lattice with the B-sites which are in between planes not shown.

The presence of Jahn-Teller active transition metal cations at the B-site leads to a host of interesting properties and in many cases phase transitions which lead to very complex crystal structures. These transitions arise as a result of orbital order and/or charge ordering phase transitions. A summary of some of the known orbital and charge ordering transitions is made below.

The only known examples of binary (X = Y) spinel oxides are Mn_3O_4 (hausmannite), Fe_3O_4 (magnetite) and Co_3O_4. Both Co_3O_4 and Mn_3O_4 have the normal spinel structure $A^{2+}B^{3+}{}_2O_4$ and so no charge ordering transitions are expected. The presence of a Jahn-Teller active d^4 (HS) cation at the B-site in Mn_3O_4 leads to a tetragonal $a \sim a_c/\sqrt{2}$, $c \sim a_c$ distortion (Figure 2.2) of the cubic $Fd\bar{3}m$ symmetry to $I4_1/amd$ phase which persists up to a temperature of 1443 K, before the cubic structure is realised.[61] The large tetragonal distortion ($c/a\sqrt{2}$ = 1.16) at ambient temperatures, results in the stabilisation of the d_{z^2} orbitals with respect to the $d_{x^2-y^2}$. The B-sites in Co_3O_4 on the other hand are d^6 low spin, and so no tetragonal distortion is observed.[62] Fe_3O_4 is an inverse spinel with semivalent $Fe^{2.5+}$ ($d^{5.5}$ high-spin) B-site cations

and exemplifies the often very complex nature of the charge and orbital order in these systems. It is the main subject of this thesis, the background to which will be discussed in the proceeding sections.

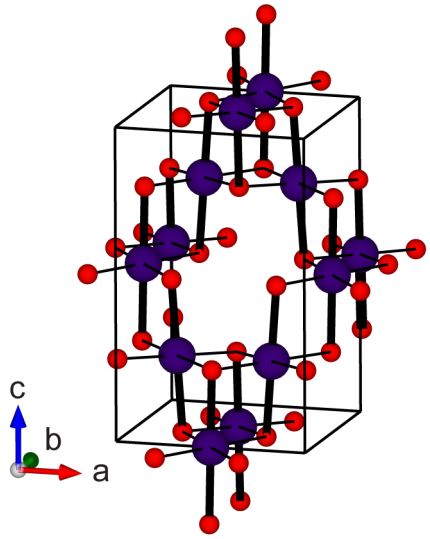

Figure 2.2: Crystal structure of Mn_3O_4,[61] only the B-site (purple) and oxygen (red) are depicted. The Jahn-Teller short (1.93 Å) and long (2.28 Å, in bold) bonds are in the *ab* plane and along *c* lattice directions respectively.

These three primary transition metal oxides broadly represent three possible cases in the spinel structure. (1) There is no orbital degeneracy such as in spinels with B-sites with d^0, d^3 ($CoCr_2O_4$ and $MnCr_2O_4$), d^5 HS ($ZnFe_2O_4$) , d^6 LS (Co_3O_4) d^8 ($SiNi_2O_4$). In this case no orbital ordering is expected, although magnetic (spin ordering) is often observed on both A and B-sites. (2) There is degeneracy of the e_g orbitals such as in d^4 HS (Mn_3O_4). (3) The t_{2g} orbital is degenerate, d^1($MgTi_2O_4$) , d^2 (MgV_2O_4) , d^4 LS , d^5 LS d^6 HS d^7 ($GeCo_2O_4$)[63] . The semivalent B-site cation derivatives (and hence inverse spinels) form a subset of both of (2) and (3) such as $d^{0.5}$ ($LiTi_2O_4$), $d^{2.5}$ (AlV_2O_4), $d^{3.5}$ HS ($LiMnO_4$), $d^{5.5}$ HS (Fe_3O_4), $d^{4.5}$ ($CuIr_2S_4$) in which charge ordering is also to be expected if electrons localise in their ground states.

In case (1) no orbital ordering or structural distortions are expected. However, in $MgCr_2O_4$ at very low temperatures (13 K) distortions are observed that are concomitant with the AFM magnetic order and act to relieve its geometric frustration. [64] Similar distortions are also observed in ACr_2O_4 (Cd, Zn). The transitions in all of these materials may be understood as being driven by energetically favoured spin antiparallel pairing resulting in a doubling of the period of the lattice long one direction (the spin-Peierls effect).[65]

A review, highlighting some of the complex orbital ordering patterns in orbitaly degenerate spinels of type (2) and (3) was made in 2005,[66] and this is summarised below along with some more recent findings.

In $MgTi_2O_4$ (case (3)), Ti is in a d^1 state, the orbital ordered structure (T_{MI} = 260 K, $a_c/\sqrt{2} \times a_c/\sqrt{2} \times a_c$) is associated with a dimerisation of spins and long range ordering, resulting in short Ti-Ti bonds being evident in the crystal structure. Diffraction studies have revealed that alternating short and long bonds are arranged in independent helices running along opposite edges of the Ti_4 tetrahedra (Figure 2.3(a)) such that they never intersect one another accounting for the chiral space group $P4_12_12$ / $P4_32_12$.[67] The structure can be understood in terms of its pyrochlore lattice. As highlighted in ref. [66], there is a limiting number (6) of distinct possible local orbital interactions within each B_4 tetrahedron. Of this, only one has two dimer bonds per tetrahedron, with both bonds having the same orbital character (d_{xz} or d_{yz}). The bonds are therefore orthogonal and on adjacent sides of the tetrahedra. As bond dimerisation may not occur using the same orbital twice on a Ti the next tetrahedra must have its orbital interaction rotated by 120 ° with respect to the first interactions, and in this manner the two orbital ordered helices may never intersect each other.

In $LiMn_2O_4$, an electrode material in lithium rechargeable batteries, a phase transition at 290 K is observed, that is predominantly characterised by a tetragonal compression as expected for transition metal ion with a degenerate e_g set. However, the true structure is much more complicated (orthorhombic, Fddd, $a_c \times a_c \times 3a_c$) due to the long range charge ordering of the semivalent $Mn^{3.5+}$ which arrange themselves in columns of Mn^{3+} and Mn^{4+} that are projected along the c-axis (Figure 2.3(b)).[68]

In AV_2O_4 (A=Mg, Zn, Cd, Mn) (case (3)), orbital ordering transitions are also evident. However, much controversy remains still over their nature. The orbital ordering physics is rather subtle here, and it becomes significant that the point group of the octahedral sites in the aristotypical space group of spinels is not cubic, but trigonal ($\bar{3}$m). This implies that additional crystal field splitting of the e_g / t_{2g} orbitals must already be present. In ZnV_2O_4 a cubic to tetragonal ($I4_1/amd$) transition at 51 K occurs resulting in a *c*-axis compressed.[69] Long range AFM order at 40 K is observed, and inelastic neutron scattering evidences a change from 3-d to 1-d coupling at the structural phase transition.[70] In the cubic phase, the trigonal distortion is very small and the orbital ordering physics is believed to be driven by

spin orbit coupling leading to cooperative orbital ordering. In MnV_2O_4 the space group of the orbital ordered phase is somewhat contentious, but a recent ^{51}V NMR study[71] support assertions that it is $I4_1/a$ in which the presence of two crystallographically distinct B-sites precludes a simple ferro or antiferro orbital ordering but is consistent with a recently proposed model in which chains of B-sites along *a* and *b* have their orbitals rotated 45 ° with respect to each other.[72] Because of the larger trigonal distortion already present in the cubic phase, the spin orbit coupling in this instance acts only as a weak perturbation. MgV_2O_4 has a cubic ($F\bar{4}3m$) to tetragonal transition at 65 K, with AFM order 42 K.[73] Recent work has highlighted it may be somewhere in between the cases of MnV_2O_4 and ZnV_2O_4. The trigonal distortion and spin orbit coupling are of very similar magnitude and one may not be considered to be a perturbation of the other, and instead complex orbitals must be considered.[74]

AlV_2O_4 is a yet more complicated case having a semivalent $V^{2.5+}$ (d^2/d^3) state above its believed charge ordering (CO) temperature (T_{co} = 700K). Below its CO transition a sharp increase in electronic resistivity along with a drop in magnetic susceptibility is observed, suggesting that a spin dimerisation may be responsible for the transition.[75] Due to the site multiplicities of the trigonal crystal structure,[75, 76] a simple fractional charge ordering $V^{2.5+d}/V^{2.5-d}$ does not appear to be possible. Instead a rather complex orbital ordering occurs consisting of a V_7 heptamer unit and a lone V (Figure 2.3 (c)). The heptamer consists of two vertices sharing V_4 tetrahedrons and is predicted to have a singlet ground state, of 18 electrons across 9 bonds, consistent with the drop in susceptibility observed at T_{CO}. This leaves a lone vanadium site which must be V^{3+} (d^2), leading to the rather unusual charge ordering of $V^{2.5+\delta}$ / V_7 $^{17.5-\delta}$. There is no evidence for any further charge or spin ordering transitions.

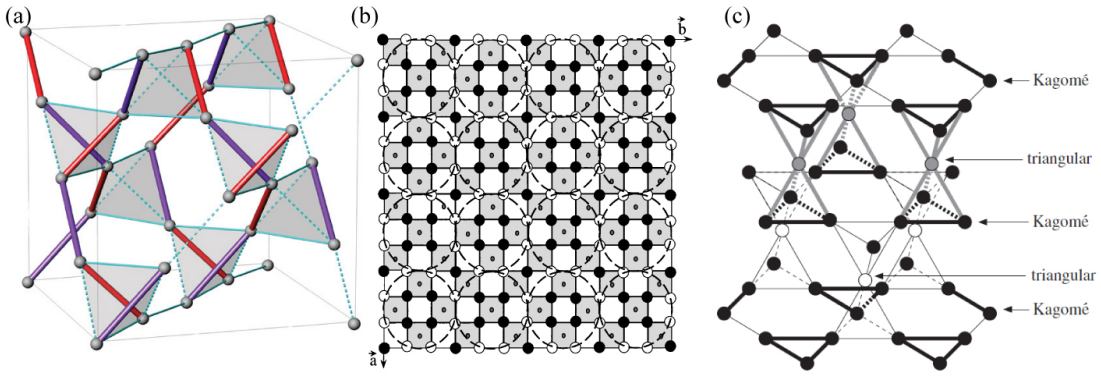

Figure 2.3: (a) The dimerised structure of $MgTi_2O_4$ with chiral helices consisting of alternative short (red) and long (purple) Ti –Ti distances. Figure taken from ref. [66]. (b) The charge ordered structure of $LiMn_2O_4$ with pillars of Mn^{4+} (closed circles) inside columns of Mn^{3+} (open circles). Figure taken from ref. [68]. (c) The low temperature structure of AlV_2O_4 with orbital ordered $V_7^{17-\delta}$ (black and grey filled circles) units and lone $V^{2.5+\delta}$ (open circle). Figure reproduced from ref. [77].

Although not a metal oxide, the case of $CuIr_2S_4$ is worth considering. In this material a complex bond dimerisation of the d^5 LS Ir^{4+} ions occurs at the charge ordering transition, leading to singlet ground states. The Ir^{4+} and Ir^{3+} arrange themselves into hexagons that are different kagomé planes of the pyrochlore structure. Each Ir_6^{4+} hexagon has two non-coplanar Ir_3^{4+} triangular appendages which are in the kagomé plane of the Ir_6^{3+} hexagons and vice versa.[78]

Unlike perovskites, there is a rather limited number of spinel systems which can be readily synthesised, and of these an even smaller number in which consensus has been reached about the ground state ordering, meaning that it is very hard to predict any trends in the rich orbital physics these compounds exhibit, with most of them being their own paradigm.

2.2. Magnetite and the Verwey transition

The discovery of magnetite dates back 3,000 years and its name is believed to originate from the region it was discovered in (Magnesia, North Greece). The first documentation of magnetite and its magnetic properties was by the Romans Lucretius and Pliny the Elder (23-79 AD).[79] It was Pierre Pelerin de Maricourt, a 13th century French scholar, who wrote the first treatise describing what was known about magnets and magnetite, the strongest naturally occurring magnet. In his work he described freely pivoting compass needles, whose application was shortly afterwards found in medieval navigation. It was not until

1601 that a more detailed account of magnetite and magnetism was produced by William Gilbert[80] who first noted that the world was a giant magnet, as well as observing that magnetic materials heated in a flame would lose their magnetism. Magnetite has been at the centre of understanding magnetism. However, until the advent of structure determination by diffraction at the start of the 20th century, little was understood about the mechanisms at the atomic level that determine magnetic ordering.

The structure of magnetite was determined in 1915 by x-ray diffraction[60] and Néel first proposed the ferrimagnetic structure of magnetite[81] in which moments are all oriented along the [1 1 1] direction (Figure 2.4). The structure, which was later confirmed by neutron diffraction,[82] can be rationalised in terms of superexchange[25] between A-O-B resulting in antiparallel alignment of A and B moments with each other due to bond angles substantially < 180 °.

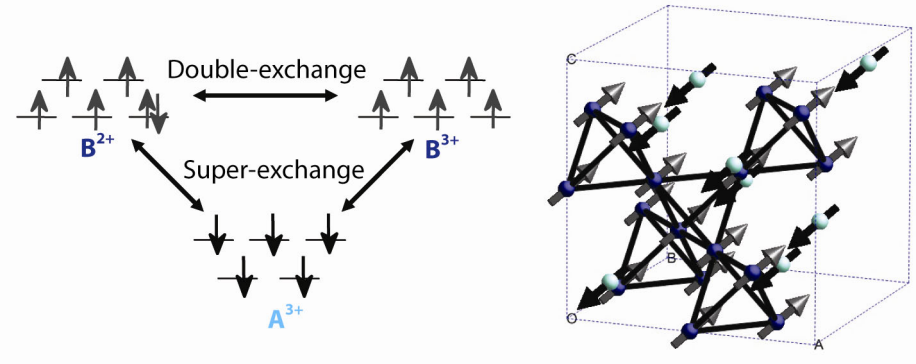

Figure 2.4: Superexchange and double exchange interaction between A and B sites (left) which give rise to the ferrimagnetic structure (right) in which the moments are aligned parallel / antiparallel to the [1 1 1].

The first evidence of a temperature dependent phase change in magnetite was observed in 1926, when a discontinuity in the heat capacity of Fe_3O_4 was observed near 120 K.[83] This was later thought to be linked to change in magnetic behaviour, and an observed change in lattice constant of Fe_3O_4 was found to be coincidental with the discontinuity of the heat capacity,[84] suggesting that a structural change had occurred. As a result of the high conductivity observed in magnetite Verwey surmised that the structure was that of an inverse spinel, with Fe^{3+} ordered on the A-sites and an average valence $Fe^{2.5+}$ on the B-sites whose itinerant electron was responsible for the observed high conductivity. [85] In 1939 Verwey observed a dramatic increase in resistivity of magnetite on cooling below 120 K (Figure 2.5, left).[2] It is these observations which led him to postulate that the phase transition was driven by the ordering of the delocalised electrons inducing a structural phase transition –

this was the first observation of a so called charge ordering phase transition. He went on to propose a possible model based on orthorhombic symmetry in which the average valent $Fe^{2.5+}$ on the B-sties orders into crystallographically distinct Fe^{2+} / Fe^{3+} (Figure 2.5,right).[86] The specifics of the model have since been shown to be wrong, and even the assertion that the structural transition is of charge ordering nature has been questioned. Despite over 70 years of research since Verwey's conjecture, the ground state structure of magnetite has remained an unsolved mystery.

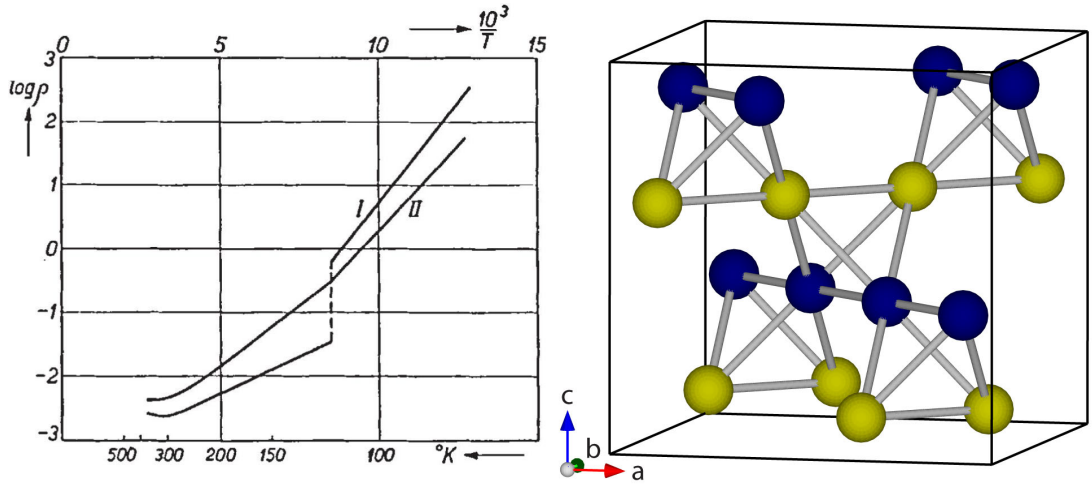

Figure 2.5: Verwey's observation of discontinuity in resistivity at 120 K, left reproduced from ref. [2] and his charge ordered model of magnetite shown in the pseudo cubic setting,[86] which has underlying orthorhombic symmetry, blue and yellow spheres are Fe^{2+} and Fe^{3+} respectively.

Initial neutron diffraction experiments confirmed the presence of superstructure peaks,[87] and several further studies seemed to support an orthorhombic model,[88, 89] consistent with Verwey's models. An x-ray diffraction study observed the presence of six domains in a single crystal of magnetite cooled through its Verwey transition temperature (T_v) implying that the crystal class must be equal to or lower than orthorhombic.[90] Despite the number of supporting papers for Verwey's model in the 1950s, subsequent high resolution neutron diffraction data could not be indexed on the proposed body centred orthorhombic superstructure,[91] and initial neutron diffraction experiments have since been shown to be flawed, due to multiple scattering effects.[92] Not until 1977 was a unit cell proposed on which all the superstructure reflections could be indexed.[93] Owing to the large number of degrees of freedom of the superstructure (space group Cc) a subsequent refinement (Iizumi et al.) against single crystal neutron diffraction data was performed in a sub-cell (Pmca, $a_c/\sqrt{2} \times a_c/\sqrt{2} \times 2a_c$).[94] Later, a combined neutron and x-ray powder diffraction study (Wright et al.) performed in the same pseudo symmetry identified charge order based on the refined atomic displacements, finding a bimodal distribution of BVS.[95, 96] However, although much progress

has been made in elucidating the Verwey structure of magnetite, even the space group of the low temperature structure is not unanimously supported by all experimental evidence, and observation of triclinic domains by x-ray topography has brought the existence of the c-glide plane into question.[97] In addition, observation of the magnetoelectric effect along the monoclinic *b*-axis below T_v has also been taken as evidence that symmetry is no higher than P1.[98]

2.3. Previous structural models

Details of the structural model[96] of Wright et al. in Pmca pseudo symmetry are now given, as it will be instructive to compare this with the results obtained here, later.

The structural distortion is believed to be principally rhombohedral. Formally the rhombohedral distortion must be described as an elongation along the lattice direction [-1 1 1] or [-1 1 -1] rather than the normally assumed [1 1 1] which would require either a change of coordinate basis set from left hand to right handed or a resulting monoclinic structure with a monoclinic distortion with an angle $\alpha \neq 90$ rather than $\beta \neq 90$ both of which are against IUCr convention. Here, in Figure 2.6 the [-1 1 1] is chosen giving rise to a rhombohedrally distorted cell where $\alpha = 90 + \delta$, $\beta = 90 + \delta$, $\gamma = 90 - \delta$ ($\delta \sim 0.3$) in the pseudo cubic setting which gives rise to monoclinic cell in which $a_m > b_m$ and $\beta_m > 90$, consistent with previously published refinements in P2/c.[96]

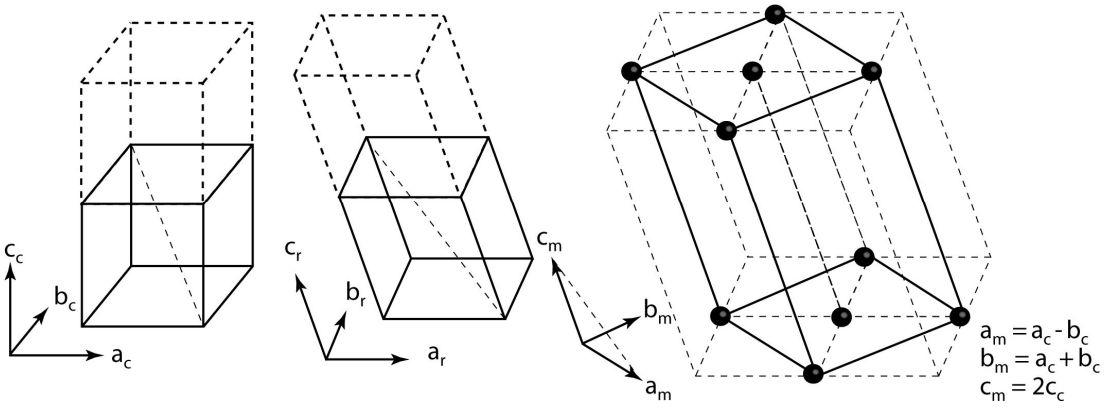

Figure 2.6: The structural distortion in magnetite below T_v is believed to be primarily rhombohedral in nature. The elongation here is drawn along the [-1 1 1] direction which gives rise to the correct monoclinic unit cell with respect to IUCr convention.

As mentioned, the model of ref. [96] was not able to be refined in the full unit cell ($\sqrt{2}a_c \times \sqrt{2}a_c \times 2a_c$), but was instead refined in a sub cell (P2/c, $a_c/\sqrt{2} \times a_c/\sqrt{2} \times 2a_c$) whose relationship to the cubic and Cc structure is shown in Figure 2.7. In both lattice transformations it is the m(XY) mirror plane which contains the rhombohedral axis, (operator -y,-x,z) which is preserved from the cubic structure. In the centro-symmetric subcell approximation the two fold 2(XY) is also preserved.

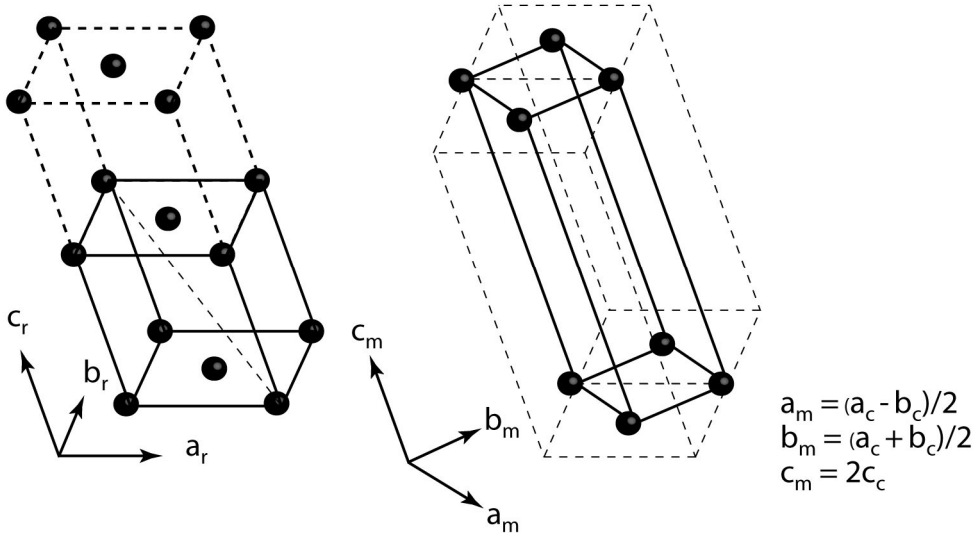

Figure 2.7: The ($a_c/\sqrt{2} \times a_c/\sqrt{2} \times 2a_c$) subcell used in the single crystal refinement of Iizumi et al.[94] and the powder diffraction refinement of Wright et al.[96].

In the subcell refinement there are two A-sites (all general), six B-site cations (4 special, 2 general), and 8 oxygen (4 generals and 4 special). As such the model was still too unconstrained and the introduction of orthorhombic pseudo symmetry was necessary in order for the refinements to be stable. Both Iizumi and Wright et al. refinements give essentially the same results. However, the latter has been analysed in terms of bond valence sums and the findings will be discussed below.

Atom	BVS
A(1)	2.80
A(2)	2.77
B(1a)/ B(1b)	2.49
B(2a)/ B(2b)	2.73
B(3)	2.71
B(4)	2.52

Table 2.1: Bond Valence sums for the Pmca structural model published by Wright et al.. [96]

The four distinct octahedral sites are split into two high valence and two low valence states, (Table 2.1) although the separation is only about 0.2 e^-. The low and high valence states order in alternative layers along the c-axis such that every second layer contains only one valence state and every other layer contains a mixture of valence states. There is a primary charge ordering modulation with propagation vector [0 0 1] with respect to the cubic structure. A secondary modulation of the charge ordering with propagation vector [0 0 ½] accounts for the *c*-axis doubling (Figure 2.8).

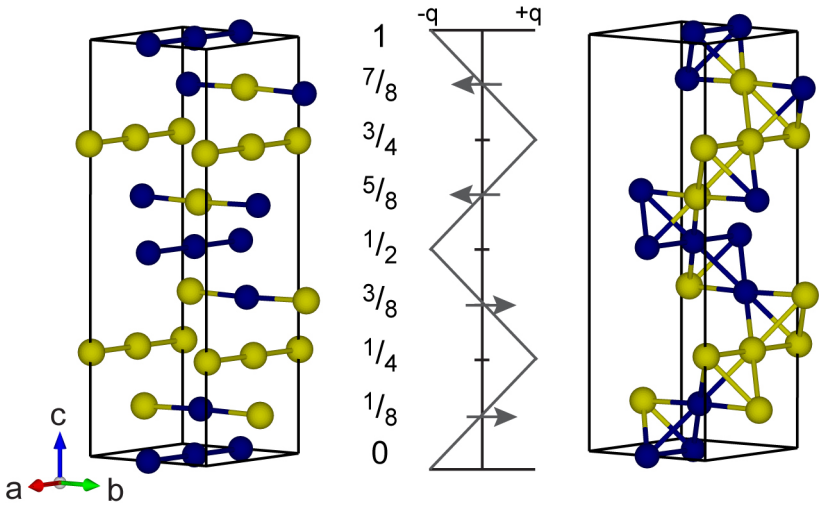

Figure 2.8: A charge density wave (indicated by solid lines) is evident in the Pmca structure with propagation vector [0 0 1]c and additional charge modulation with propagation vector [0 0 ½]c (indicated by directions of arrows) is also present. The B_4 tetrahedra in the Pmca model do not conform to Anderson's rules. Figure is adapted from ref. [96].

The four distinct octahedral sites in the P2/c (Pmca pseudo symmetry) model were believed to be split in a 1:3 ratio into high and low valence sites in the true Cc cell. This means that the valence states observed in P2/c are an average of one high and three low valence states or vice versus. It has been shown that such a 1:3 splitting of the sites gives rises to 16 possible

charge ordered models, in which at most 5 of the 8 Anderson type tetrahedra can be satisfied.[99] Anderson's rules for short range Coulombic repulsions are hence not believed to be satisfied in the Verwey state. This is an important conclusion as large amounts of previous literature including electron diffraction results,[100] have been interpreted in terms of Anderson type ordering of tetrahedra.

The pseudo symmetry refinement has been used as a reference for interpretation of a large amount of research over the past 10 years In particular a large amount of resonant x-ray scattering and theoretical investigations have been undertaken on the ground state of magnetite using the published coordinates. Recent literature is summarised in the next section.

2.4. Recent results

Although there is still much controversy surrounding the nature of the ground state of magnetite, several themes have emerged. The increase in coherence of research findings has no doubt been aided by the acceptance of the importance of the use of a highly stoichiometric samples which display a sharp first order (rather than second order) phase transition. Recent literature published since the structural model of Wright et al.[96] is reviewed in this section along with selected literature which is relevant to the discussion.

A band gap of about 100 meV is believed to exist below T_v.[101, 102] However, many studies maintain that a band gap already exists above T_v and that this represents only an opening up of about 50 meV at T_v.[102-104] Charge carriers of the semiconducting high temperature phase have been proposed to be small polarons possibly of Jahn-Teller (JT) type,[101, 103] with the transition a by product of their condensation.[101] Raman scattering studies on the other hand have found evidence of a spin wave gap below T_v.[104]

X-ray photoelectron studies at the Fe L_3 edge have attributed the valance band structure near the Fermi level to be almost entirely due to B-site ions with Fe^{2+} character.[105] This is consistent with previously published results from magnetic circular dichroism (MCD) which implement Fe^{2+} and Fe^{3+} states on the B-site rather than average valence state to model results.[106] Although resonant X-ray diffraction at the Fe K-edge has been used to conclude

that the B-sites are identical above T_v on a time scale of 10^{-16} s,[107] subsequent investigations by the same group using EXAFS have concluded that local distortions are already present above T_v,[108] and that only a change of regime from static to dynamic occurs at the transition.

It is detailed NMR experiments which have confirmed the space group symmetry of the Verwey state to be Cc, identifying all 8 A-sites,[109, 110] and 16 B-sites[110]. They reveal that there is a rather continuous distribution of B-site resonant frequencies while the A-site frequencies are closely grouped. The continuous distribution of the B-sites is rather hard to reconcile with a charge ordering model. However, muon studies support the existence of charge ordering,[111] and along with EPR results point towards no Anderson-type tetrahedra.[112] NMR data show that there are still significant rearrangements to the underlying atomic arrangement in the temperature range 90 – 120 K.[110]

Resonant X-ray scattering has been the most prolifically used technique to study magnetite in the last 10 years despite limitations arising from absorption, multiple scattering, extinction and twinning which make reliable interpretation of the data problematic. The structural modulation with [0 0 1] propagation vector is generally accepted to arise from a charge ordering like transition.[113-115] However, findings also point to the fact that the structural distortions with period [0 0 ½] propagation vector can be modelled considering only the anisotropy of the tensor of susceptibility of the Cc cell, and it need not be as a result of a charge modulation. This is a surprising result as it was previously believed that the charge ordering gave rise to the superstructure. Detailed resonant X-ray scattering studies at the iron K-edge by Bald et al. [113] have modelled some aspects of the further structural displacements required to produce the full Cc model using the Pmca coordinates of Wright et al. as a starting point. They find that some sites in the Pmca model (B3 and B4) have a significant charge segregation with respect to their site splitting in the Cc structure, indicating that a 1:3 averaging of the valence states of these sites in the Cc model is possible. However, other sites (B1, B2) show almost no charge segregation.[116]

Although charge ordering is now widely accepted by the resonant x-ray scattering community the question now seems to be whether it is truly bimodal, or of a continuous nature with no real definition between 2+ and 3+ states. A recent highly constrained structural refinement in C2/c symmetry against synchrotron powder diffraction data has reached similar conclusions.[117]

Advances in methodology and computational power mean that it has recently been possible to perform electronic structure calculations and optimise the ground state structure of magnetite using only the observed crystallographic unit cell and space group as constraints. The importance of using an onsite Coulombic repulsion term (U) was highlighted early on as being necessary to implement charge ordering in the ground state of magnetite.[118] However, early models just implemented a Verwey type charge ordered structure in which no structural distortion was considered, and the charge ordering was then induced only by the selection of an appropriately large U value in the LDA approximation.[118, 119] These studies neglected that the charge ordering is coupled to the structural distortion, and that there is believed to be a second charge modulation with k-vector [0, 0, ½].[96]

Electronic structure calculations in the subcell refinement $a/\sqrt{2} \times a/\sqrt{2} \times 2a$ in the Pmca model of ref. [96] and the $Pmc2_1$ model of ref. [94] using self interaction correction (SIC)-LSD DFT do not appear to support charge ordering. Here the valence states are explicitly introduced, to see if a particular charge ordering pattern is stable with respect to the SCF-calculation. It has been pointed out,[120] that although the SIC-LSD study of ref. [121] has used the experimental coordinates, a Verwey type ordering was implemented neglecting the experimentally observed charge modulation [0, 0, ½] of ref. [96], and so it is maybe not surprising that this is found to be unstable with respect to the delocalised state. A LDA + U calculation using the model of Wright et al. has rectified this and charge disproportionation of similar magnitudes as in ref. [96] are found,[120] and orbital ordering has been identified in the experimental structure.[122, 123] LDA + dynamic mean-field theory (DMFT) electronic structure calculations suggest the multi orbital electronic correlations arising from the Jahn-Teller distortions are the driving force for the Verwey transition. While differences in minority spin density of the t_{2g} electrons on the B-sites are found to be significant, charge screening means that the overall charge disproportionation of the 3d is rather small, explaining why the experimental BVS separation is also small.[123]

The first attempt at structure optimisation of the Verwey phase was made by Jeng et al.,[124] in which both sub cell and optimisations in the full Cc unit cell were performed. It was found that the coordinates did not change significantly for subcell refinements but did shift significantly in the Cc model from their starting positions. In addition dimer like features in the unrelaxed structure were found to be unstable with respect to structure optimisation.[124] Orbital ordering features have been identified in the relaxed structures, and the ferroelectricity of magnetite has been rationalised in terms of local dipoles at octahedral sites

with a noncentrosymmetric arrangement.[125] However, experimental determination of the Verwey structure is still required to resolve the controversies regarding the nature of the ground state of magnetite.

3. Solution of the Verwey structure of magnetite by single crystal x-ray diffraction

This chapter is divided into four main sections. In Section 3.1 the crystallographic considerations which are specific to studying the Verwey structure of magnetite are detailed, and these were taken into account when designing the experiments of Section 3.2 and 3.3. In Section 3.2 the 'provisional data' are analysed, which gave insight into the nature of the twinning below T_v, but ultimately its analysis did not lead to a full structural model being proposed. The experiment of Section 3.3 has been performed with the short comings of the provisional data in mind, and the quality of this 'final data' and the fit of the proposed structural model are investigated in this section. In Section 3.4 the physical meaning of the refined crystal structure of the Verwey phase is examined.

3.1. Experimental design and crystallographic considerations

The full low temperature structure of magnetite has remained unsolved for over 70 years despite the fact that its unit cell and symmetry are known. There are many barriers which need to be overcome in order to solve the structure. The structure has a large unit cell with 56 atoms in the asymmetric unit, all of which sit on general positions. The scattering from Fe-sites also dominates over that scattering from the O-sites making it harder to determine the positions of the oxygen atoms precisely. Additionally, most of the scattering intensity originates from the fundamental reflections which are already present in the high temperature structure, and hence hold little further information about the subtle nature of the structural distortion. But by far the biggest problem in solving the Verwey structure has been the severe crystal twinning which occurs below the transition.

Some of the problems which need to be overcome in order to solve the Verwey structure of magnetite are highlighted in this section and are illustrated by provisional diffraction data that was collected at ID11, ESRF (see Section 1.3.4 on Instrumentation and production of radiation.)

3.1.1. Extinction, multiple scattering and saturation

Multiple scattering and extinction effects are very prevalent in magnetite and have caused false structural conclusions to be reached in the past[89] and arise due to the high mosaicity typically observed in crystals of magnetite. Upon cooling below T_v, the reduction in extinction as a result of lattice strain (and mosaicity), has been observed to have a far greater impact on the diffraction profile than any structural effects.[126] For any detailed structural studies such effects of extinction and multiple scattering must therefore either be carefully modelled or negated. This can be achieved by operating close to the true kinematic theory of diffraction in which the transmission of a single crystal is assumed to be 100%. Figure 3.1 shows how by using a small crystal and very hard energies (80 keV) it is possible to achieve this. The consequence of this is however, that the interaction of matter is very weak, and hence a source with a high brilliance is required to counteract this effect. The existence of multiple scattering / extinction can be tested for by measuring the same reflections with different orientations of the crystal with respect to the beam, making it possible to discern spurious from true diffraction intensity. Even relatively small multiple scattering effects could prove to be significant in a structure determination where the super structure peaks are up to four orders of magnitude weaker than the fundamental peaks.

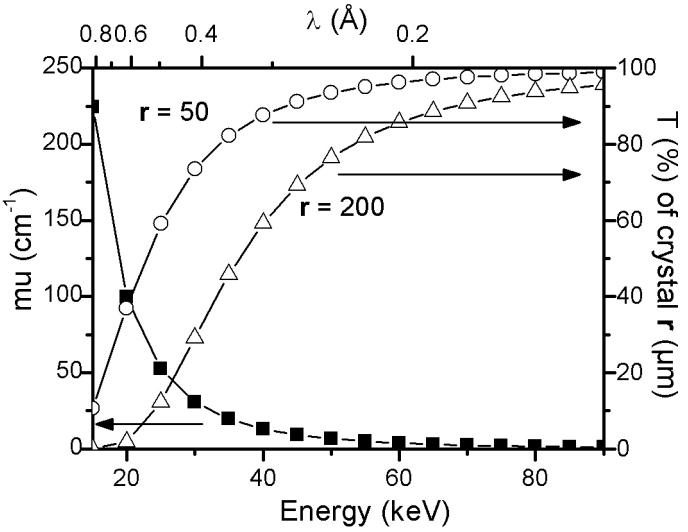

Figure 3.1: Theoretical absorption and transmission of a crystal of Fe_3O_4 with two different radii (r). Absorption and transition values calculated using online web utility 'Compute X-ray Absorption'.[127]

The fact that the observed intensities span 3-4 orders of magnitude is in itself a problem as it requires a detector with a large dynamic range. Saturation of the detector by strong

reflections can make the accurate estimation of intensities of nearby weak reflections impossible as is evident in Figure 3.2. However, by far the biggest problem to overcome in solving the low temperature structure of magnetite is the presence of multiple domains below the transition due to micro-twinning which make indexing and reliable integration of the data very hard. The problem of twinning is discussed below.

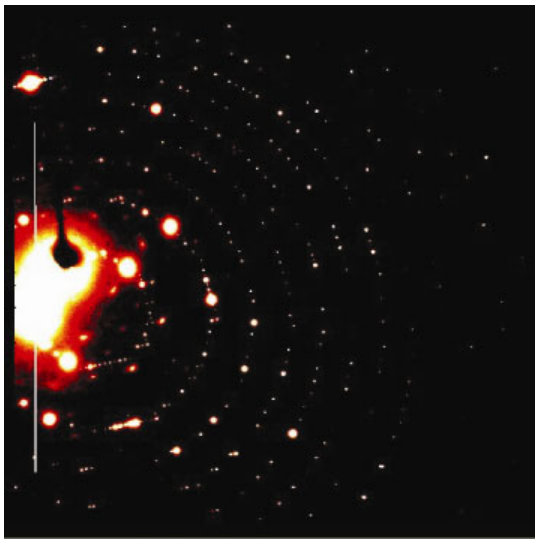

Figure 3.2: A diffraction image of a grain of magnetite (r = 50 μm) collected at ID11 in the front hutch. Large portions of the image are poisoned due to the saturation of the detector from the fundamental Bragg peaks preventing an accurate integration of many of the weak superstructure peaks.

3.1.2. Twinning

The possible types of twinning which can occur at the Verwey transition in magnetite can be analysed using coset decomposition (See Section 1.2.4). The order of the point group ($m\bar{3}m$) of the space group $Fd\bar{3}m$ is 48 and the order of the point group of the space group Cc (m) is 2. Therefore, 24 twin laws are expected. In order to ascertain the possible twin laws for the space group Cc it is necessary to identify the correct element of the space group $Fd\bar{3}m$ which is present in the space group Cc. This is indicated in Figure 3.3, and accordingly the coset decomposition of $m\bar{3}m$ with respect to the point group m(XY) is given in Table 3.1. Here the grouping of the elements related by inversion symmetry has been indicated (coset decomposition done with respect to point group 2/m(XY)), as inversion twins do not give rise to new diffraction spots in reciprocal space.

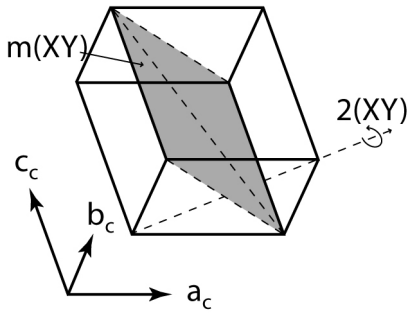

Figure 3.3: Rhombohedrally distorted cubic cell with the preserved symmetry element (m(XY)) that is present in the low symmetry monoclinic Cc structure indicated. The 2-fold 2(XY) is also shown that with m(XY) generates inversion symmetry.

		Element (M)		Inverse of Element (M)	
Coset	Double coset	**a**	**b**	**a**	**b**
1	1	1	m(XY)	$\bar{1}$	2(XY)
2	2	2(X)	$\bar{4}_3$(Z)	m(X)	4_3(Z)
3		$\bar{4}_1$(Z)	2(Y)	4(Z)	m(Y)
4	3	2(Z)	m($\bar{X}Y$)	m(Z)	2($\bar{X}Y$)
5	4	3_2(XYZ)	$\bar{4}$(X)	$\bar{3}_2$(XYZ)	4(X)
6		$\bar{4}$(Y)	3_2(XY$\bar{Z}$)	4(Y)	$\bar{3}_2$(XY$\bar{Z}$)
7		3(XYZ)	$\bar{4}_3$(Y)	$\bar{3}$(XYZ)	4_3(Y)
8		$\bar{4}_3$(Y)	3(XY$\bar{Z}$)	4_3(Y)	$\bar{3}$(XY$\bar{Z}$)
9	5	3($\bar{X}$YZ)	m($\bar{Y}$Z)	$\bar{3}$($\bar{X}$YZ)	2($\bar{Y}$Z)
10		m(XZ)	3_2($\bar{X}$YZ)	2(XZ)	$\bar{3}_2$($\bar{X}$YZ)
11	6	3(X$\bar{Y}$Z)	m(YZ)	$\bar{3}$(X$\bar{Y}$Z)	2(YZ)
12		m($\bar{X}$Z)	3_2(X$\bar{Y}$Z)	2($\bar{X}$Z)	$\bar{3}_2$(X$\bar{Y}$Z)

Table 3.1: The symmetry elements of point group $m\bar{3}m$ grouped in terms of their coset and double coset derived from the decomposition with respect to point group m(XY). The cosets are grouped with their inversion related pairs, giving rise to 24 distinct domains possible in the low temperature structure of magnetite, and 12 where inversion twinning is ignored. Cosets which are within each other's double coset are separated by a broken line. A twin law generated from different symmetry elements within the same coset are equivalent under the lattice degeneracy of $m\bar{3}m$.

In order to apply the twin law to the monoclinic setting, the symmetry operator must be transformed by using the triple product $T^{-1}MT$ where T is that lattice transformation of

Section 2.3 and M is the lost symmetry element of $m\bar{3}m$ which generates the twinning – it is of vital importance that the selected symmetry operator and the lattice transformation are consistent with each other. Four of the possible twin laws are summarised in Table 3.2. The remaining 19 may be generated as a product of these, and by considering the degeneracy of the cubic to monoclinic lattice transformation. Table 3.2 is summarised graphically in Figure 3.4.

T is:

$$T = \begin{pmatrix} 1 & 1 & 0 \\ -1 & 1 & 0 \\ 0 & 0 & 2 \end{pmatrix}$$ Where the lattice transformation is: $(a,b,c)T = a-b, a+b, 2c$

Symmetry element	Matrix form (M)	Twin Law	Name
1	$\begin{pmatrix} 1 & 0 & 0 \\ 0 & 1 & 0 \\ 0 & 0 & 1 \end{pmatrix}$	$\begin{pmatrix} 1 & 0 & 0 \\ 0 & 1 & 0 \\ 0 & 0 & 1 \end{pmatrix}$	Principal domain
$\bar{1}$	$\begin{pmatrix} -1 & 0 & 0 \\ 0 & -1 & 0 \\ 0 & 0 & -1 \end{pmatrix}$	$\begin{pmatrix} -1 & 0 & 0 \\ 0 & -1 & 0 \\ 0 & 0 & -1 \end{pmatrix}$	Inversion twin
2(X)	$\begin{pmatrix} 1 & 0 & 0 \\ 0 & -1 & 0 \\ 0 & 0 & -1 \end{pmatrix}$	$\begin{pmatrix} 0 & 1 & 0 \\ 1 & 0 & 0 \\ 0 & 0 & 1 \end{pmatrix}$	Orthorhombic twin a/b
2(Z)	$\begin{pmatrix} -1 & 0 & 0 \\ 0 & -1 & 0 \\ 0 & 0 & 1 \end{pmatrix}$	$\begin{pmatrix} -1 & 0 & 0 \\ 0 & -1 & 0 \\ 0 & 0 & 1 \end{pmatrix}$	Monoclinic twin a/-a
3_2(XYZ)	$\begin{pmatrix} 0 & 0 & -1 \\ -1 & 0 & 0 \\ 0 & -1 & 0 \end{pmatrix}$	$\begin{pmatrix} 0.5 & 0.5 & -1 \\ -0.5 & -0.5 & 1 \\ 0.5 & -0.5 & 0 \end{pmatrix}$	Tetragonal twin

Table 3.2: The twin laws for the four types of twin domains which can be present in magnetite below T_v. The twin laws may be used to transform the *hkl*s indexed of one domain to that of another domain.

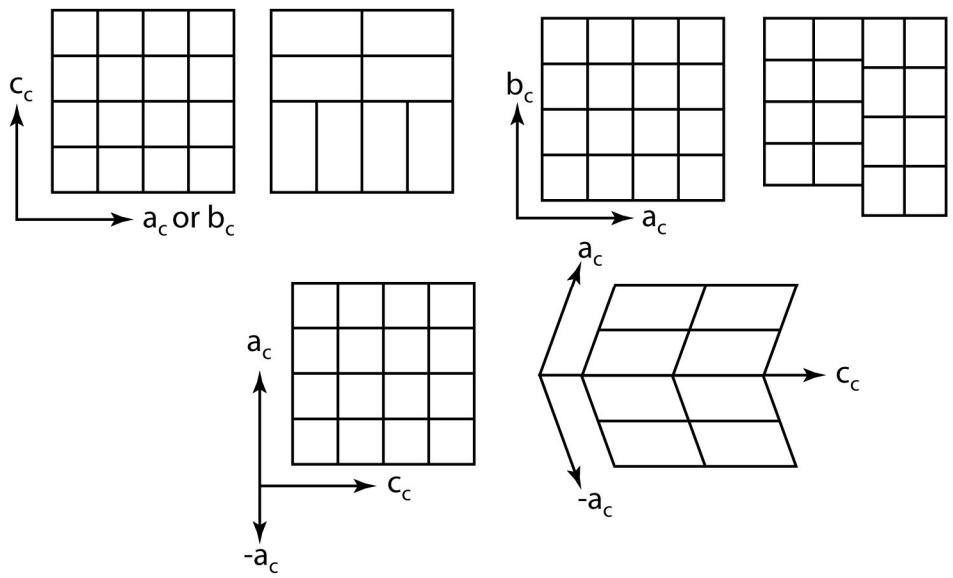

Figure 3.4: The three essential types of lattice twinning in magnetite are illustrated in appropriate planes. All combinations thereof, coupled with inversion twinning (where the lattice remains unchanged) are possible, giving rise to 24 domains.

In single crystal experiments twinning can manifest itself in different ways. If the twinning is merohedral, a single orientation matrix can still be used to index the pattern, and all reflections from the various domains are overlapped in reciprocal space. In the Verwey phase only the inversion twin is truly merohedral, and due to the fact that the anomalous scattering arising from Fe and O at hard energies (75 keV) is negligible, its existence would not hinder accurate structure determination. However, other types of twinning which cause an averaging of the structure factors, may be treated in the pseudo merohedral twins. In this, a twin lattice within a certain tolerance may be indexed and its intensities integrated under the same orientation matrix. In such incidences where the twin lattice and that of the principal domain are coincident, it is normally possible to perform data reduction successfully; however, determination of the correct space group will often be problematic. The twinning will have two effects in this case; it will cause the diffraction pattern to appear to have a higher Laue class than the metric symmetry; and due to contamination of systematic absences by twin domains, determination of the correct space group will often be problematic.

In the case of the low temperature structure of magnetite where the space group has been established independently, the violation of the extinction conditions can be used to ascertain the degree of twinning. In the Cc space group, the $(2h\ 0\ 2l+1)_m$ reflections are expected to be absent in this setting but the $(0\ 2k\ 2l+1)_m$ are not.[43] As the orthorhombic twin law in Table

3.2 interchanges these two conditions, it is therefore expected that the twin fraction (n) can be calculated from the ratio of the intensity of these two reflections I_{0kl} and I_{h0l}:

$$n = \frac{1}{\left(I_{0kl} / I_{h0l} \right) + 1}$$

Unfortunately no such condition can be derived for the monoclinic *a* / *-a* type twinning as these domains have the same extinction conditions with respect to each other, and only the inspection of the diffraction pattern, or a reciprocal space reconstruction will reveal the degree of twinning. Figure 3.5 shows such a splitting of diffraction spots at the edge of a detector due to the breakdown in the merohedral approximation of the monoclinic type twinning. The full twin law is given below, but as the off-diagonal term has a value of approximately -5.6 x10^{-3} only for *hkl*s where *h* and *l* are large, will a splitting of reflections be observed.

$$\begin{pmatrix} -1 & 0 & \frac{2a\cos\beta}{c} \\ 0 & -1 & 0 \\ 0 & 0 & 1 \end{pmatrix}$$

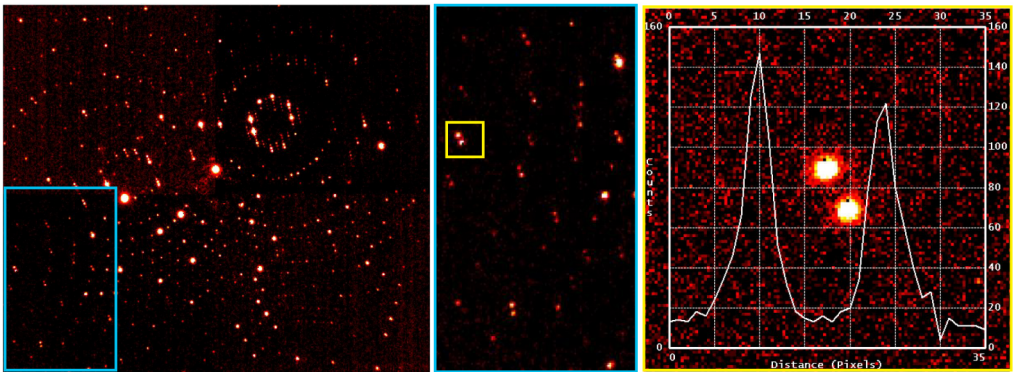

Figure 3.5: A diffraction image collected at ID11(left hand panel) on a crystal of magnetite at 90K displaying near 50% fraction of the monoclinic twin domain. The twinning is most evident at high angles (central panel) for *hkl*s where the indices *h* and *l* are large. In the right hand panel the intensity profile is shown for a twinned reflection showing that they are clearly resolved.

Tetragonal type twinning gives rise to half integer reflections which respect the low temperature cell ($\sqrt{2}a_c \times \sqrt{2}a_c \times 2a_c$). Here the approach is to index all the data on a pseudo cubic cell $2a_c \times 2a_c \times 2a_c$ in which the degree of twinning can be ascertained by comparing

relative ratios of the $(h/2\ k\ l)_c$, $(h\ k/2\ l)_c$ and $(h\ k\ l/2)_c$ reflections. In such a manner the uniqueness of the *c*-axis doubling maybe established.

3.2. Provisional Data

A provisional data set was collected by Jon Wright at ID11, ESRF on a grain of magnetite taken from the sample previously used for the powder diffraction study of ref. [96]. The crystal was mounted on the phi axis of the diffractometer in the rear hutch and scans were collected at exposure times of 1 and 5 seconds per frame with phi rotations of 0.1 °, 0.2 ° and 1 °. The wavelength for the data collection was $\lambda = 0.26471(5)$ Å.

The initial data were integrated on 16 × 16 × 16 cell using in house software "peaksearch"[128] to test for the degree of twinning. In Figure 3.6 the indexed reflections have been split up into three classes, according to whether the *hkls* are half-integer *h*, *k* or *l* with respect to the high temperature cubic structure. A principal cell doubling axis is clearly established along **c***, with half integer reflections along **a*** and **b*** about two orders of magnitude weaker. The clear dominance of the intensity of the half integer *l* reflections over those with half integer *h* or *k* is promising, but as superstructure peaks are typically orders of magnitude weaker than the fundamental peaks, even these small populations of tetragonal type twin domains could systematically corrupt the true intensities in a single domain refinement.

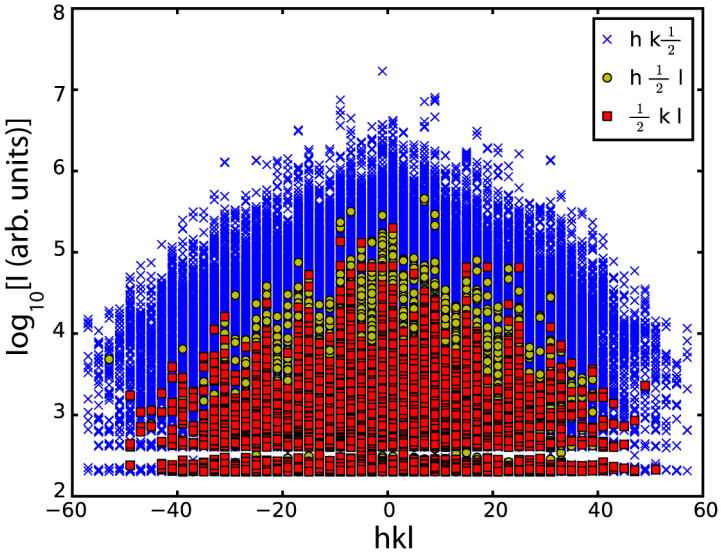

Figure 3.6: Intensity for reflections of half integer type indexed with respect to the high temperature cubic unit cell. It is evident that the *l*/2 reflection intensities are orders of magnitude greater than the *h*/2 or *k*/2 reflections, indicating that the *c*-axis is unique to a good approximation.

The complete absence of $(h\ 0\ 2l{+}1)_m$ type reflections would both confirm the presence of the c-glide plane in the monoclinic space group Cc and absence of any orthorhombic type twinning. As the crystallographic space group is well established, it is taken here in Figure 3.7, as an indication of the presence of a small fraction of the orthorhombic type twin domains in the low temperature crystal.

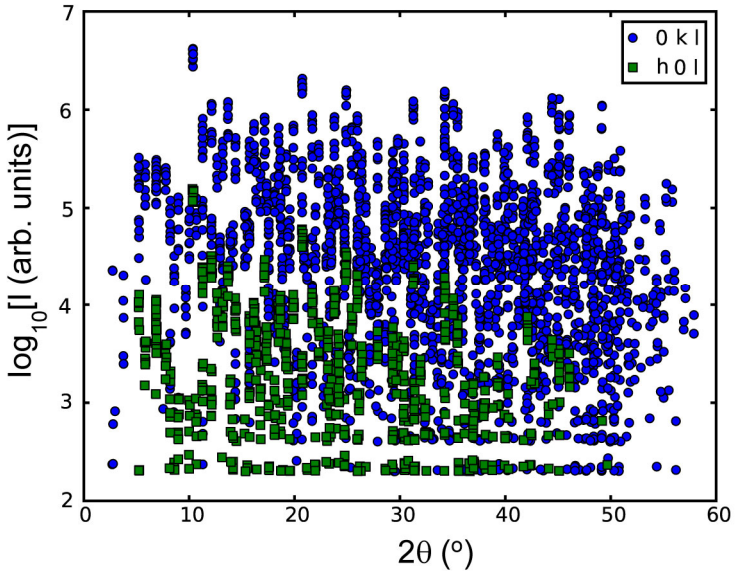

Figure 3.7: Reflections of $(h\ 0\ 2l{+}1)_m$ and $(0\ k\ 2l{+}1)_m$ type indexed on the monoclinic cell $\sqrt{2}a \times \sqrt{2}a \times 2a$ reveal that there is a principal domain with respect to the orthorhombic *a*/*b* type twinning.

An attempt at quantifying the magnitude of the twinning is made in Figure 3.8 by plotting the intensity of the same reflection arising from different domains against each other, a regression line fit can be made and a twin ratio of about 3% established. The weak correlation of the plot is probably due to the fact that the intensity of the reflections arising from the twin domains are only marginally above the noise levels, and therefore subject to large errors.

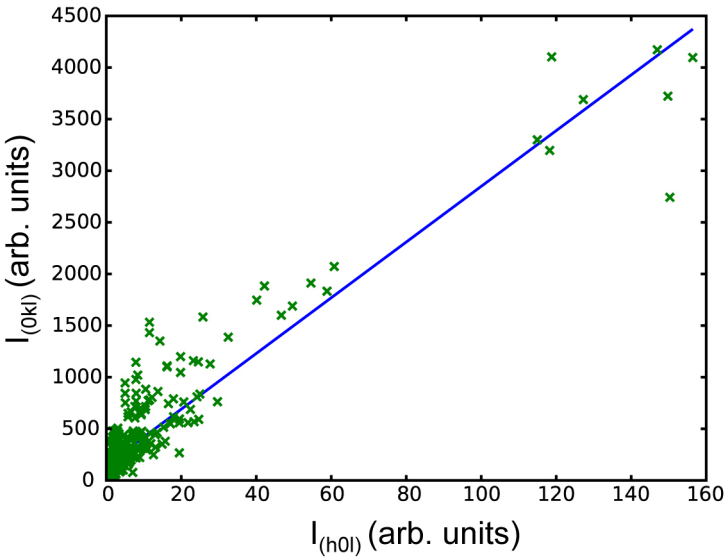

Figure 3.8: Intensity of twin related reflections for the orthorhombic type twinning plotted against each other. A least squares regression line is shown on the plot.

It is important to ascertain if sufficient numbers of reflections corresponding to the various characters of the superstructure are observed. The superstructure may be viewed as the sum of the distortions to the high temperature cubic structure arising from the (0 0 0), (0 0 ½), (0 1 0) and (0 1 ½) propagation vectors. These points in reciprocal space, are conventionally labelled as Γ, Δ, X and W respectively with respect to the Brillouin zone (BZ, which defines the reciprocal space around a lattice point) of the face-centred cubic cell (Figure 3.9). [129] Distortions arising from these points in the BZ will have different extinction conditions, and it is hence be possible to test if the data are likely to be sensitive to a particular type of distortion.

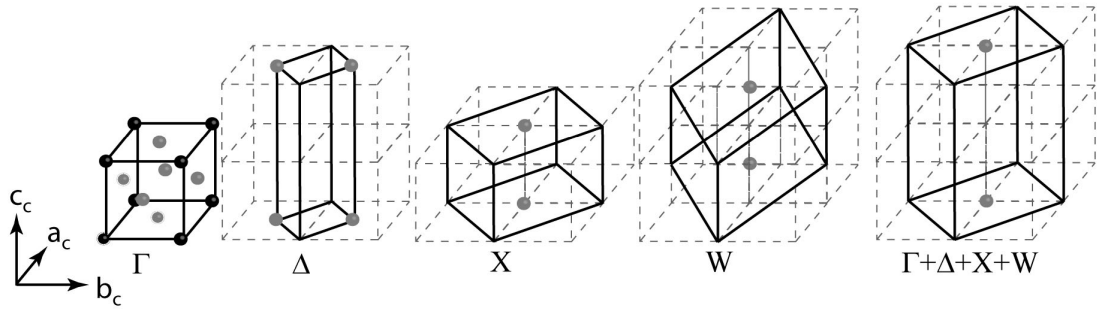

Figure 3.9: The unit cells implied by the relevant points / lines of the Brillouin zone of the face centred Fe_3O_4 structure below Tv. All points are contained within the C-centred unit cell on the right. For ease of visualisation here only, a right hand axis basis set is used rather than the conventional left handed basis.

Summarised in Table 3.3 are the allowed reflection conditions for the various lines and points of the BZ of the face centred structure of magnetite, which have order parameters that are active below the transition. It can be seen from Figure 3.10 that the Γ-point reflections are over an order of magnitude more intense than the Δ point reflections which are themselves an order of magnitude greater than the X and W point reflections. The X and W reflections for the most part are those not captured by the Pmca subcell approximation. Here, it can be seen that there are a large amount of these reflections, and that any unconstrained refinement should be highly over determined.

Point	*k* =	Reflection conditions cubic setting.	Reflection conditions Cc.	No. of parameters
Γ	[0, 0, 0]	h+k, h+l =2n, k+l =2n	h=2n, k=2n, l=4n	25
Δ	[0, 0, ½]	h+k = 2n, l = n/2	h=2n, k=2n, l=n	34
X	[0, 1, 0]	h, k, l = n	h+k=2n, l=2n	67
W	[0,1, ½]	h, h = n, l= (2n+1)/2	h+k=2n, l=2n+1	42
Overall				168

Table 3.3: Reflection conditions arising from the distortions occurring in various points of the BZ of the cubic structure. The number of distortion modes associated with each point on lowering of the symmetry to Cc are also given.

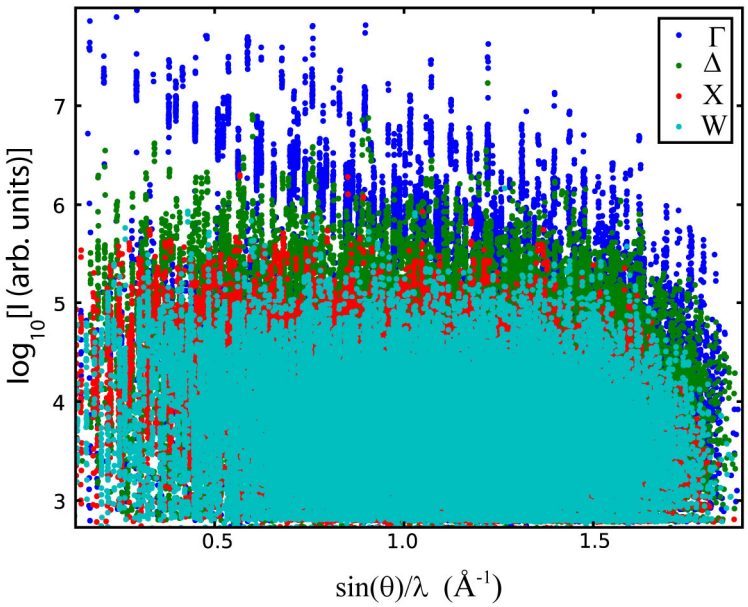

Figure 3.10: Intensity of the reflections belonging to each *k* point of the face centred cubic lattice that are involved in the distortion to Cc symmetry. The Γ point reflections are over an order of magnitude stronger than the Δ point reflections which themselves are almost an order of magnitude more intense than the X and W reflections. The reflections are taken from images collected from phi-scans with and exposure time of 5 s / 0.2 °. In house software Peaksearch[128] was used for the data reduction.

Attempts at merging the different data sets (integrated in SAINT[130]) of varying exposure time were unsuccessful, leading always to the majority of the weak peaks being omitted by programs SADABS[131] or SORTAV[132]. Initial refinements were therefore performed in P2/c ($a/\sqrt{2} \times a/\sqrt{2} \times 2a$) against a data set collected with low exposure time (1 second) in Crystals,[133] the details are given the Appendix A. In this setting the weakest class of reflections (h_m , k_m , l_m = odd) are not present as they become half integer with respect to the subcell setting. It can be seen that these reflections are very weak (Figure 3.11) in this data set, and attempting to model the full superstructure led to refinements that were unstable.

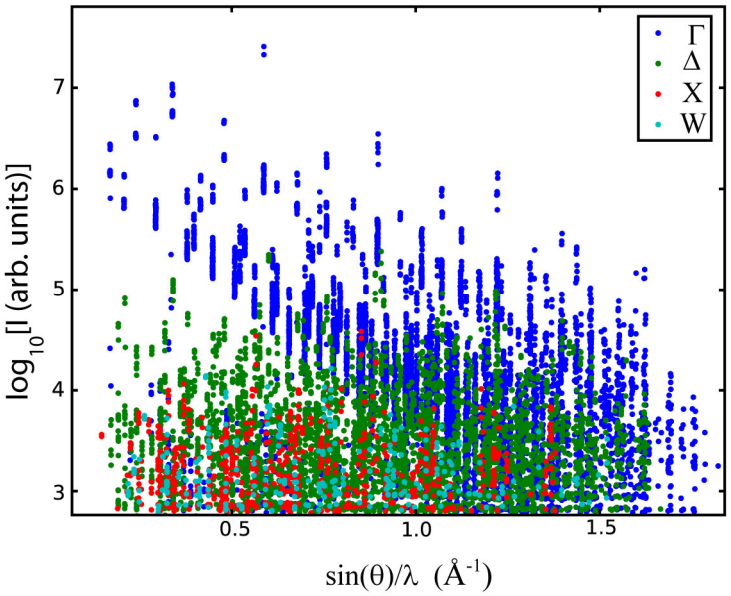

Figure 3.11: Integrated intensities from a data set collected with 1 s / 1 ° exposure time. Insufficient reflections are observed in the X and W point to warrant a refinement in the full unit cell.

A twin law consistent with the two fold rotation about *z* axis was found by the program ROTAX[134] which is incorporated into Crystals. This is the monoclinic type twinning, and the refined twin fraction of ~ 0.5 is consistent with that expected from comparing the relative ratios of intensities of twinned reflections such as was done for this crystal in Figure 3.5. However, the final R factor of 14 % indicates that the model is far from complete.

The results from the refinement are compared against a previously published model in Pmca Appendix A. Although the agreement looks reasonable, the calculated bond valence sums (Table 3.4) from the model differ significantly from those of ref. [96]. The largest disagreements are between A(1) and B(4) sites with all others sites in fair agreement. B(2a) / B(2b) which are averaged in the Pmca pseudo symmetry constraints of ref. [96] are substantially split in the refined model here.

Atom	BVS	BVS of ref. [96]
A(1)	2.635	2.80
A(2)	2.798	2.77
B(1a) / B(1b)	2.42 / 2.49	2.49 / 2.50
B(2a) / B(2b)	2.640 / 3.00	2.73 / 2.73
B(3)	2.71	2.71
B(4)	2.62	2.52

Table 3.4: Bond Valence sums for the P2/c refinement compared with those the P2/c with Pmca pseudo symmetry refinement [96].

At this stage no further analysis was made as data of superior quality were collected from different crystals.

3.3. Full structural solution

3.3.1. Experimental

Six microcrystals of radius 20-200 μm of highly stoichiometric magnetite were taken in turn from grains of the powder sample used in ref. [96] and were fished from a paratone oil suspension into a litholoop with a diameter of 40-200 μm. The litholoop was mounted on a goniometer and placed on the omega / phi Huber diffractometer in the first hutch of the undulator source at ID11, ESRF. Each crystal was aligned on the centre of rotation of the diffractometer, and in the centre of the 100μm focused beam. Diffraction images were collected of the crystals at RT to verify that they were single domains. The crystals were then aligned with the use of a bar magnet (~ 0.1 T at sample) and their own magnetic moment such that the easy-axis of the magnetite crystal was aligned with the poles of the bar magnet. Once aligned, the crystal was cooled to 130K to freeze the paratone oil, and the bar magnet was moved into closer proximity in order to effect saturation of the alignment of magnetic domains. After 20 minutes the crystal was cooled below its Verwey transition to 90K and the magnet removed. The crystal was again verified to be on the centre of rotation of the goniometer axis, and in the centre of the beam. The 2K Frelon camera was centred on the direct beam for the majority of the data collection, but some data were collected out to higher resolution with the beam stop at one edge of the detector. Omega scans were

collected at phi = 0 ° and phi = 180 ° at 0.5 s / 1 ° up to 5 s / 0.2 ° exposure time, with varying degrees of beam attenuation as appropriate. The wavelength was calibrated to be λ = 0.16653(1) Å by measuring the Si (1 1 1), (3 3 3) and (5 5 5) reflections. An incident angle correction for the efficiency of the phosphor of the detector was calculated by measuring the intensity of the scattering from a vial of water as a function of 2θ. [135]

3.3.2. Discussion of crystal and data quality

Crystals were screened in order to obtain data sets which had the lowest degree of twinning. One crystal was discarded straight away (Xtal5), as although it appeared as a single grain under a microscope, diffraction images revealed almost power like rings. Xtal1 a shard of dimensions 20 × 20 × 80 μm proved to be too weakly scattering while Xtal3 (r = 100 μm) was found to be very severely twinned after initial data collection.

Initial attempts at detwinning the crystals (Xtal1 – Xtal3) with respect to achieving a unique *c*-axis, were unsuccessful. These involved collecting enough data to index a crystal at 130K and then attempting to align it so that the [1 1 1] magnetic easy axis was along the direction of the magnetic field of a bar magnet. Once this was achieved, after a period of time, the crystal was cooled through its Verwey transition. Figure 3.12 demonstrates that there is a significant amount of *c*-axis twinning present in Xtal2 to which this method was applied. Xtal4 and Xtal6 data sets were, on the other hand, collected on crystals which were aligned by allowing the crystals to freely rotate in the external magnetic field of the bar magnet as detailed in the experimental sections 3.3.1. Data collected from crystals treated in this manner show significant less twinning as is evident from Figure 3.12, with Xtal6 having an entirely unique cell doubling direction.

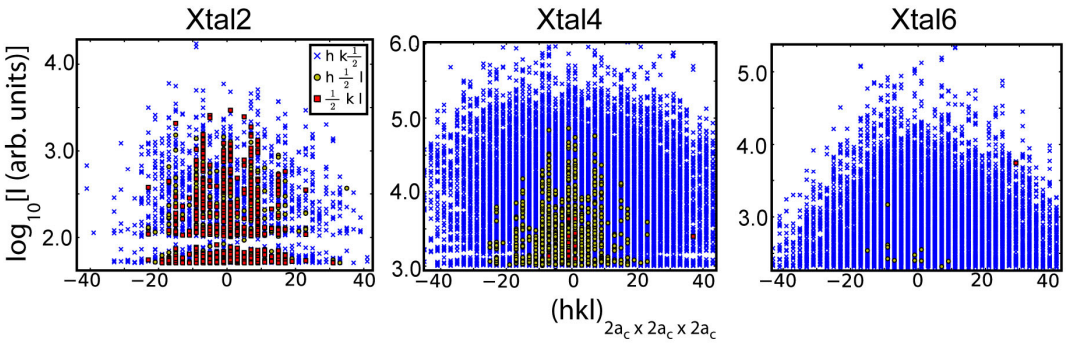

Figure 3.12: The degree of the uniqueness of the supercell axis doubling in the three most promising crystals measured at ID11. The crystals, Xtal2, Xtal4 and Xtal6 have radii of 40 μm, 100 μm and 20 μm respectively.

Data collection time was hence focussed on Xtal4 and Xtal6 which were deemed to be the two most promising candidates for structural solution, being of far superior quality to the previous mounted crystals (Xtal1-Xtal3). Although it is evident from Figure 3.12 that both have an almost unique *c*-axis, Figure 3.13 illustrates that Xtal4 has a significant twin fraction of the orthorhombic type twin. However, Xtal6 superstructure reflection could prove to be too weak for an unconstrained refinement as its scattering power is at least an order of magnitude less than that of Xtal4.

The reciprocal space reconstruction (Figure 3.14) reveals that even Xtal6 is not completely untwinned with a small amount (~ 10 %) of twinning of the monoclinic type present. However, in Xtal4 both monoclinic domains are present in equal fractions. Integration of the separate domains in SAINT for these crystals, and least squares refinements of the structure in Shelxl with the appropriate twin laws, confirm the twin fractions estimated by visual inspection of the data.

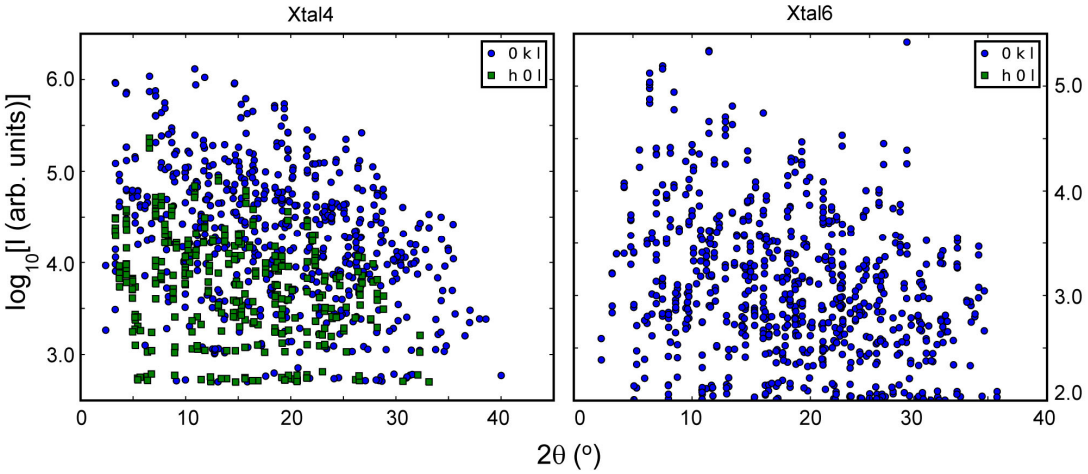

Figure 3.13: The degree of orthorhombic twinning present in Xtal4 and Xtal6 as evidenced by the violation of the *c*-glide reflection (*h* 0 *l*) for *l* = odd. Xtal4 has at least 10% of a secondary twin domain while Xtal6 appears only to have one orthorhombic type domain.

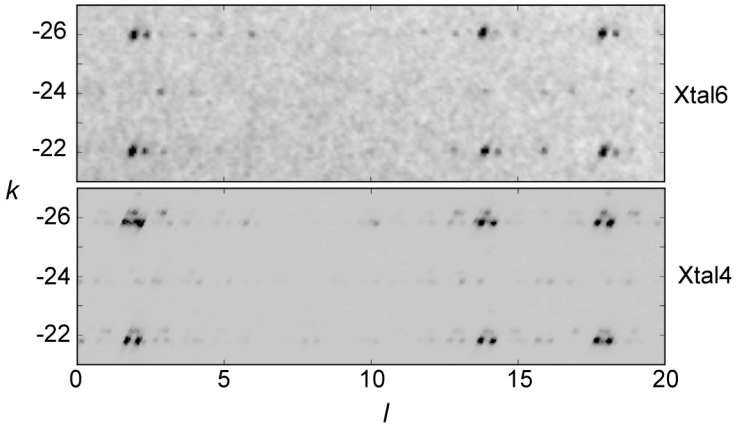

Figure 3.14: Reciprocal space reconstruction of the $h = 50$ plane for Xtal4 and Xtal6. Peak splitting due to the monoclinic type twinning is evident in both crystals, but much weaker in Xtal6. The weak reflections just above the main intensities in Xtal4 are from the orthorhombic twin domain. The reciprocal space reconstruction for Xtal6 is noisier compared to that of Xtal4 as the crystal was much smaller.

Despite the degree of twinning present in Xtal4 it is still appealing, as the data set contains some 370,000 reflections, whereas Xtal6 only contains about 170,000 reflections, of which many of the superstructure reflections are very weak as is evident in Figure 3.15.

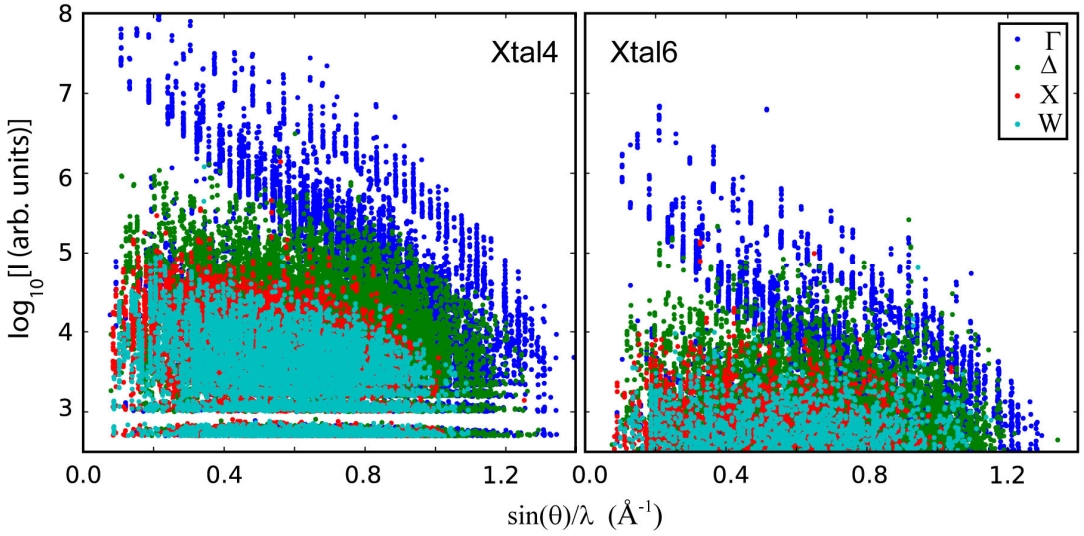

Figure 3.15: Plot of reflection intensity against resolution from different k-point reflections. In Xtal6 many of the reflections from the W and X points are very weak.

The cubic structures were refined for Xtal4 and Xtal6 from data collected at 130K to verify the structure and check for the existence of multiple scattering. Summaries in Table 3.5 are some details of the high temperature refinements; these can be seen to be in very good agreement especially between Xtal6 and the model of ref. [96].

	Model		
Parameter	Xtal4	Xtal6	Wright 2002
O (x)	0.25497(1)	0.25490(2)	0.25490(5)
A (U_{eq}) ($Å^2$)	0.00262(1)	0.00274(1)	0.00117(8)
B (U_{eq}) ($Å^2$)	0.00414(1)	0.00423(1)	0.00307
O (U_{eq}) ($Å^2$)	0.00427(1)	0.00438(2)	0.00285

Table 3.5: Refined parameters against integrated data from Xtal4 and Xtal6 collected at 130K compared with those published in ref. [96]. $R_1 = 0.0283$, $wR_2 = 0.0461$ for 1706 unique reflections for Xtal4 and $R_1 = 0.0137$, $wR_2 = 0.0206$ for 594 unique reflections for Xtal6.

It is noteworthy that a few weak reflections corresponding to the violation of diamond glide systematic absences (0 2k 2l) are evident in the Xtal4 reflection set. Although these are very weak with respect to the fundamental peaks with intensities 5-6 orders of magnitude weaker, they are an indicator that multiple scattering and hence extinction is present. The presence of multiple scattering is potentially problematic. Although these intensities arising from the multiple scattering are very small (being less than 0.005% the intensity of the fundamental reflections), relative to the weakest superstructure peaks present below T_v, this becomes a potentially significant error of about 5%.

Attempts at integrating the different domains of Xtal4 and Xtal6 were made in SAINT[130]. Although integrated twin fractions agreed well with those expected from visual inspections of the reciprocal space reconstructions (Figure 3.14), merging of data did not proceed smoothly due to the large amount of null intensity observed for the superstructure reflections of the minority component domains. So instead, integrations with a large box size were performed in Saint to encompass the intensities of diffraction spots from both domains.

The reciprocal reconstruction of Figure 3.14 shows that the spots are resolved in reciprocal space at high *h* index, and it is important to establish whether the integration program is integrating the intensity of both domains simultaneously or only that of the principal domains. This was tested by performing integrations on data with different integration box sizes. Figure 3.16 illustrates how reflections with a high *h* index have an increase in intensity as a function of integration box size, but those that have a low *h* index (and are therefore poorly resolved in reciprocal space) have no such increase. This increase corresponds to the inclusion of the second twin component as the integration box size is

increased from about 5/100 ° to 7/100 °. It can be seen from the reciprocal space reconstruction of Figure 3.17 that the corresponding reflections with high *h* index are clearly well resolved, and hence the larger integration box size is needed to capture the intensity of the second domain.

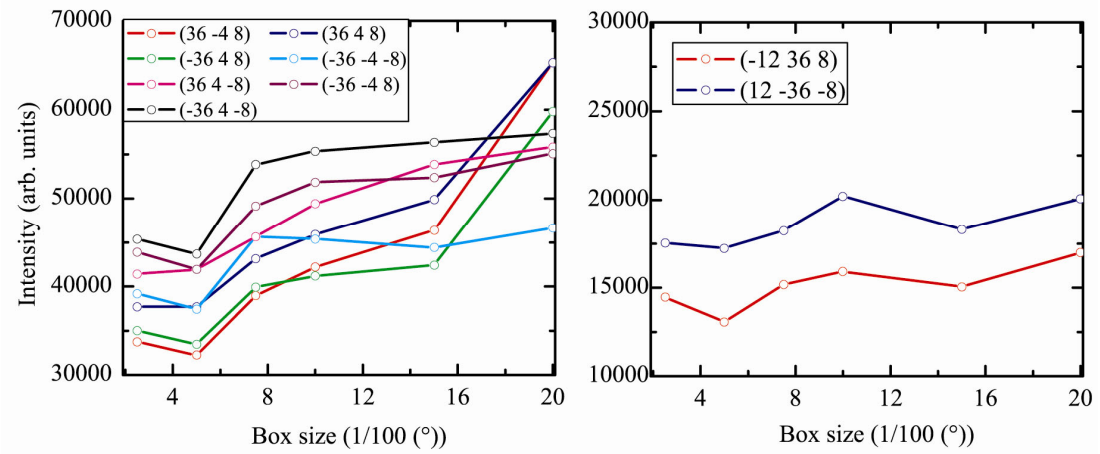

Figure 3.16: Intensity of reflections for Xtal6 as a function of integration box size (in 1/100 °). A jump between 5/100 and 7/100 is observed for reflections with high *h* (left figure) due to the inclusion of the second twin domain, but no such jump is observed for reflections with low values of *h* where the twin reflections have a high degree of overlap even at small box sizes (right figure). (Figure reproduced courtesy of Jon Wright)

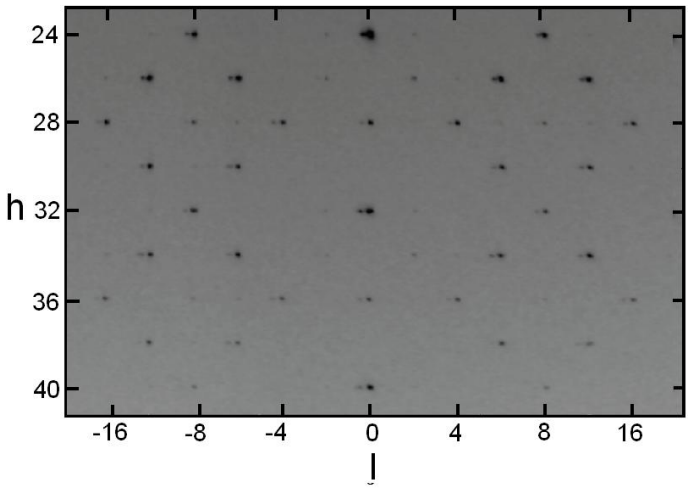

Figure 3.17: Reciprocal space reconstruction of the k = 4 plane. The divergence of the diffraction spots arising from the two domains of Xtal6 as *h* increases is evident.

Refinements against data integrated in two different manners are compared in Table 3.6. The fit of the data can be seen to be considerably worse for the instance where the SAINT program attempts to automatically resize the box size (such as is often used as the default option), whereas the fit where the box size is constrained to be 10/100 ° has greatly improved R values. The Fcalc versus Fobs plots are shown for the two refinements for the W-point

reflections in Figure 3.18. It can be seen that there is a substantial difference between the two fits, but also that the fits differ significantly for reflections with high *h* versus those with low *h* index for the 'automatically resize' integration.

Integration box size	R(int)	R(sigma)	Rw	R1
Resized automatically	0.0535	0.0711	0.1325	0.0552
10/100 °	0.0438	0.0644	0.1037	0.0411

Table 3.6: Table of refinements for Xtal6 (anisotropic Fe, isotropic O thermal parameters) against data integrated with two different box sizes. Twinning is modelled in the merohedral approximation with a monoclinic twin law in Shelxl.

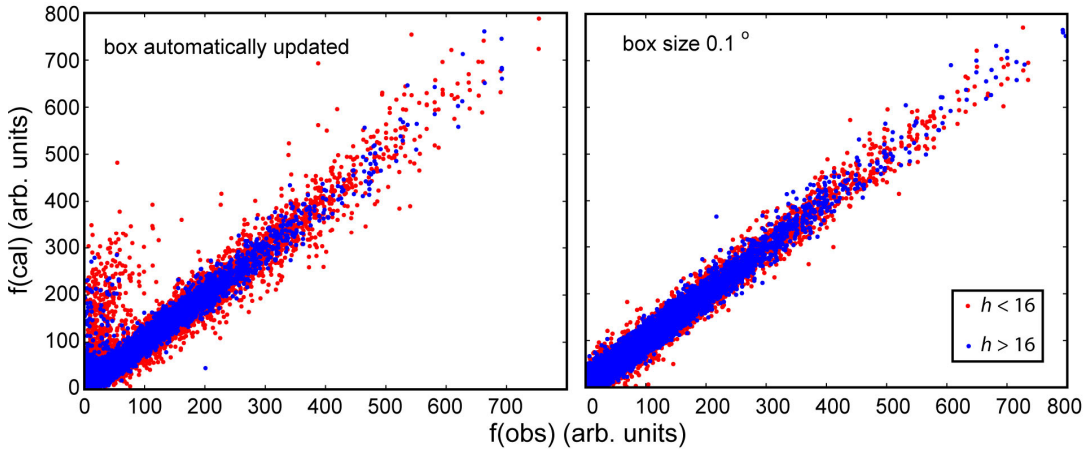

Figure 3.18: Fcal versus Fobs plots for refinements against two different integrations for Xtal6. The difference between the fit of many reflections with *hkl* with large h versus those with small h for the refinement where the box size was automatically updated by the integrating program indicates that the integration is systematically missing the twin component.

Refinements of the integrated data sets of Xtal4 and Xtal6 in Shelxl[136] were performed by generating random perturbed starting coordinates from both the high temperature and the Pmca model of ref. [96]. False minima were observed in the refinement surface of both Xtal4 and Xtal6 but about 30% of the time the global minimum was reached having in both cases a R_1 value at least 1% lower than any local minimum. In Figure 3.19 the refinement of Xtal4 and Xtal6 have been compared in terms of their distortions modes, whose strong correlation points to the fact that the two structures derived from different data sets are essentially the same.

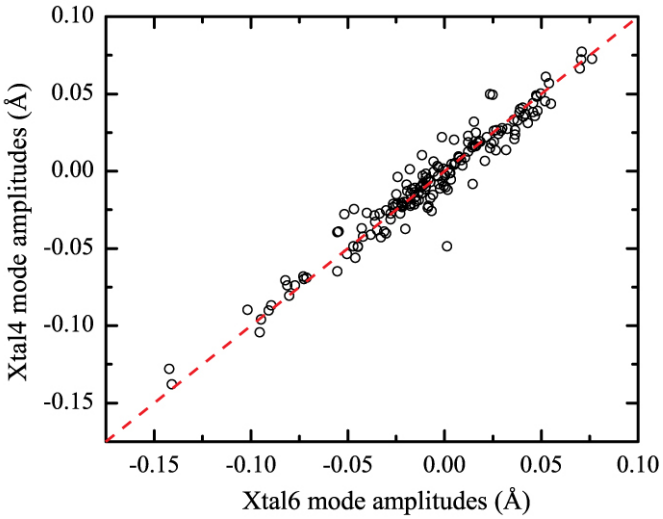

Figure 3.19: Distortion mode amplitudes from refinements against Xtal4 data plotted against refinements against Xtal6 data. Good correlation between the refinements is an indicator that the two structures are essentially the same. The distortion mode analysis here is performed with respect to the Pmca model of ref. [96].

Investigation of the anisotropic thermal parameters reveals that all 56 sites are positive definite and have physically reasonable values for Xtal6. However, for Xtal4 some no longer have a physically meaningful interpretation, and many have taken on rather elongated shapes as described by their ORTEP (Oak Ridge Thermal Ellipsoid Plot) like representations (Figure 3.20). This behaviour of the thermal parameters in the Xtal4 model means that any derived fractional coordinates should be treated with caution.

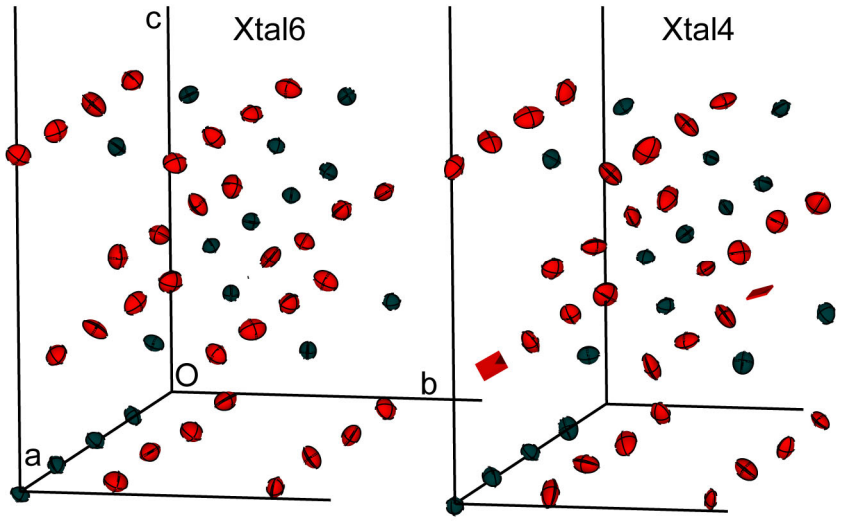

Figure 3.20: ORTEP-like representations (shown at 99% probability) for xtal6 and Xtal4 refinements illustrated in the asymmetric unit (a, b/2, c/2), only B-sites (Dark green) and Oxygen (Red) atoms are shown for clarity. Non-positive definite thermal parameters are shown as planes.

In light of the non-positive definite thermal parameters, larger degree of twinning, and possible existence of multiple scattering, Xtal4 refinements are deemed less reliable with respect to Xtal6. Although the end conclusions reached are invariant as to whether Xtal4 or Xtal6 data sets are used (and the majority of analysis has been performed on models from both data sets), it is desirable to report a single set of coordinates at the end of the analysis so that future experimental and theoretical work will be referencing their work relative to the same model. For the rest of this thesis therefore only the refinements of Xtal6 will be discussed unless otherwise indicated.

3.3.3. Validation of the final model of the Verwey structure

The final model refined against Xtal6 data, is a full anisotropic refinement performed in Shelxl with 506 parameters with a R_1= 5.08 %, wR_2 = 6.96 % against 91,433 unique reflections. Full details of the refinement and all the fractional and anisotropic displacement parameters are given in Appendix A. The fitting statistics are given by the *k* points the reflections are associated with in Table 3.7 and Figure 3.21Figure 2.1. The overall R_1 value will be dominated by the fitting statistics of the Γ-point but it can be seen that fitting statistics for X and W-points are still R_1 < 8 % even though these peaks are 2 orders of magnitude weaker than those of the Γ-point. In addition the structure is highly over determined with a parameter to observation ratio of 1 : 181.

Point	Reflection conditions	No. of parameters	No. of reflections	<I> (arb. units)	$R(F^2)$
Γ	h, k =2n l=4n	75	23748	19366	0.0310
Δ	h, k =2n l=n	102	21952	2048	0.0656
X	h+k=2n l=2n	201	22858	895	0.0723
W	h+k=2n l=n	126	22810	853	0.0791
Overall		504	91433	5964	0.0518

Table 3.7: Fitting statistics by class of reflection for the final model.

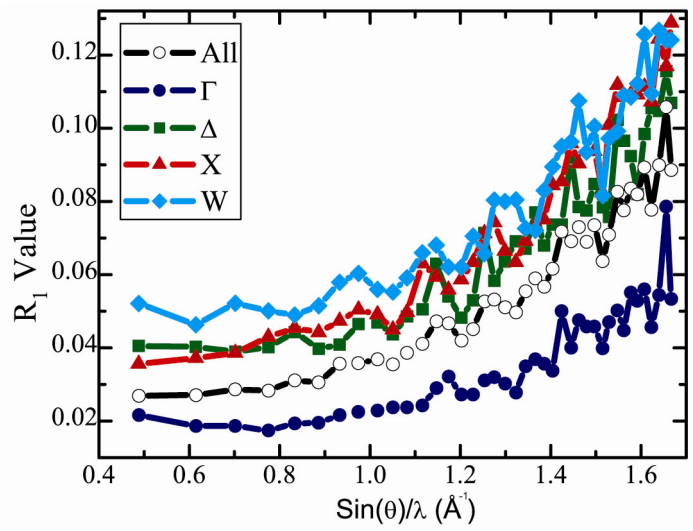

Figure 3.21: The fitting statistics as a function of resolution shell for different classes of reflections.

The fact that all 338 thermal parameters refine to give anisotropic thermal displacement that are physically reasonable is further assurance of the quality of the data. However, to test whether or not it is justifiable to refine all of the thermal parameters the Hamilton significance test [137] was used. The different models tested are summarised in Table 3.8. In order to perform a Hamilton significance test, it is necessary to consider the dimension of the hypothesis (the difference in number of degrees of freedom of some unconstrained model with respect to some constrained model(b)), the degrees of freedom of the unconstrained model (number of observations(n) – variables(m)), and the ratio of the fitting statistics (R) of the constrained and the unconstrained model. In the refinement here, the dimensionality of the hypothesis and number of degrees of freedom are beyond that of Hamilton's original tablulation.[137] However, R value ratios can be converted to F ratios as follows:

$$F = \frac{(R^2 - 1)(n - m)}{b}$$

In Table 3.8 the hypotheses are made as to whether a constrained model (no. 1-5) is allowed with respect to an unconstrained model (no. 6), and only accepted if $F < F_{b,\ n\text{-}m,\ \sigma}$ where sigma (σ) is the significance level. Here, a σ of 0.1% is used which means that in 1/1000 times there is a danger of falsely rejecting a constrained model in favour of an unconstrained model. From a look-up table,[138] $F_{500,\ 1000,0.001} = 1.21$ which is always much smaller than the F values of Table 3.8. Therefore in all instances the hypothesis is rejected, and in the event that all sources all error are due to random noise, the unconstrained model should always be used in favour of any constrained model.

No.	Model	wR_2	b	R	m	n	F
1	[A],[B],[O] isotropic	0.0771	335	1.175	173	28838	32.4
2	A, B. [O] isotropic	0.0741	22	1.130	195	28838	25.00
3	A,B,O isotropic	0.0737	53	1.123	226	28838	26.3
4	A, B anisotropic. [O], isotropic	0.0673	142	1.026	315	28838	7.7
5	A, B anisotropic. O isotropic	0.0669	173	1.020	346	28838	7.0
6	A, B, O anisotropic	0.0656		-	508	28838	-

Table 3.8: The different thermal parameter models to which the Hamilton significance test was applied. Square brackets indicate that atom type was constrained to have one isotropic thermal parameter only. The refined wR_2 values, number of parameters (m) and number of observations (n) are given for each model. The dimension of the hypothesis (b), and the ratio of the wR_2 values (R) is always with respect to model 6 as the unconstrained model. The tabulated F values are for the constrained models (1-5) with which the hypothesis of the unconstrained model is tested. The constrained models are rejected in all instances.

To test if all the additional refined parameters of the unconstrained model are simply fitting noise in the data, a stringent R-free refinement was performed. In this, a subset of reflections were randomly selected as the working set, and the remaining reflection retained as the test set. The refinement was performed against the working set of reflections and R_1 values calculated against both sets. A significantly better fit of the working set over the test set is an indication that the refinement is fitting noise. Here, the abundance of data means that a working set of only 50 % of the reflection has been selected, producing R_1 values of 0.0526 for the test set versus 0.0516 for the work set. This indicates that the bias of the model towards fitting noise is very slight and unlikely to be significant.

It has been demonstrated in this section that the model is robust, significant and free of systematic errors such as twinning and multiple scattering.

3.4. Discussion: Rationalisation of structural distortions

In the following sections the physical meaning of the refined structural model will be interpreted.

3.4.1. Distortion modes

Distortion mode analysis was performed with the aid of ISODISPLACE,[33] with respect to the high temperature cubic structure. A script was created using the output from ISODISPLACE which allowed for the rapid conversion between Shelxl files and mode amplitudes. Reconstructed modes were verified directly by refinements in Topas[35]. This was found to be a useful approach for verifying the reproducibility of the solution as in Section 3.3.2, but the modes also have a physical meaning and help to classify the nature of the structural distortion. A summary of the space groups for which the reconstructed modes form POP is given in Figure 3.22. These space groups are by necessity always of type 1 maximal non-isomorphous subgroups (with respect to the international tables) of $Fd\bar{3}m$ if they belong to the Γ and of type 2 if they arise due to a Δ, X, or W point distortion. In addition they must also be parent space groups of C1c1. It can be seen that many of the pseudosymmetry candidates used in previous refinements ($R\bar{3}m$, Pmca, C2/c) do not appear as such space groups in Figure 3.22 as their corresponding OPDs are already branched in this mode analysis producing space group symmetries which are instead subgroups of these. With some careful analysis of the relative magnitude of the branches of the primary order parameters it is possible to ascertain the degree of pseudo symmetry with respect to these pseudo symmetry space groups.

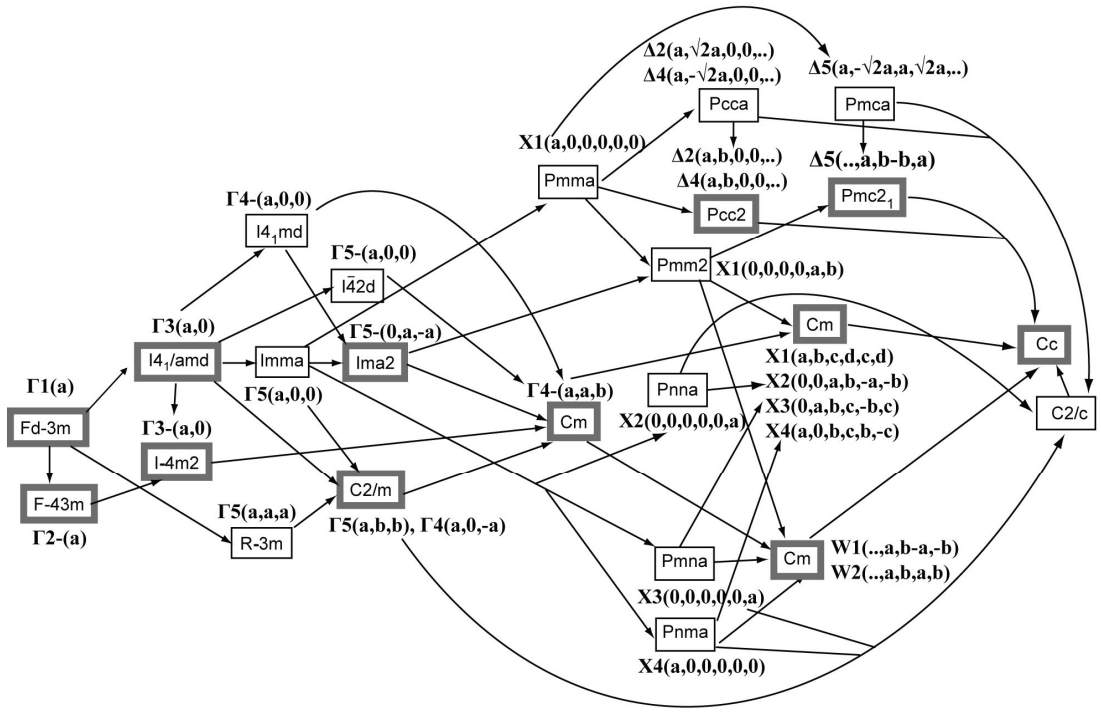

Figure 3.22: Descent of symmetry from $Fd\bar{3}m$ to Cc. The space groups for which the modes form POPs (The kernels), are shown in bold boxes along with the *k* point, OPD and branching labels. Additional space groups in which the POPs are not branched are also shown. The transformation basis set and origin shift for the space groups with respect to the high symmetry structure are given in Appendix B.

In Figure 3.23 the magnitudes of the modes are plotted according to the site (A, B or O) and point (Γ , Δ, X, W, see Figure 3.9) they belong to. In addition they are arranged as those modes present in the centric C2/c superstructure (of which there are 80) and the additional modes (88) active in the acentric Cc model. Only the single Γ_{1+} mode is active in the high temperature structure. It can clearly be seen that the Γ-point modes are very small in amplitude (Figure 3.23, left) and any structural model such as a rhombohedral approximation is a very poor description of the structure. In the rhombohedral approximation ($R\bar{3}m$, see Figure 3.22) the Γ_5(a) and Γ_5(b) branches should be equal, and although this appears to be more or less true (possibly accounting for the good description of the metric symmetry), the relatively large magnitude of the Γ_3 (responsible for pseudo tetragonal distortion) and substantial amplitude of the modes in Δ, X and W point, mean that this is not really a useful pseudo-symmetry approximation. Strikingly, the acentric modes in the Γ-point are almost of equal magnitude as of the centric, and the ferroelectric modes Γ_{4-} seem to have significant amplitudes.

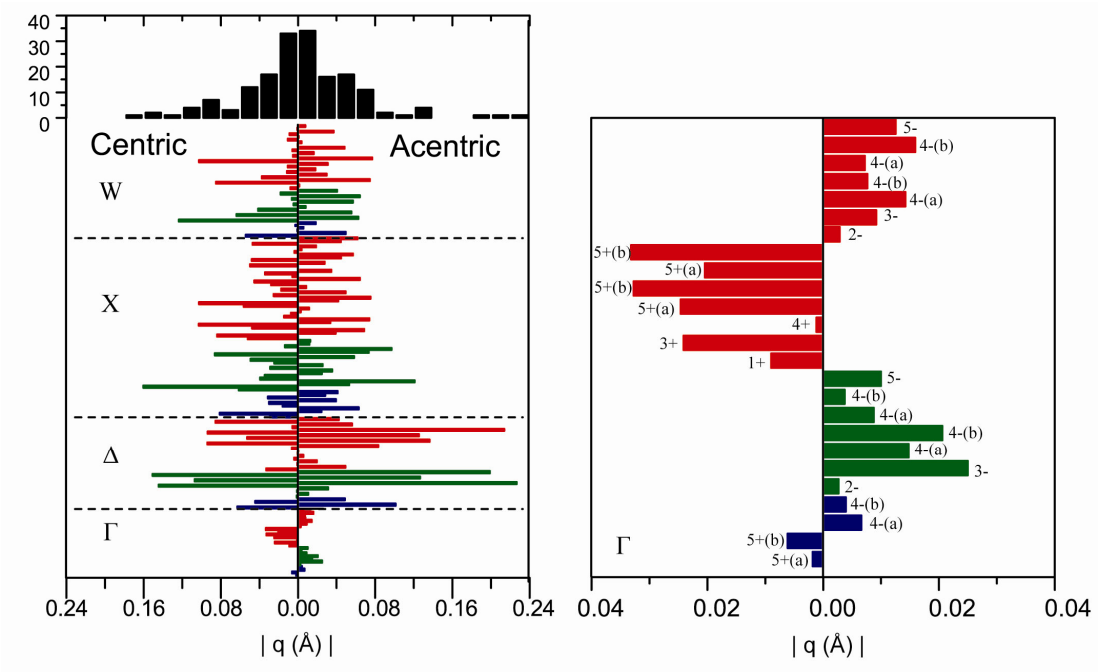

Figure 3.23: Left, the 168 distortion modes active in the Cc structure of which only 80 (left) are active in the centric (C2/c) structure and an additional 88 are needed to describe the acentric nature. Modes are shown in blocks divided by dotted lines corresponding to the point in the BZ of the face centred cell that they belong to, and are colour coded as to whether they belong to an A-site (blue), B-site (green) or oxygen atom (red). Right: Expansion of the gamma points labelled with the various order parameter directions. The branching of modes is indicated by the bracketed letters.

It is less trivial due to the large amount of branching to ascertain how well the structure is described by Pmca symmetry. The subgroup relationships for the symmetry descent from $Fd\bar{3}m$ to Cc are shown in Figure 3.22. The Pmca space group which has the irreps. Γ_1, Γ_3, Γ_5, X_1, and Δ_5 is not one of the subgroups implied by a POP of $Fd\bar{3}m \rightarrow$ Cc, as the inversion centre has already been lost in the Γ-point. However, by comparing the different branches of the POPs, it is possible to ascertain the degree of pseudosymmetry with respect to Pmca. The degree of distortion away from the pseudosymmetry group can be seen from Figure 3.22 to be given by the deviation of the various Δ_5(a) and Δ_5(b) branch amplitudes from the ratio $\sqrt{2}$ as shown in Figure 3.24. It is hence clear that the acentric nature of the Δ-point is somewhat overstated in Figure 3.23 and the off-centre distortions have amplitudes in the range of 0.05 – 0.1 Å rather than being ~ 0.2 Å. The large magnitude of the Δ_5 modes and near zero magnitude of Δ_2 and Δ_4 explains why Pmca is such a good pseudo symmetry candidate within the subcell approximation.

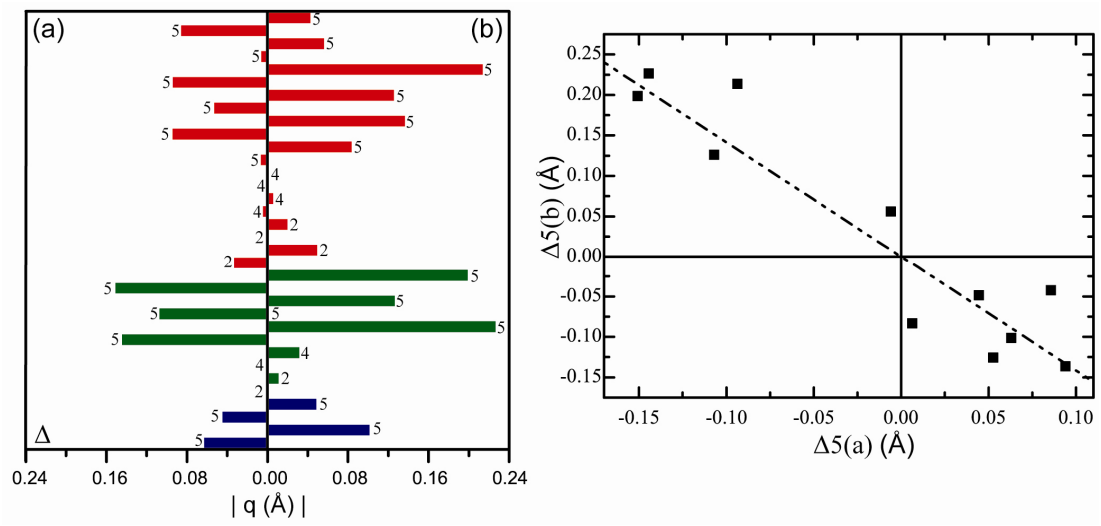

Figure 3.24: The magnitude of the various order parameters of the Δ-point, the different branching (a and b) are plotted on the left and right hand sides respectively of the left hand figure. The Δ5 (a) and (b) branches are collapsed onto each other in the Pmca approximation and correspond to $\Delta5(b) = -\sqrt{2}\ \Delta5(a)$ as shown by the dotted line in the right hand graph. The approximation is found to be reasonable as most mode amplitudes (squares) are within 0.05 Å of this line.

Although the Pmca approximation captures well the magnitude of the Δ_5 frozen phonon modes, it ignores all of the X_2, X_3, X_4 and W–point modes as well as the branching in the X_1 mode, all of which can be seen from Figure 3.23 to have substantial amplitudes. The branching of the X-point modes with respect to various space groups is shown Table 3.9. Cm is on the symmetry descent path from $Fd\bar{3}m$ to Cc. The necessary constraints on the branching with respect to inversion symmetry can be ascertained by considering the mode analysis of $Fd\bar{3}m$ with respect to C2/m. From this it can be seen that the centric modes are, $X_1(b)$, $X_1(d)$, $X_2(b)$, $X_3(a)$, $X_3(c)$, $X_4(c)$ and the acentric modes are $X_1(a)$, $X_1(c)$, $X_2(a)$, $X_3(b)$, $X_4(a)$, $X_4(b)$. The acentricity of the X-point is captured in Figure 3.25 which shows that its magnitude is similar to that of the centric distortions. The breakdown of the Pmca model is evident, as only the $X_1(b)$ modes should be present in this pseudo symmetry approximation, and all other modes must have zero amplitude.

Mode	Cm	C2/m	P
X1	(a,b,c,d,c,d)	(0,a,0,b,0,b)	mma (0,a,0,0,0,0)
X2	(0,0,a,b,-a,-b)	(0,0,0,a,0-a)	-
X3	(0,a,b,c,-b,c)	(0,a,0,b,0,b)	mna(0,a,0,0,0,0)
X4	(a,0,b,c,b,-c)	(0,0,0,a,0,-a)	-

Table 3.9: The branching of the X-point modes in various space groups. All Space groups have the basis (1, 1, 0), (-1, 1, 0), (0, 0, 1) for centred cells and (½, ½, 0), (- ½, ½, 0), (0, 0, 1) for primitive cells with respect to the high symmetry structure. The origin shifts are in all cases (0 ,0 ,0) with respect to the cubic structure.

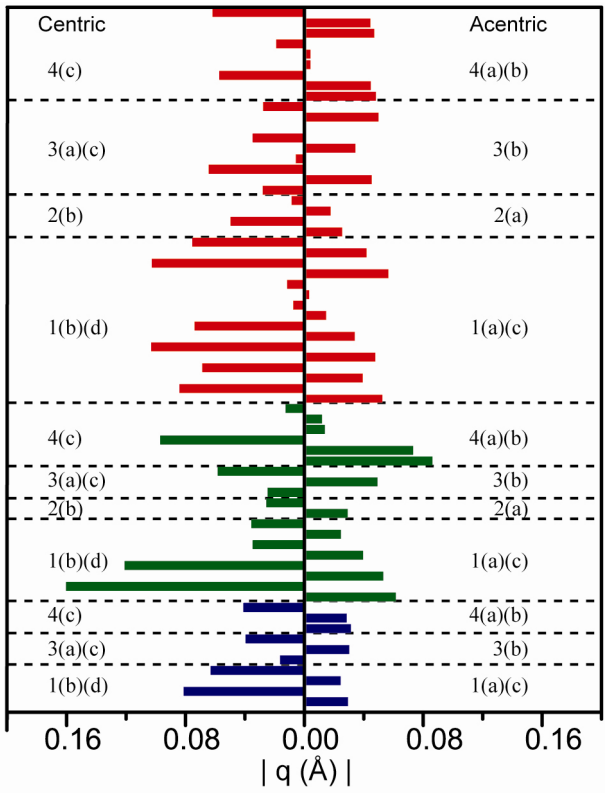

Figure 3.25: The magnitude of the various branches of the X_1, X_2, X_3 and X_4 modes. The modes are divided as to whether they belong to a A, B or O-site, and divided into OPDs by horizontal dashed lines. The branches are labelled sequentially alphabetically as indicated with many OPDs having several branched modes.

In a similar manner, the degree of pseudo symmetry of the W-point can be ascertained by considering the distortion mode analysis of the parent space group with respect to C2/c and comparing the resulting branching with that of the symmetry mode analysis for Cc. This reveals that in the C2/c approximation $W_1(a) = W_1(b)$ and $W_2(a) = -W_2(b)$. Accordingly in Figure 3.26 the amplitudes (rather than the magnitude of the amplitudes) of the (a) and (b) branches are plotted overlaid along with a trace indicating their difference. Again the acentricity of the structure has been slightly overstated in Figure 3.23 but the trace of Figure 3.26 reveals the off-centre displacements are still very significant.

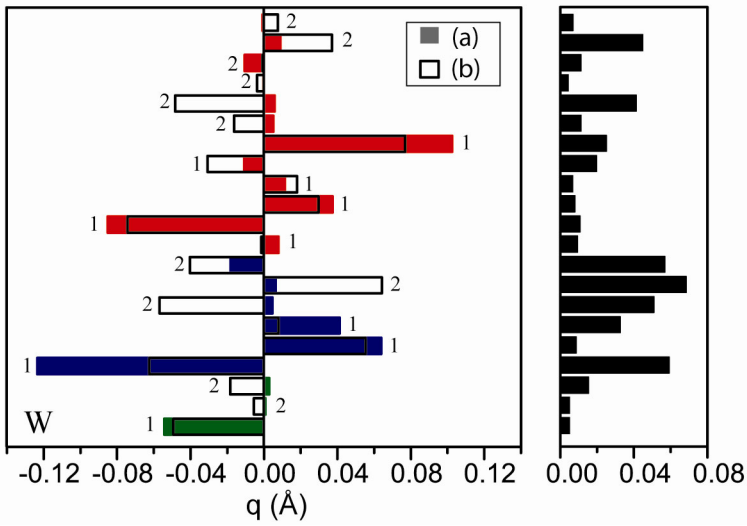

Figure 3.26: W-point distortion mode amplitudes, those of (a) and (b) branches are plotted as filled and outlined bars respectively. In the C2/c approximation the amplitudes of the (a) and (b) branches are required to be equal for W_1 and opposite for W_2, and hence the difference trace on the right of the figure is an indicator of the acentricity of W-point.

As discussed, the mode density of states of Figure 3.23 is rather continuous and suggests that there are no clear modes that act as order parameters and no obvious subset that captures the nature of the distortion. Refinements in Topas with modes that fall below a certain value constrained to zero (Table 3.10) also do not suggest that a small subset of these modes can be usefully used to describe the structural distortion. Additionally, the failure of pseudosymmetry refinements (Table 3.11) to produce acceptable fits to the data, confirm the conclusions of the above mode analysis.

|Mode amplitude cut off (Å)|	Number of non-zero modes	R_1 (%)	wR_2 (%)
0	168	5.76	8.28
0.01	122	5.84	8.48
0.02	93	7.10	9.47
0.03	78	7.80	10.78
0.04	51	10.14	15.51

Table 3.10: Distortion mode refinements in which modes falling below certain amplitude are constrained to be zero before further refinement cycles are run. The R values indicate that even a large subset of the 168 modes fails to produce a reasonable fit to the data. Each model is constrained to having only three isotropic thermal parameters [A], [B] and [O].

Space group	Number of parameters	R_1 (%)	wR_2 (%)
Cc	168	5.76	8.28
C2/c	80	9.34	14.57
$Cmc2_1$	92	10.84	15.70

Table 3.11: Psuedo symmetry refinements statistics for fits to Xtal6 data in Topas, each model is constrained to having only three isotropic thermal parameters [A], [B] and [O].

It has been demonstrated in this section that it is not possible to describe the structure in terms of a few frozen phonons or a collection of sub-symmetries. It is also evident that although certain modes have larger amplitude than others it is not possible to identify a clear primary order parameter for the phase transition. Although modes such as Δ_5 and X_4 have large amplitudes consistent with spectroscopic measurement on magnetite above T_v these are in no way unique from all the other many active modes. It might therefore be expected that the structural distortion is driven by local ordering rather than phonon condensation, as will be investigated in the following section.

3.4.2. Local modes

The B-sites have pseudo octahedral symmetry with respect to their oxygen coordination and it is possible to analyse the distortions in the Verwey structure in terms of frozen normal vibrational modes of these sites. As the point group of each B-site below T_v is 1, in principle the full distortion is described by a summation of all 21 symmetric displacements. Due to the low point group symmetry, there is a degeneracy in the way the local coordinate system can be chosen meaning that it is not trivial to compare displacements between different octahedra. However, local axes of octahedra may be taken as being defined by the B-O bonds, neglecting the small deviations of O-B-O bond angles from 90 °. This means that at most for any one distortion, a three fold degeneracy must be considered when calculating the symmetric displacements.

The A_{1g} breathing mode distortion, which has relevance for charge ordering, is given as $Q_{rad} = ((d_{+x} + d_{-x} + d_{+y} + d_{-y} + d_{+z} + d_{-z})/6 - d_{av})$, where the B-O distances d_i in each octahedron are labelled to reflect the direction along the pseudo cubic axis and d_{av} is the global average. The E_g modes suffer from a two or three-fold degeneracy in the manner that d_x, d_y and d_z are chosen, making it more tricky to compare their values between different octahedra. For

example the E_g model corresponding to the tetragonal JT type distortions can be calculated along each direction of the octahedra (x, -x, y, -y, z and -z) as $Q_x = (2(d_{+x} + d_{-x}) – (d_{+y} + d_{-y} + d_{+z} + d_{-z}))/2\sqrt{3}$, where x, y and z may be permuted and d represents a distance from the centre to a vertex of the octahedra. In this manner three different values for the magnitude of the tetragonal JT distortion may be obtained (Q_1, Q_2 and Q_3). In the pseudo tetragonal approximation this should be equivalent in two of the three cases and unique in one direction when the JT axis is correctly selected. One might chose the largest magnitude of Q as the tetragonal JT axis, i.e Q_1 where $|Q_1| > |Q_2| > |Q_3|$. The problem with this is that sites with distortions with orthorhombic type JT character, will also give a contribution to Q_1. This is illustrated in the ideal case were $(d_{+x} + d_{-x}) = q$, $(d_{+y} + d_{-y}) = -q$ and $(d_{+z} + d_{-z}) = 0$ for the orthorhombic case and -2q, q, q for the ideal tetragonal case returning Q_1 values of $-3q/2\sqrt{3}$ and $-6q/2\sqrt{3}$ respectively. However, $Q_3 = 0$ for an orthorhombic type JT distortion and $3q/2\sqrt{3}$ for tetragonal JT distortion. A better estimation of the tetragonal JT distortion (Q_{JT}) is hence given as $-2Q_3$ which in the tetragonal limit is equal to Q_1. The orthorhombic contribution to the JT distortion (Q_O) may then be estimated as $Q_1 – Q_{JT}$ and so hence $Q_O = Q_1 + Q_3/2$.

Derived quantities, including BVS, $Q_{Rad,}$ Q_{JT} from the fractional coordinates refined against Xtal6 data are reported in Table 3.12 for the B-sites, and BVS are reported for the A and O sites in Appendix A. The bond valence sums of the B-sites have a rather large range (0.58). Notably the highest valence (2.96) is significantly larger than the highest A-sites which all have BVS in the range 2.76-2.82 (average 2.79). The sites are ranked low valence to high valence in Table 3.12, and it is clear that what in the charge ordering limit would be assigned as the highest valent 2+ (site 8, B1b_2) and the lowest valent 3+ (site 9, B3_1) have a very small BVS separation (0.02). In fact the BVS and average bond distances form a rather continuous distribution which has no bimodal character. This is in contrast to the refinement of Wright et al.[96] where clear charge segregation was evident. Several of the B-sites have much higher BVS than those previously reported. It can be seen from the site labelling that only in two instances (B2 and B4) are the high valence states averaged with low valence states in the Pmca approximation, contrary to the 1:3 or 3:1 splitting of the pseudo symmetry sites predicted by ref. [99].

Site	Label	<Fe-O> (Å)	Q_{Rad} (Å)	BVS	Q_1 (Å)	Q_{JT} (Å)	Q_O (Å)
1	B4_4	2.087	0.027	2.38	-0.060	-0.057	-0.029
2	B1a_2	2.079	0.019	2.44	-0.060	-0.048	-0.003
3	B4_1	2.080	0.020	2.44	-0.058	-0.029	0.001
4	B1b_1	2.075	0.015	2.47	-0.057	-0.038	-0.009
5	B2b_1	2.075	0.015	2.48	-0.042	-0.039	-0.002
6	B1a_1	2.074	0.015	2.48	-0.057	-0.028	-0.003
7	B4_2	2.067	0.008	2.54	-0.054	-0.058	0.010
8	B1b_2	2.066	0.006	2.56	-0.054	-0.026	-0.026
9	B3_1	2.063	0.003	2.58	-0.060	-0.008	0.006
10	B3_2	2.061	0.001	2.61	-0.035	0.016	-0.018
11	B3_3	2.058	-0.001	2.64	-0.028	0.009	0.001
12	B2a_2	2.053	-0.007	2.67	0.017	0.017	-0.005
13	B2a_1	2.040	-0.019	2.77	0.019	-0.009	-0.008
14	B3_4	2.035	-0.024	2.81	0.023	0.007	-0.020
15	B4_3	2.023	-0.037	2.93	-0.017	-0.004	0.004
16	B2b_2	2.020	-0.040	2.96	0.011	0.008	-0.008

Table 3.12: Relevant local order parameters derived from the coordinates refined against Xtal6 data, arrange from low to high BVS.

Despite the poor charge segregation, the tetragonal JT distortion (Q_{JT}) is found to have a strong correlation with BVS and Q_{Rad}. Q_{JT} is observed to form a good bimodal distribution as evident from the histogram in Figure 3.27. 8 of the sites have significant negative amplitude, with their distribution centred on -0.04 Å while the other 8 sites have a distribution centred on 0 Å. The significantly negative amplitude of Q_{JT} for 8 of the sites is evidence for a Jahn-Teller distortion (compression along one axis) expected for a d^6 high spin Fe^{2+} state and its negative correlation with Q_{Rad} is consistent with the larger ionic radii expected for Fe^{2+} versus Fe^{3+}. Importantly Fe^{3+} which is d^5 high spin is not expected to be JT active and this is evident by its Q_{JT} distribution which is centred on 0 Å. As the observed orbital order is indicative of the charge order state, hereafter the two distinct groups of B-sites are referred to as 2+ and 3+ as appropriate. The validity of this approximation will be further probed later in this section. In Figure 3.28 a plot of Q_{Rad} against the orthorhombic JT distortion parameter (Q_O) is made. The lack of correlation between Q_{Rad} and Q_O lends weight to the argument that Q_{JT} should be considered as the local ordering parameter.

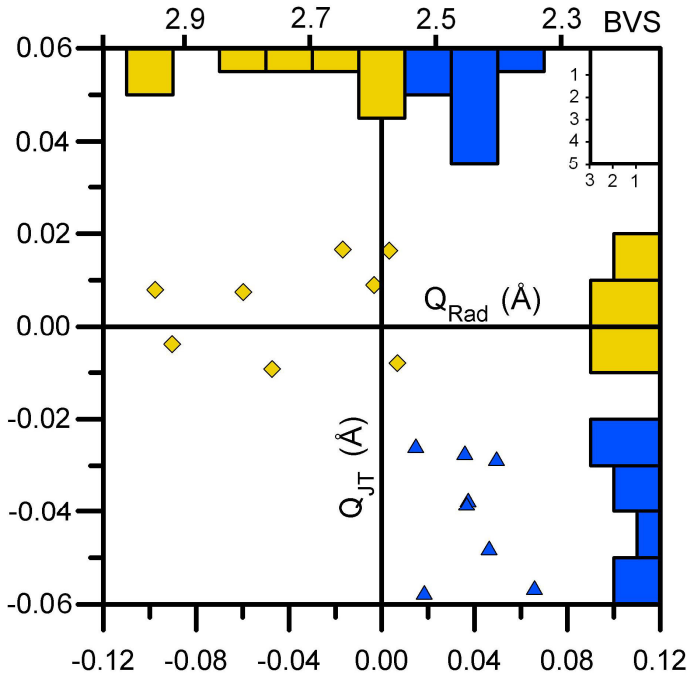

Figure 3.27: A plot of Q_{Rad} versus Q_{JT} for the 16 B-sites. Approximate BVS are shown above the Q_{Rad} values. The distributions of Q_{Rad} and Q_{JT} are indicated by the histograms and the number density is shown in the small inset scale in the top right hand corner. The 8 sites with the most negative Q_{JT} and most positive Q_{Rad} values are assigned as 2+ state and coloured blue. And those 8 with the highest Q_{Rad} are assigned to be 3+ state and coloured yellow.

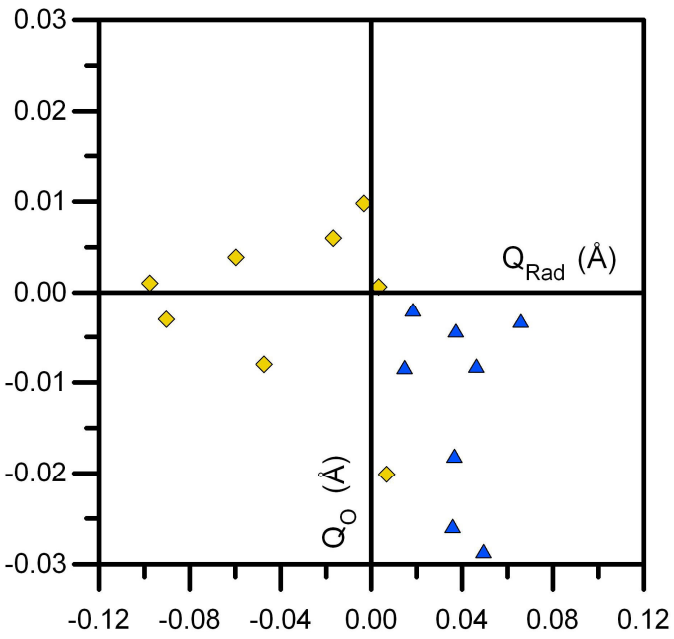

Figure 3.28: Plot of Q_{Rad} versus Q_O for the 16 B-sites. There is no obvious correlation between the two parameters.

There is nothing immediately striking about the charge ordering arrangement shown in Figure 3.29. The plot of D-site $(Fe^{2+})_n(Fe^{3+})_{4-n}$ tetrahedra reveal that only two out of 8 tetrahedra (in the asymmetric unit) meet Anderson's criteria (n = 2) of charge neutrality with the other six being equally distributed between n = 1 and n = 3 type tetrahedra. As the relative charge separations are rather small between most of the sites, it is not surprising that short range minimisation of Coulombic repulsion is not a driving force for the formation of the Verwey ground state. Surprisingly, despite how complicated the specifics of the crystal structure are, the Pmca pseudo symmetry model of Wright et al. is recovered by only exchanging two sites with each other in the asymmetric unit, as indicated by the arrow in Figure 3.29. Interestingly the n = 3 tetrahedra which have only one Fe^{3+} in them are those with the lowest BVS (B31, B32, B33). Another interesting feature of the structure is that the Fe^{3+} and Fe^{3+} sites arrange themselves in some manner to form infinite sheets and ribbons respectively (Figure 3.30).

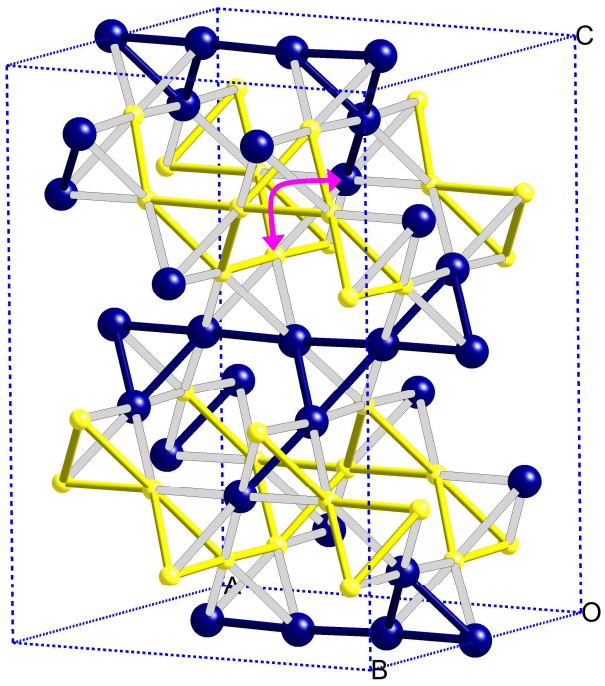

Figure 3.29: Charge ordering shown for B_4 tetrahedra. All tetrahedra are comprised of 2+ (blue) and 3+ (yellow) cations. The exchange of the sites indicated by the arrow (B2B1 and B43) leads to a centric arrangement such as described by Pmca subcell approximation.

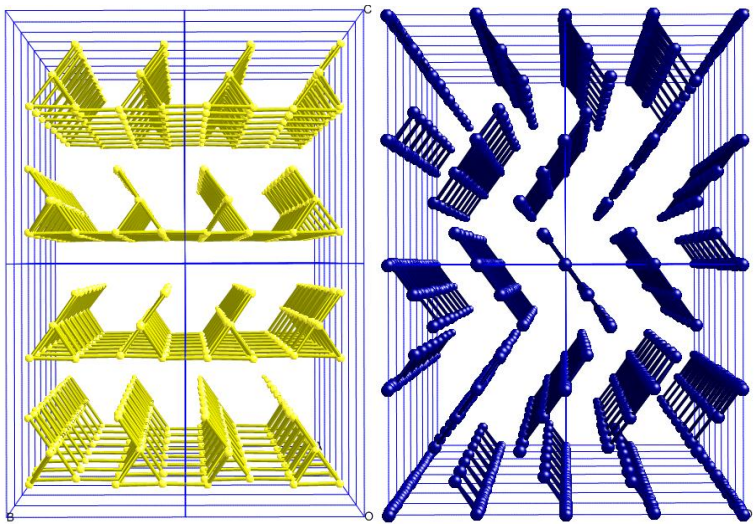

Figure 3.30: Infinite sheets of Fe^{3+} and ribbons of Fe^{2+} B-sites projected along the a-axis of the Cc cell.

The connectivity of the JT distortions are shown for the asymmetric unit in Figure 3.31 which revealed that the distortions are highly cooperative in nature, with many oxygens involved in 2 or 3 JT short bonds. In fact, only 9 oxygens (Table 3.13) are involved in JT short bonds. The zig-zag arrangement of the JT short bonds along a_m has quite an appealing cooperative nature. However, the overall distribution of the JT short axes is unsymmetrical, and if this distortion is the driving force for the Verwey transition it is unclear why a more cooperative arrangement (Figure 3.31, right) is not adopted in which only 8 oxygen atoms are involved in the 16 JT short bonds. The simple answer is that this symmetric arrangement would not cause such a complicated distortion, but this does not explain why the distortion is so complicated.

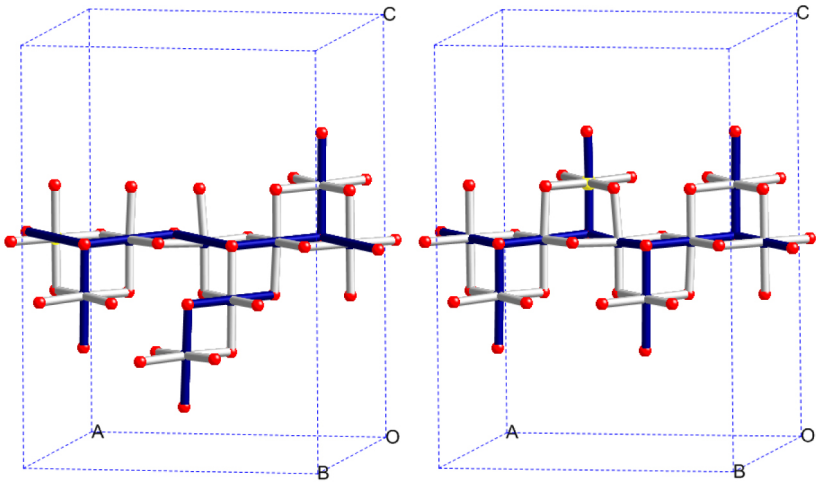

Figure 3.31: Left, the direction of the JT-short bonds (drawn in bold) in the crystal structure which arrange themselves in a highly cooperative manner with only 9 of 32 oxygens in the asymmetric unit involved in distortions. Right: Idealised symmetric structure in which only 8 oxygens are involved in JT distortions.

The arrangement of the JT short bonds may be to minimise strain along each unit cell direction. In the symmetrical arrangement the short bonds fall along a_c, b_c, c_c axis in the ratio 4 : 4 : 8 whereas the observed structure has a more even distribution of internal strain with a 5 : 5 : 6 distribution. However, larger super cells could lead to a more even distribution of JT short bonds in the structure, so this alone cannot be the driving force for the ground state structure of magnetite.

Oxygen	O11	O12	O13	O14	O41	O44	O5B1	O5B3	O6A4
No. JT	2	3	3	2	1	1	1	2	1

Table 3.13: The number of JT short bonds incident at each oxygen. Those not involved in any JT short bonds are not shown.

The orbital ordering and charge ordering configuration is found to be very similar to that predicted in a recent computational study in which structure optimisation was performed in Cc symmetry in the DFT + U approximation.[124, 125] The independent assertion of the orbital ordered structure from the crystal coordinates gives added confidence in the interpretation. The specifics of the computational model will be discussed in reference to the results of Chapter 4.

3.4.3. Three site-distortions

A histogram of B-B bond distances (Figure 3.32) reveals that they have a rather large range in the structure of almost 0.3 Å. Surprisingly, the shortest bond lengths are not between Fe^{2+} - Fe^{2+} as expected from electrostatics, but rather those of Fe^{2+} - Fe^{3+} type. More specifically, 14 of the B-B bonds which are orthogonal to a JT short bond on the Fe^{2+} are anomalously short while the rest of the bonds are in line with what is expected from electrostatic repulsion. While 13 of these short bonds are between Fe^{2+}-Fe^{3+} it appears that one of them is between Fe^{2+} - Fe^{2+}. The explanation for this unexpected shortening of bonds lies in the fact that the orbital ordering of the Fe^{2+} implies that the minority spin electron density is in its t_{2g} orbital orthogonal to its JT short axis, which is then directed towards, in most cases, an Fe^{3+} but in one case at a doubly degenerate t_{2g} orbital of an Fe^{2+}. This ordering greatly reduces the electrostatic repulsion between the pairs of B-sites and hence a shortening of the bond distance is observed. This as yet unobserved phenomenon of the delocalisation of the

minority spin across two bonds shown in Figure 3.33 is termed a trimeron in keeping with the dimeron description of JT two site polarons of ref. [139]. In Figure 3.33 a trimeron is depicted which has its centre at the vertex of two intercepting B_4O_4 cubes. The Fe^{2+} at the centre has its ordered minority spin electron in a t_{2g} orbital direct in this case at two B^{3+}.

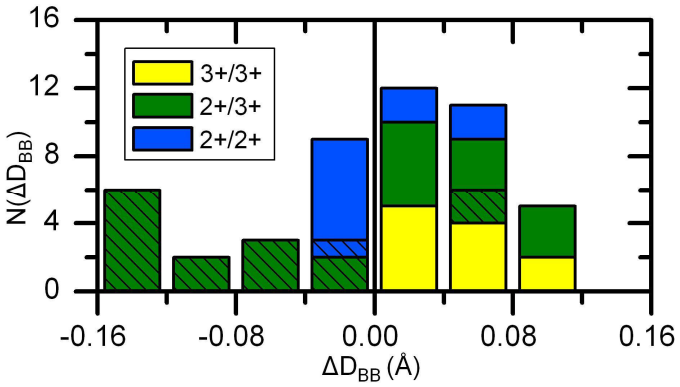

Figure 3.32: Histogram of all the B-B bond distances in the structure (relative to the average D_{BB} = 2.967 Å). The bonds are coloured according to whether they are between Fe^{2+} - Fe^{2+} (blue), Fe^{2+} - Fe^{3+} (green) and Fe^{3+} - Fe^{3+} (yellow). The bonds which are orthogonal to JT short Fe-O bonds are indicated by hatching of the bars. The two long bonds which are orthogonal to the JT short Fe-O bonds are B34-B1B2 (3.012 Å) and B31-B41 (3.018 Å).

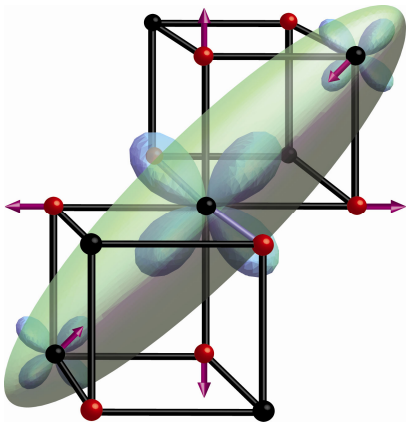

Figure 3.33: A trimeron centred at the interception between B_4O_4. The delocalisation of the minority spin electron from the central B-site across three sites, is illustrated by a scalene ellipsoid encompassing the three sites which is coined here as a "trimeron". The distortions associated with trimeron ordering are indicated ay arrows, except for the shortening of the JT bonds which are indicated by the light blue bonds coming out of the plane of the page.

As for the orbital ordering, the trimerons order in a highly cooperative manner (Figure 3.34) with none appearing in isolation, and often with three meeting at one Fe^{3+}. The arrangement is almost symmetric, but a trimeron pendant with a Fe^{2+} - Fe^{2+} bond breaks the centre of symmetry. Trimerons meet at Fe^{3+} at either 60 ° or 120 ° to each other allowing for a corporative distortion facilitating the shortening of two or three Fe^{2+} - Fe^{3+} bonds simultaneously. Unsurprisingly trimerons are never observed to meet at 180 ° to each other

which leads to a scenario in which a Fe^{3+} is unable to distort to satisfy the shortening of both bonds simultaneously.

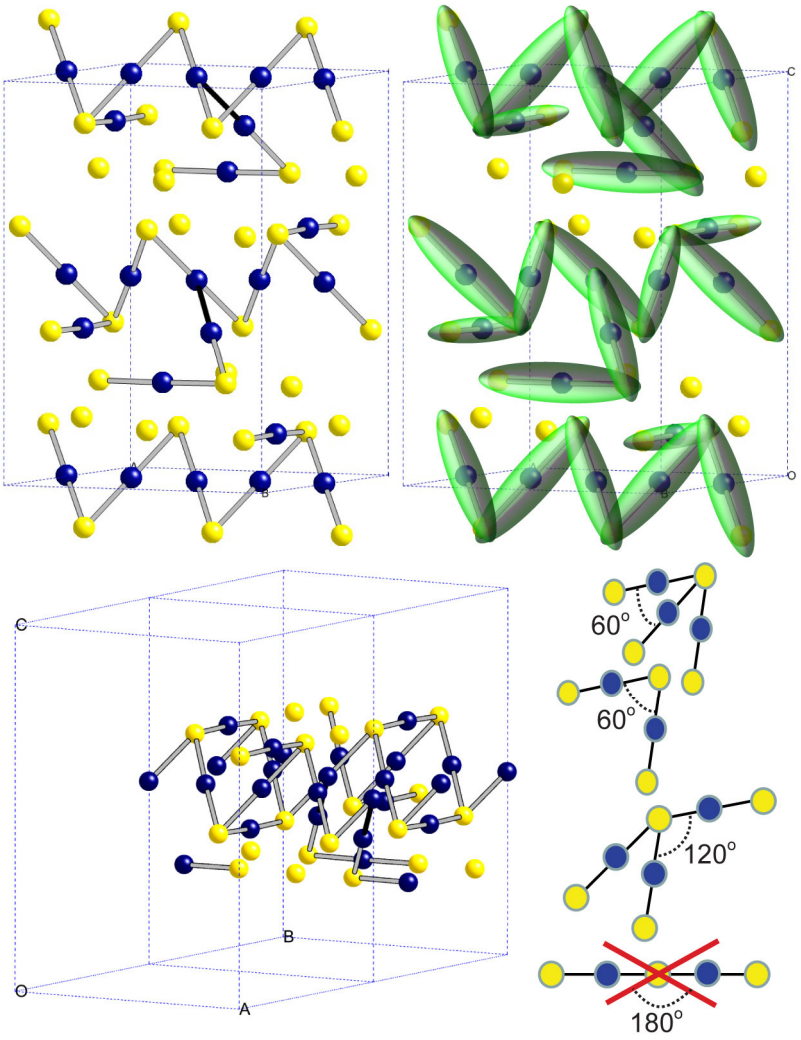

Figure 3.34: The connectivity of the trimerons in the unit cell of the Cc structure. Fe^{2+} sites are shown as blue spheres and Fe^{3+} as yellow spheres. The trimeron bonds are indicated in the top left hand panel, and ellipsoids showing how the delocalisation of the minority spins over three sites units occurs is shown in the top right hand panel. The single Fe^{2+} - Fe^{2+} trimeron interaction is indicated by a bold bond in the top left hand panel. The connectivity beyond the unit cell is shown in the bottom left panel revealing the 120 ° degree connectivity of some trimerons. The different types of trimeron connectivity observed in the structure are shown bottom right. 180 ° connectivity of trimerons is never observed, and trimerons never appear in isolation.

Trimerons offer an explanation as to why the BVSs of the Fe^{3+} (Table 3.12) have such a large distribution. The Fe^{3+} sites are no longer electronically equivalent, being involved in different numbers of trimeron bonds. Table 3.14 shows that the sites with no incident trimerons have the highest BVS which are even higher than those of the A-sites. Those with progressively lower BVS have more incident trimerons. A very crude fit may be made by assuming that the maximum BVS for the B-sites is around 2.9 and that each trimeron

interaction reduces this by about 0.1 as illustrated in Figure 3.35 which reproduces the trend exceptionally well, apart from one outlier (discussed below).

Site	B2a_1	B2a_2	B2b_2	B3_1	B3_2	B3_3	B3_4	B4_3
BVS	2.77	2.67	2.96	2.58	2.61	2.64	2.81	2.93
No. T	1	2	0	3	3	3	3	0

Table 3.14: The number of trimerons incident at each Fe^{3+} B-site and their BVS values.

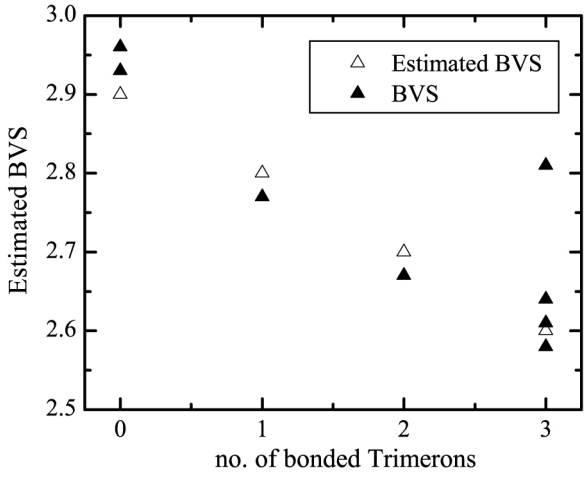

Figure 3.35: A plot of BVS versus number of trimeron bonds (closed symbols) indicates a very good negative correlation. A crude attempt at fitting this trend is made (open symbols) by assuming the maximum BVS is 2.90 and that every trimeron interaction reduces the charge by 0.1.

The outlier of Figure 3.35, site B3_4, which has a high BVS despite having three incident trimerons, is possibly an outlier due to the fact that one of its trimeron bonds is one of the two anomalously long ones (within the trimerons approximation) in Figure 3.32. It can be seen from Table 3.15 that the other two trimeron bonds to B3_4 are also rather long and only marginally lower than the global average of 2.967 Å, which explains why the BVS of this site is quite high. The B3_4 site has trimerons meeting at 120 ° and presumably this is less favourable than those in which all trimerons meet at 60 ° in which a mutual distortion of the Fe^{3+} will more readily satisfy the shortening of all trimerons bonds. The trimeron connectivity for the only other site Fe^{3+} (B3_1) which has trimerons meeting at 120 ° is also shown in Table 3.15. It, however, behaves as expected having a greatly reduced BVS of 2.58 which is the lowest valence state of any Fe^{3+}. Interestingly the two sites B3_1 and B3_4 have a trimeron bond in common via B1B_2, which has an exceptionally short bond to B3_1 and an anomalously long bond to B3_4 as indicated in Figure 3.36. An explanation now emerges for these two anomalously long bonds within the trimerons interpretation, in

which one dimeron is formed between B3_1 and B1B_2 consistent with the sites being the lowest valent Fe^{3+} and highest valent Fe^{2+} respectively. The dimeron formation means that B3_4 now only has two incident trimerons which are 120 ° rather than 60 ° explaining why the remaining bond lengths are relatively large, and the reduction in BVS is still modest compared with the other Fe^{3+} with two incident trimerons. However, dimeron formation may not be implicated in other cases, as a double dimeron implies a Fe^{1+} like state which is physically unreasonable, and the trimeron approximation remains the most useful one for describing the structure. The formation of the dimeron here breaks one of the 120 ° trimeron interactions, and so possibly it only occurs so as to relieve the internal strain.

Distance (Å)	B1B_2	B1A_2	B4_4*
B3_4	3.012	2.914	2.946
Distance (Å)	B1B_2	B1A_1	B4_1*
B3_1	2.821	2.925	3.018

Table 3.15: The trimeron bond distances incident at the Fe^{3+} B-Sites B3_4 and B3_1 both of which have one of the anonymously long bonds from the histogram of Figure 3.32 and have a trimeron bond which meets at 120 ° to the other two (indicated by a *).

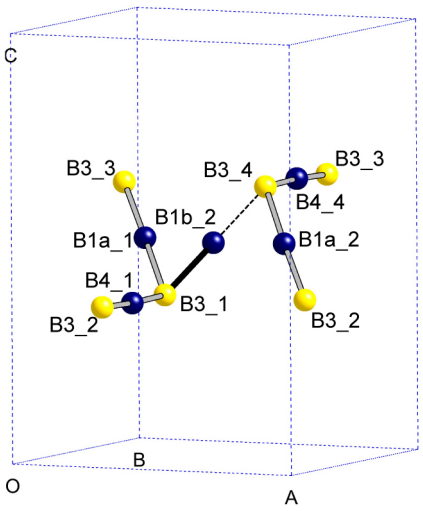

Figure 3.36: Trimeron connectivity of site B3_4 which has an anomalously high BVS in Figure 3.35. The bond distance B3_1- B1b_2 which has been investigated for dimeron formation in the above text is drawn in bold, and the corresponding broken trimeron bond is drawn as a dotted line.

Although the local distortions in the structure have been rationalised, a reason for this precise arrangement of trimerons has not yet presented itself. The fact that trimerons are observed to end not only at B^{3+} but also at B^{2+} places relatively few constraints on trimeron connectivity.

Below a simple scenario is investigated in which trimerons must start and end at a B^{3+} and have a B^{2+} in the centre to ascertain if all trimeron bonds may be realised in the structure without the need for empty B^{2+} t_{2g} orbitals acting as acceptors.

3.4.4. Trimeron connectivity

There at 48 bonds in the asymmetric unit in between the 16 B sites. Each trimeron occupies two Fe^{2+} - Fe^{3+} so 16 bonds are require to accommodate them. The charge ordered model can be viewed in terms of a network of $(Fe^{2+})_n(Fe^{3+})_{4-n}$ tetrahedra such as drawn in Figure 3.29. For each type of tetrahedra of n = 0, 1, 2, 3, 4 it is trivial to calculate the number of possible Fe^{2+} - Fe^{3+} bonds. With the simplified constraints that a trimeron must start and end at a Fe^{3+} and that no Fe^{2+} can occur in two trimerons, it is possible to calculate the number of possible trimeron bonds per tetrahedra as listed in Table 3.16. The different possible types of charge ordered models with respect to these tetrahedra are given in Table 3.17 along with the number of possible Fe^{2+} - Fe^{3+} and trimeron bonds. Straightaway it can be seen that a large number of these models fail to have the minimum of 16 bonds required to accommodate all the trimerons and can be discounted in this approximation. In fact, no possible model has more than 16 such bonds (although many have a much larger number of Fe^{2+} - Fe^{3+} bonds), indicating that this is quite a heavy constraint on the structure. It is not trivial to prove if it is possible to simultaneously realise all 16 trimeron bonds in any of these models within this approximation.

$(Fe^{2+})n(Fe^{3+})_{4-n}$	0	1	2	3	4
Fe^{2+} - Fe^{3+} per tetrahedra	0	3	4	3	0
No T bonds per tetrahedra	0	1	2	3	0

Table 3.16: The number of Fe^{2+} - Fe^{3+} bonds per tetrahedra and the number of allowed trimeron bonds.

	N=					No. B^{2+}-B^{3+} bonds	No. of T bonds
Class	0	1	2	3	4		
A		2	4	2		28	16
B		3	2	3		26	16
C	1	1	4	1	1	22	12
D	1	1	3	3		22	16
E		3	3	1	1	18	10
F	1		5	2		26	16
G		2	5		1	26	12
H	1	2	1	4		22	16
I		4	1	2	1	22	12
J*	0	0	8	0	0	32	16
K*	0	4	0	4	0	24	16

Table 3.17: The possible types of charge ordering model with respect to types and numbers of charge ordered $(Fe^{2+})n(Fe^{3+})_{4-n}$ tetrahedra. Adapted from ref. [99]. Additional models are indicated by *.

A possible reason that the model which fulfils Anderson's criteria (J^*) is not realised in the Verwey structure is illustrated in Figure 3.37. Here in order for all of the 16 trimeron bonds to be realised, a large number of them must meet at 120 ° to each other. Although Figure 3.37 is not the only way for such an arrangement of bonds to be made it can clearly be seen that any Fe^{3+} which has trimerons which are exclusively in different tetrahedrons will always result in 120 ° interactions.

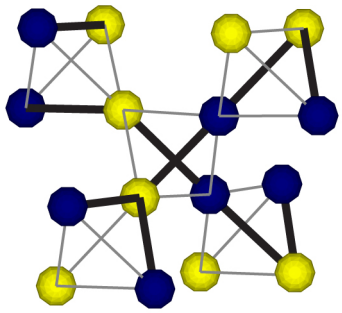

Figure 3.37: A charge ordered model consistent with Anderson's type charge ordering. Fe^{2+} and Fe^{3+} are shown as blue and yellow spheres respectively and trimeron bonds are drawn in bold.

Although the analysis is not conclusive it can be seen that the observed Verwey structure which is of type model B of Table 3.17, has the lowest number of n = 2 type tetrahedra of those models which are not electrostatically highly unfavourable (containing n = 0 or n = 4 tetrahedra). It is possible therefore that the structure in fact selects a ground state with the

minimum number of n = 2 (Anderson) tetrahedra as their coupling in the structure results in strained trimeron interactions. Any model possessing more than half n = 2 type tetrahedra will presumably have a significant number of these interactions. On the other hand, model B has only two of these types of tetrahedra, and the Verwey structure (Figure 3.29) can be seen to possess no instances in which two n = 2 tetrahedra share their vertices.

3.4.5. Ferroelectric polarisation

The discovery that charge ordered phase of $LuFe_2O_4$ is ferroelectric as a result of the polar arrangements of Fe^{2+} and Fe^{+3} ions in the structure,[19] has recently lead to experimental[140] and theoretical investigations[125, 141] into the ferroelectric polarisation in the charge ordered phase of magnetite.

From the experimental Cc crystal structure, polarisation may be calculated in the point charge approximation as:

$$P = \left(\sum_{i}^{n} q_i \left((x_i - x_0) + (y_i - y_0) + (z_i - z_0) \right) \right) \Big/ V_n \ ,$$

Where the 0th atom at (x_0, y_0, z_0) corresponds to any atom that was at an inversion centre in the cubic $Fd\bar{3}m$, x, y and z define the orthogonal coordinates of the atoms in the crystal in meters, q_i is the point charge on a site in Coulombs, and V_n is the volume containing the atoms over which the sum is made.[28, 142] In principle the sum should be made in the limit $-\infty \rightarrow \infty$ but in practice the calculation converges over a relatively small number of unit cells. The polarisation calculated from the Verwey structure in the point charge approximation is given in Table 3.18 along the crystallographic directions *a* (P_a), *c* (P_c) and their calculated resultant (P). Due to the symmetry of the charge ordered phase, no polarisation can be developed along *b*. P_a is rather small with the majority of the polarisation being along *c*. The values calculated are almost an order of magnitude larger than those reported from theoretical work,[125] and about four times larger than those found experimentally from thin film (P = 0.11 C m^{-2})[140]. However, with thin films ambiguity exists in the direction of polarisation being probed, and crystal twinning always acts to reduce the observed values.

The comparison of the P values calculated by considering the formal charge ordered valence states (P = 0.422 C m^{-2}) with those from an average valent B-site (P = 0.355 C m^{-2}) reveal

that the majority of the polarisation developed below T_v is as a result of the off-centre distortions of the cations, rather than because of the acentric arrangements of point charges. This is not surprising, as, as indicated in Figure 3.29 only two sites must be exchanged with each other in the asymmetric unit in order to restore centricity. It is noteworthy that in this sense the trimerons are coupled to the development of ferroelectric polarisation, as they are responsible for the large off-centre distortions of the B^{3+} site. The B-sites sit on an inversion centre in their cubic structure. The distortion away from their high symmetry positions in the low temperature structure, leading to a loss of the inversion point symmetry, is a direct consequence of the trimeron formation.

Direction / Model	Formal point charge C m^{-2}	Average point Charge C m^{-2}
P_a	0.118	0.080
P_c	0.405	0.346
P	0.422	0.355

Table 3.18: Polarisation calculated along *a* (P_a), *c* P_c and the resultant P in the point charge approximation. Values are given assuming the formal valence states of the charge ordered B-sites as determined in Section 3.4.2 and those considering only the average 2.5 + B-site charge.

3.4.6. Entropy

The observed change in entropy at the T_v of ~0.7R,[143] is smaller than that expected for the ordering of fully disordered Fe^{2+} / Fe^{3+} which is R ln 4 per mole.[144] The model presented here for the Verwey structure, which additionally has orbital ordering of the triply degenerate Fe^{2+} state, is expected to give rise to an even larger change in entropy at T_v of R ln 12.

Historically attempts have been made to resolve the discrepancy between experimental and theoretically expected values of the entropy change by considering the existence of short range ordering above T_v. This is consistent with diffuse scattering observations above T_v suggesting that short range correlations may already exist well above the transition. Estimations based on the condensation of short range ordered Anderson type tetrahedra leads to an entropy change (R ln(3/2) = 0.4 R) which is much smaller than that observed experimentally.[144] However, as the long range ordering has now been shown to be of non-Anderson type with respect to the pyrochlore lattice, this calculation is no longer relevant.

In the computational study of ref. [124] the structure has been relaxed, obtaining a charge ordering which is the same as the experimental model reported here with respect to the number of n = 1, 2 and 3 $(Fe^{2+})_n(Fe^{3+})_{4-n}$ tetrahedra (model type B of Table 3.17). The authors go onto to consider the entropy of an ensemble of n= 1 / n = 3 tetrahedra which they report as R ln 2 in good agreement with the experimental value. The experimental structure does not just consist of n =1 and n = 3 tetrahedra but also contain some n = 2 tetrahedra so the analysis does not quite hold. The experimental findings of this work indicate that if short range order exist above T_v, that trimerons and not $(Fe^{2+})_n(Fe^{3+})_{4-n}$ tetrahedra are the quasiparticles which should be considered. As detailed in Section 3.4.4 trimeron connectivity appears to favours n = 3 tetrahedra and hence this entropy calculation may capture some essence of the true problem. However, as experimentally trimerons are observed to terminate at B^{2+} as well as B^{3+} the constraints which may be imposed on short range order above T_v are rather weak, and it is non-trivial to calculate the entropy of this model.

3.5. Comparison of Xtal6 and Xtal4 models

In this section the model refined against Xtal4 data is compared with that discussed above derived from the Xtal6 data, and is shown to be essentially the same with respect to the interrogated parameters such as the average bond length, BVS and JT distortions. Here the parameters derived from oxygen positions are chosen to make the comparison between the models of Xtal4 and Xtal6, as these are the least well determined in the crystal structure.

In Figure 3.38 on the left, Q_{Rad} is plotted against Q_{JT} for both models refined against Xtal6 and Xtal4 data using anisotropic thermal parameters. It is evident that the Q_{Rad} values are in very good agreements between the refinements, but the Q_{JT} distortions have a slightly larger distribution, with two sites being significantly different between Xtal4 and Xtal6. These differences are a result of relatively small changes in B - O bond lengths which result in the direction of the chosen JT axis for Q_{JT} to change. The differences probably arise due to correlations between oxygen thermal parameters and oxygen fractional coordinates in the Xtal4 model, which lead to non-positive definite thermal parameters for several oxygen atoms as discussed in section 3.3.2. In Figure 3.38 on the right, Q_{JT} and Q_{Rad} extracted from

isotropic Xtal4 and Xtal6 refinements are compared. Here all the thermal parameters are positive and physically reasonable, and the agreement between the models refined against the difference data sets is much better. Only one site has a substantially different Q_{JT} value, and this is for a B^{3+} site where no well defined JT axis is expected.

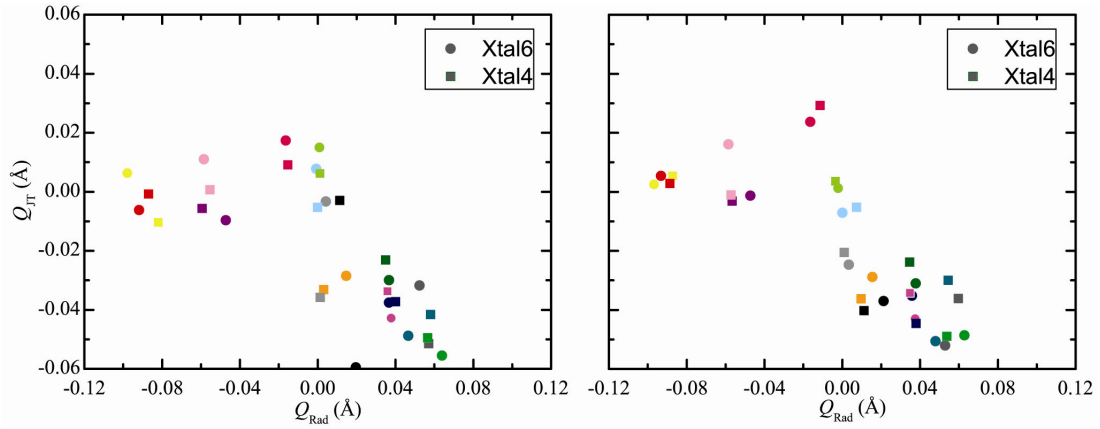

Figure 3.38: Comparison of plot of Q_{Rad} versus Q_{JT} for models refined against Xtal4 and Xtal6 data. Q_{Rad} and Q_{JT} values are extracted from refinements in which the thermal parameters were modelled as anisotropic (left) and isotropic (right).

The Q_{Rad} versus Q_{JT} plots from the isotropic model do not quite exhibit the clear bimodal Q_{JT} distribution of Figure 3.27. This is due to the site B3_1 which is the lowest valent 3+ and in the isotropic model has a more pronounced JT distortion which possibly has some physical precedent in light of the discussion of section 3.4.3.

It has been shown in this section that essentially the same structure is obtained from refinements against a second data set, and this lends weights to the conclusions derived from the model refined against Xtal6 data in the previous section.

3.6. Conclusions

The Verwey structure of magnetite has been solved at 90 K in the space group Cc with 504 freely refined parameters. The crystal structure has been verified by refinement against data collected against a second micro-crystal. The fitting statistics and the lack of violation of systematic absences in the nearly untwinned Xtal6 data confirm the long proposed space group.

The structure has been demonstrated to be charge ordered as evidenced by orbital ordering to the first approximation and is found to be consistent with a previously reported model. A more insightful understanding of the low temperature structure can be gained by considering the delocalisation of the minority spin electron of the ordered t_{2g} orbital of a Fe^{2+} to two acceptor t_{2g} orbitals (a trimeron). This explains the rather continuous distribution of BVS observed which has caused much controversy in the resonance x-ray scattering community and explains why many studies find only very small charge disproportionations.

The results can be reconciled with spectroscopic measurement above Tv which cite JT polarons as being the charge carriers[101, 103] which would be consistent with a fluctuating state of trimerons above T_v. Trimerons may also offer explanations for the diffuse scattering observed just above T_v and the unexpectedly small change in entropy (~ 0.7 R)[143] on cooling through the transition.

4. Electronic structure calculations on the Verwey ground state

In this chapter, the electron density implied by the proposed coordinates for the experimental Verwey structure will be examined via self-consistent field (SCF) calculations in the DFT + U approximation. Methodology employed is in line with that used in the published structure optimisation of the ground state of Fe_3O_4 in Cc symmetry.[124, 125, 145] Comparison of the coordinates of the optimised structure of ref. [124] with the experimental coordinates of Chapter 3, will also be made, and the models will be referred to as the Jeng and the experimental model respectively.

4.1. Calculation details and convergence test

Electronic structure calculations were performed in the framework of density functional theory with the full-potential augmented plane-wave plus local orbital method as implemented in the WIEN2K code.[146] The spin-polarised calculations were performed for the full Cc crystal structure with 112 atoms in the primitive unit cell, using the structure determined in Chapter 3 at 90 K. The 3s, 3p, 3d, and 4s orbitals of Fe and the 2s and 2p orbitals of O were treated as valence states, and additional local orbitals were used for Fe s and p states and O s states. Electron exchange and correlation were considered in the generalised gradient approximation (GGA)[57] with additional treatment of on-site Coulomb repulsion using the DFT + U approach.[147] An on-site Coulomb energy of U = 4.5 eV and an exchange parameter J = 0.9 eV were used for all Fe d states as in previous work.[124, 125, 145] Brillouin zone integration was performed on a regular mesh of 6 × 6 × 2 *k* points with 21 *k* points in the irreducible part of the Brillouin zone. Atomic sphere muffin tin radii (RMT) of 1.86 bohr and 1.65 bohr were chosen for Fe and O, respectively, and the largest plane-wave vector K_{max} was given by $R_{MT}K_{max} = 8$. Spin-orbit coupling was not considered.

Convergence for invariance of the total energy of the structure was tested against non-physical parameters such as the number of *k* points and the largest plane-wave vector used in the calculation as illustrated in Figure 4.1. The tests were performed for calculations in which spin polarisation was not considered, and those for the optimisation of the number of *k*

points were performed only on the cubic structure as larger calculations for the convergence test would have been too computationally expensive. The change in total energy beyond 60 *k* points appears to be less than 0.02 mRy per site and less than 2 mRy between $R_{MT}K_{max}$ = 8 and 12. Although it would be desirable to perform calculations at $R_{MT}K_{max}$ > 8 if total energies are to be compared meaningfully, this was found to be too computationally demanding, and hence total energies of the cubic and the Cc structure are not compared here. Instead, convergence with respect to the electron density distribution was confirmed by comparing the $R_{MT}K_{max}$ = 8 results with those calculated at $R_{MT}K_{max}$ = 7 for the electronic structure calculation of the experimental model, as illustrated in Figure 4.2.

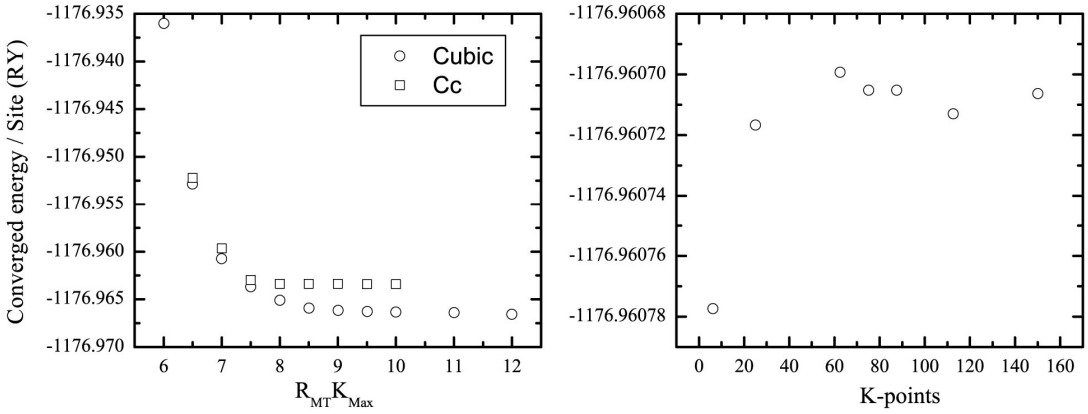

Figure 4.1: Convergence test for the total energy of the structure against $R_{MT}K_{max}$ and against the number of *k* points used. The calculations were performed in the converged limit of $R_{MT}K_{max}$ = 8 and 74 *k* points.

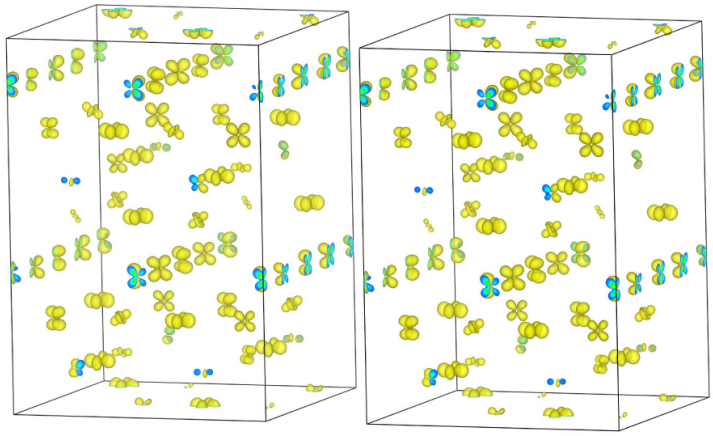

Figure 4.2: Electron density distribution isosurface plots in Vesta[148] for SCF calculations performed at $R_{MT}K_{max}$ = 7 (left) and $R_{MT}K_{max}$ = 8 (right). The distribution of electron density appears to be converged in respect to the maximum plane wave cut of energy.

Convergence of the SCF cycle was taken at the point the total energy change between cycles was less than 0.1 mRy. Convergence was only reached after several days of calculations

running the *k* point calculations in parallel across over 100 nodes. It was deemed too computationally demanding to attempt structure optimisation, as this would require a SCF calculation step after each force minimisation cycle. The partial forces on each atom after convergence are reasonable with no site experiencing an unbalanced force greater than 0.3 $eVÅ^{-1}$ and the average being below 0.06 $eVÅ^{-1}$ per site. In light of the fact that the structure has been obtained at 90 K but the electronic structure calculation is for the structure at its zero point energy, these values do not give any cause for concern. The average moment of 3.99 μB per formula unit indicates that the calculated spin polarisation is consistent with what is expected from the ordered moment in magnetite.

4.2. Interpretation of calculated electron densities

The density of states (DOS) from the electronic structure calculation is shown in Figure 4.3 compared with a calculation on the cubic structure[96] performed in the same manner. The cubic structure can clearly be seen to have a very substantial DOS at the Fermi level (FL), consistent with the conducting nature of magnetite above T_V. The conduction band can be seen to be almost entirely composed of B states (d-orbitals) with minority spin character, with only a small contribution from the O states (p-orbitals). In the Cc structure, an opening up of a band gap is evident of about 500 meV. This is consistent with the insulating nature of the Verwey state and that of a published optimised structure,[124] but somewhat larger than the experimentally observed 100 meV.[101] The narrow band which falls in the range -460 and 0 meV is almost entirely of minority spin B site d-orbital character ($Q_{B:d\downarrow}$). It is the spatial distribution of this electron density in this energy range which is of interest in ascertaining the degree of charge and orbital ordering and it is this which will form the majority of the investigation in this section.

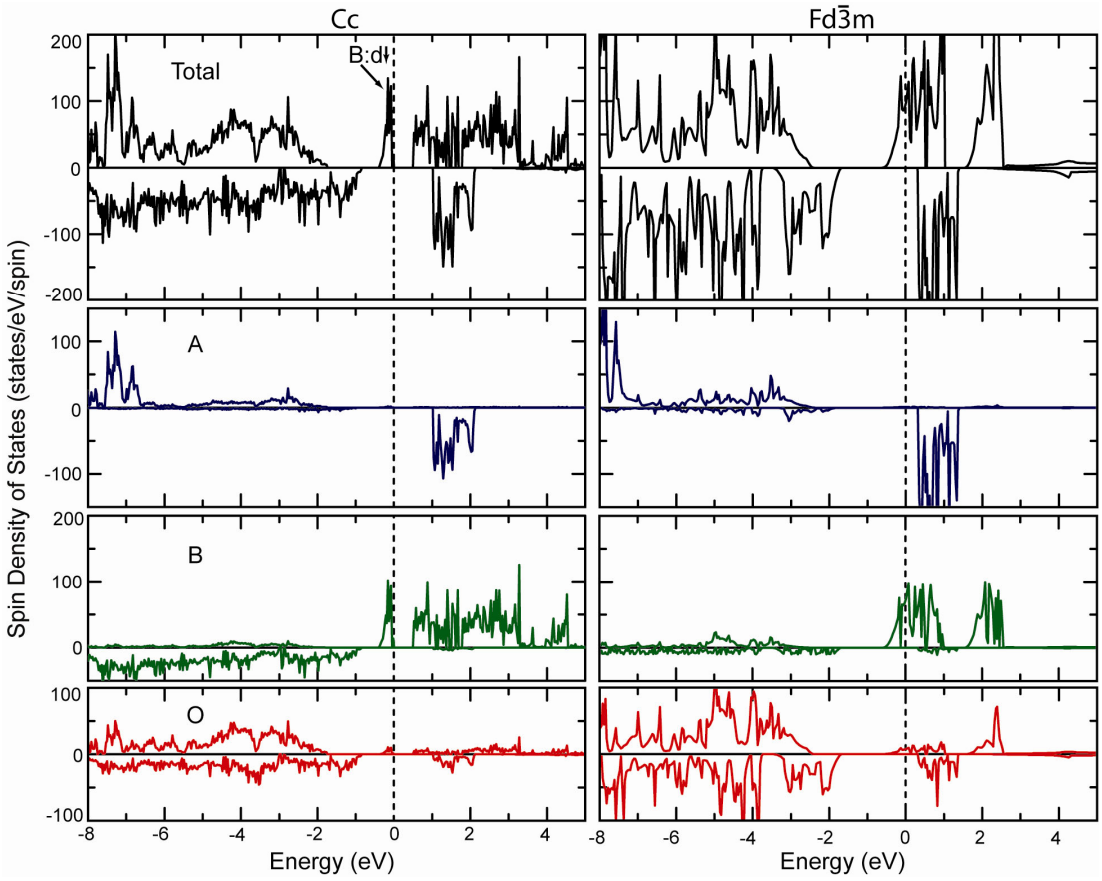

Figure 4.3: Density of states for magnetite calculated from the low temperature Verwey structure of Chapter 3 and from the cubic structure of ref. [96].

The total integrated charges (Q_{Tot}) on each B-site and those for the minority spin *d*-state ($Q_{B:d\downarrow}$) are listed in Table 4.1 and plotted against their corresponding BVS values in Figure 4.4. It can be seen that Q_{Tot} values are in agreement with the small separation of BVS for Fe^{2+} and Fe^{3+} states observed experimentally. The situation is somewhat improved in considering $Q_{B:d\downarrow}$ rather than Q_{Tot}. The double-y axis plot of Figure 4.4 has graduations of equal magnitude in Q_{Tot} and $Q_{B:d\downarrow}$, making the previously identified charge screening evident.[123] Although $Q_{B:d\downarrow}$ spans a range of 0.35 e, Q_{Tot} spans a range of less than 0.15 e explaining why the charge ordering is experimentally often not observed to be very pronounced.

Site	Charge	Q_{Tot}	$Q_{B:d\downarrow}$	d_{z^2}	$d_{x^2-y^2}$	d_{xy}	d_{xz}	d_{yz}	d_{Max}
	(e^-)	(e)							
B1a_1	2	23.57	0.93	0.06	0.08	0.41	0.12	0.26	0.41
B1a_2	2	23.57	0.93	0.05	0.08	0.38	0.12	0.31	0.38
B1b_1	2	23.57	0.93	0.06	0.08	0.43	0.12	0.24	0.43
B1b_2	2	23.51	0.82	0.06	0.10	0.29	0.14	0.22	0.29
B2a_1	3	23.44	0.67	0.22	0.16	0.07	0.17	0.06	0.22
B2a_2	3	23.47	0.73	0.12	0.13	0.18	0.16	0.14	0.18
B2b_1	2	23.56	0.90	0.52	0.21	0.05	0.09	0.03	0.52
B2b_2	3	23.42	0.61	0.11	0.17	0.07	0.20	0.06	0.20
B3_1	3	23.49	0.77	0.07	0.12	0.17	0.16	0.25	0.25
B3_2	3	23.47	0.74	0.15	0.19	0.09	0.15	0.16	0.19
B3_3	3	23.47	0.74	0.12	0.17	0.10	0.16	0.19	0.19
B3_4	3	23.44	0.66	0.11	0.18	0.09	0.18	0.10	0.18
B4_1	2	23.57	0.93	0.50	0.28	0.03	0.08	0.03	0.50
B4_2	2	23.54	0.87	0.06	0.09	0.26	0.13	0.33	0.33
B4_3	3	23.42	0.61	0.11	0.17	0.07	0.20	0.07	0.20
B4_4	2	23.57	0.93	0.49	0.30	0.03	0.08	0.04	0.49

Table 4.1: Total integrated charges and minority spin electron densities for the B-sites from the SCF calculation.

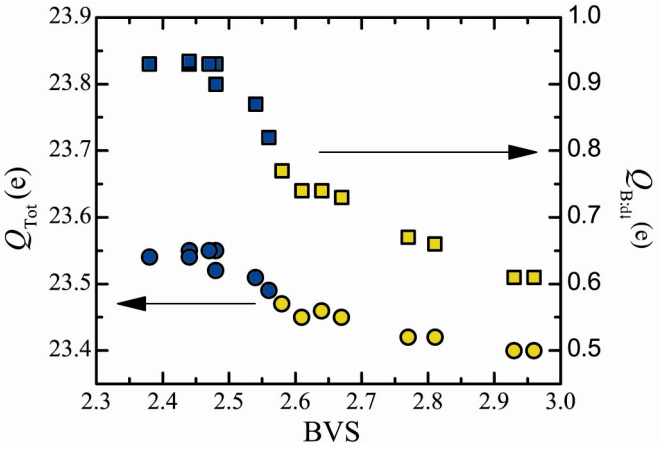

Figure 4.4: Total integrated charge (Q_{Tot}) and spin density in the minority spin d-orbital ($Q_{B:d\downarrow}$) for the B-sites versus their BVS values.

The charge screening is investigated further in Figure 4.5 in which it can be seen that a large amount of the screening effect is due to the majority B-atom d-states ($Q_{B:d\uparrow}$), which act to reduce the Q_{Tot} by up to 0.12 e^- accounting for the greatly reduced charge separation observed in Figure 4.4.

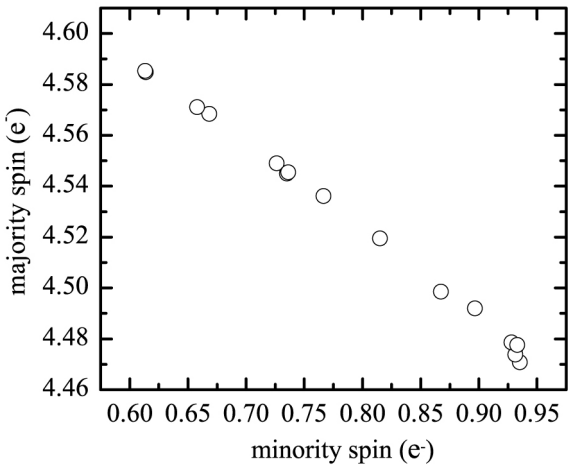

Figure 4.5: Majority ($Q_{B:d\uparrow}$) versus minority spin density ($Q_{B:d\downarrow}$) of the B-atom d states. The screening effect is evident in the negative correlation between $Q_{B:d\downarrow}$ and $Q_{B:d\uparrow}$ of about -⅓.

The distribution of $Q_{B:d\downarrow}$ among the d-orbitals (Table 4.1) does not seem to follow what might be expected for the JT active sites, where a single t_{2g} orbital should contain the majority of density. The range of the spin density in the maximally occupied d-orbital (d_{Max}) is only about 0.35 e^- across the 16 B sites, and no larger than the range of $Q_{B:d\downarrow}$. The lowest valent B^{3+} and the highest valent B^{2+} are indicated in Figure 4.6, where their separation in $Q_{B:d\downarrow}$ is of similar magnitude to that of d_{Max}. All the B^{3+} sites have a rather narrow range of d_{Max} in contrast to their $Q_{B:d\downarrow}$ values, whereas B^{2+} sites have a large range of d_{Max} compared with their $Q_{B:d\downarrow}$ values. This difference arises as the orbitals are not projected along the conventional local symmetry axis (i.e. e_g orbitals along bonds, t_{2g} in-between bonds). For B^{3+} states this makes little difference as the t_{2g} orbitals are degenerate and all projections will return a rather similar d_{Max} value. However, for B^{2+} states certain projections will split $Q_{B:d\downarrow}$ between several orbitals. Due to the unity point group symmetry of the octahedrally coordinated sites it is nontrivial to pick a globally consistent projection of orbitals along local pseudo symmetry axes without introducing a bias in the result.

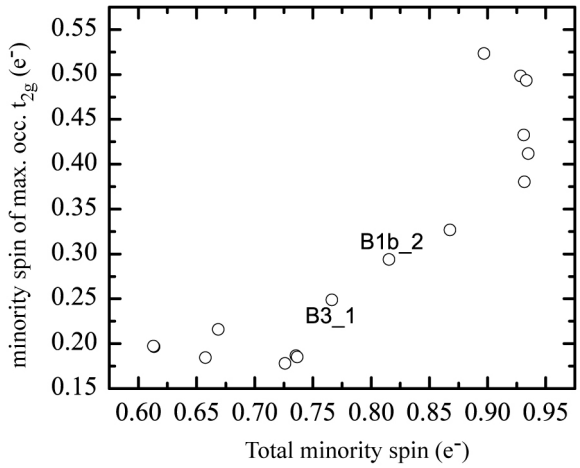

Figure 4.6: Total minority spin of d states ($Q_{B:d\downarrow}$) for each site plotted against spin density of the minority d-orbit which has the maximum occupation (d_{Max}), (see Table 4.1). The highest valent B^{2+} and lowest valent B^{3+} are labelled.

To avoid this problem of projecting atomic orbitals, electron density is investigated by the visualisation of its spatial distribution through the uses of isosurface plots (Figure 4.7). The B^{2+} states (1-8) all have a spatial distribution of the $Q_{B:d\downarrow}$ which is of singly degenerate t_{2g} orbital character with little variation in isosurface size between the sites. Additionally, all their lobes are pointing along the direction of the trimeron bonds that were predicted in section 3.4.3. The B^{3+} states (9-16) have a rather large variation in character as expected by the trimeron model. Those not involved in trimeron bonds (15 and 16, B2b_2 and B4_3 respectively) have almost no visible $Q_{B:d\downarrow}$ at the $\rho = 0.1$ eÅ^{-3} isosurface level consistent with their BVS values which are close to 3. Sites 12 (B2a_2) and 13 (B2a_1) which have two and one incident trimeron bonds respectively have substantial isosurface but are significantly smaller than those of sites 1-8. Their distributions are also not as isotropic as expected for fully degenerate t_{2g} orbital set. In sites 10 (B3_3), 11 (B3_2) and 14 (B3_4) where there are three trimerons incident at the site, the electron densities are again somewhat more isotropic as all of the t_{2g} orbitals are participating in a trimeron bond, and hence some degree of degeneracy is still maintained. Site 9 (B3_1) again is hard to reconcile within the orbital ordered / trimeron picture as it has an isosurface which has a singly degenerate t_{2g} character. Its lobes do not point directly along any one trimeron bond, but are almost aligned along the direction of site 8 (B1b_2), pointing towards a possible degree of dimeron formation between these two sites as discussed in section 3.4.3.

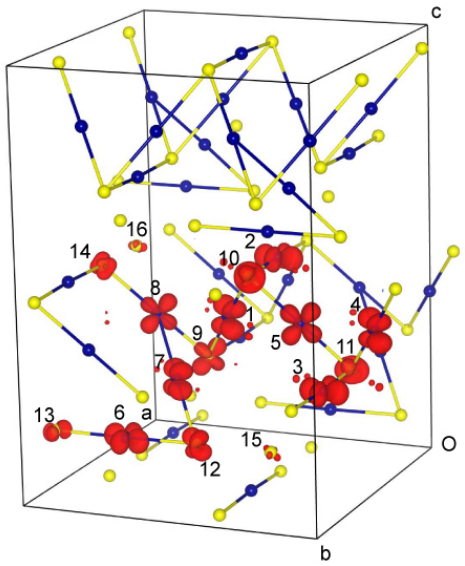

Figure 4.7: Electron density isosurface plotted in Vesta[148] at a level of ρ = 0.1 e Å^{-3}. Sites are numbered from high to low electron density. Trimeron bonds predicted in Section 3.4.3 are indicated in the unit cell while the electron density is only shown for the asymmetric unit.

If delocalisation of the minority spin from a B^{2+} to two B^{3+} occurs, at some ρ, isosurfaces connecting the relevant sites should be evident. An attempt at displaying this is made in Figure 4.8, where somewhere between ρ = 0.005 and 0.01 e Å^{-3}, most of the relevant sites are connected by the isosurface. It is however, not very easy to quantify this interaction, especially when different trimerons become connected at different ρ isosurface levels. A two-dimensional slice of the ρ is plotted for three B-sites in Figure 4.9 showing a trimeron interaction. However, 48 such plots are required to visualise all these possible interactions, and the interpretation as to whether a trimeron bond exists will still depend on the graduation of the ρ contours picked.

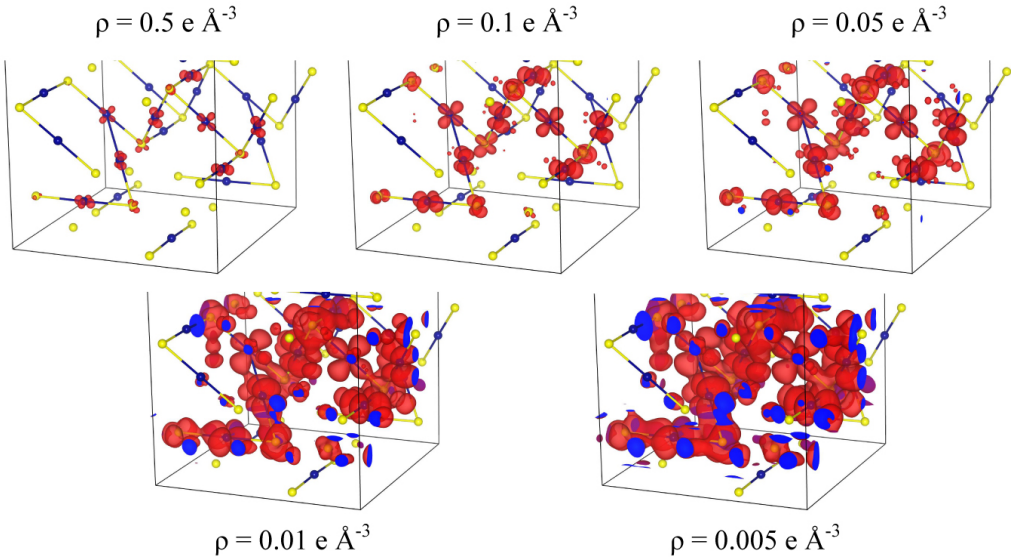

Figure 4.8: Evolution of the spatial distribution of $Q_{B:d\downarrow}$ with respect to the isosurface electron density level. The electron density is only shown in the asymmetric unit, and cell orientation is as in Figure 4.7.

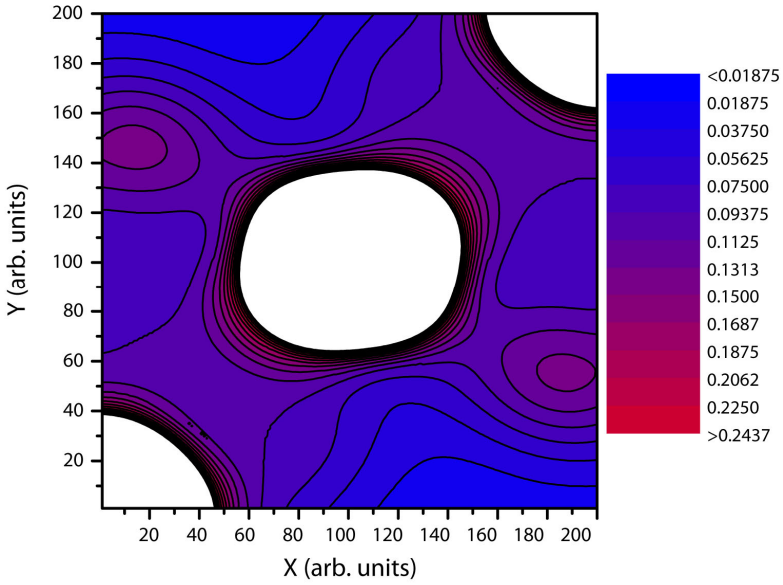

Figure 4.9: Minority electron density ($Q_{\downarrow}$) plot of trimeron B3_2-B1b_1-B3_3, the x and y axis are approximately orthogonal and ~4 Å long and demarcate the centre of the two B^{3+} sites.

For continuous comparison of the ρ, vectors connecting each B-site with its nearest neighbour are shown in Figure 4.10. As the electron density near the core of each site is not of much interest in resolving the question of trimeron bonding, only the density in the middle ~ 1 Å of the bond is plotted corresponding to the distance in-between the two muffin tin spheres of the sites. The plots are arranged in terms of the linear chain of B-sites propagating through the structure, of which eight are symmetry unique. Four of these have a period of eight sites, and four have a period of four sites with respect to the Cc unit cell. The

electron density between the atoms is significant in cases where trimeron bonds are predicted to form, and negligible in all other cases, excepting sites along the chain of direction [1 1 1] with respect to the Cc unit cell. The key difference in this chain is that its trimerons are separated by three or five bonds, whereas, in all other chains, separations of four or eight are always observed. Two trimerons with their centres separated by only two atoms implies a significant stretching out of B^{3+} - B^{3+} distance in the crystal structure. This will ultimately be unfavourable as the B^{3+} sites each have two bonds to common oxygen atoms. The strain introduced into these bonds will counter the lengthening of the B – B distance.

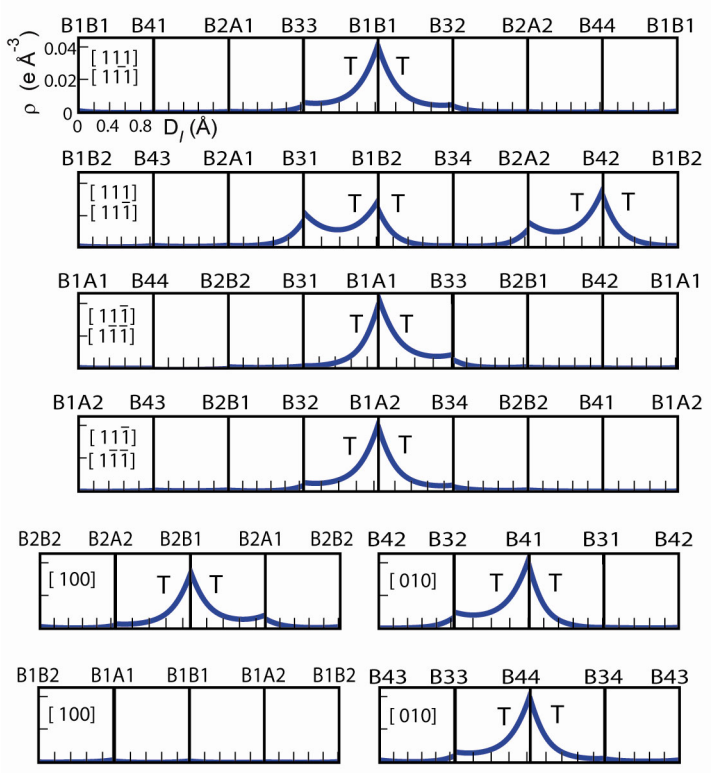

Figure 4.10: Electron density plotted along the eight unique B-B chains propagating through the structure. Only the middle ~ 1 Å is plotted corresponding to that in-between the muffin tin spheres.

A possible explanation for the observed electron density in the chain containing two trimerons, is that the trimeron bond of B1_b2 would, in fact, prefer to be located at B3_1, leading to an even distribution of trimeron centres, but the connectivity of the crystal structure appears to make this unfavourable. The frustrated interaction is hence relieved by the formation of an intermediate state which looks more like a dimeron (where the $t_{2g}^{\downarrow}$ electron is shared between two sites). Despite this slight perturbation to the trimeron picture, it is evident from Figure 4.11 that the 16 bonds predicted from the trimeron approximation are those with the highest average $Q_{B:d\downarrow}$ electron density, even though some of them are

significantly longer than the non-trimeron distances. In this respect the trimeron model is reinforced with respect to the conclusions of section 3.4.3. It is also noteworthy that all B^{2+}-B^{2+} distances contain almost no $Q_{B:d\downarrow}$ electron density, except for the one case where the distance is part of a trimeron bond, validating this assignment.

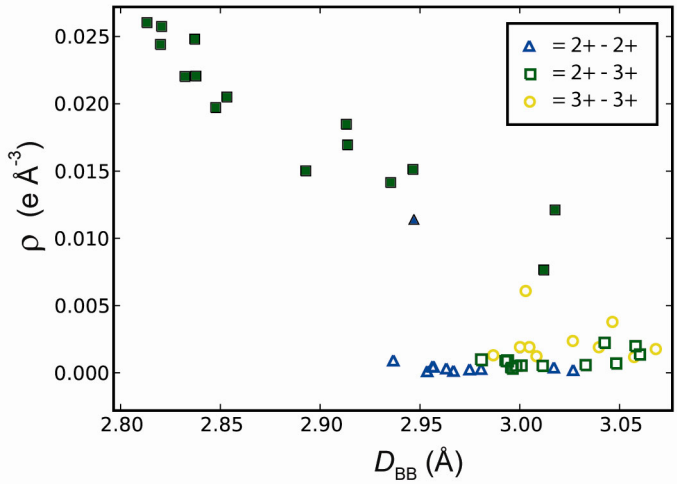

Figure 4.11: Average electron density of $Q_{B:d\downarrow}$ between B-sites calculated from Figure 4.10 plotted against the distance between the sites (D_{BB}). Filled symbols indicate that they are predicted to be part of a trimeron bond. The bonds are between B-sites with formal charges as indicated by the legend. The average ρ can be seen not just to be a trivial function of D_{BB}.

The validation of the trimeron model also requires evidence for charge transfer between the nominally Fe^{2+} and Fe^{3+} states. Although this has been illustrated in Section 3.4.3 in terms of BVS analysis of the Fe^{3+} states, for completeness, here it is illustrated in terms of the ρ obtained from the SCF calculation. Figure 4.12 is similar to Figure 4.10 but this time the electron density has been plotted from the core of each site rather than from the edge of the muffin tin sphere. To accommodate the large differences in the magnitude, a log scale is used so that the ρ at the core and in-between the atoms may be visualised simultaneously. The maximum density near the core of each trimeron centre along the vectors plotted in Figure 4.12 is given in Table 4.2. The average of the maximum density near the core of each trimeron centre is ρ = 3.572 e $Å^{-3}$ while at the terminus it is ρ = 0.491 e $Å^{-3}$, about 10% of this. For directions not involved in trimeron bonds this value is significantly smaller (ρ = 0.066 e $Å^{-3}$) despite the fact that this average contains the maximum ρ near the core of many Fe^{2+} states. The charge transfer in the trimeron bonds is hence supported by the electronic structure calculation.

The electron density obtained by SCF calculation on the experimental coordinates of Chapter 4 support the proposed trimeron model of the Verwey state of magnetite. However, the question still remains if trimerons are stable with respect to relaxation of the structure in the DFT + U approximation. Although this computationally demanding task of relaxing the structure is beyond the scope of this work, exploring the previously published optimisation coordinates[124] may provide insight into the trimeron model.

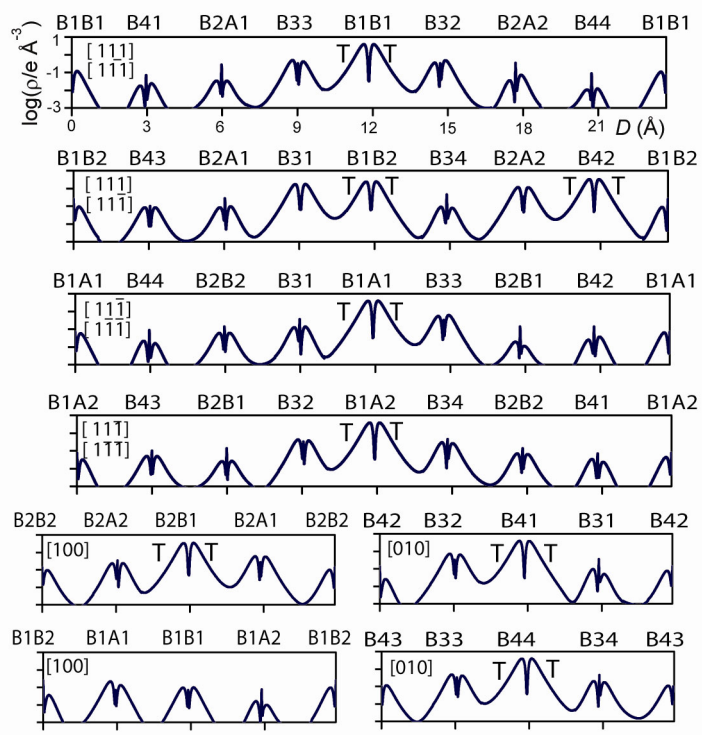

Figure 4.12: Electron density of $Q_{B:d\uparrow}$ plotted on a log scale along the 8 unique B-B chains propagating through the structure. The density at the core is shown to illustrate charge transfer.

Chain1	Density at max		Chain2	Density at max		Chain3	Density at max		Chain4	Density at max	
B1b1	0.1192		B1B1	0.0934	A	B1A1	0.0647		B1A2	0.0436	
B41	0.0239		B43	0.0846		B44	0.0217		B43	0.0502	
B2A1	0.0338		B2A1	0.0961		B2B2	0.0618		B2B1	0.0264	
B33	0.4934	A	B31	1.7320	A	B31	0.1365	A	B32	0.4287	A
B1B1	3.8444	T	B1B2	2.3979	T	B1A1	3.9349	T	B1A2	3.8674	T
B32	0.4775	A	B34	0.0899	A	B33	0.6102	A	B34	0.2975	A
B2A2	0.0726		B2A2	1.1624	A	B2B1	0.0192		B2B2	0.0697	
B44	0.0106		B42	3.2219	T	B42	0.0373		B41	0.0340	
Chain5	Density at max		Chain6	Density at max		Chain7	Density at max		Chain8	Density at max	
B2B2	0.0994		B42	0.0774		B1B2	0.0973		B43	0.1158	
B2A2	0.2387	A	B32	0.7230	A	B1A1	0.2179		B33	0.4813	A
B2B1	3.4364	T	B41	3.9424	T	B1B1	0.0980		B44	3.9327	T
B2A1	0.5951	A	B31	0.0968	A	B1A2	0.0161		B34	0.2026	A

Table 4.2: Maximum ρ taken from Figure 4.12 near the core of each atom along each B-B chain is indicated. Sites are labelled as being at the centre of a trimeron (T) or as an acceptor (A) at the end of a trimeron.

4.3. Comparison of experimental and computational model

Optimisation of the experimental coordinates is beyond the scope of this work. However, in this section the computationally optimised coordinates of Jeng et al.[124] are investigated and compared to the experimental structure reported in Chapter 3. It is found that, despite the fact that the models look very similar from the point of view of visual inspection of charge and orbital ordering, the fit of the optimised model to the single crystal data is very poor with $wR_2 = 33.7$, making it much worse than either the $Cmc2_1$ or C2/c pseudo symmetry fits of section 3.4.1.

Although the Jeng and experimental models can almost be superimposed with respect to charge ordering (Figure 4.13), there is a subtle difference with respect to the charge modulation with period $k = [0, 0, ½]$. The superposition of the optimised model with Xtal6 may be brought about by shifting the optimised coordinates by y + ¼ with respect to the *c*-glide operator as illustrated in Figure 4.13. It must be stressed that this is not an allowed origin shift in the space group C1c1 where only the x and z axis are floating and therefore only an origin shift of y + ½ (centring operator) is allowed.

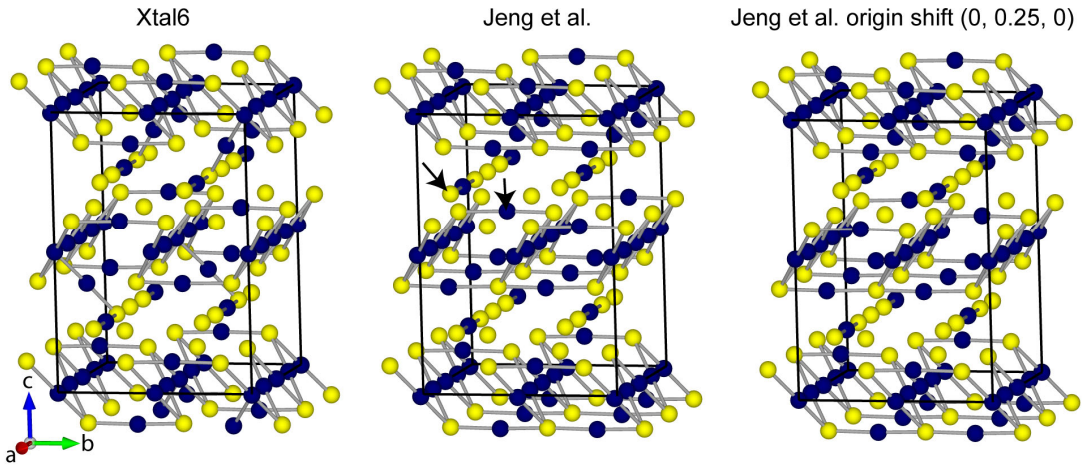

Figure 4.13: The charge and trimeron order of the experimental structure compared with the model of Jeng et al. interpreted in the trimeron approximation. The model of Jeng et al. has an origin shift of y + ¼ with respect to the Xtal6 model, but here the unit cell has been drawn in line with the experimental structure. The arrows indicate sites with rows of atoms in them which differ in their arrangement of charges with respect to the experimental model. On the right hand side, the structure of Jeng et al. has an origin shift applied making it equivalent to the experimental structure with respect to charge ordering.

It is unclear whether the Jeng model is the global minimum of the optimisation surface, or corresponds only to a falls (local) minimum. The energies between the Jeng model with and without the origin shift should be very small. Yamauchi et al.[125] who cite their structure optimisation as being essentially the same as that of Jeng et al. also appear to be missing an expected modulation between z = ¼ and z = ¾ layers while all other layers at intervals of z + ⅛ are in agreement with the experimental model. Given that both optimisations were started from the same coordinates it is unsurprising that they have reached the same answer.

The fit against the experimental data for the two possibilities of the theoretical models are summarised in Table 4.3. Although the Jeng (y + ¼) model has a lower R_1 value than that where the origin has not been shifted, they both have very poor fits to the data. On refinement however, the Jeng (y + ¼) model converges to the same R_1 value as the experimental structure in only 13 cycles, whereas the Jeng model ends up in a false minimum at a considerably higher R_1 value. This suggests that the Jeng model may represent a false minimum on the optimisation surface of the DFT+U calculation.

	Xtal6	Jeng	Jeng (y + ¼)	Jeng refined	Jeng (y + ¼) refined
R_1	5.44 %	17.42 %	18.60 %	9.78 %	5.44 %

Table 4.3: R_1 values for different models compared with the experimental structure factors. Fits are made in the refinement program Topas with all models having isotropic temperature factors constrained to be the same for A, B and O-sites.

The theoretical model may hence not be considered to be the same as the experimental charge ordering configuration, although from the point of view of local bonding details its has many comparable features. The eight Fe^{2+} and eight Fe^{3+} states have the same local connectivity with respect to the pyrochlore lattice on which they sit as observed experimentally. The eight Fe^{2+} as evidenced by Q_{Rad} are again the ones with the largest Jahn-Teller compression, with the Fe^{3+} states having a tight distribution around $Q_{JT} \sim 0$. In fact, the Jeng model appears to overstate the local ordering with respect to the experimental model as evident from Figure 4.14. The charge segregation is much more pronounced than that experimentally observed, and from this point of view there is little evidence of charge transfer between B^{2+} and B^{3+} states. Q_{JT} is also more idealised with its range almost twice that observed experimentally. Hence, notwithstanding a significant rearrangement of the crystal structure in the range 0 – 90 K, it is possible that the onsite Coulomb energy of U = 4.5eV used for the d-states in the DFT + U calculation is a little high, resulting in the local ordering being overstated with respect to the minimisation of the total energy of the crystal structure.

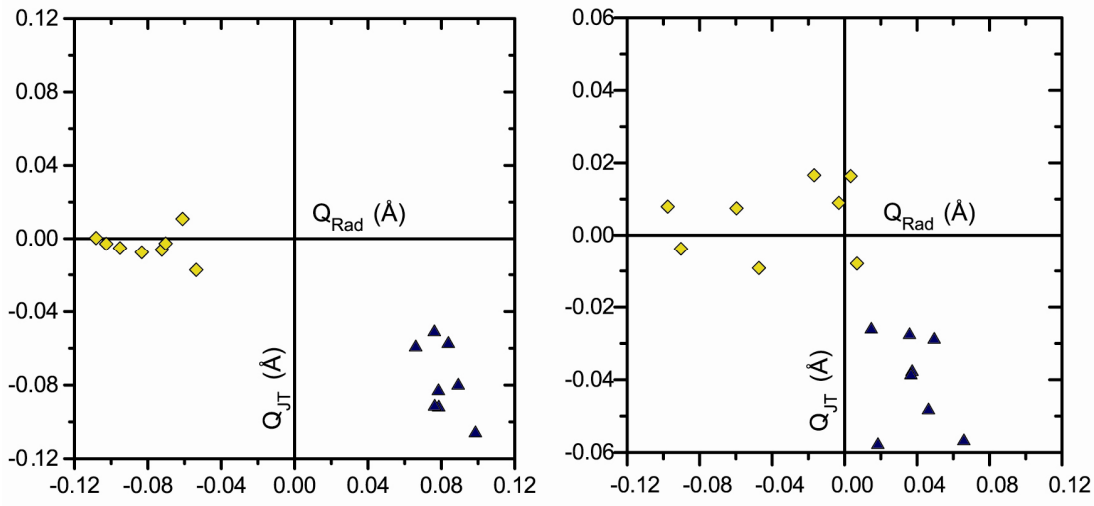

Figure 4.14: Left, Q_{Rad} versus Q_{JT} calculated from the Jeng model. Right, experimental distribution of Q_{Rad} and Q_{JT} taken from Figure 3.27. Note, the y-scale is twice the magnitude in the left than that of the right hand graph.

The pattern of trimeron ordering also bears a remarkable similarity between the Jeng model and the experimental structure. Convincing trimerons are observed in six out of eight cases, with a possibly dimeron formation to relieve frustration of end to end trimeron bonding in one case (Figure 4.13, centre and right). A histogram of the ΔD_{BB} is plotted for the coordinates of the Jeng model (Figure 4.15) for comparison with that obtained experimentally. The distribution of ΔD_{BB} is somewhat narrower than that observed experimentally, and all trimeron bonds start and end at B^{3+}. In fact, the only difference in connectivity between Jeng (y + ¼) model and the experimental models, is that the B^{2+} which is in the experimental structure at the centre of a trimeron donating to another B^{2+} now appear to have an end to end trimeron bond donating to a B^{3+}. This implies also that the JT axis of this one site is different in the two structures. The would-be end to end trimeron distance in the experimental structure is D_{BB} = 3.043 Å and 2.981 Å versus 3.036 Å and 2.887 Å in the theoretical model. The incorrect assignment of this trimeron bond can hence be viewed as rather improbable in the experimental structure. So either there is some further rearrangement of bond distance on cooling to base temperature, or the theoretical model does not quite capture the true physics of the Verwey ground state.

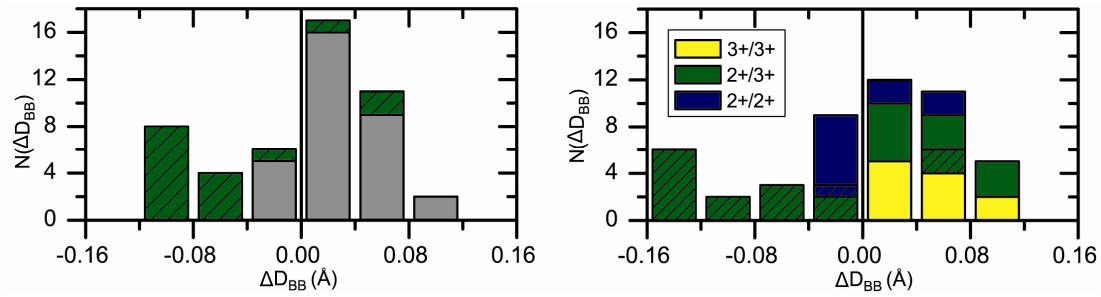

Figure 4.15: Left, histogram of ΔD_{BB} distances from the Jeng model with respect to the global average of the experimental structure. The figure is plotted on the same x-scale and y-scale as the figure on the right which is reproduced from the experimental results (Figure 3.32). Hatching indicates distances that are orthogonal to the JT short bonds of a B^{2+}, all other distances are shown in grey in the left hand figure.

4.4. Conclusion

In this section it has been demonstrated that the ideas proposed in Chapter 3 on the arguments of bond distances, are consistent with those obtained from the electronic structure calculations, and in some respect the assertions of orbital ordering and trimeron bond formation are strengthened as the 16 D_{BB} with the highest average electron density are those predicted from the trimeron model. The breakdown of the trimeron model is still evident in

one of the 8 B-B symmetry unique chains, and the observed electron density is clearly less symmetric about the two trimerons in this chain, suggesting that their mutual arrangement in the chain is frustrated.

Previous theoretical work has been shown to bear striking similarities in terms of local ordering. The charge ordering is of the same type with respect to the number of $(Fe^{2+})_n(Fe^{3+})_{4-n}$ tetrahedra, and orbital ordering is the same in all except one instance. The shortening of the B-B distances orthogonal to the JT short bonds lends itself to interpretation of the structure in terms of trimerons. The published coordinates of ref. [124] however, do not have the same charge modulation with k = [0, 0, ½] as observed experimentally. An origin shift of the coordinates with respects to the *c*-glide plane has been shown to reproduce the experimentally observed charge modulation, and produces a superior fit to the experimental data. A good agreement between many aspects of the theoretical and experimental structures lends weight to the conclusions reached in both this chapter and Chapter 3.

Section C: Charge, orbital and magnetic order in the 6H-perovskites $Ba_3ARu_2O_9$

5. Review of the ruthenate perovskites and the 6H-perovskites

The perovskite structure ABX_3 consists of a cubic close packed array of anions (X, commonly oxygen), with a quarter of the octahedral holes occupied by B-sites cations. The 12-coordinate voids in the structure are occupied by the A-sites (Figure 5.1, 3C). The structure is referred to as the 3C polymorph to reflect the fact that along the cubic body diagonal there are layers of close packed anions (which have a three fold periodicity). Related structure may be generated by adding layers of hexagonal close packed anions along the body diagonal. The structure of the 4H phase (Figure 5.1, 4H) may hence be visualised as stacking arising due to layers of cubic (c) and hexagonal (h) close packed structure of period, (chch). This arrangement leads to both corner-sharing BO_6 octahedra and face-sharing B_2O_9 octahedra within the structure. There are in principle an infinite number of structures which can be generated considering different ratios of corner- and face-sharing BO_6 octahedra. The 6H structure (cchcch) and the 9R (chhchhchh) are two other common phases (Figure 5.1). The 2H phase (hh) which is less common consists of face-sharing octahedra only.[149]

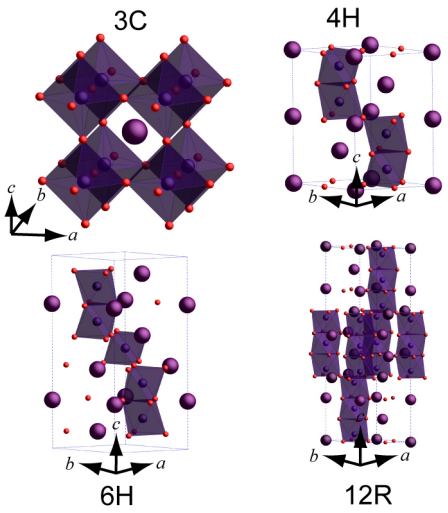

Figure 5.1: The polymorphs of $BaRuO_9$ which adopt the 3C cubic close packed perovskite structure, and the 4H, 6H and 9R phases all of which have varying ratios of hexagonal and close packed layers.

In general the abundance of perovskite related structures makes them ideal for systematic studies of structure-property relationships. However, for the ruthenates there are a rather limited number of ternary perovskites and related phases. In the first part of this chapter (Section 5.1) a brief summary of the known ternary perovskite phase will be made. As there are relatively few of these, in Section 5.2.2, quaternary perovskite and the simplest related hexagonal phases (the 6H) will be reviewed. The focus of the discussion will be on the 6H phase whose structure is that of the material investigated in Chapter 6 and 7.

5.1. Ternary ruthenate perovskites

There are relatively few examples of $ARuO_3$ perovskites with only A = Ca, Sr,[150] Ba, Pb,[151] La and Pr[152] being reported in the literature, of which only $CaRuO_3$ and $SrRuO_3$ may be readily synthesised at ambient pressure. The Goldschmidt tolerance factor for ideal cubic close packed structures dictates that, $(r_O + r_A) = t\sqrt{2}(r_O+r_{Ru})$ where t is the Goldschmidt tolerance factor which must be close to unity.[153] This constraint implies that a 12 coordinate A-site must have an ionic radius ~ 1.46 Å for A^{2+} / Ru^{4+} and 1.54 Å for A^{3+} / Ru^{3+}. Sr^{2+} (r_{Sr} = 1.44 Å) is therefore an ideal candidate for the A-site, and A = Ca^{2+} (r_{Ca} = 1.34 Å) may also be made though it has a far more distorted structure than A = Sr. The A = Ba^{2+} (r_{Ba} = 1.61 Å), which implies a t > 1, may only be synthesised by high pressure methods (18 GPa),[154] with ambient pressure phases preferring a 9R phase, although 4H and 6H polymorphs may also be stabilised (Figure 5.1) with more modest pressure or obtained from flux reactions.[155]

$ARuO_3$ (A = Ca, Sr, Ba) are metallic in character[154, 156] with low spin configuration of Ru^{4+} (t_{2g}^4). They all exhibit paramagnetism at high temperature which follows Curie-Weiss behaviour, but A = Sr and Ba undergo FM ordering transitions at 164 and 60 K respectively.[157-159] A = Ca remains paramagnetic down to base temperature.[159] Long range magnetic ordering remains unobserved in A = Pb^{2+} by neutron powder diffraction,[160] but a structural change accompanied by an increase in conductivity is observed below 90 K.[160, 161] The physical properties of A = La^{3+} and Pr^{3+} are poorly characterised in the literature.

Other than the aforementioned hexagonal polymorphs of $BaRuO_3$ there are relatively few hexagonal phases of the type $ARuO_3$, with most compositions adopting the pyrochlore structure at ambient conditions. The quaternary perovskite phase is reviewed below which has a richer morphology.

5.2. Quaternary perovskites

5.2.1. Double perovskites

Unlike in the manganites, in which extensive A-site doping has been carried out, often resulting in charge ordered phases being observed, in the ruthenates, only for $SrRuO_3$ has any charge doping of the A-site been reported. Here it is found that the charge doping rapidly suppresses the FM transition. The half doped state $Sr_{0.5}La_{0.5}RuO_3$ is predicted to be metallic and no evidence of long range charge ordering of the $Ru^{3.5+}$ semi-valent state is observed. [162]

The chemistry involved in the B-site doping of $ARuO_3$ is much richer than that of the A-site doping. The B-site ordered double perovskites with $Sr_2B'RuO_6$[163] and $Ba_2B'RuO_6$ (B' = Ln, Y) have been extensively characterised. Sr_2LnRuO_6 crystallise in the monoclinic space group $P2_1/n$ and undergo AFM transitions at low temperatures (T_n = 26 – 44 K).[163] For $Ba_2B'RuO_6$ the larger cations (La^{3+}, Nd^{3+}, Pr^{3+})[164-166] adopt the same monoclinic structure while the smaller rare earth cations have a cubic ($Fm\bar{3}m$) structure[167, 168]. In all cases the cation ordering maps onto the rock-salt lattice. T_N for the $Ba_2B'RuO_6$ series does not follow

an obvious trend based on cation size or symmetry with values ranging from T_N = 37 – 117 K. Moments on both B' and Ru sites are reported to order at the same temperature, with a small canting of the moments away from the *c*-axis. The magnetic structures map onto the A-type or C-type structures of the ABO_3 perovskites (see Section 1.1.3, Figure 1.8). In contrast to the cubic perovskites $BaRuO_3$, Ba_2RuBO_6 are Mott insulators characterised by 3 dimensional variable-range hopping.[169]

For $BaB_xRu_{(1-x)}O_3$, the hexagonal perovskite phases are thermodynamically in close competition with those of the double and 1:2 perovskite phase.[170] The simplest ordered hexagonal structure which the B-site doped perovskites are observed to adopt is that of the 6H perovskite ($BaB_{⅓}Ru_{⅔}O_3 \equiv Ba_3AB_2O_9$). A summary of the known 6H perovskites is made below.

5.2.2. Structure of the 6H-perovskites $Ba_3AB_2O_9$

The structure of the 6H phase is shown in Figure 5.2. A key feature of the structure is the short B-B distance in the face-sharing B_2O_9 dimers (2.50 – 2.9 Å). The large size of the 12-coordinate Ba is a key ingredient in stabilising the hexagonal perovskite phase and 6H-perovskites of the type $Sr_3AB_2O_9$ are unknown. In fact, only one example of a quaternary 6H-perovskite that does not contain Ba is reported, that of the high pressure air sensitive perovskite $K_3NaRe_2O_9$. [171] A summary of the known 6H phases of type $Ba_3AB_2O_9$ is made in Table 5.1.

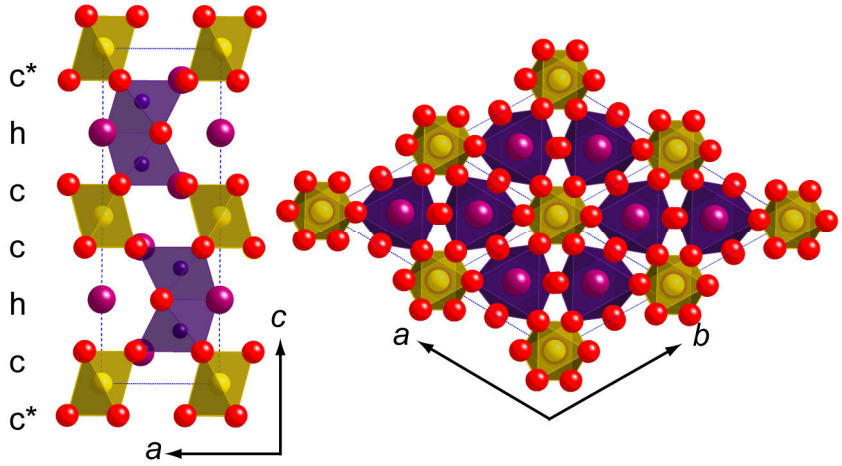

Figure 5.2: The 6H-perovskite structure of composition $Ba_3AB_2O_9$. Corner-sharing cations (A) are shown as yellow polyhedra, face-sharing (B) as dark purple polyhedra. Ba and O are shown as light purple and red spheres respectively.

B_2 / A	Ru	Ir	Sb	Os	Cr	Mn	Fe	Co	Nb	Ta
I	Li[6], Na[6]	Na[c,172], Li[172]		Li[173], Na[173]						
II	Mg[174], Ca[174], Sr[b,174],	Mg[175],Ca[b,175],Sr[b,175]	Mg[176],Ca[b,177], Sr[b,177]						Sr[a,178]	Sr[a,178]
3d	Ti[179], Mn, Fe[180], Co[c,181], Ni[181], Cu[b,180], Zn[181]	Sc[175],Ti[175],Zn[175],Ni	Mn[b],Co[182],Ni[d,183],Cu[a,184],Zn[176]							
4d	Zr[185], Ru[e,158], Cd[174]	Zr[175], Cd[b,175]			Mo[186]					
5d					W[a,186]		W[d,187]	W[d,188]		
III	In[180]									
IV										
V	Bi[b,189]	Bi[b,190]								
VI							Te[d,191]			
RE	Y[169], Ln[169](Nd[c])	Y[192], Ln[192](La[b],Nd[b])				Er[b,193]				

Table 5.1: Summary of all known 6H-perovskites of type $Ba_3AB_2O_9$. Explanatory notes are: [a] Ambient phase is hexagonal other than $P6_3/mmc$, [b] ambient phase is orthorhombic, monoclinic or triclinic, [c] phase transition below ambient temperature reported, [d] A/B disorder and [e] high pressure stabilised.

The $Ba_3ARu_2O_9$ family of compounds form the largest group of 6H-perovskites. They are also the one in which the highest percentage of members crystallise in the aristotypical space group $P6_3/mmc$ at room temperature. $Ba_3AIr_2O_9$ forms the only other large group of

compounds in which the B cation can adopt variable oxidation state. Despite the fact that Ir^{n+} has ionic radius only ~0.005 Å larger than Ru^{n+}, many more B = Ir derivatives crystallise in the distorted monoclinic C2/c structure at room temperature. For A-sites where single ion effects may be ruled out, in B = Ru only A = Sr (r_{Sr} = 1.18 Å) has the monoclinic space group. However, in B = Ir, A = Sr, Ca, Cd and La are all observed to have monoclinic or even triclinic distortions. In the case of B = Sb, the series is confined to $A^{2+}(Sb^{5+}O_6)$. The ionic radius of Sb^{5+} is 0.600 Å, and is somewhere between the size of Ru/Ir^{4+} and Ru/Ir^{5+}, but surprisingly only small A^{2+} cations (< 0.8 Å) appear to result in the aristotypical symmetry, and the chemistry of $Ba_3ASb_2O_9$ is much poorer than that of either B = Ru or Ir.

For B = Cr, Mn, Fe and Co, face-sharing B_2O_9 dimers appear to only be stabilised by A = W or Mo. It is presumably only the 6 + oxidation state of W and Mo which can accommodate the 3+ oxidation states preferred by these 3d transition metals. $Ba_3SrNb_2O_9$ and $Ba_3SrTa_2O_9$ are maybe the two most surprising members of the family, Nb^{5+}/Ta^{5+} having no electrons to participate in a bonding interaction of the face-sharing octahedra. Hence a big A-cation (Sr), which results in large intra dimer distance, is required to stabilise the structure.

The null observation of the 6H phase for many other B compositions is not necessarily a reflection on their inherent instability, but rather on the stability of the 1:1 and 1:2 B-site ordered/disordered double perovskite phases which are closely competing. This chemistry is particularly rich for the 4d and 5d transition metals B = Mo, W, Nb, Re, Ta. Consequently, 6H-perovskite $Ba_3AB_2O_9$ with these cations incorporated on either the A or B site are only found in a few instances.

5.2.3. Magnetic and electronic properties of $Ba_3AB_2O_9$

For B = Ru, magnetic ordering transitions have been evidenced through susceptibility measurements but magnetic structures of the ordered Ru moments determined by neutron diffraction have only been reported for A = Ni^{2+} and Co^{2+}.[181] The $(Ru^{5+})_2O_9$ spin dimers are antiferromagnetic and are coupled to ordered Ni/Co spins. For A^{3+} = RE (rare earth) and Y, broad features in the magnetic susceptibility and specific heat measurements at high temperatures have been interpreted as evidence for local antiferromagnetic pairing within Ru_2O_9 dimers. Néel transitions have been observed in these compounds T_N < 28 K, but only magnetic structures corresponding to the AFM ordering of the RE moment have been

reported.[169] A = Nd^{3+} is the only exception in the RE series in which a transition to C2/c symmetry has been reported at 110 K in addition to FM ordering of Nd moments at 25 K.[194]

For B = Ir, A^{2+} ($Ir^{5+}{}_2O_9$), temperature dependence of μ_{eff} which diminishes to zero at 0 K is observed. The observation can be explained by spin orbit coupling of Ir^{5+} ($t_{2g}{}^4e_g{}^0$).[175] However, for A^{4+}, strong antiferromagnetic interactions within the $Ir^{4+}{}_2O_9$ dimers are believed to be responsible for the observed non Curie-Weiss behaviour, and magnetic specific heat measurements evidence an antiferromagnetic paring of spins.[175, 195] Semivalent $Ir^{5.5+}{}_2O_9$ and $Ir^{4.5+}{}_2O_9$ (A^+ and A^{3+} respectively) members of the family exhibit additional anomalies in their magnetic heat capacity and divergence between ZFC and FC susceptibility measurements, suggesting that the magnetic ordering occurs at low temperatures.[172, 195] No magnetic structures have however, been reported for B = Ir, but this may just reflect the lack of sensitivity of neutron diffraction experiments on these compounds due to the high absorption cross section of Ir.

The electronic properties of $Ba_3AB_2O_9$ are not that well characterised. However, recently some of these systems have been reinvestigated. The opening up of a spin gap in $Ba_3BiB_2O_9$ (B = Ru^{4+} , Ir^{4+}) [196,197] at low temperature resulting in negative thermal expansion, coupled with a transition to C2/c symmetry at 176 K and 74 K respectively has recently been reported. For the semivalent $B^{4.5+}/B^{5.5+}$ derivatives of $Ba_3AB_2O_9$, only in the case of A = Na^+, B = $Ru^{5.5+}$ has charge ordering been reported.[6] For $Ba_3NaOs_2O_9$, no phase transition is observed down to 2K,[173] whereas in $Ba_3NaIr_2O_9$, a phase transition at ~200 K[198] which is apparently unrelated to charge ordering is observed.

The 6H-perovskites, $Ba_3AB_2O_9$ have recently been identified as geometrically frustrated systems, and are potentially suitable materials for observing spin liquid type behaviour. To this end, $Ba_3ASb_2O_9$ (A = Ni^{2+},[199], Cu^{2+},[200]) containing $SbAO_9$ dimers in quasi two dimensional layers have been investigated.

An investigation of the structural, electronic and magnetic properties of several $Ba_3ARu_2O_9$ is presented in the following two chapters.

6. *Charge ordering transitions in $Ba_3NaRu_2O_9$*

Despite the existence of many semivalent Ru 6H-perovskites $Ba_3ARu_2O_9$ (A^{1+} or A^{3+}), only one instance of charge ordering has been reported, that for A = Na.[6] In this material, ruthenium is in an unusually high oxidation state (5.5+). The material can be obtained by flux synthesis in NaOH and crystallises in the aristotypical symmetry of the 6H-perovskite structure. However, unlike in $Ba_3ARu_2O_9$ (A^{2+}, A^{3+}, A^{4+}), $Ba_3NaRu_2O_9$ is a semiconductor at high temperature but has an insulator transition at 210 K[201] which is accompanied by a discontinuity in the magnetic susceptibility. A structural transition is reported by single crystal x-ray diffraction at 173 K (Cmcm, $2a \times 2\sqrt{3}b \times c$).[6] It is assigned as being due to charge ordering of the Ru_2O_9 dimers. The charge ordering is reported to occur across three crystallographically independent sites, with two dimer sites being assigned ~ 5+ oxidation state and one site (with twice the multiplicity of the prior) ~ 6+. The structure hence has lower symmetry than that of the simplest structure which would raise the degeneracy of semi valent $Ru^{5.5+}$ state.

In this chapter, the charge ordering of this phase is reinvestigated by high resolution, synchrotron x-ray and neutron powder diffraction and by single crystal x-ray diffraction. The structure is revealed to consist of a simple striped arrangement of $Ru^{5+}{}_2O_9$ / $Ru^{6+}{}_2O_9$ dimers. At lower temperatures a second phase transition is observed corresponding to a novel 'charge melting' of the ordered phase. Results of an in situ high pressure x-ray diffraction study on $Ba_3NaRu_2O_9$ give insight into the trends across whole $Ba_3ARu_2O_9$ series.

6.1. Experimental: Synthesis and physical properties

$Ba_3NaRu_2O_9$ was prepared from RuO_2 (1.00 mmol, 0.1331 g), $Ba(OH)_2{\cdot}8H_2O$ (3.25 mmol 1.0280 g) and ~300 equivalence of NaOH (~ 11.6 g). The reagents were heated in a covered alumina crucible to 700 °C at 600 °C/hr. After 12hrs, the flux was cooled slowly to 600 °C at 15 °C/hr, and then to room temperature by shutting off the furnace.[6] The flux was dissolved in methanol with the aid of a sonicator bath. The sample was confirmed to be a single phase by powder x-ray diffraction (Cu-$K_{\alpha 1}$) on a representative part of the sample which was finely ground. High resolution synchrotron x-ray powder diffraction data (λ =

0.39983(4) Å) were collected at the beamline ID31, ESRF, in the temperature range 10 – 300 K. High resolution neutron powder diffraction data were collected at the time-of-flight diffractometer WISH, ISIS on a 0.1464 g sample loaded in a vanadium can with a 3 mm diameter within a cryostat, at temperatures of 1.6, 10, 110 and 300 K. Single crystal x-ray diffraction data (Mo-K_α) were collected at 293 and 110 K. Field cooled (1000 Oe) and zero field cooled susceptibility data were collected in the range 2 – 300 K.

For the high pressure study, a single crystal of $Ba_3NaRu_2O_9$ of size 40 × 40 × 10 was cut from a hexagonal plate crystal obtained from the flux growth. This was loaded in a Boehler-Almax-type DAC equipped with a gas driven membrane. The pressure-transmitting media was helium which was loaded in an autoclave. Holes of about 150(10) μm in diameter in tungsten gasket preindented to a thickness of 38(3) μm served as the sample chamber. In situ high-pressure synchrotron single crystal x-ray diffraction data were collected at beamline ID09A at the ESRF (λ = 0.414498(18) Å) using a MAR555 flat panel detector. Pressure was determined by monitoring the laser-induced ruby-fluorescence[202] before and after the data collection. The sample to detector distance was 400 mm giving a maximum 2θ = 25°. Diffraction images were indexed and integrated in the program CrysAlisPro.

6.2. Charge ordering transition at 210 K

6.2.1. Synchrotron powder diffraction study

The synthesis was rather sensitive to the cooling rate of the flux, and the use of dry reagents appeared important. Successful attempts yielded laminar hexagonal plate like crystals (Figure 6.1), portions of which were ground up and confirmed to be single phase by lab x-ray diffraction. Synchrotron x-ray diffraction data collected at 293 K confirmed the proposed high temperature structure, and Rietveld refinement produced a good fit to the data (Figure 6.2). Fitting statistics and refined parameters, which are in good agreement with those previously published,[6] are summarised in Appendix C. A phase transition between 210 K and 230 K was observed as previously reported. However, the presence of monoclinic as well as orthorhombic peak split meant that the data could not be satisfactorily indexed on the previously proposed Cmcm $2a \times 2\sqrt{3}a \times c$ cell. Instead, a much smaller monoclinic primitive cell ($a \times \sqrt{3}a \times c$) was found to be able to account for the reflection positions and

the systemic absence of the reflections (h 0 l), l = 2n are consistent with the space ground P2/c.

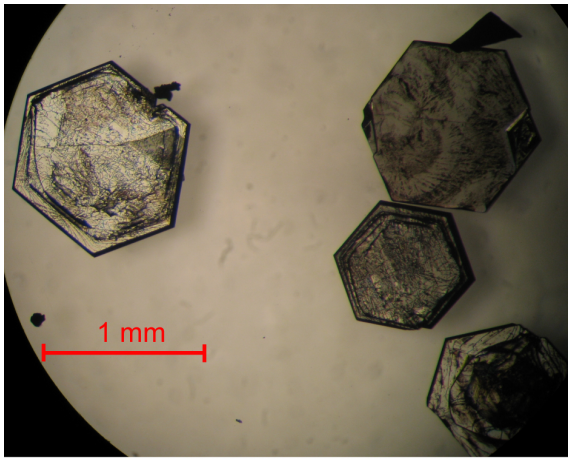

Figure 6.1: Hexagonal shaped crystal of $Ba_3NaRu_2O_9$ obtained from flux synthesis.

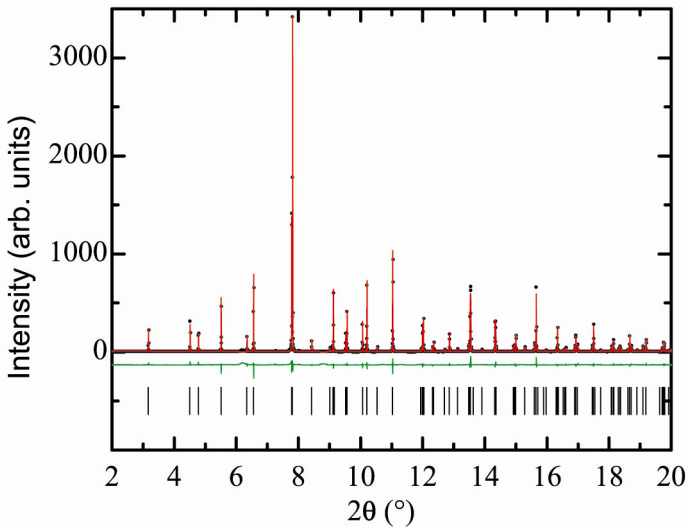

Figure 6.2: Rietveld fit of $P6_3/mmc$ structure against data collected at ID31 (λ = 0.39997(3) Å) at 293 K.

Rietveld refinement starting from randomly perturbed coordinates in the P2/c space group produced a good fit to the data (Figure 6.3) with a χ^2 = 1.94. The results from the Rietveld refinement are summarised in Appendix C. Although the fit to the data is good, the model has 55 refined parameters, of which 26 are fractional coordinates for oxygen positions. The relative lack of sensitivity of the x-ray powder diffraction data to the oxygen positions, and the availability of reasonably sized large single crystals meant that it was desirable to

perform a single crystal diffraction experiment to improve the precision to which these parameters were determined.

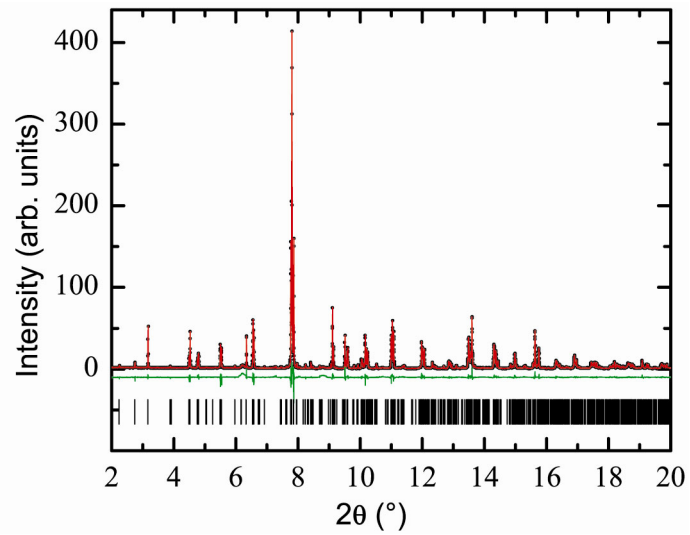

Figure 6.3: Rietveld fit of charge ordered phase in space group P2/c against data collected at ID31 at 110 K.

6.2.2. Single crystal diffraction study

A single crystal of dimensions 0.45 × 0.45 × 0.13 mm was used for the diffraction study. The results of the refinement against the integrated data are summarised in Appendix C, and are consistent with the Rietveld refinement against synchrotron x-ray radiation. Diffraction images collected at 110 K appeared to index on a $\sqrt{3}a \times \sqrt{3}a \times c$ super cell indicating the existence of twin domains. Prior knowledge of the correct unit cell and space group of the low temperature phase from the high resolution powder diffraction means that the twinned data set could be correctly treated.

The order of the high temperature phase point group 6/mmm is 24 and the order of the low temperature phase point group 2/m is 4, so a total of six domains are expected as summarised in Table 6.2. A graphical representation of the twinning is given in Figure 6.4, left, illustrating the three fold degeneracy of the hexagonal to orthorhombic transformation giving rise to so called 'trilling' in the crystal. Orthorhombic domain may additionally be subject to monoclinic type twinning (Figure 6.4, right).

		Element			
Coset	Double coset	**a**	**b**	**c**	**d**
1	1	1	2(XY)	$\bar{1}$	m(XY)
2	2	6(Z)	2(2)	$\bar{6}$(Z)	m(2)
3		2(1)	6_5(Z)	m(1)	$\bar{6}_5$(Z)
4	3	3(Z)	2(Y)	$\bar{3}$(Z)	m(Y)
5		2(X)	3_2(Z)	m(X)	$\bar{3}_5$(Z)
6	4	2(Z)	2(3)	m(Z)	m(3)

Table 6.1: Coset decomposition of point group 6/mmm with respect to 2(XY)/m. In the orthorhombic point group mmm only three domains would be possible consisting of cosets 1 + 6, 2 + 5 and 3 +4.

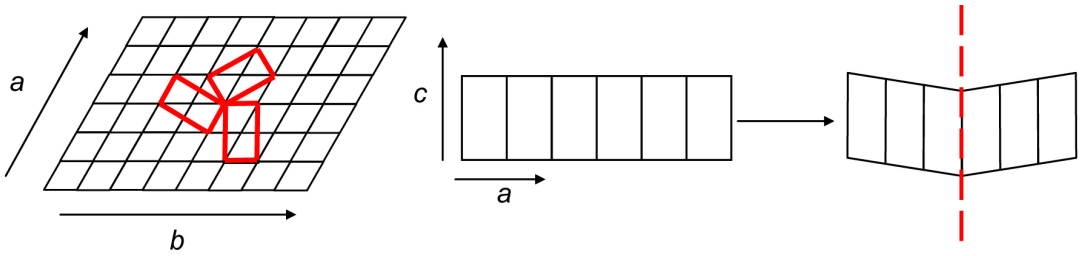

Figure 6.4: Graphical representation of the 'trilling' and monoclinic twinning possible in the phase transition from symmetry with point group 6/mmm → 2/m.

The six possible twin laws are given by considering the triple product $T^{-1}MT$, where M is the element in Table 6.1 in matrix form and T is the appropriate lattice transformation which retains the 2(XY)/m symmetry elements. In this case T is given as:

$$T = \begin{pmatrix} 1 & 1 & 0 \\ -1 & 1 & 0 \\ 0 & 0 & 1 \end{pmatrix}$$ Where the lattice transformation is: $(a,b,c)T = a-b, a+b, c$

The resulting twin laws are given in Table 6.2.

Symmetry element	Matrix	Twin Law	Domain	Refined Twin fraction
1	$\begin{pmatrix} 1 & 0 & 0 \\ 0 & 1 & 0 \\ 0 & 0 & 1 \end{pmatrix}$	$\begin{pmatrix} 1 & 0 & 0 \\ 0 & 1 & 0 \\ 0 & 0 & 1 \end{pmatrix}$	Principal	0.1656(15)
$\bar{6}$ (Z)	$\begin{pmatrix} 0 & 1 & 0 \\ -1 & 1 & 0 \\ 0 & 0 & 1 \end{pmatrix}$	$\begin{pmatrix} 0.5 & 0.5 & 0 \\ -1.5 & 0.5 & 0 \\ 0 & 0 & 1 \end{pmatrix}$	2nd orthorhombic	0.169(3)
6_5(Z)	$\begin{pmatrix} -1 & 1 & 0 \\ -1 & 0 & 0 \\ 0 & 0 & -1 \end{pmatrix}$	$\begin{pmatrix} -0.5 & 0.5 & 0 \\ -1.5 & -0.5 & 0 \\ 0 & 0 & -1 \end{pmatrix}$	Monoclinic twin of 3rd orthorhombic	0.169(3)
$\bar{3}$ (Z)	$\begin{pmatrix} -1 & 1 & 0 \\ -1 & 0 & 0 \\ 0 & 0 & 1 \end{pmatrix}$	$\begin{pmatrix} -0.5 & 0.5 & 0 \\ -1.5 & -0.5 & 0 \\ 0 & 0 & 1 \end{pmatrix}$	3rd orthorhombic	0.168(3)
3_2(Z)	$\begin{pmatrix} 0 & 1 & 0 \\ -1 & 1 & 0 \\ 0 & 0 & -1 \end{pmatrix}$	$\begin{pmatrix} 0.5 & 0.5 & 0 \\ -1.5 & 0.5 & 0 \\ 0 & 0 & -1 \end{pmatrix}$	Monoclinic twin of 2nd orthorhombic	0.165(3)
M(Z)	$\begin{pmatrix} 1 & 0 & 0 \\ 0 & 1 & 0 \\ 0 & 0 & -1 \end{pmatrix}$	$\begin{pmatrix} 1 & 0 & 0 \\ 0 & 1 & 0 \\ 0 & 0 & -1 \end{pmatrix}$	Monoclinic twin of principal domain.	0.1674(15)

Table 6.2: Summary of twin laws used in single crystal refinement in the program Crystals,[133] which are consistent with those suggested by the program ROTAX[134]. Refined twin fractions are indicated.

The single crystal diffraction data was reindexed in SAINT[130] on the $a \times \sqrt{3}a \times c$ unit cell with the two additional orientation matrices consistent with the appropriate twin laws for the orthorhombic domains. Merging of data was performed in Twinabs,[131] and twin fractions of 0.370, 0.307 and 0.323 were estimated for the orthorhombic type domains. Refinements in Shelxl[136] against the resulting HKLF5 file confirm the twin fractions estimated by Twinabs. However, the refinement ended at R_1 = 6.03 % with large electron density peaks in the Fourier difference map. It is unfortunately not possible to include additional twin laws in a Shelxl refinement where a HKLF5 file is being used, and so the presence of the monoclinic twinning could not be tested for. To overcome this problem, a refinement was performed in Crystals[133] with the derived twin laws of Table 6.2 against data integrated using a single orientation matrix (HKL4 file). The R_1 value dropped from 11.38 % to 4.38 % on inclusion

of the orthorhombic type twinning and the addition of the three extra monoclinic twin laws resulted in a final R_1 value of 2.80 %. The refined twin fractions are summarised in Table 6.2, refined fractional coordinates are given in Table 6.3 along with U_{iso} or U_{equiv} as appropriate, full refinement details are given in Appendix C.

Label	x	y	z	$U_{iso/equiv}$ ($Å^2$)
Na1	0	0	0	0.0044(5)
Na2	0.5	0.5	0	0.0052(5)
Ba1	0	0.00689(4)	0.25	0.0051
Ba3	0.5	0.48195(5)	0.25	0.0052
Ba2	0.50537(14)	0.15771(3)	0.91817(2)	0.0053
Ba4	0.00413(14)	0.68674(4)	0.90174(2)	0.0057
Ru1	0.49931(19)	0.16087(3)	0.15941(2)	0.00395(9)
Ru2	0.00241(19)	0.65572(4)	0.15151(3)	0.00426(9)
O1	0.7317(6)	0.2404(4)	0.2461(6)	0.0054(8)
O3	0.2065(7)	0.7367(4)	0.2361(3)	0.0040(8)
O4	0	0.4843(6)	0.75	0.0095(12)
O5	0.5	-0.0109(6)	0.75	0.0096(12)
O2	0.2694(14)	0.0793(9)	0.4087(5)	0.0128(19)
O6	0.8090(9)	0.5704(5)	0.4236(3)	0.0083(9)
O7	0.0074(15)	0.1905(4)	0.9177(3)	0.0045(7)
O8	0.4920(16)	0.6846(4)	0.9122(3)	0.0040(7)
O9	0.7365(10)	0.0857(7)	0.4108(4)	0.0025(14)
O10	0.2827(8)	0.6028(5)	0.3892(3)	0.0080(9)

Table 6.3: Refined fractional coordinates and thermal parameters for the charge ordered phase of $Ba_3NaRu_2O_9$ against twinned single crystal diffraction data collected at 110K.

It is desirable to calculate the atomic distances derived from the fractional coordinates of the single crystal refinement using the lattice parameters from the ID31 Rietveld refinement

which have a higher absolute accuracy. However, the monoclinic splitting (β = 90.2627(3) °) which should couple to the structural distortion, is clearly resolved in the powder diffraction data, but is not evident in the unit cell derived from the single crystal diffraction data (β = 89.991(1)°) due to the averaging of the monoclinic twin domains. In order to use the parameters derived from the synchrotron x-ray diffraction study it is, hence, necessary to confirm if the setting of the principal domain with respect to the integration of the single crystal data corresponds to β = 90.26 ° or β = 180- 90.26 °. The comparison of the Rietveld fits using the single crystal coordinates with the two possible choice of the beta angle is made in Figure 6.5, indicating that β = 90.26 ° is the correct choice for the metric cell. Accordingly the bond distances from the single crystal refinement were calculated using β = 90.26 °.

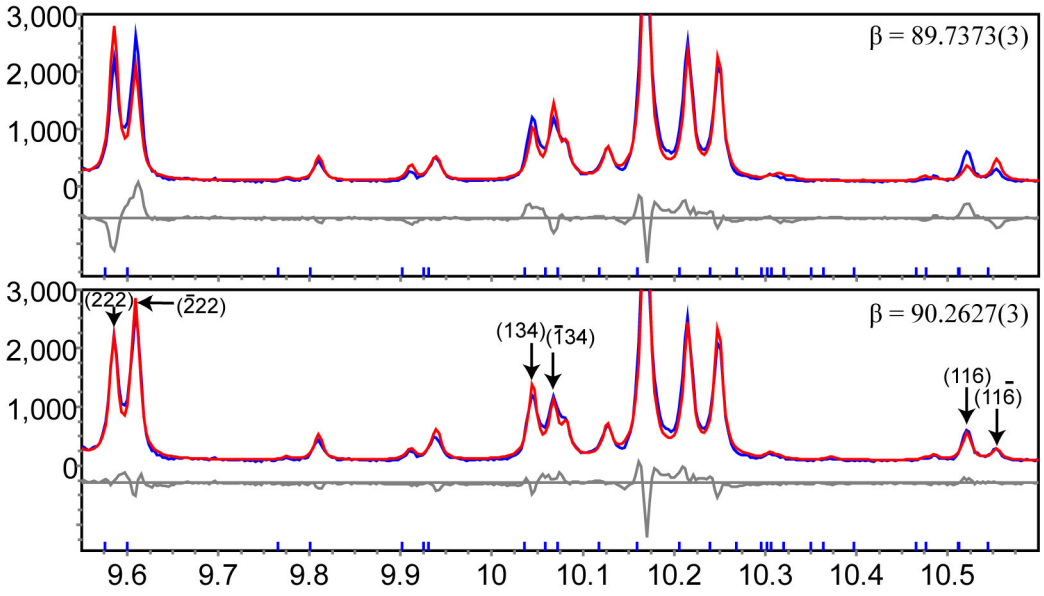

Figure 6.5: Rietveld fit using the coordinates from the single crystal refinement at 110K of the P2/c phase. The fit for which the coordinates are used in conjunction with the metric cell β = 90.2627 ° is considerably better than that where β = 89.7373 °.

6.2.3. Interpretation of the charge ordered phase

The refined structure reveals two inequivalent Ru sites in the asymmetric unit. The two Ru sites occupy different dimers of the unit cell, such that, by symmetry, there are two inequivalent Ru_2O_9 dimers. The coordination environments of these two dimers are summarised in Table 6.4. The two dimers have very different intra Ru-Ru dimer distances ($D_{(Ru-Ru)}$). The shortest distance (2.62 Å) is close to that found in metallic Ru (2.648 Å [203]),

whereas the longer (2.85 Å) distance is greater than that observed in the high symmetry phase of $Ba_3NaRu_2O_9$ (2.74 Å). $D_{(Ru\text{-}Ru)}$ has a near linear relationship with Ru oxidation state as evident from Figure 6.6, in which $D_{(Ru\text{-}Ru)}$ values have been taken from $Ba_3ARu_2O_9$ with ionic radii of A^{n+} in the range 0.87 – 1.03 Å. Above the phase transition, $D_{(Ru\text{-}Ru)}$ does not deviate significantly from the value expected from the trend line for the Ru oxidation state of 5.5+. Below the transition, the distances clearly correspond to oxidation states of 5+ and 6+ respectively and values of 4.86(16)+ and 6.11(16)+ are estimated from the linear fit of $D_{(Ru\text{-}Ru)}$ of Figure 6.6. Figure 6.6, right displays a regression fit of oxidation state against average dimer Ru-O bond distance ($D_{<Ru\text{-}O>}$). Below the transition, the two $D_{<Ru\text{-}O>}$ are clearly well separated either side of the $D_{<Ru\text{-}O>}$ value above the transition. The lack of tabulated values for Ru^{6+} ionic radii, and the proximity of metal centres means that BVS analysis cannot be carried out in this case, but the separation of $D_{(Ru\text{-}Ru)}$ and $D_{<Ru\text{-}O>}$ supports a near integer charge separation in the two crystallographically distinct dimers below the transition. Hereafter this low temperature phase is referred to as the charge ordered phase.

110K single crystal data	Ru-Ru (Å)	Ru-O (Terminal) (Å)	Ru-O (Face) (Å)	Trans pair average (Å)
Dimer 1 $(Ru5+)_2$ t_{2g}^3	**2.6194(7)**	1.863(8)	2.059(7)	1.961(8)
		1.877(6)	2.044(8)	1.961(7)
		1.887(4)	2.014(5)	1.951(5)
Mean		1.876(6)	2.039(7)	**1.957(6)**
Dimer 2 $(Ru6+)_2$ t_{2g}^2	**2.8481(7)**	1.821(5)	1.919(4)	1.870(5)
		1.862(4)	2.016(5)	1.939(5)
		1.794(5)	2.176(4)	1.985(5)
Mean		1.826(5)	2.037(4)	**1.931(2)**

Table 6.4: Summary of coordination environment of the Ru sites at 110 K. Bond distances are calculated from single crystal fractional coordinates and the metric cell obtained from Rietveld refinements.

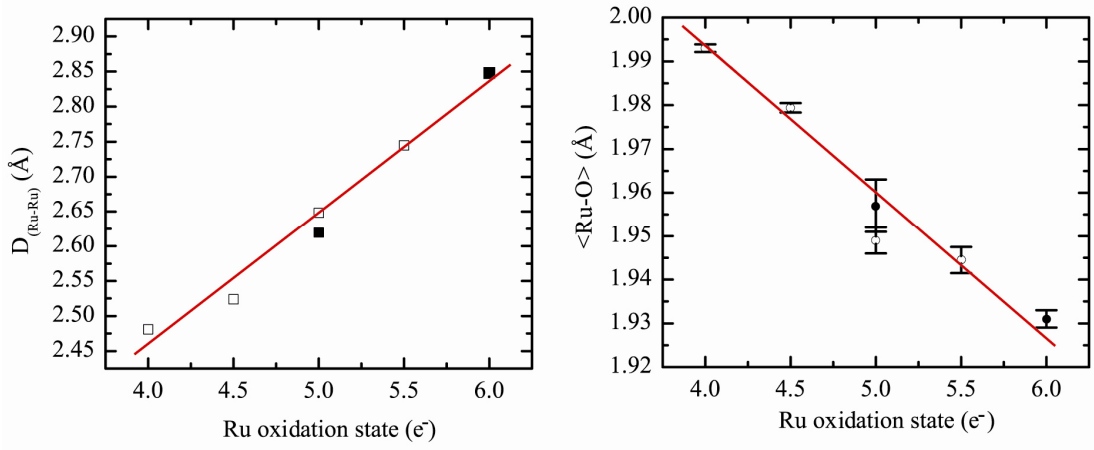

Figure 6.6: Linear trend and fit of $D_{(Ru-Ru)}$ and <Ru-O> distances against the Ru oxidation state. Open symbols correspond to ambient temperature data from A = Na^+, Ca^{2+},[174] Nd^{3+},[194] Ce^{4+} [204] which have similar ionic radii, giving formal oxidation states of Ru of 5.5+, 5+, 4.5+ and 4+ respectively. Value for the charge ordered phase (closed symbols) are placed at 5+ and 6+ as appropriate.

The coordination environments of $Ru^{6+}{}_2O_9$ / $Ru^{5+}{}_2O_9$ are also supportive of a charge ordered picture in which the Ru^{6+} ($t_{2g}{}^2$) exhibits a greater irregularity than the Ru^{5+} ($t_{2g}{}^3$) ion. The trans O pair average (Table 6.4) has a range within the standard uncertainty of 1.951(5) - 1.961(8) for Ru^{5+} ions but a much larger range of 1.870(5) – 1.985(5) is observed for Ru^{6+} ions. The coordination environment of the Ru^{6+} ion does not quite correspond to the 'two long, four short' picture expected for the ideal tetragonal Jahn-Teller distortion of a d^2 ion, but this is not surprising given the low symmetry of the charge ordered phase and the highly constrained connectivity of the octahedra.

The CO transition observed by x-ray diffraction is also coincident with the semiconductor to insulator transition (T_1) of Figure 6.6. This should correspond to an opening up of a gap at the Fermi level, as a result of the charge ordering. A jump in the magnetic susceptibility (Figure 6.8) at T_1 suggests either a substantial decrease in μ_{eff} and / or an increase in antiferromagnetic exchange below the charge ordering temperature. A singlet ground state formation of $Ru^{5+}{}_2O_9$ would leave only $Ru^{6+}{}_2O_9$ contributions to the susceptibility. A fit in Figure 6.8 to the 40 - 200 K region of the data may be made by considering the Heisenberg type antiferromagnetic exchange within a dimer between two S = 1 ions. The appropriate expression for fitting the data is constructed from the Van Vleck equation (neglecting the second order Zeeman effect) [23]:

$$\chi = \frac{2Ng^2\mu_B^2}{kT}\frac{e^{2J/kT} + 5e^{6J/kT}}{1 + 3e^{2J/kT} + 5e^{6J/kT}}$$

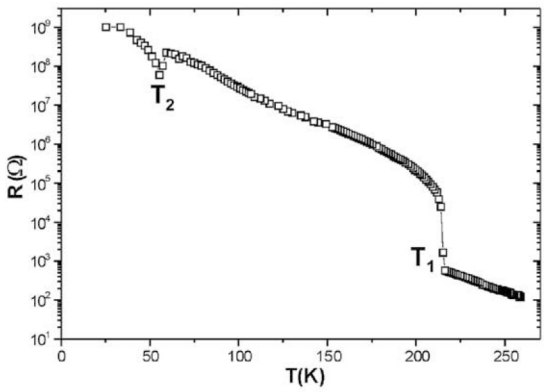

Figure 6.7: Semiconductor to insulator transition in $Ba_3NaRu_2O_9$ evident in the jump in resistance (R) at 210 K. Figure taken from ref. [201]. Feature at T_2 is most likely due to an impurity.

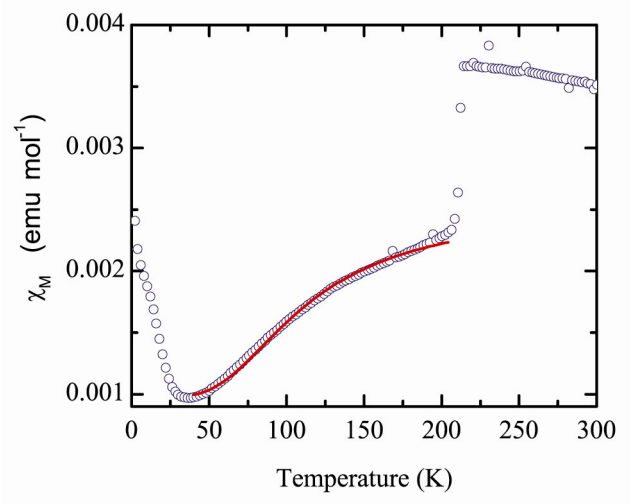

Figure 6.8: Susceptibility plot against temperature for $Ba_3N_aRu_2O_9$. Dimer S = 1 correlation model fit indicated by the red line (J = -162(2) K).

The lattice of the low temperature structure is visualised in Figure 6.9 in terms of the charge ordered $Ru^{n+}{}_2O_9$ units. The three fold degeneracy of the triangular lattice in the *ab* plane is clearly lifted by the striped arrangement of the charge ordering along *a*. Overall, the lattice may be visualised as a hexagonal close packed network of dimers. The charge ordering is then seen to obey the 'Ice rules' in which every tetrahedron consists of $[Ru^{5+}{}_2O_9]_2[Ru^{6+}{}_2O_9]_2$. In accordance with Anderson's rules, this also minimises short range Coulombic repulsion. The structural distortion that accompanies the charge ordering removes this highly degenerate arrangement of charges on the hexagonal close packed lattice. Experimentally, the fraction of the six twin components refined in Table 6.2 is as expected from the

degeneracy of an assembly of fluctuating $[Ru^{5+}{}_2O_9]_2[Ru^{6+}{}_2O_9]_2$ tetrahedra which condense out at T_{CO}.

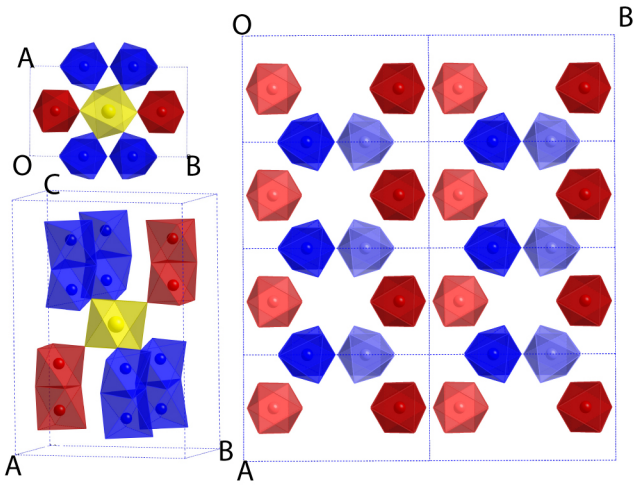

Figure 6.9: Striped arrangement of charge ordered $Ru^{5+}{}_2O_9$ / $Ru^{6+}{}_2O_9$ dimers and their arrangement on a triangular lattice. Red and blue denote 5+ and 6+ dimers respectively and dark and light dimers located at z = ¾ and ¼ respectively, yellow denotes Na^+.

Of all the derivatives of $Ba_3ARu_2O_9$ (A^+ / A^{3+}, $Ru^{5.5+}$ / $Ru^{4.5+}$), A = Na^+ is alone in exhibiting a charge order transition. In an attempt to understand this anomaly in the series, a plot of cell volume versus the cube of the A and Ru ionic radii ($2r_{Ru}{}^3 + r_A{}^3$) is made in Figure 6.10. In order to make the plot it is important to understand that r_{Ru} varies with the oxidation state of Ru and hence the oxidation state of A. For non-integer Ru oxidation states, r_{Ru} is obtained from linear interpolation from ionic radii which are tabulated[205]. The trend of the cell volume with $r_{Ru}{}^3 + r_A{}^3$ is linear as evident from Figure 6.10. A = Na^+ however, (unlike A = Li^+) deviates significantly from this linear relationship. This deviation which should be due to bond angles differing from 180 ° is investigated further in Figure 6.11, where Ru-O-A vs r_{Ru}/r_A is plotted. Although r_{Ru} / r_A does not appear to act as a predictor for the Ru-O-A angle it does seem to indicate that for a given r_{Ru} / r_A there is a maximum Ru-O-A angle which can be supported by the packing in the crystal structure. A = Na clearly lies at the extreme of the Ru-O-A distribution as is evident from the histogram of all of the Ru-O-A angles in Figure 6.11, right.

The extremes in both the ratio of the relative Ru-A distance (r_{Ru} / r_A) and the Ru-O-A bond angle for $Ba_3NaRu_2O_9$, may point to the fact that the exchange pathways are significant in whether or not charge ordering is observed. The weakening of this exchange in A = Na with respect to the rest of the series may ultimately facilitate the charge ordering, and explains

why it is not observed in any other compounds of the series. Additionally, all derivative A = Fe, Co, Ni, Cu, In,[206] Ce, Pr, Tb[204] and Y, La, Sm, Eu, Lu[207] exhibit a resistivity which may be modelled by a two-dimensional Mott variable-range hopping (VRH) model ($\rho \propto \exp((T_0/T)^{1/3})$), presumably on account of Ru-O-A exchange pathways. In contrast, for A = Na, VRH of any dimensionality does not account satisfactorily for the observed trend in resistivity,[201] providing a further indicator that the exchange pathways in A = Na are weakened with respect to the rest of the series.

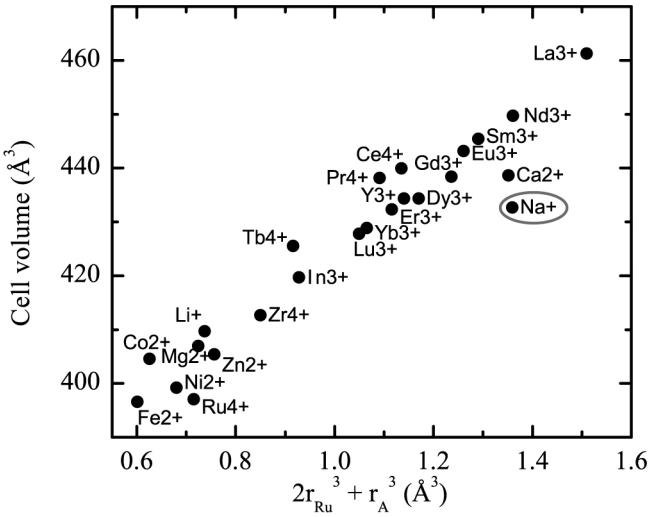

Figure 6.10: Unit cell volume versus the $2r_{Ru}^3 + r_A^3$ for all known derivatives of $Ba_3ARu_2O_9$ that crystallise in $P6_3/mmc$ at room temperature. Ionic radii taken from ref. [205] and cell volumes from experimental values of this work and that of ref. [180, 194, 204, 207] and [174]. A = Na deviates significantly from the linear trend.

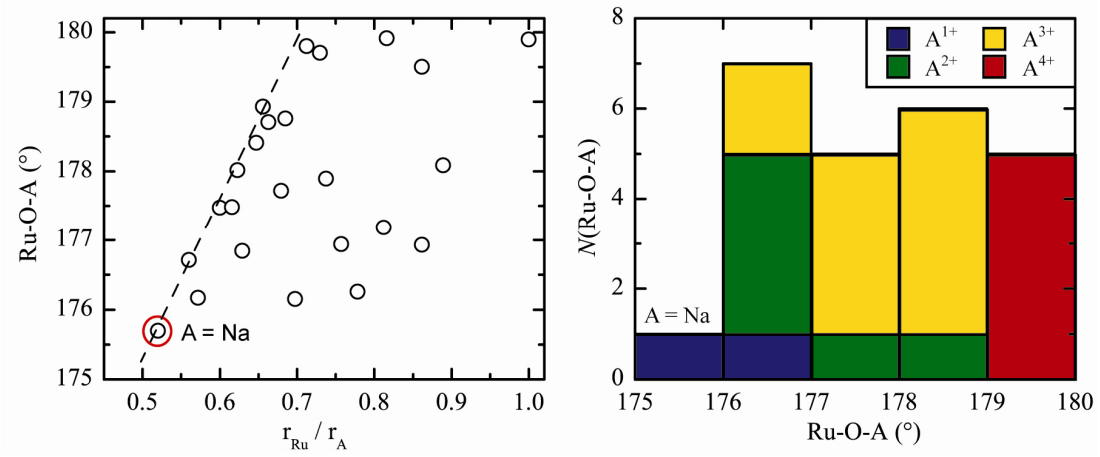

Figure 6.11: Left, Ru-O-A bond angle versus r_{Ru}/r_A. The dash line indicates an apparent maximum in Ru-O-A / (r_{Ru}/r_A). A = Na is at both the extreme of the Ru-O-A bond angle and r_{Ru} / r_A ratio distributions. Right, histogram of Ru-O-A bond angles.

6.3. Irradiation induced charge melting transition at 40 K

A second phase transition was observed between 50 and 30 K in the synchrotron x-ray diffraction data. The phase transition appears to correspond to a gain in centring with respect to the charge order P2/c phase as evident by the disappearance of (*h k l*), $h + k$ = even peaks at 30 K (Figure 6.12). This is unusual, in that, phase transitions on cooling must result in structures with lower entropy, higher order and therefore lower symmetry. All reflections of this new phase can be indexed by the space group C2/c with the existing ($a \times \sqrt{3}b \times c$) unit cell. The fit of the Rietveld refinement is given in Figure 6.13 and refinement details are given in Table 6.5. The significant feature of the model is that it is described by only one crystallographically unique Ru site, prohibiting the existence of any charge ordering in the phase. As the synchrotron x-ray diffraction data is very sensitive to the Ru position, the equivalence of the Ru_2O_9 dimers within the unit cell is determined with a high certainty. The Ru-Ru distance is 2.7309(16), which is in good agreement with an average valence state of $Ru^{5.5+}$ (see Figure 6.6). Other Rietveld modes in noncentrosymmetric space groups C2, Cm and Cc were tested in an attempt to explain the apparent reversal of thermodynamics, but these yielded unstable fits which were not significantly improved with respect to the C2/c model.

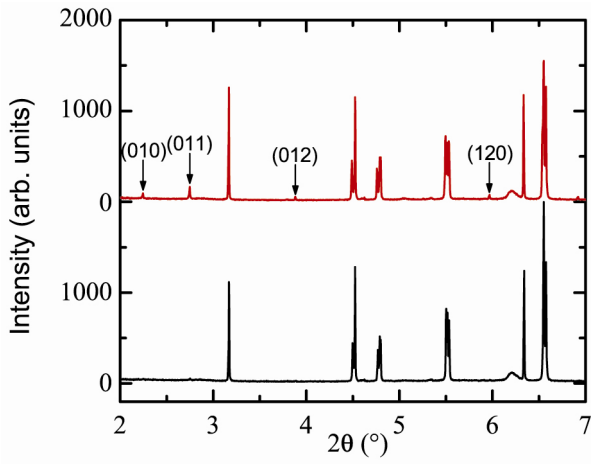

Figure 6.12: The gaining of lattice centring on cooling of $Ba_3NaRu_2O_9$ at ID31 from 50 K (upper) → 30 K (lower) as evident from the disappearance of the $h + k$ = odd reflections at 30 K.

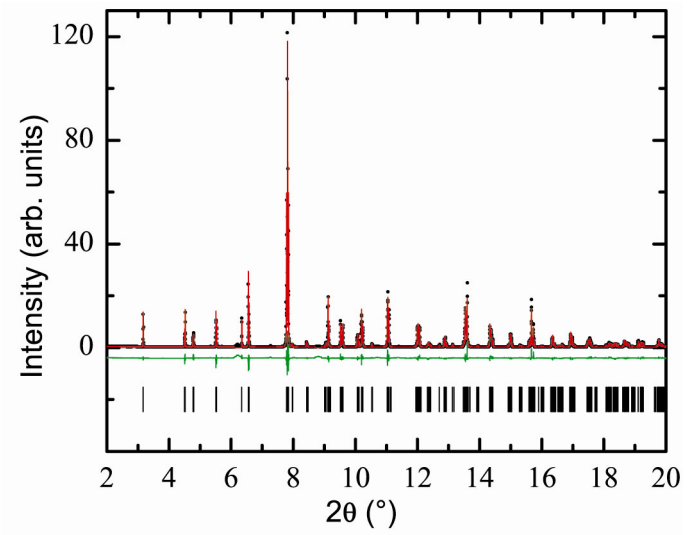

Figure 6.13: Rietveld fit of C2/c 'charge melted' model to ID31 data (λ = 0.39983(4) Å) at 10 K.

Cell setting, space group		Monoclinic, C2/c		
a,b,c (Å)		5.84470(2), 10.17706(3), 14.45866(5)		
β(°)		90.2151(3)		
V(Å^3)		860.022(5)		
Parameters		35		
wR_p, R_p, χ^2		11.83 %, 9.46 %, 5.210		
	x	y	z	B_{iso} (Å^2)
Ba1	0.49538(18)	0.17129(11)	0.59088(5)	0.511(8)
Ba2	0	-0.00811(14)	0.25	0.511(8)
Na1	0	0	0	0.511(8)
Ru1	0.49587(21)	0.16134(13)	0.15557(6)	0.511(8)
O1_1	0.7141(17)	0.0796(10)	0.0840(7)	0.40(6)
O1_2	-0.0105(17)	0.8177(9)	0.0871(7)	0.40(6)
O1_3	0.2499(17)	0.9126(10)	0.5971(7)	0.40(6)
O2_1	0.2780(16)	0.2381(10)	0.2564(7)	0.40(6)
O2_2	0	0.5147(14)	0.25	0.40(6)

Table 6.5: Results from the Rietveld refinement against ID31 data (λ = 0.39983(4) Å) at 10 K to the C2/c charge melted phase of $Ba_3NaRu_2O_9$.

Time resolved data collected at ID31 provides an explanation for this novel charge melted phase. In this, the sample was cooled from room temperature to 10 K with the shutter of the beam closed. The shutter was then opened, and rapid diffraction data collected as a function

of time in the 2θ range 2 – 20 ° every minute. The results are summarised in Figure 6.14. The (0 1 1) peak rapidly diminishes with time, and has completely disappeared after 2 minutes corresponding to the P2/c → C2/c phase transition. The difference between $D_{(Ru\text{-}Ru)}$ for the 5+ and 6+ dimers approaches zero after 120 – 180 s with an exponential time constant 75(8) s. This corresponds to the average valence state of 5.5+ being adopted by the Ru sites. The lattice relaxes at the same rate at which the charge ordering melts, with a reduction in the macrostrain (*b* / *a*) being evident (Figure 6.14, right).

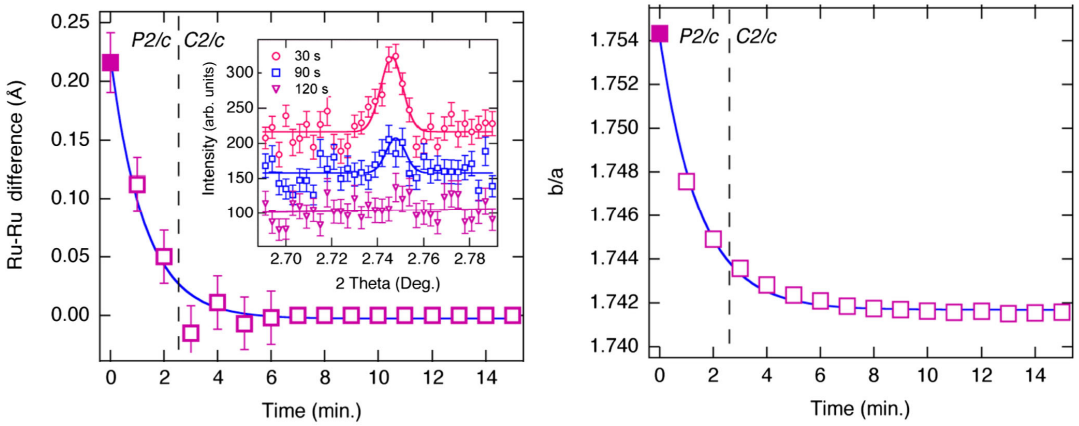

Figure 6.14: Time resolved synchrotron x-ray diffraction study for $Ba_3NaRu_2O_9$. Left, the difference between the Ru-Ru distances between the $Ru^{5+}{}_2O_9$ and $Ru^{6+}{}_2O_9$ dimers at 10 K with time after initial irradiation. The inset evidences the gain of centring with time. Right, evolution of macrostrain (*a* / *b*) with time. Figure reproduced courtesy of Simon Kimber.

The P2/c phase persists for some time under irradiation, and is always recovered on warming above 40 K. At 10 K the charge melted phase is observed to be stable for several hours, indicating that is only a question of rate as to whether the phenomenon is observed. Presumably above 40 K, the rate constant of C2/c → P2/c is greatly enhanced and the density of photons impinging on the samples does not pump electrons from valence (or core) to the conduction band at a sufficient rate to counter their relaxation back to valence band.

Neutron powder diffraction data collected at the time of flight diffractometer WISH, ISIS confirms the fact that the x-ray radiation participates in the charge melting phase transition. Figure 6.15 shows an overlay of the data at 1.6 K and 110K, with almost no difference in peak intensity evident. Indeed the P2/c model refined against single crystal data (with fixed coordinates) has a very good fit to the data collected at both 10 K and 110 K (Figure 6.16).

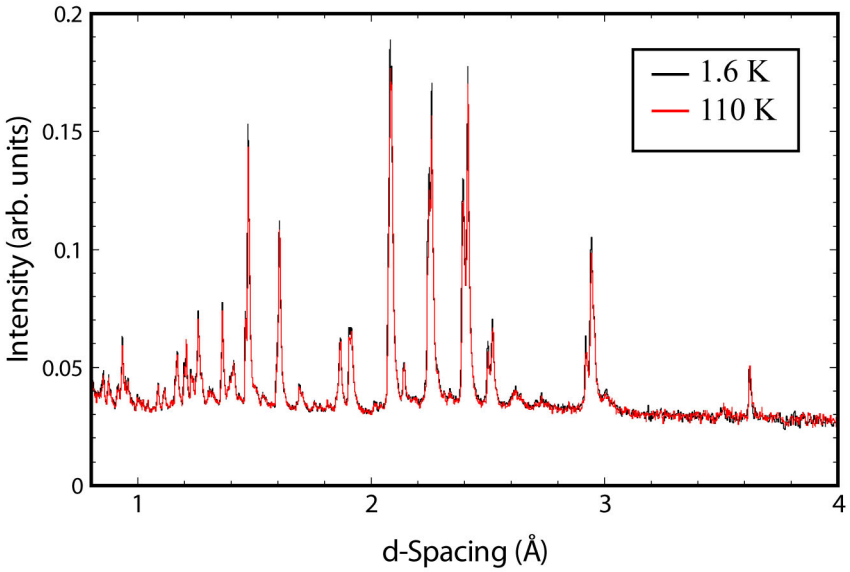

Figure 6.15: Overlay of the WISH diffraction patterns from the back scattering bank at 1.6 K and 110K, evidencing an absence of any phase transition.

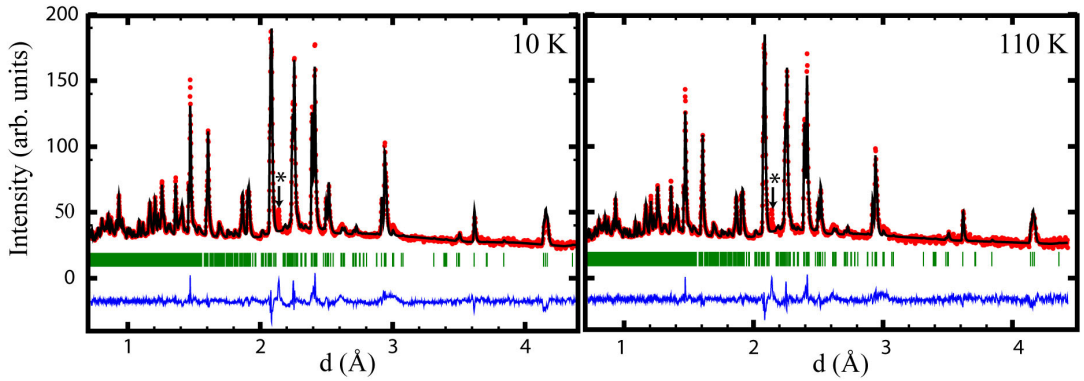

Figure 6.16: Rietveld fit of P2/c charge ordered model against WISH data collected at 10 K and 110 K. Coordinates are taken from the single crystal refinement at 110 K and fixed, lattice parameters were refined against data. A peak from the vanadium sample can is indicated (*).

A comparison of normalised unit cell parameters determined at 10 K from both neutron and x-ray diffraction data reveal that they deviate substantially. The evolution of the cell parameters for both the WISH and ID31 experiments is investigated further in Figure 6.17. It is evident that the *a* and *b* lattice parameters which diverge away from hexagonal symmetry at T_{CO} appear to continue their divergences below 40 K (T_2) in the neutron data, but start to converge back towards $a\sqrt{3} / b = 1$ in the x-ray data. This additional phase transition at (T_2), observed only in the x-ray data, implies that it must be linked to the interaction of the matter with the x-ray radiation. It is evident that the P2/c phase persists down to base temperatures in the neutron powder diffraction data.

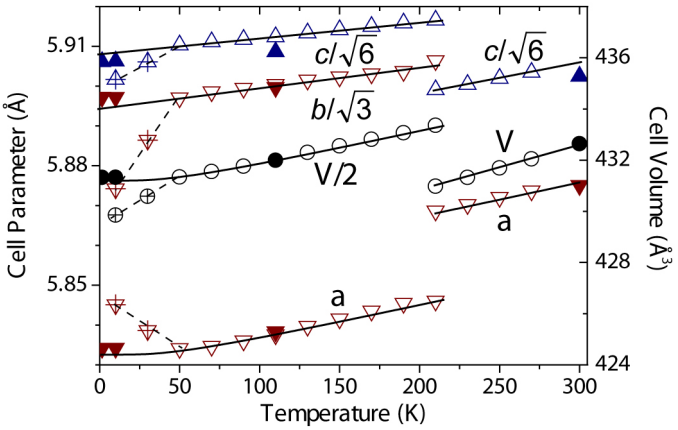

Figure 6.17: The evolution of lattice parameter with temperature for $Ba_3NaRu_2O_9$. Values are taken from Rietveld refinements against x-ray (open symbols) and neutrons (closed symbols) diffraction data.

6.4. High pressure synchrotron x-ray diffraction studies

In order to investigate the nature of the metal-metal bond within the Ru_2O_9 dimers, high pressure diffraction experiments were performed at ID9A, ESRF. The single crystals used for the experiment were taken from the same flux reaction used for the ambient temperature single crystal diffraction study. The diamond anvil cell (DAC) was loaded with He as the pressure transmitting medium. The indexing and integration of the diffraction images at each pressure was performed in the program CrysAlisPro. The pressure was measured by monitoring the laser induced fluorescence of a ruby chip present in the DAC[202] before and after the data collection. The volumes calculated from the cell parameters and the average pressures at which they were measured at are plotted in Figure 6.18. The evolution of the volume with applied pressure may be accounted for by a second-order Birch-Murnaghan equation of state. A fit in the web based program PASCAL[38] gave:

$$V(P) = V_0\left(1 + B_0' \frac{P}{B_0}\right)^{-1/B_0'}$$ $B_0 = 87.4(4)$ GPa, $V_0 = 431.1(2)$ Å^3, $B_0' = 4$ (fixed)

The fit to the data is plotted in Figure 6.18.

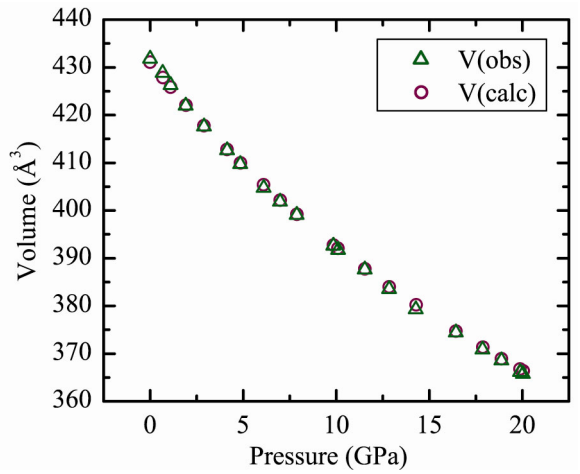

Figure 6.18: Equation of state fit for the evolution of volume with pressure for $Ba_3NaRu_2O_9$ using a second-order Birch-Murnaghan model.

V_0 is in good agreement with the volume extracted from the Rietveld refinement from ID31 data (432.73(1) Å^3) at ambient pressure and temperature, (see Appendix C). The bulk modulus is quite a lot lower than that of the cubic perovskite $SrRuO_3$ with B_o = 192(4) GPa,[208]. At 20 GPa, the unit cell volume of $Ba_3NaRu_2O_9$ is just 84 % of the volume that it occupies at ambient pressure. The fact that the hexagonal perovskite has a much higher compressibility than the simple cubic close packed perovskite is not surprising considering that only one third of the layers in the 6H structure are cubic close packed.

The lattice parameters at their average pressures are plotted in Figure 6.19. The *c* lattice parameter has been divided by √6 to make its relationship to the cubic perovskite unit cell evident. At ambient pressure, $c/\sqrt{6}$ is greater than *a*. However, at about 10 GPa there is a crossing such that $a > c/\sqrt{6}$. At pressures above 17 GPa, the trend is again reversed to that observed at ambient pressures with $a < c/\sqrt{6}$. This curious behaviour of the lattice parameters does not make itself evident in any anomalies in the volume with respect to the equation of state fit in Figure 6.18.

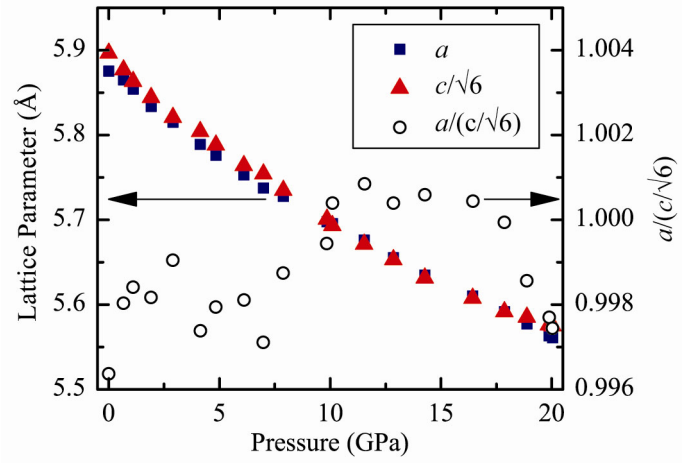

Figure 6.19: The evolution of lattice parameters with pressure for $Ba_3NaR_2O_9$. Lattice parameters are extracted from indexing single crystal data, and the pressure from the fluorescent signal of a ruby chip present in the diamond anvil cell. Standard errors for pressures and lattice parameters are within plotted symbols.

Unfortunately, an insufficient number of reflections were observed in the high pressure experiments for the internal coordinates of the structure to be determined accurately. To investigate the behaviour of the a / $c/\sqrt{6}$ ratio crossing, the results are compared to ambient pressure results for the rest of the $Ba_3ARu_2O_9$ phases.

Although comparisons of high pressure phase with ambient pressure structures (i.e. the analogy of 'chemical pressure') must be made with caution, it is nevertheless interesting to compare the high pressure results of $Ba_3NaRu_2O_9$ with ambient pressure phase of $Ba_3LiRu_2O_9$[6]. From Figure 6.20, it is evident that of all of the known $Ba_3ARu_2O_9$ derivatives only Li has a ratio a / (c/√6)) > 1 as observed in $Ba_3NaRu_2O_9$ in the pressure range 10 – 17 GPa. Additionally, the cell volume of $Ba_3NaRu_2O_9$ at ~5 GPa is the same as that of $Ba_3LiRu_2O_9$ at ambient pressure (410 $Å^3$)[6]. This system is hence to some degrees analogous to $Ba_3NaRu_2O_9$ in the pressure region of interest. In Figure 6.20, right, a link between the fractional unit cell $D_{(Ru\text{-}Ru)}$ distance ($D_{(Ru\text{-}Ru)}/c$ as bond is along c-axis) and a / ($c/\sqrt{6}$) is established for the $Ba_3ARu_2O_9$ series of compounds. At high $D_{(Ru\text{-}Ru)}/c$, a linear relationship exists with a / ($c/\sqrt{6}$), with little variation in $D_{(Ru\text{-}Ru)}/c$ with varying a / ($c/\sqrt{6}$). Below 0.175, a down-turn in the relationship is evident, presumably representing some kind of hard limit to the minimum value of $D_{(Ru\text{-}Ru)}/c$.

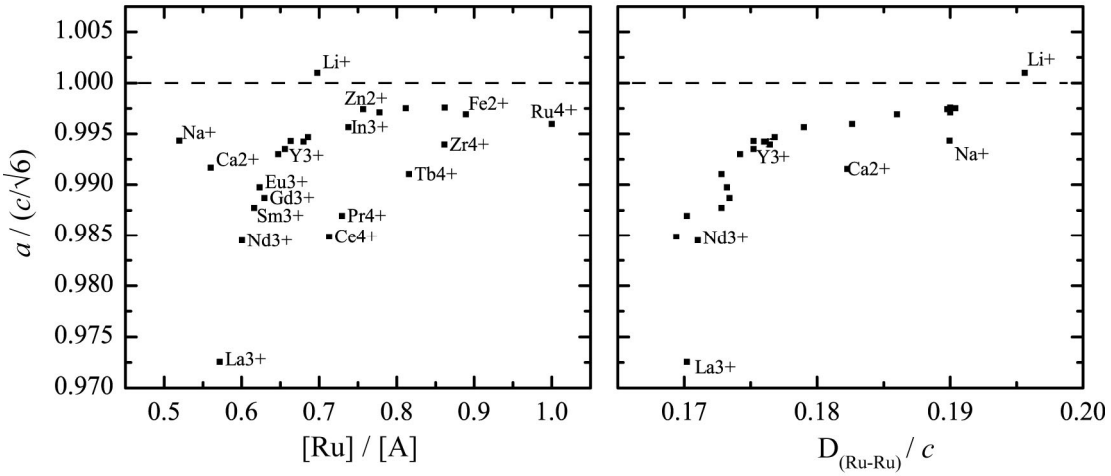

Figure 6.20: Left, trend of *a*/*c* lattice parameters versus the ratio of Ru and A ionic radii ([Ru]/[A]). Right, *a*/*c* ratio versus the fraction $D_{Ru\text{-}Ru}$ ($D_{(Ru\text{-}Ru)}/c$).

One might hence speculate that the change in a / ($c/\sqrt{6}$) in the high pressure data $Ba_3NaRu_2O_9$ corresponds to a change in $D_{Ru\text{-}Ru}/c$. That is, there is a change in the stiffness of $D_{Ru\text{-}Ru}$ with respect to the rest of the structure. This could correspond to an initial desire of the system to minimise $Ru^{5.5+}$ Coulombic repulsion (0 – 16 GPa) by increasing $D_{Ru\text{-}Ru}/c$, followed by a bonding interaction (above 17 GPa) resulting in a softening of the bond distance (Figure 6.19). In order to test this theory, better high pressure diffraction data would be required so that the internal coordinates of the structure could be refined.

The stiffness of the Ru-Ru distance may be investigated further by analogy with chemical pressure. Figure 6.21 illustrates that the volumes have an approximately linear relationship with $D_{(Ru\text{-}Ru)}/c$ for each $Ba_3A^{x+}Ru^{n+}{}_2O_9$ (x = 1, 2, 3 , 4, n = 5.5, 5, 4.5, 4 respectively) family of compounds. Linear regression fits to each family of compounds are made with the constraint that they must have the same gradient (that determined from the largest family of compounds) but with individual intercepts. $D_{(Ru\text{-}Ru)}/c$ which is purely an internal measure of strain proves to be a very good predictor for the unit cell volume (and hence chemical pressure). The *y*-intercepts of the fit of the four series of compounds $Ba_3A^{x+}Ru^{n+}{}_2O_9$ is plotted in Figure 6.21, right, against the ruthenium oxidation state squared (n^2). Although the correlation with Coulomb's law is rather weak, the reduction in volume on moving between the x = 1 ($Ru^{5.5+}$) to x = 4 (Ru^{4+}) series is evident. The additional 'chemical pressure' (volume increase) experienced by the system on increasing the Ru oxidation is hence demonstrated to depend only on the Ru oxidation state to a good first approximation. Additionally, as the unit cell volumes of $Ba_3ARu_2O_9$ are well accounted for in most cases by considering $2r_A^3 + r_{Ru}^3$ (Figure 6.10), the above analysis gives a means for accurate

prediction of the $D_{(Ru\text{-}Ru)}$ of a target composition. This analysis should prove to be more general than just the $Ba_3AB_2O_9$ (B = Ru) series, and should provide a means for understanding why 6H perovskites of certain compositions do not form.

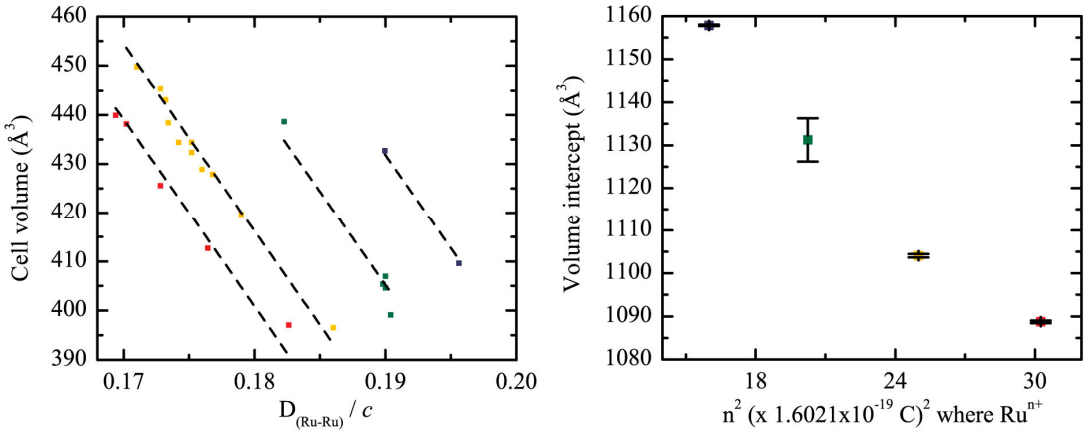

Figure 6.21: Volumes versus $D_{(Ru\text{-}Ru)}$ / c for $Ba_3ARu_2O_9$. A^{4+}, A^{3+}, A^{2+} and A^{1+} are shown as red, yellow green and blue symbols respectively. Linear regression lines of best fit to each A^{x+} series are indicated by dashed lines and are all constrained to have the same gradient (3820(240) Å^3), which was derived from a least square fit against the A^{3+} series . On the right the intercepts are plotted against the square of Ru^{n+} oxidation state n^2, reflecting Coulomb's law.

6.5. Conclusion

The true nature of the charge ordered phase of $Ba_3NaRu_2O_9$ has been elucidated by high resolution x-ray powder diffraction and twinned single crystal diffraction. The charge ordering is shown to be near integer and the ground state relieves the degeneracy of a charge fluctuating state of $Ru^{5+}{}_2O_9$ and $Ru^{6+}{}_2O_9$ dimers on a hexagonal close packed lattice. The null observation of charge ordering in the rest of the $Ba_3ARu_2O_9$ series has been rationalised in terms of Ru-O-A exchange pathways. A novel synchrotron x-ray induced phase transition has been observed corresponding to a melting of the charge ordered phase. The melting of the charge ordering is shown to be coupled to a relaxation of the macrostrain of the lattice. High pressure x-ray diffraction experiments point to some potentially interesting behaviour related to the stiffening of the $D_{(Ru\text{-}Ru)}$ distance in the structure, which requires further investigation. The volumes of the $Ba_3ARu_2O_9$ 6H-perovskites are shown to be predicted well by the internal strain of the $D_{(Ru\text{-}Ru)}$ distance ($D_{(Ru\text{-}Ru)}/c$), and the volume increase between the $Ba_3NaRu^{4+}{}_2O_9 \rightarrow Ba_3NaRu^{5.5+}{}_2O_9$ series of compounds appears to have a mainly Coulombic origin.

7. Magnetic ordering in $Ba_3ARu_2O_9$ (A=Y, La, Nd, Ca)

Magnetic ordering transitions are known to be evidenced in several $Ba_3ARu_2O_9$ materials through susceptibility measurements, but spin arrangements of the ordered Ru moments have only been determined by neutron diffraction for A = Ni^{2+} and Co^{2+}. The $(Ru^{5+})_2O_9$ spin dimers are antiferromagnetic and are coupled to ordered Ni/Co spins.[180, 181, 209] A^{3+} = RE (rare earth) and Y materials all remain hexagonal down to 2 K and have Néel transitions at T_N < 25 K which are believed to be coupled to an AFM ordering of the rare earth moments.[169] A = Nd^{3+} is the exception in the rare earth series, with a transition to C2/c symmetry reported at 110 K, in addition to a FM magnetic ordering transition of the Nd moments at 25 K. Broad features in magnetic susceptibility and specific heat measurements at high temperatures for all A = RE have been interpreted as evidence for local antiferromagnetic pairing within Ru_2O_9 dimers.[169] In this chapter, the ordered magnetic structures of $Ba_3ARu_2O_9$ (A= La^{3+}, Y^{3+}, Nd^{3+}) are reported, and the short range ordering in A = Ca^{2+} is investigated. The exchange mechanism responsible for the ordering in these compounds is suggested and the apparent anomalous behaviour of A = Nd^{3+} is explained.

7.1. Experimental

Samples of $Ba_3ARu_2O_9$ (A = La, Y, Nd, Ca) were prepared by calcining pellets made from stoichiometric amounts of RuO_2, $BaCO_3$ and A_2O_3 or $CaCO_3$ at 900 °C. The pellets were then heated to between 1000 and 1400 °C for 72hrs with multiple cycles of re-grindings and repelletisation, following previously reported methods of preparation.[194, 207] The samples were found to be phase pure by x-ray diffraction (Cu-Kα_1). High resolution synchrotron x-ray powder diffraction data (λ = 0.39983(4) Å) were collected at the beamline ID31, ESRF for A = La, Y at room temperature and for Nd in the range 10 – 295 K. High resolution synchrotron x-ray powder diffraction data (λ = 0.50014(2) Å) at beamline BL19B2, Spring8 were collected in the temperature range 120 – 300 K for A = Ca. High resolution neutron powder diffraction data were collected for A = La and Y at the time-of-flight diffractometer HRPD, ISIS from room temperature down to 10 and 2 K respectively. All samples were also measured down to 1.6 K at the time-of-flight neutron powder diffractometer WISH, ISIS out to a d-spacing of 30 Å. Magnetisation-field hysteresis loops were collected for the A = Nd

samples at 2, 15, 20, 30 and 150 K and field cooled and zero field cooled susceptibility measured in the range 2 – 200 K on a SQUID magnetometer.

7.2. Magnetic ordering in $Ba_3ARu_2O_9$ (A=Y, La)

7.2.1. Structural refinements

Initially, high resolution diffraction studies were performed at HRPD to ascertain if charge ordering was evident in this series of semivalent $Ru^{4.5+}$ compounds as was found for the $Ru^{5.5+}$ compound $Ba_3NaRu_2O_9$ in Chapter 6. However, the structures were found to retain the aristotypical symmetry $P6_3/mmc$ down to 2 K (Table 7.1), with little change in the diffraction profile, and no observed anomalies over the transition temperatures evident in the physical property measurements of ref. [169]. Weak peaks which were not indexed by the space ground were found across the entire temperature range for which the data were collected for A = La (Figure 7.1). Similar peaks in A = Y were also observed. It was possible to index the peaks using the ID31 data for A = La on an unidentified impurity with orthorhombic unit cell a = 4.1678(3) Å, b = 5.8979(2), c = 9.6355(4). It is not anticipated that these very small unaccounted-for intensities will have a significant effect on the values extracted from the Rietveld refinements of A = Y and La.

A =	La	Y
a (Å)	5.9492(1)	5.86560(9)
c (Å)	14.9981(4)	14.4817 (2)
Ba2 z	0.8909(1)	0.9061(1)
Ru z	0.16556(8)	0.16418 (7)
O1 x	0.4873(1)	0.4892(1)
O2 x	0.17889(8)	0.17663(9)
O2 z	0.40471(4)	0.3532(2)
Ba U_{ISO} ($Å^2$)	0.0081(3)	0.0026(2)
A U_{ISO} ($Å^2$)	0.0066(3)	0.0026 (3)
Ru U_{ISO} ($Å^2$)	0.0024(2)	0.0016(2)
O U_{ISO} ($Å^2$)	0.0108(2)	0.0060(1)
wR_p	6.66 %	5.75 %

Table 7.1: Rietveld structural refinement model for $BaARu_2O_9$, A = La and Y at 11 and 2 K respectively against neutron powder diffraction data (HRPD, ISIS). There are six crystallographic unique sites in the structure described within $P6_3/mmc$ symmetry: Ba1 (0, 0, ¼), Ba2 (⅓ ,⅔, z), A (0, 0, 0), Ru (⅓ ,⅔, z) , O1 (x, 2x, ¼) and O2 (x, 2x, z). Refined lattice parameters, fractional coordinates and U_{ISO} are summarised below along with wR_p values and are in line with those published for the structure at ambient temperature.[207]

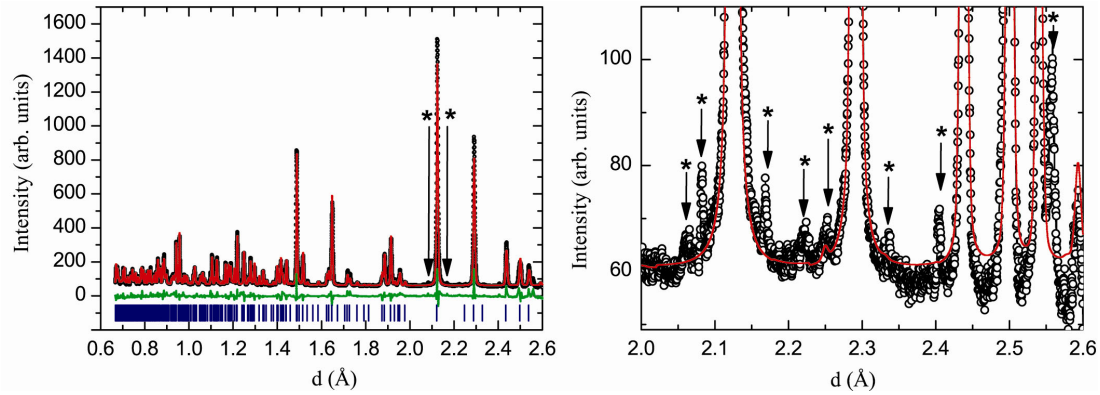

Figure 7.1: Rietveld refinement fits for $Ba_3LaRu_2O_9$ against data collected from the back scattering bank of HRPD, ISIS at 300K. The fit to the data is reasonable, but very weak peaks (*) which are not indexed on the hexagonal phase are observed and are assigned as belonging to an unknown impurity phase (a = 4.1678(3) Å, b = 5.8979(2) Å, c = 9.6355(4) Å, α = β = γ = 90°)

7.2.2. Magnetic structures of $Ba_3ARu_2O_9$ (A=Y, La)

Additional peaks due to magnetic scattering were observed in the neutron powder diffraction profiles for A = La and Y samples below 25 and 6 K respectively (Figure 7.2), consistent with previously reported anomalies observed in the magnetic susceptibility.[169] The magnetic

peaks are indexed by the (0 ½ 0) propagation vector, equivalent to the $a_o = a$, $b_o = \sqrt{3}a$, $c_o = c$ orthorhombic Cmcm superstructure of the hexagonal $P6_3/mmc$ cell. The irreducible representations and basis vectors of the Ru spins in $P6_3/mmc$ under the propagation vector k = (0 ½ 0), generated from the program BasIReps[32] of the Fullprof suite, are shown in Table 7.2.

Models containing antiferromagnetic Ru_2O_9 spin-dimers, as proposed from previous magnetic heat capacity results,[207] did not fit the magnetic intensities of $Ba_3LaRu_2O_9$. However, a model (Figure 7.3, inset) of ferromagnetic dimers, described by basis vectors from two different representations, accounts well for the observed magnetic diffraction intensities (Figure 7.3). The $\Psi_1(\Gamma5)$ basis fits the (0 ½ *l*) magnetic peaks but predicts zero intensity for the (1 ½ 0) peak (Figure 7.4) which is clearly observed in Figure 7.3; hence the need for an additional $\Psi_2(\Gamma3)$ component. $\Psi_1(\Gamma5)$ and $\Psi_2(\Gamma3)$ respectively describe Ru spin components parallel to the a_o and c_o vectors of the orthorhombic supercell, with values m_x = 1.3(1) μ_B and m_z = 0.6(2) μ_B, and resultant moment 1.4(2) μ_B, at 1.6 K.

For A = Y the ordering temperature was considerably lower, and the observed AFM peaks much weaker. Although the (1 ½ 0) magnetic reflection is evident for A = Y (Figure 7.2, inset), fits implementing Ψ_2 (Γ_3), were not significant, with the refined values within the standard error, (Γ_5):0.4(3) μ_B, m_y: Ψ_2 (Γ_3): 0.2(5) μ_B. Instead a refinement just considering Ψ_1 (Γ_5) was performed leading to a net moment of 0.5(1) μ_B.

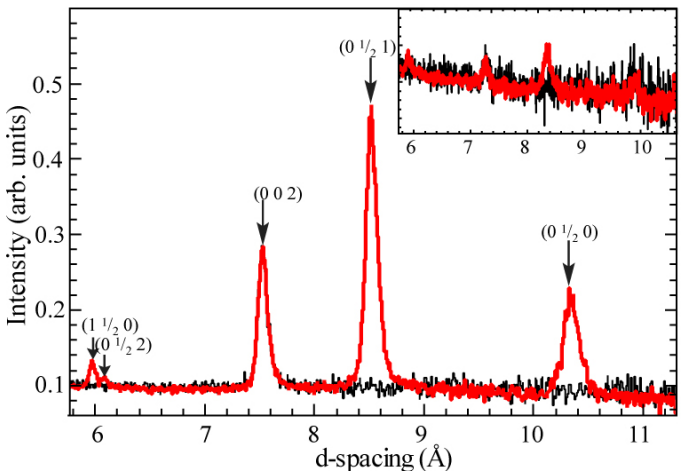

Figure 7.2: Magnetic Bragg peaks for $Ba_3LaRu_2O_9$ in the 56 ° scattering bank of WISH evident at 10 K (red) and absent at 40 K (black). In the inset, peaks are shown for Ba_3YRu2O_9 at 1.6 K (red) and absent at 8 K (black). Indexation is given with respect to $P6_3/mmc$ unit cell.

Irred. reps	Basis vectors	x, y, z			-x, -y, z + ½			x-y, -y, -z			-x+y, y, -z+ ½		
		m_x	m_y	m_z	m_x	m_y	m_z	m_x	m_y	m_z	m_x	m_y	m_z
Γ_1	Ψ_1	1	0	0	-1	0	0	1	0	0	-1	0	0
Γ_2	Ψ_1	1	2	0	-1	-2	0	-1	-2	0	1	2	0
	Ψ_2	0	0	1	0	0	1	0	0	-1	0	0	-1
Γ_3	Ψ_1	1	2	0	-1	-2	0	1	2	0	-1	-2	0
	Ψ_2	0	0	1	0	0	1	0	0	1	0	0	1
Γ_4	Ψ_1	1	0	0	-1	0	0	-1	0	0	1	0	0
Γ_5	Ψ_1	1	0	0	1	0	0	1	0	0	1	0	0
Γ_6	Ψ_1	1	2	0	1	2	0	-1	-2	0	-1	-2	0
	Ψ_2	0	0	1	0	0	-1	0	0	-1	0	0	1
Γ_7	Ψ_1	1	2	0	1	2	0	1	2	0	1	2	0
	Ψ_2	0	0	1	0	0	-1	0	0	1	0	0	-1
Γ_8	Ψ_1	1	0	0	1	0	0	-1	0	0	-1	0	0

Table 7.2: Basis vectors of the space group $P6_3/mmc$ for the Ru site (4f) (⅓, ⅔, z) (where z = 0.16556 and 0.16418 for A= La and Y respectively) under the propagation vector k = (0 ½ 0) . The magnetic structure of $Ba_3LaRu_2O_9$ in Figure 7.3 is a combination of the basis vectors Ψ_2 (Γ_3) and Ψ_1 (Γ_5).

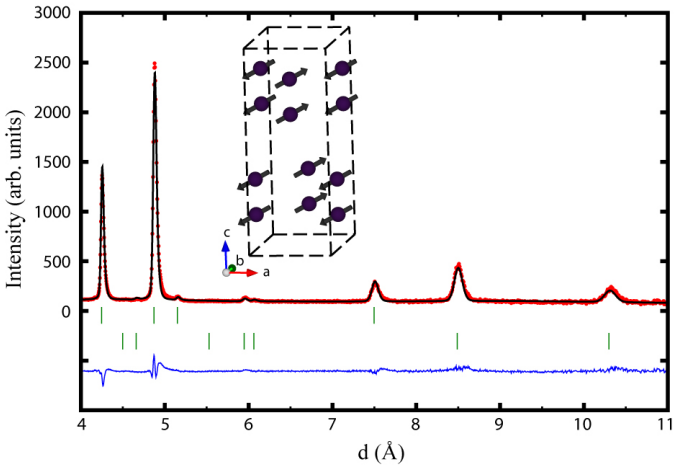

Figure 7.3: Rietveld refinement fit of A = La at 1.6 K. The magnetic structure is modelled with propagation vector (0 ½ 0) (lower tick marks) with moments 1.4(2) μB and 0.5(1) μB for A = La and A = Y respectively, and is shown in the inset.

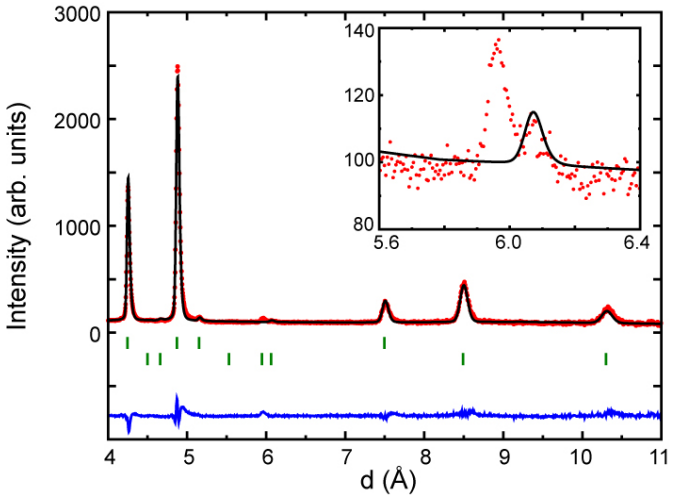

Figure 7.4: The failure of the Rietveld refinement to fit the structure with a single basis vector Ψ_1 (Γ_5). This model does not predict any intensity for the observed (1 ½ 0) magnetic reflection.

The moments in both materials are significantly reduced from the ideal value of 2.5 μB, consistent with a frustrated order. Nearest neighbour Ru-Ru alignments are ferromagnetic along one side and antiferromagnetic on two sides of each plaquette in the triangular ab-plane lattice. This breaking of the degeneracy of the triangular lattice should lead to an orthorhombic distortion of the hexagonal lattice. This was tested by fitting the orthorhombic Cmcm superstructure to the low temperature HRPD data, but no significant deviation of the a_o/b_o ratio was found, as illustrated in Figure 7.5. The energies associated with the distortion required to raise this degeneracy of the triangular lattice may be very small, and it is possible that even with low temperature synchrotron x-ray powder diffraction that the structural phase transition would remain unobserved.

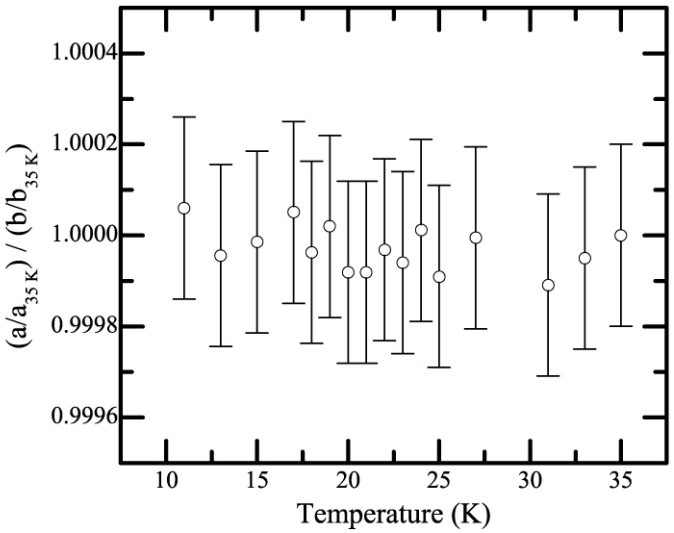

Figure 7.5: Cell parameter trends as a function of temperature extracted from Rietveld refinement against data collected in the backscattering bank of HRPD for $Ba_3LaRu_2O_9$ modelled in a Cmcm ($a \times \sqrt{3}\ a \times c$) supercell.

The mechanism for the magnetic ordering in these structures is two-fold. The FM interaction within the dimers is here proposed to be due to double exchange of the minority spin of the partial field t_{2g} orbitals ($t_{2g}^{\uparrow:3} t2_g^{\downarrow:\mathbf{0.5}} eg^0$) which are in close separation in the dimers (Ru-Ru ~2.5Å). This interaction is notably different from the previously reported magnetic structure of A = Co^{2+} and Ni^{2+} [181], in which the configuration on Ru^{5+} is $t_{2g}^3 e_g^0$, which would lead to AFM double exchange by the same mechanism. Hence, in general for this series of compounds, one might expect AFM dimer interactions for A^{n+}, $n \leq 2$ and FM for $n \geq 3$.

It is, however, unclear what the exchange pathways for the magnetic interaction between the two dimers might be which facilitate the long range ordering. The general increase in lattice parameters (see Figure 6.10), with increasing A^{3+} radii in the series $In^{3+} < La^{3+}$, does not support super-superexchange (Ru-O-O-Ru') as the dominant ordering mechanism as previously proposed.[169] This is evident as the increase in unit cell volume also implies an increase in Ru-O-O-Ru' distance (where Ru and Ru' are in different dimers). On the other hand, although the Ru-O-A-O-Ru' pathways become longer in absolute terms, relative to the Shannon ionic radii of the A-site $r_{A^{3+}}$, the A-O-Ru distance ($D_{A\text{-}Ru}$) becomes smaller. Hence for A = La, which has the highest T_N, the ratio $D_{A\text{-}Ru} / r_{A^{3+}}$ is the smallest. The near linear positive correlation of $r_{A^{3+}}$ with T_N is strong evidence for the fact that the magnetic interaction between the different Ru_2O_9 dimers is mediated by the A^{3+} site, even when A^{3+} itself is non-magnetic.

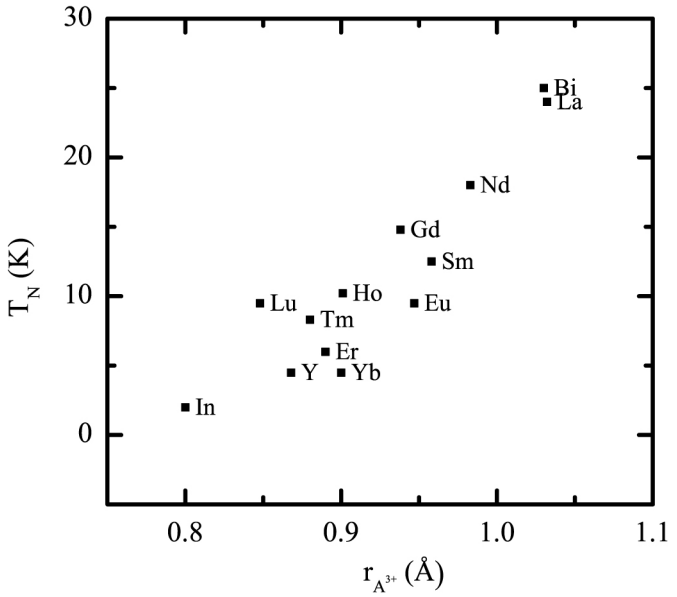

Figure 7.6: The magnetic ordering transition temperature T_N for rare earth RE^{3+} ion,[169] Y^{3+}, In^{3+} (spin glass)[210] and Bi^{3+} which is tentatively assigned from its magnetic heat capacity[196]. The positive trend between ordering temperature (T_N) and ionic radii ($r_{A^{3+}}$), points towards Ru-O-A-O-Ru superexchange being dominant in these systems.

As mentioned before, the Ru_2O_9 when considered as units, form a triangular lattice (Figure 7.7, left). These triangular lattices are stacked in layers along *c*, with their orientation rotated by 180 ° between z = ¼ and z = ¾. In between the layers, the A-site sits at z = ½ as shown in Figure 7.7, right, and it is via this site that superexchange is proposed to occur. The distance ($\mathbf{d}_1$, $\mathbf{d}_2$ and $\mathbf{d}_3$) from the A-site to each vertex of the triangular lattice is indicated in Figure 7.7. In the space group $P6_3/mmc$, where the A-site occupies a Wyckoff position with point symmetry $.\bar{3}m$, $|\mathbf{d}_1| = |\mathbf{d}_2| = |\mathbf{d}_3|$ and hence only three distinct distances for the exchange interaction between Ru_2O_9 dimers must be considered. These are, $J_1 \sim -2\mathbf{d_1} = -2\mathbf{d_2} = -2\mathbf{d_2}$, $J_2 \sim \mathbf{d}_1 - \mathbf{d}_2 = \mathbf{d}_2 - \mathbf{d}_3 = \mathbf{d}_1 - \mathbf{d}_3$ and $J_3 = -\mathbf{d}_2 - \mathbf{d}_3 = -\mathbf{d}_1 - \mathbf{d}_3 = -\mathbf{d}_1 - \mathbf{d}_2$. While it is evident from Figure 7.7 that J_1 is always FM exchange, J_2 and J_3 would be required to describe both FM and AFM interactions, proving that the degeneracy $|\mathbf{d}_1| = |\mathbf{d}_2| = |\mathbf{d}_3|$ must be lifted under the proposed magnetic structure, leading to $|\mathbf{d}_1| = |\mathbf{d}_2| \neq |\mathbf{d}_3|$, $J_1 \sim -2\mathbf{d_1} = -2\mathbf{d_2}$, $J_1' \sim = -2\mathbf{d_3}$, $J_2 \sim \mathbf{d}_1 - \mathbf{d}_2$, AFM: $J'_2 = \mathbf{d}_2 - \mathbf{d}_3 = \mathbf{d}_1 - \mathbf{d}_3$, $J_3 = -\mathbf{d}_1 - \mathbf{d}_2$, $J_3' = -\mathbf{d}_2 - \mathbf{d}_3 = -\mathbf{d}_1 - \mathbf{d}_3$. This results in the lowering of the point group symmetry from $.\bar{3}m$ to no higher than 2/m, which is consistent with the change of Wyckoff symmetry of the A^{3+} from $2b \rightarrow 4b$ as expected for a $P6_3/mmc \rightarrow Cmcm$ phase transition. Low temperature high resolution synchrotron x-ray diffraction data will be required in order to verify this assertion of the orthorhombic nature of the ground state structure of $BaLaRu_2O_9$ and $BaYRu_2O_9$.

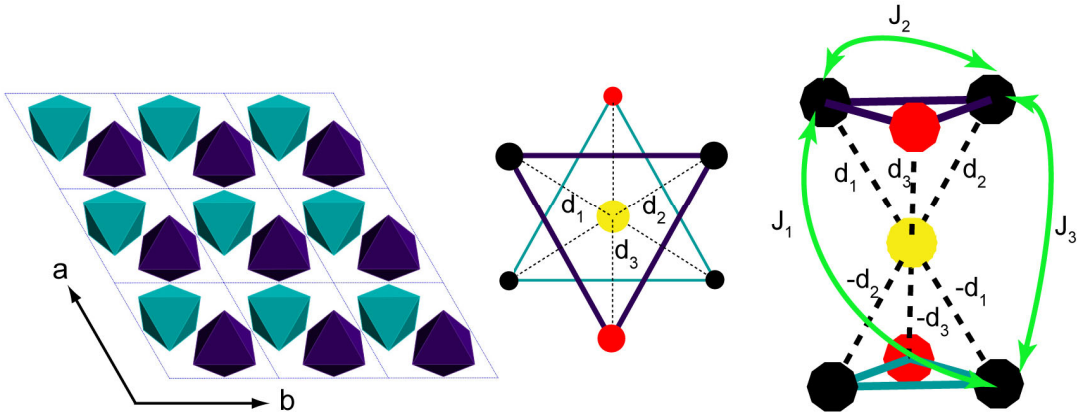

Figure 7.7: The arrangement of the Ru_2O_9 dimers in $Ba_3ARu_2O_9$ into a triangular lattice in the *ab* plane at z = ¼ (light blue) and z = ¾ (dark purple) is shown on the left. On the right, the distance of the vertices of the triangles (the centre of the dimer) at z = ¼ and ¾ are indicated from A^{3+} (yellow) located at z = ½. Spin up and down are represented by back and red colours respectively.

7.3. Magnetic ordering in $Ba_3NdRu_2O_9$

The results relating to the magnetic phase transition in $Ba_3NdRu_2O_9$ will be discussed in this section. The addition of a magnetically active A-site appears to lead to a more complex magnetic ordering. This ordering is shown to be characterised by two distinct magnetic transitions at T_1 = 25 K and T_2 = 18 K. These transitions are shown to be related to the structural phase transition which occurs at much higher temperatures.

7.3.1. Structural phase transition

The prepared sample of A = Nd^{3+} appeared to consist of a single phase which at room temperature was consistent with the previously published structure. [194] Very careful analysis of ID31 data reveals that a small amount of the double perovskite related phase[166] Ba_2NdRuO_6, which has considerable peak overlap with the hexagonal phase, is also present. In Figure 7.8, the impurity phase has been incorporated into the Rietveld refinement fit and its contribution to the overall fit is illustrated on a natural log scale. It is only evident by the shoulders on some peaks. Perovskite phases are known for many A = RE cations[169] and are closely competing with the hexagonal phases.

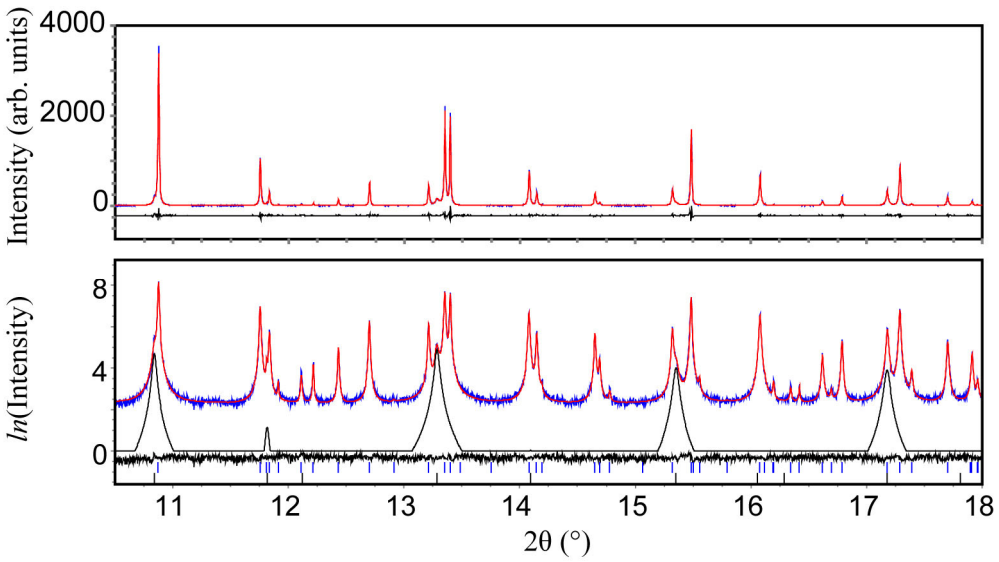

Figure 7.8: Rietveld refinement fits for $Ba_3NdRu_2O_9$ for a portion of the data collected at ID31. In the top panel fits are given on a linear intensity scale, while on the bottom panel, they are plotted on a natural log scale with the contribution from the Ba_2NdRuO_6 impurity (5.8% by weight) plotted above the difference curve. Upper and lower tick marks represent indexation of the main and impurity phase respectively. Rietveld refinement fits with the impurity phase lead to fitting statistic of r_p = 6.29 % and χ^2 = 1.72.

The previously reported phase transition[194] of $Ba_3NdRu_2O_9$ is observed to occur between 90 and 120. The structure refined at 10 K against ID31 data in the C2/c supercell $a \times \sqrt{3}b \times c$ is given in Table 7.3 and is consistent with the previous publication, although one or two oxygen parameters are somewhat outwith their standard errors. Previously unreported anisotropic peak broadening is evident in the powder diffraction profile either side of the transition which has been accounted for satisfactorily by Stephens' anisotropic peak broadening model.[39]

As the anisotropic broadening is present above the transition, initially the refinements were performed in which the monoclinic strain parameters were constrained under hexagonal symmetry leading to a wR_p of 12.43 %, falling to 10.21 %, once the constraints were relaxed for an additional 6 parameters. The end fit of the model to the data is good, as is evident from Figure 7.9. However, the anisotropic peak broadening implementation was less successful for the neutron time of flight data due to added complications arising from peak shape asymmetry, and consequently, structural refinement results are not reported for these data.

	x	y	z
Ba1	0	-0.00162(16)	0.25
Ba2	0.00477(12)	0.33353(15)	0.09885(4)
Nd	0	0	0
Ru	-0.00943(15)	0.3334(2)	0.83514(5)
O1	0	0.5068(15)	0.25
O2	0.2675(17)	0.2406(11)	0.2435(6)
O3	0.0173(18)	0.8233(11)	0.0931(6)
O4	0.2919(18)	0.0919(12)	0.0820(6)
O5	0.7490(18)	0.0895(12)	0.0970(6)

Table 7.3: Rietveld structural refinement model for $Ba_3NdRu_2O_9$ at 10 K in the space group C2/c against high resolution synchrotron diffraction data collected at ID31. Refined cell parameters are a = 5.91869(2) Å, b = 10.24358(4) Å, c = 14.77499(7) Å and β = 90.8633(4) °, B_{iso} for all positions are constrained to be equal and is 0.155(5) Å^2 and R_p = 8.139 % and χ^2 = 2.078. Results are consistent with previously published literature.[194]

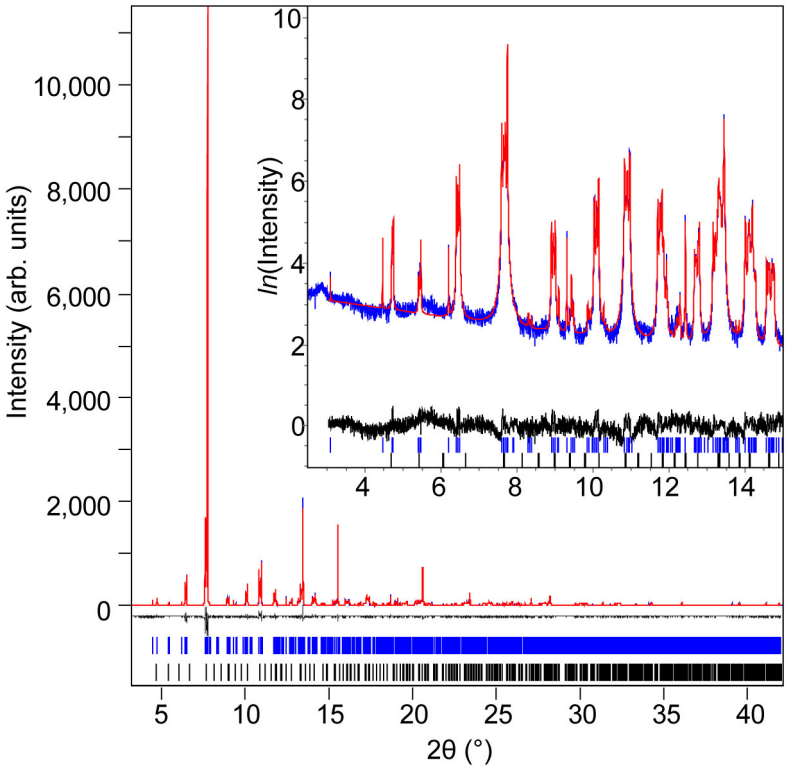

Figure 7.9: Rietveld refinement at 10 K of the C2/c structure of $Ba_3NdRu_2O_9$. In the inset, the fit of the low angle portion of the diffraction pattern is shown on a natural log scale.

The powder diffraction profile published in ref. [194] suggests that this anisotropic broadening may also have been present, and this suggests that it is not just a sample artefact. Figure 7.10 indicates that the phase transition relieves the microstrain. This trend may only be a

correlation of peak broadening with the monoclinic splitting of the hexagonal peaks. However, the lattice parameter trend plotted in Figure 7.11 shows that, at the phase transition, the macrostrain in *a* is relieved by the monoclinic phase transition. It is, therefore, probable that the decrease in microstrain at the transition is related to the phase transition. The thermal expansion of *c* is close to 0 % over the temperature range for which data was collected (Figure 7.11), with a slight cusp at the $P6_3/mmc \rightarrow C2/c$ phase transition, and an upturn towards 0 K.

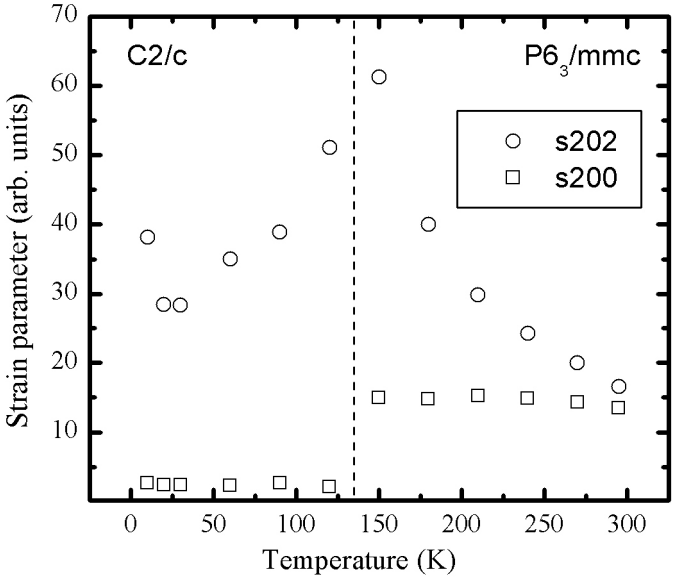

Figure 7.10: Anisotropic strain parameter for $Ba_3NdRu_2O_9$ extracted from Rietveld refinements against ID31 data.

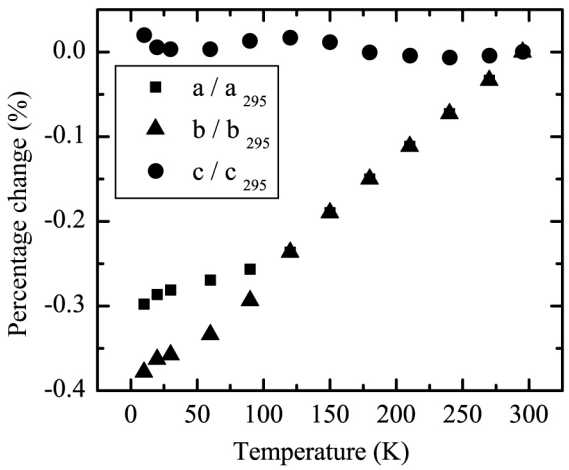

Figure 7.11: Lattice parameter trends for $Ba_3NdRu_2O_9$ extracted from Rietveld refinements against ID31 data.

7.3.2. Magnetic ordering

A ferromagnetic transition, at T_1 = 25 K was observed as previously reported.[194] Magnetic diffraction (Figure 7.12) was observed at 20 K that indexed on a (0 0 0) propagation vector of the C2/c cell. This was fitted by Rietveld refinement (Figure 7.13) by a ferromagnetic order of Nd^{3+} moments parallel to *c* (Figure 7.14), corresponding to the Ψ3 (Γ2) basis for (0 0 0) order in Table 7.4. The refined magnitude of 1.56(7) μ_B at 20 K is consistent with a previously published result obtained from neutron powder diffraction,[194] and with the observed saturated magnetisation of 1.4 μ_B / formula unit (Figure 7.16). No direct evidence for simultaneous ordering of Ru moments is observed, although this is known in materials such as the double perovskite $Ba_2NdRu_2O_6$. Fits to the data show that any ferromagnetically ordered Ru component has a magnitude < 0.4 μ_B.

Below 18 K, additional magnetic peaks characterised by two propagation vectors appear (T_2, Figure 7.13). The (0 0 1) peak, which is systematically absent in the nuclear scattering, evidences a further (0 0 0) antiferromagnetic Nd spin component. This has a refined magnitude 0.5(1) μ_B at 1.6 K and can be modelled in the *a* or *b* directions of the Nd^{3+} moments. However, canting parallel to b is most likely as this is described by the $\Psi_2(\Gamma_2)$ basis vector belonging to the same representation as the ferromagnetic $\Psi_3(\Gamma_2)$ Nd spin component (Table 7.4). The magnetic Bragg peaks (½ 1 2), (½ 1 1) and (½ 1 0) (Figure 7.12) belong to the propagation vector (½ 0 0). Symmetry analysis of the space group C2/c under this propagation vector is summarised in Table 7.4 for the Ru sublattice. The analysis implies that Ru is split into two sites through the loss of the (-x, y, -z+ ½) operator which is responsible for rendering the two Ru sites within a dimer equivalent. The limited data available meant that it was not possible to consider these two orbits independently and only models with either parallel or anti-parallel constraints on the moments of these sites were considered. A model with parallel Ru-moment constraints (Figure 7.14), which transforms under Γ_1 of Table 7.4 was found to give the best fit when considering the possible ireps. of the space group C2/c under the propagation vector (½ 0 0). However, there are still some discrepancies in the fitted intensities, and a more extensive set of magnetic diffraction data would be needed to determine the full spin ordered structure.

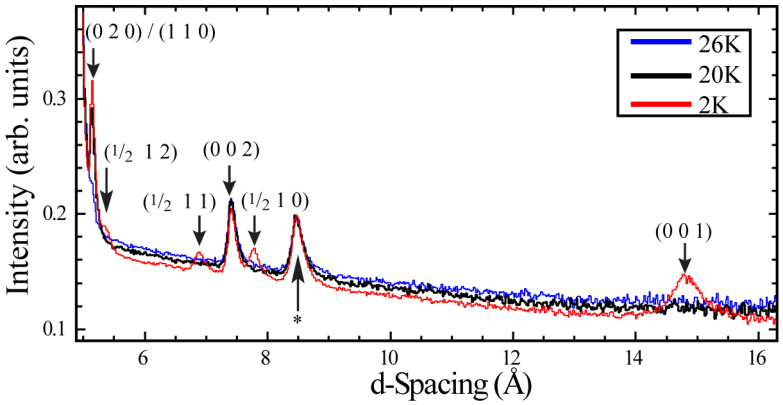

Figure 7.12: Evolution of magnetic peaks in $Ba_3NdRu_2O_9$ for data collected in the forward scattering bank of WISH. A peak from the magnetic ordering of the impurity phase (Ba_2NdRuO_6) is indicated by an asterisk (*).

Ired. Reps.	Basis vectors	Ru(x, y, z) / Ru(-x, y, -z+ ½) / Nd(x, y, z)			Ru(x, -y, z + ½) / Ru(-x, -y, -z) / Nd(-x, y, -z+ ½)		
		m_x	m_y	m_z	m_x	m_y	m_z
Γ_1	Ψ_1	1	0	0	-1	0	0
	Ψ_2	0	1	0	0	1	0
	Ψ_3	0	0	1	0	0	-1
Γ_2	Ψ_1	1	0	0	1	0	0
	Ψ_2	0	1	0	0	-1	0
	Ψ_3	0	0	1	0	0	1

Table 7.4: Basis vectors of the space group C2/c for site Ru (8f) under propagation vectors k = (½ 0 0) and for Nd (4a) under k = (0 0 0). Ru (8f) is split such that its moments are independent into Ru1 (0.994, 0.332, 0.836)[194] and Ru2 (0.006, 0.332, 0.664) through the loss of the (-x, y, -z+ ½) operator while Nd is described by one site (0, 0, 0). Γ_2 depicts the Nd FM ordering and canting under propagation vector k = (0 0 0) and Γ_1 describes the magnetic ordering of the Ru sublattice under propagation vector k = (½ 0 0) as shown in (Figure 7.14).

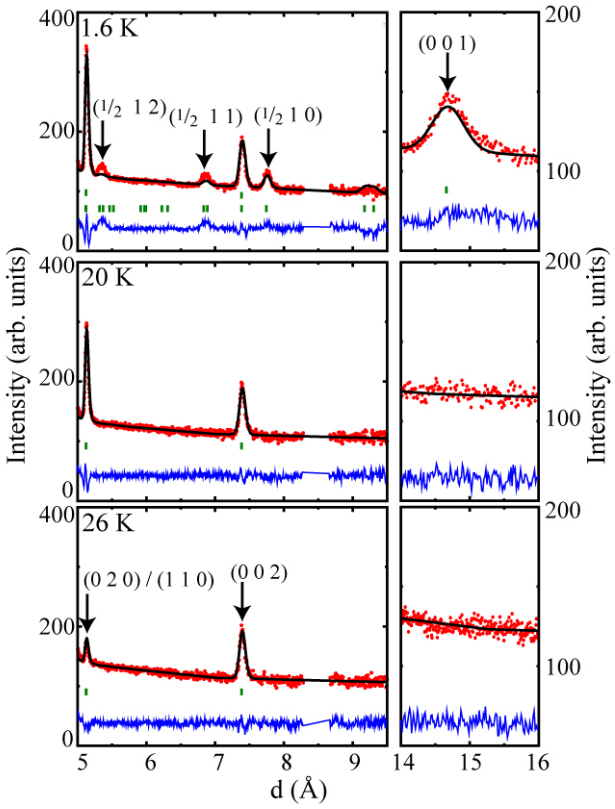

Figure 7.13: Rietveld refinement fits of the two distinct magnetic phases at 20 and 1.6 K, performed against the 38 ° and 58 ° scattering banks of WISH, ISIS.

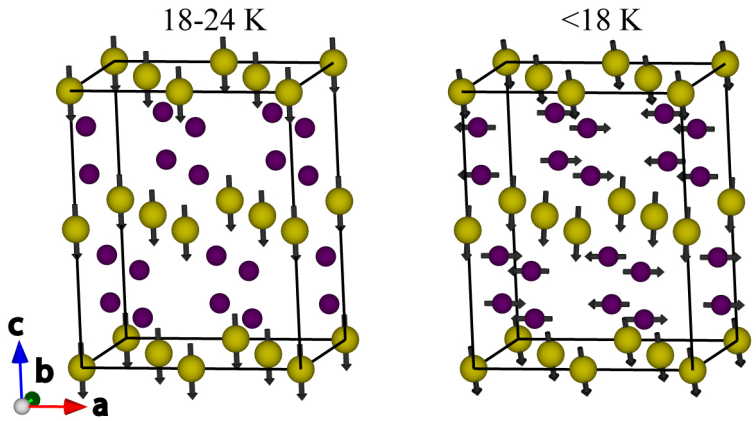

Figure 7.14: Proposed magnetic structure for the two distinct ordering temperatures of $Ba_3NdRu_2O_9$.

The evolution of three magnetic components is shown in Figure 7.15. The FM ordering of Nd with basis vector $m_z(0\ 0\ 0)$ ($\Psi_3(\Gamma_2)$) can clearly be seen to preempt either the AFM canting of the Nd moments ($m_y(0\ 0\ 0)$, $\Psi_2(\Gamma_2)$) or the AFM ordering ($m_x(½\ 0\ 0)$, $\Psi_1(\Gamma1)$) of the FM coupled Ru dimers which appear both to be concomitant (T_2). The concomitant ordering of $\Psi_2(\Gamma_2)$ with $\Psi_1(\Gamma_1)$ which belong to the k = (0 0 0) and (½ 0 0) respectively,

implies that the two basis sets may not be considered independently and doubling of the Γ point is expected at T_2.

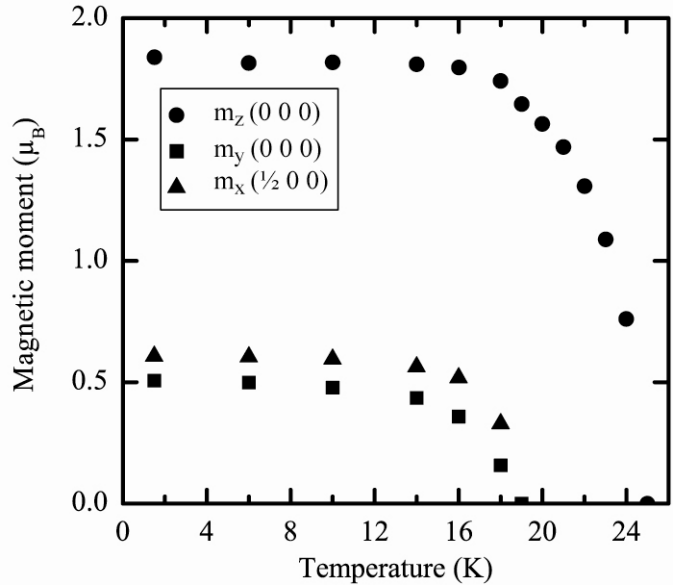

Figure 7.15: Evolution with temperature of the basis vectors that describe the magnetic structures of $Ba_3NdRu_2O_9$. The basis vector m_z(0 0 0) and m_y(0 0 0) describe the ordering of the magnetic moments of Nd, m_x(½ 0 0) describes the ordering of the moments on Ru. At 1.6 K, m_z(0 0 0) = 1.8(1) μ_B, m_y(0 0 0) = 0.5(1) μ_B = m_x(½ 0 0) = 0.6(1).

Magnetic hysteresis loops are shown in Figure 7.16. At 20 K there is no hysteresis evident and the saturated moment (1.4 μ_B / f.u.) at 3 T is in good agreement with that refined against the neutron powder diffraction data. At 15 K the hysteresis loops start to open up and the saturation magnetic moment seems somewhat higher (1.6 μ_B / f.u.). At 2 K the hysteresis loop is now opened and the saturation moment (1.4 μ_B) is lower than at 15 K and about equal to that at 20 K. The slope of the saturated region is also somewhat shallower than at 15 or 20 K indicating that AFM interactions are stronger at this temperature. There appears to be a step at about third the magnetisation (0.4 μ_B).

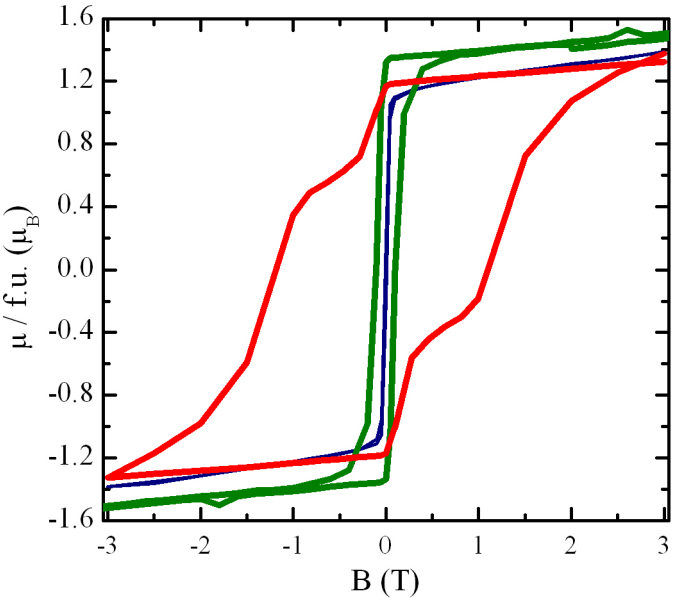

Figure 7.16: Magnetic hysteresis loops for $Ba_3NdRu_2O_9$ collected at 20 K (blue), 15 K (green) and 2 K (red).

Two possible explanations for this behaviour are as follows. At 2 K only the Nd^{3+} moment contributes to that observed moment at saturation. At 15 K two explanations present themselves:

i) AFM canted moment of Nd^{3+} $m_y(0\ 0\ 0)$ becomes FM, with only a small applied field. The resultant of the saturated $m_z(0\ 0\ 0)$ moment at 20K with the refined $m_y(0\ 0\ 0)$ moment is $\sqrt{(1.2^2 + 0.6^2)} = 1.34$ μB, in good agreement with the increased saturated moment of Figure 7.16.

ii) FM ordering of Ru $m_x(\ ½\ 0\ 0)$ under field, adding to Nd $m_z(0\ 0\ 0)$ moment: $\sqrt{(1.2^2 + 0.5^2 + 0.5^2)} = 1.39$ μB).

Neutron diffraction at field would be required in order to see which peaks were suppressed in order to decide between case (i) and (ii). At 2 K the behaviour of the hysteresis could be explained:

i) As field is reversed beyond a certain value, initially, AFM canting of Nd^{3+} $m_y(0\ 0\ 0)$ component is aligned with the field . This would explain the step of about 0.6 μ_B at 0.5 T. As the field is increased further, the $m_z(0\ 0\ 0)$ component is aligned with the field but remains frustrated with $m_y(0\ 0\ 0)$ explaining the net reduction of moment observed 15 → 2 K.

ii) As the field is reversed beyond a certain value, initially, AFM interactions of Ru $m_x(½\ 0\ 0)$ are broken, giving a net moment. As field is increased further, the $m_z(0\ 0\ 0)$ moments align with field but are frustrated with $m_x(½\ 0\ 0)$ and so the net moment observed is reduced with respect to the 15 K loop.

Figure 7.17 shows the anisotropic thermal expansion which occurs between 2 and 30 K coincident with the magnetic transitions, which are evidenced by a decrease in paramagnetic scattering (T_1) and the evolution of (½ 1 0) peak (T_2). T_1 appears to exert a magnetostrictive force which leads to an expansion along *c* and compression in the *ac* plane. The induced strain is relieved by T_2, presumably by the AFM canting (m_y(0 0 0)) of the Nd. This also suggests that the canting of the Nd drives the magnetic ordering of the Ru sub-lattice.

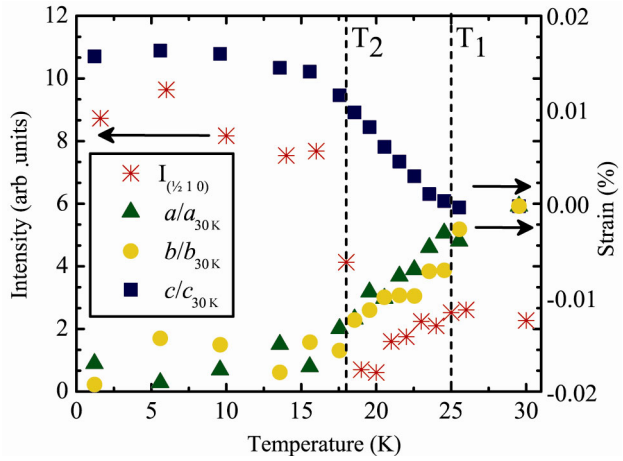

Figure 7.17: Evolution with temperature of the integrated area (I) under the AFM peak (½ 1 0), and the strain along the lattice parameter directions expressed as a percentage of their 30 K values.

It can often be instructive to plot the strain along the principal axis (X) of the strain tensor. In Figure 7.18, the strain tensor has been diagonalised with respect to the linear region 18 - 26 K. The strain along the orthogonal principal axis is revealed to be much more pronounced than that along the unit cell directions of Figure 7.17. While *b* falls along one of the principal strain axes (X_2), X_1 and X_3 both lie in *ac* plane, and the magnitudes of their strain are over twice that in *a* or *c*. The relationship between the principal axes and the structure is indicated in the inset of Figure 7.18. X_1 appears to act to close the monoclinic angle, which in the temperature range prior to the magnetic transitions (120 – 30 K) increases steadily up to a maximum (~ 90.9 °) just above T_1. This suggests that whatever is driving the $P6_3/mmc \rightarrow C2/c$ phase transition at 110 K is not related to the magnetic ordering transitions, and in fact the process appears to be reversed just before T_1. The strain along the principal axes as plotted reveals a discontinuity in X_1 and X_3 at T_2 pointing towards a first order structural phase transition accompanying the magnetic ordering at T_2. This is consistent with the above observations made from Figure 7.15 that the simultaneous ordering of magnetic components with propagation vector k = (0 0 0) and (½ 0 0) implies that they order under the

same irep.[211]. Hence the true Γ point must contain both of these propagation vectors implying that the parent symmetry has a subtle structural distortion with a supercell of 2**a** × **b** × **c** with respects to the monoclinic cell.

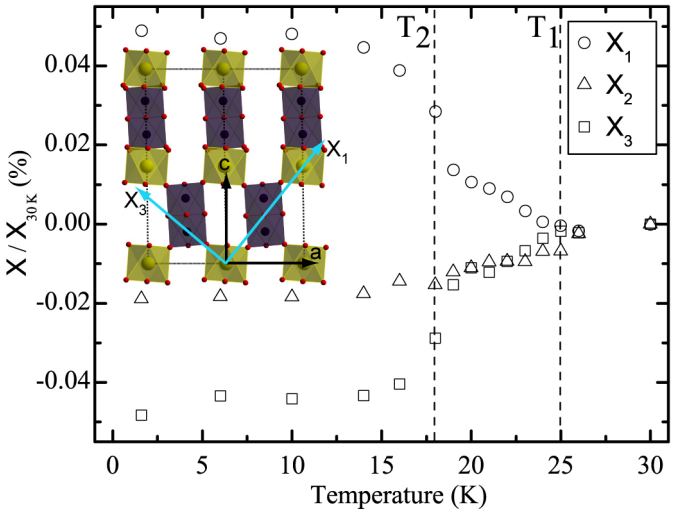

Figure 7.18: The strain along the principal axes of $Ba_3NdRu_2O_9$. The orthogonal principal axes were calculated in the program PASCAL[38] from the refined cell parameters (in the temperature range 18 – 26 K) as $X_1 = 0.895a + 0.446c$, $X_2 = b$, $X_3 = -0.952a + 0.305c$, with respect to the monoclinic C2/c cell, and are illustrated for X_1 and X_3 in the inset.

7.3.3. Crystal field effects

It is curious why of A = RE^{3+}, A = Nd^{3+} is the only $Ba_3ARu_2O_9$ derivative to undergo a phase transition. In A = Sr^{2+} [178] the space group at room temperature is the same as that of the low temperature phase of A = Nd^{3+}, but here it is clearly due to size effect of the A cation, with the Shannon ionic radii of Sr being 1.18 Å, far in excess of that of Nd (0.983 Å) [212]. This implies that the structural phase transition should be due to some electronic or magnetic ordering which differs to that occurring in the rest of the A = RE^{3+} series. Long range magnetic interactions are suggested from Section 7.3.2 not to be responsible for the phase transition. Therefore, here, the idea of the crystal field of Nd^{3+} $4f^3$ being responsible for the $P6_3/mmc \rightarrow C2/c$ phase transition is investigated.

Distortion mode analysis of the C2/c space group was made with respect to $P6_3/mmc$ using ISODISPLACE,[33] and the various OPD along with their corresponding kernels and SOP are listed in Table 7.5. Refinements of the distortion mode amplitudes against ID31 data have been performed across the whole measured temperature range in Topas.[35] The evolution of

the modes with temperature is plotted in Figure 7.19. All the modes are refined freely across the phase transition, giving an indication of the limit of the resolution of the experiment.

OPD	Kernel	SOP
$\Gamma_{1+}(a)$	$P6_3/mmc$	-
$\Gamma_{4+}(a)$	$P\bar{3}_1c$	Γ_{1+}
$\Gamma_{5+}(a,0)$	Cmcm	Γ_{1+}
$\Gamma_{6+}(a,0)$	C2/c	Γ_{1+}, Γ_{4+}, Γ_{5+}

Table 7.5: The distortion mode analysis of P63/mmc with respect to C2/c symmetry. The space groups for which the OPD form POP (the Kernels) are shown. The SOPs implied by the POP are listed.

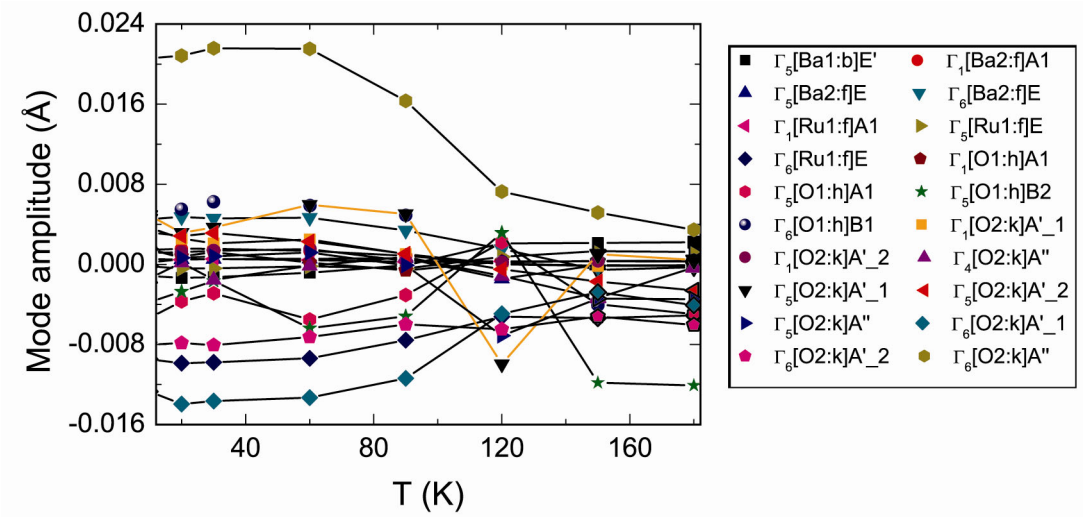

Figure 7.19: Evolution of all 20 distortions modes of $Ba_3NdRu_2O_9$ derived from the phase transition $P6_3/mmc \rightarrow C2/c$, as a function of temperature.

All of the distortion modes have rather modest amplitudes with none greater than 0.024 Å, and the vast majority not being < 0.006 Å and therefore not significantly above zero. In Figure 7.20, the magnitudes of the distortion modes are plotted in a histogram, revealing that all those with significant amplitude belong to the Γ_{6+} OPD, which is the POP for C2/c. All of the SOPs have very small magnitudes. The most active mode belongs to the oxygen atom (O2) in octahedral coordination with Nd^{3+}. Another three modes have significant amplitudes, and two of these also belong to O2, while the third belongs to Ru.

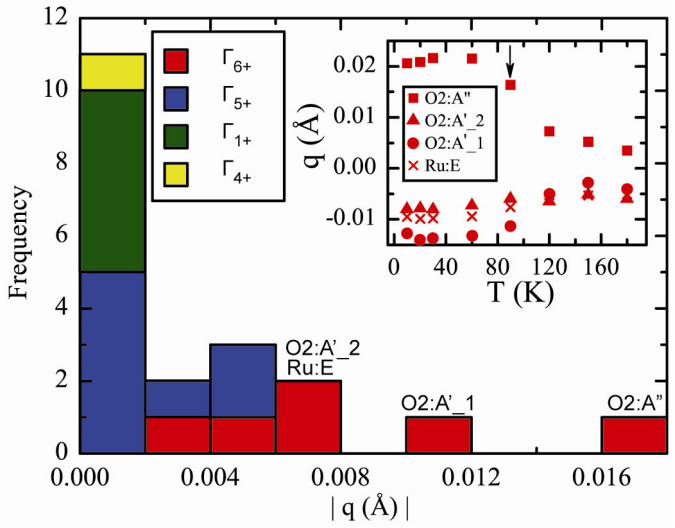

Figure 7.20: Histogram of the distortion mode amplitudes from Rietveld refinements performed at 90 K. In the inset, the evolution of the four modes with the largest amplitude as a function of temperature is shown.

To investigate if the behaviour of these Γ_{6+} modes is significant with respect to the refinement, refinements were performed in which mode magnitudes below a certain threshold ($|q| < x$) were set and constrained to zero. Refinements were performed starting first at low values of x using a previously converged model at 10 K. The results are illustrated in Figure 7.21, left, which show a large jump for x = 0.008 to 0.01 Å corresponding to the exclusion of the Γ_{6+}Ru:E mode which corresponds to a change in wR_p ~1.2 %. At x = 0.008 only four modes are refined. The addition of the extra 16 modes, corresponding to the unconstrained refinement, reduce the wR_p only by a further ~ 1.1%.

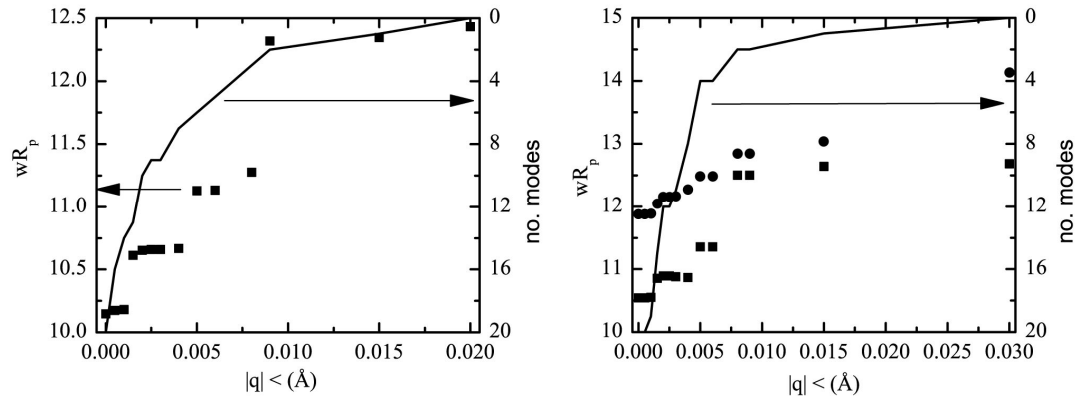

Figure 7.21: Fitting statistics for refinements against ID31 (left, squares) and combined refinements against ID31 and WISH data (right, squares and circles respectively), as a function of the amplitude under which modes are constrained to be zero ($|q| <$). The line indicates the number of modes included in the refinement at each $|q| <$.

The oxygen Γ_{6+} modes have a relatively small effect on the diffraction profile despite having the largest amplitudes. To verify their significance a combined ID31 and WISH refinement

was performed for each |q| < x (Figure 7.21, right). Although the anisotropic broadening is not modelled very satisfactorily in the TOF data, combined refinements reproduce results obtained from using ID31 data only. The jump in wR_p for the exclusion of the Γ_{6+}O2:A" mode in the neutron fit, is almost an order of magnitude larger than that observed for any prior exclusion demonstration that the Γ_{6+}O2:A" mode amplitude is significant and should be viewed as the primary order parameter for the phase transition.

The Γ_{6+}O2:A" mode is visualised in Figure 7.22 with respect to its Nd^{3+} coordination, where the mode amplitude has been multiplied by 1, 5 and 10 to exaggerate its effect. It is evident that the Nd^{3+} has a local point group symmetry of 2/m with respect to this mode rather than $\bar{1}$ implied by the C2/c symmetry. Four of the Nd – O distances are 2.276 Å while two are 2.278 Å. This rather modest difference varies steeply with the multiplier of the order parameter, such that the difference between the bond distances is 0.146 Å with a multiplier of 10, illustrating that the local Nd^{3+} environment is very sensitive to the magnitude of this mode. The fact that the pseudo symmetry about Nd^{3+} with respect to its O coordination is higher than that required by the space group suggests that local ordering effects may be driving the phase transition. In the case of Nd^{3+}, the obvious candidate for this is its Kramer's doublet ground state.

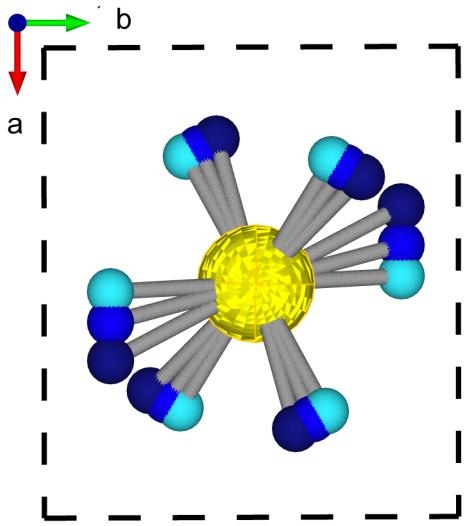

Figure 7.22: The coordination environment around Nd^{3+} at 90 K for a structure considering only the most active Γ_{6+} mode when it has been multiplied by 1 (cyan), 5 (blue) and 10 (dark blue). The elongation and contraction of the bond is evident as a function of the multiplier. The unit cell is drawn in the range, x = ¼ - ¾ , y = ¼ - ¾ and z = ¼ - ¾. Only Nd and O2 atoms are shown.

It is evident from Figure 7.23 that the increase of the beta angle follows the same trend as the Γ_{6+}O2:A" distortion mode (Figure 7.20, inset). It is reasonable to suppose that its down-turn below 30 K (Figure 7.23, inset), is related to a decrease in the Γ_{6+}O2:A" mode amplitude and hence the crystal field effect of Nd^{3+}. The down-turn in the beta angle is coincident with the FM ordering transition T_1 at 26 K. The down-turn in the beta angle could hence be linked to reduced single-ion effects of Nd^{3+} as a result of the Zeeman splitting of the Kramer's doublet by the FM locally ordered moments. It is noteworthy that the A = Nd^{3+} is the only A = RE for which a structural phase transition is observed and the only derivative for which FM ordering occurs. It is proposed that the FM ordering is a result of the C2/c structure favouring the appropriate exchange interactions, but that the FM ordering itself acts to destroy the doublet ground state of Nd^{3+}, and hence acts against the $P6_3/mmc \rightarrow C2/c$ phase transition. This would provide an explanation for the AFM canting of Nd^{3+} at T_2 which occurs in response to the reduction of the beta angle and the Γ_{6+}O2:A" order parameter (and a return to the exchange interaction present in the hexagonal phase). The canting of Nd^{3+} moments introduces AFM interactions along *c* (Figure 7.14) which is consistent with magnetic structures observed in $Ba_3TbRu_2O_9$ [204] and those proposed for the A = RE^{3+} series,[169] suggesting that these are the exchange interactions favoured in the hexagonal phase.

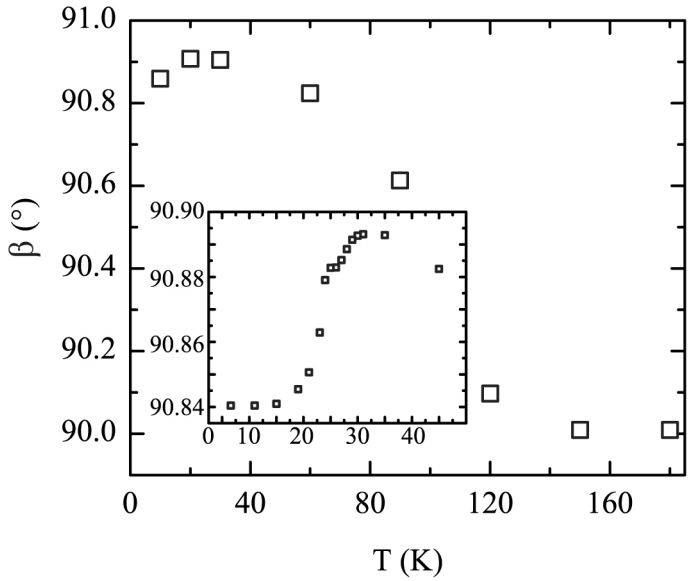

Figure 7.23: The evolution of the beta angle as a function of temperature for the C2/c phase of $Ba_3NdRu_2O_9$. Values are extracted from Rietveld refinement against ID31 data. The inset shows the beta angle taken from refinements against WISH data. The beta angle is clearly coupled to the Γ_{6+}O2:A" distortion mode which acts as a POP and is coupled to the crystal field effect.

7.4. S = 0 ground state in $Ba_3CaRu_2O_9$

In this section the magnetic ordering of $Ba_3CaRu_2O_9$ is investigated. In this compound, the oxidation state of Ru is 5+ (t_{2g}^3) rather than 4.5+ for A = La^{3+}, Y^{3+} and Nd^{3+}. It is found that no long range magnetic ordering occurs down to 1.6 K. The decrease observed in paramagnetic scattering without magnetic ordering is consistent with a S = 0 ground state formation of the Ru_2O_9 dimer contrary to the short range ordering proposed from previously reported susceptibility measurements.[174]

The background scattering in $Ba_3CaRu_2O_9$ from the WISH experiments appears to behave in a curious way. Normally, total scattering is expected to be conserved in a neutron powder diffraction experiment – incoherent paramagnetic scattering will be converted to an equal amount of coherent Bragg scattering at the magnetic ordering temperature. In Figure 7.24, the background is observed to decrease dramatically with temperature, but no magnetic ordering is observed out to a d-spacing of 40 Å. The explanation for this lies in the formation of Ru_2O_9 singlet states which have no net paramagnetic moment, and hence no long range order.

Despite this explanation of the dimer ordering which should only affect the background scattering of the neutron diffraction experiment, it was not possible to achieve satisfactory Rietveld fits to either the WISH data or the synchrotron x-ray diffraction (Spring 8) data at low temperatures. Many peak intensities appear to be systematically wrong at low temperatures, but no peak splitting is evident (Figure 7.25, upper). Although not as pronounced as for A = Nd^{3+}, it appears that this systematic failure to fit the peak intensities can be accounted for by an anisotropic broadening model. The Rietveld fit implementing just a single Lorentzian (isotropic) strain broadening parameter was poor (R_{wp} = 4.208, χ^2 = 3.194), while that using Stephen's anisotropic peak broadening model[39] was very good (R_{wp} = 2.111, χ^2 = 1.603, for an additional two parameters) as evident in Figure 7.25.

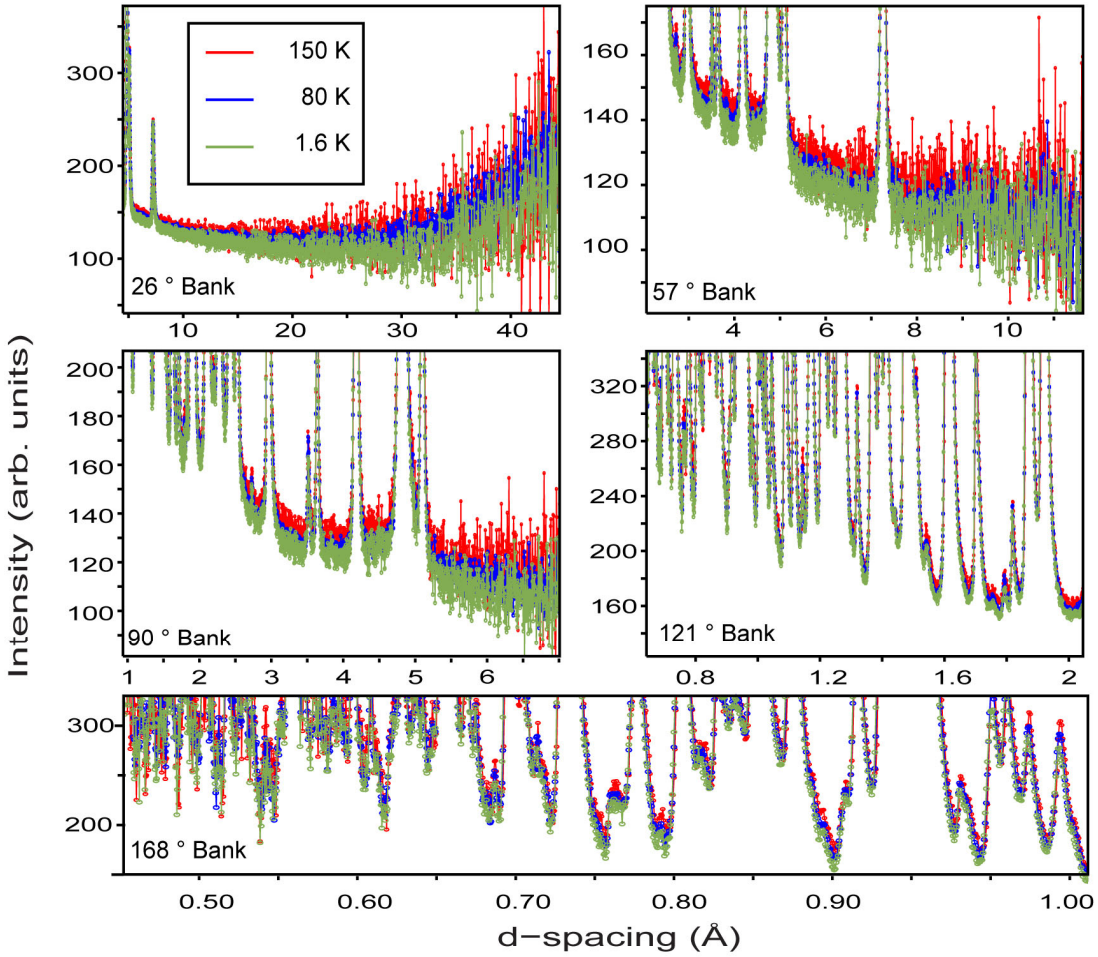

Figure 7.24: The decrease in paramagnetic background scattering in all five detector banks of WISH for $Ba_3CaRu_2O_9$ at 150, 80 and 1.6 K.

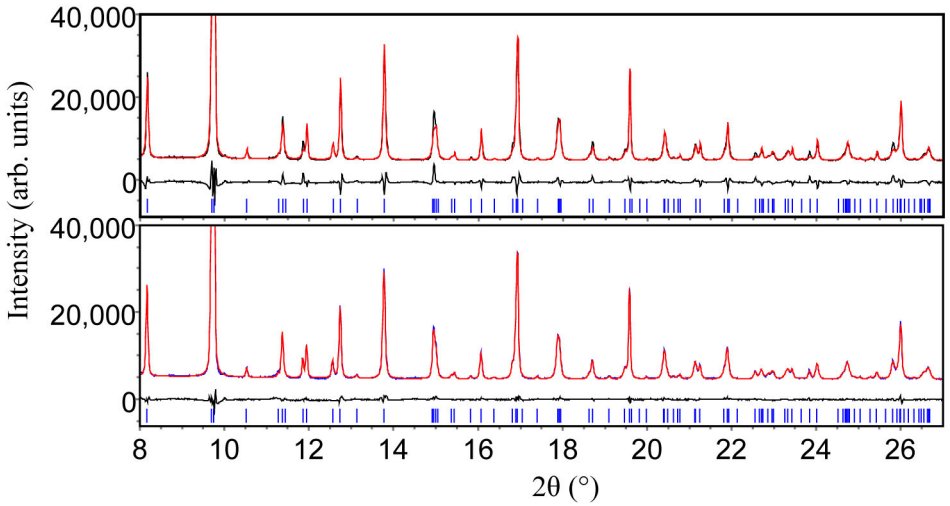

Figure 7.25: Rietveld refinement fits to Spring-8 data with isotropic strain broadening (top) and anisotropic strain broadening (bottom) models.

It is unclear what the origin of this anisotropic microstrain is, but it seems plausible that it is related to the S=0 ground state formation. It does not appear to originate from any macrostrain of the unit cell parameters (Figure 7.26). The thermal compression is almost perfectly isotropic over the temperature range 120 – 300 K as evident from the Spring 8 data, whereas the anisotropic microstrain evidenced by peak broadening of Figure 7.27, has a large S202 component which evolves rapidly with cooling. This is similar to the behaviour of the S202 strain parameter for A = Nd, where the microstrain is relieved by the structural phase transition. However, in A = Ca it does not appear that the microstrain occurs as a result any structural change.

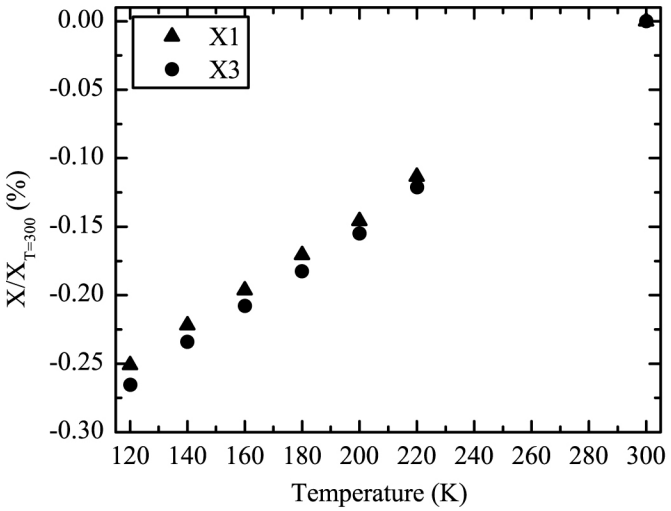

Figure 7.26: Evolution of the principal strain axis of $BaCaRu_2O_9$ as a function of temperature where, X1 = $\sqrt{2}a$ - $\sqrt{2}b$, X2 = -$\sqrt{2}a$ -$\sqrt{2}b$, X3 = c.

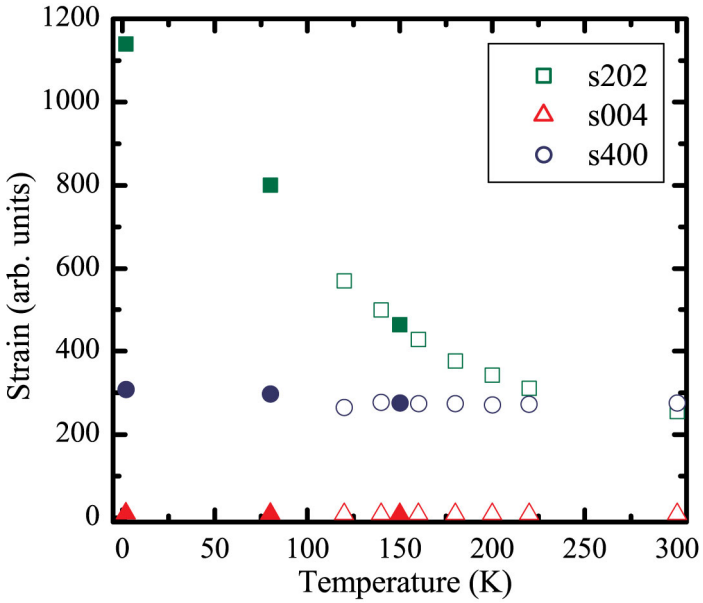

Figure 7.27: Evolution of anisotropic microstrain parameters for $Ba_3CaRu_2O_9$ as a function of temperature. Closed and open symbols are values taken from refinements against neutron and x-ray refinements respectively. Values of microstrain from the neutron data are normalised at 150 K against values from x-ray diffraction data.

To investigate the anisotropic microstrain further, the structural parameters obtained from the refinement at each temperature were examined. The formation of a spin singlet S= 0 state of the Ru_2O_9 dimers should manifest itself in some change in the crystal structure. In Figure 7.28, left, it is evident that there is no anomalous behaviour in the *a* or *c* lattice parameters or in the volume. Figure 7.28, right, plots on the same temperature scale *a* / *c* and $D_{(Ru\text{-}Ru)}$ / *c*. The apparent link between these two measures of internal strain was established in Section 6.4. Values obtained from refinements against neutron and x-ray data are distinguished with closed and open symbols respectively. There is a curious discrepancy between values obtained from neutron and x-ray diffraction data which is rather reminiscent of the charge melting phase transition observed for $Ba_3NaRu_2O_9$ in Section 6.3. In light of the reasonable unit cell volume / temperature trend in Figure 7.28, left, failure of the cryogenics in either neutron or x-ray experiments may be ruled out. Additionally, given that both *a* / *c* and $D_{(Ru\text{-}Ru)}$ / *c* are self-normalising the results reported here are not just an artefact of an error in absolute scaling between values measured by the neutron and x-ray powder diffraction. Despite these discrepancies which should have an intrinsic origin it is clearly evident that $D_{(Ru\text{-}Ru)}$ / *c* decreases rapidly with temperature, with a discontinuity ~ 150 K. The opposite trend is observed for *a*/*c* with temperature, indicating that the shortening of the $D_{(Ru\text{-}Ru)}$ from 2.655 Å at 300 K to 2.596 Å at 1.6 K is achieved by a cooperative effect between the lattice (a shortening of *c* with respect to *a*) and the internal degrees of freedom. This is the reverse picture observed for the trend in the $Ba_3ARu_2O_9$ series (Section 6.4)

where the internal degrees of freedom act to avoid the compression of $D_{(Ru\text{-}Ru)}$ implied by the contraction of the unit cell volume.

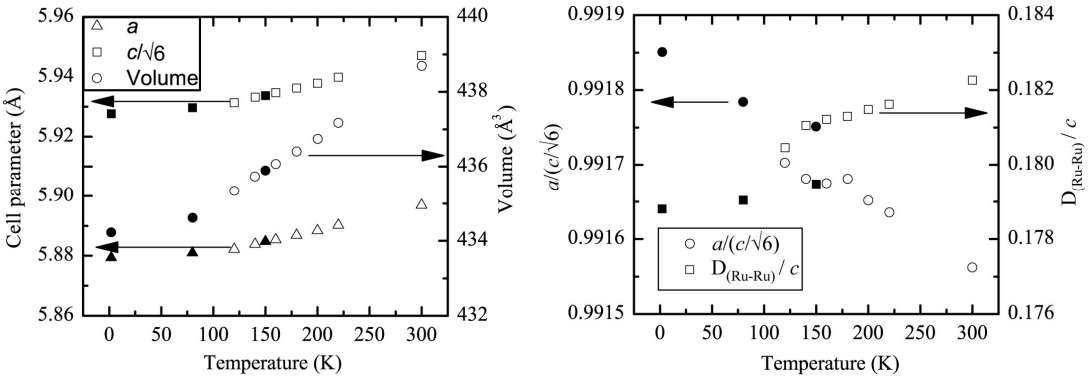

Figure 7.28: Left, cell parameter trends with temperature. Right, a / (c/√6) and $D_{(Ru\text{-}Ru)}$ / c variation with temperature. Closed and open symbols are for neutron and x-ray data respectively.

As the driving force for the change in structure (or at least the change in $D_{(Ru\text{-}Ru)}$) is facilitated by the decrease in entropy of the system on cooling, it is expected that the lattice and internal degrees of freedom should cooperate with each other in the present case of $Ba_3CaRu_2O_9$. This cooperative nature is reinforced in Figure 7.29, left which shows the good negative correlation of a / c and $D_{(Ru\text{-}Ru)}$ / c. Figure 7.29, right illustrates that there is a link between this internal macrostrain and the microstrain which result in the peak broadening.

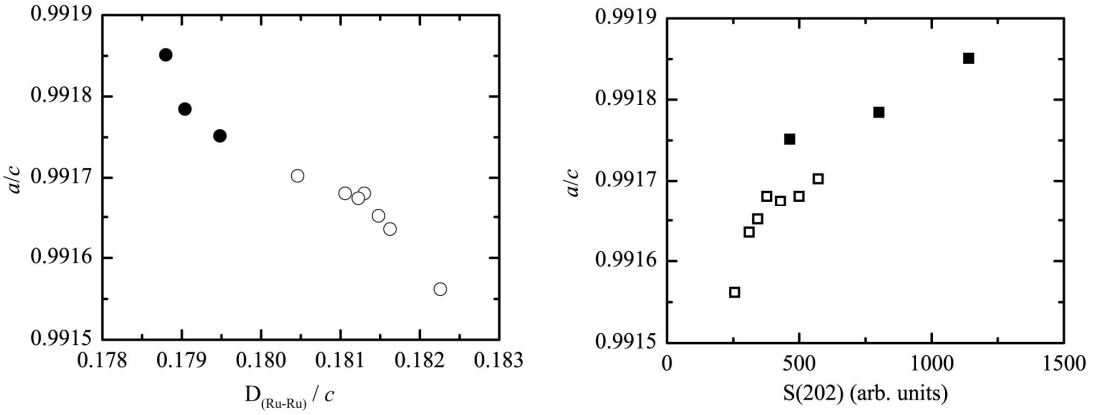

Figure 7.29: Left, the correlation between a/c and $D_{(Ru\text{-}Ru)}$ / c. Right, trend between anisotropic micro strain parameter S202 and macro a/c strain.

The above observations are consistent with the decrease of the magnetic susceptibility towards zero at base temperatures observed in ref. [174]. However, here the authors, without the benefit of neutron diffraction data, ascribe this effect to short range Heisenberg type

AFM exchange interaction within the dimers. This, however, would not lead to a net reduction of the paramagnetic moment and so can be ruled out as being the dominant process. In Figure 7.30, the magnetic susceptibility for $Ba_3CaRu_2O_9$ measured in this current work has been fitted with a simple Curie-Weiss law which is attenuated by an exponential:

$$\chi = \frac{C}{T-\theta} \times \exp(-T_D/T)$$

where T_D is the Boltzmann temperature for the dimerisation and all other parameters are as defined normally for the Curie-Weiss law. In the fit of Figure 7.30, the Curie constant C has been fixed to 2.78 emu T mol^{-1} corresponding to the expected μ_{eff} for two S = 1.5 Ru^{5+} ions. The refined values from the least square fit are θ = -398(6) K and T_D = 316(3) K are reasonable in light of the strong AFM interaction expected between the Ru ions within the dimers and the temperature range in which the dimerisation appears to occur.

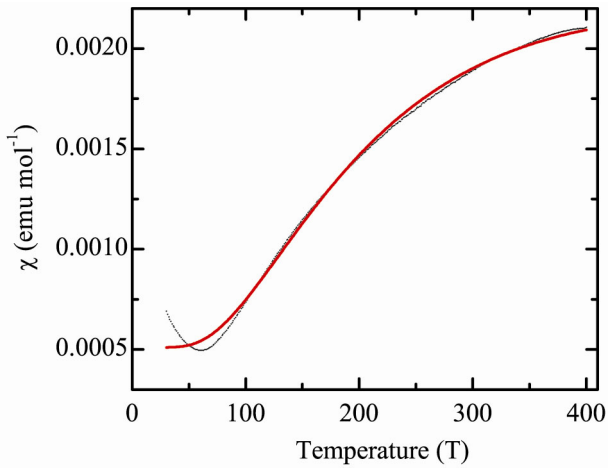

Figure 7.30: Magnetic susceptibility versus temperature for A = Ca, with a Curie-Weiss fit attenuated by an exponential (solid red line).

In summary, the diffraction data provide two clear signatures of S = 0 formation of Ru_2O_9: a substantial decrease in paramagnetic scattering; and a decrease in $D_{(Ru\text{-}Ru)}$ with temperature beyond that expected from the thermal contraction of the lattice, which is contrary to the Volume versus $D_{(Ru\text{-}Ru)}$ / *c* trend observed across the $Ba_3ARu_2O_9$ series in see Section 6.4. The contraction of the $D_{(Ru\text{-}Ru)}$ appears to induces macrostrain of *a*/*c* which causes anisotropic peak broadening due to the ensuing microstrain. The magnetic susceptibility may be modelled by a paramagnetic moment diminishing with temperature, in accordance with Boltzmann statistics. This fit to the data is consistent with the S = 0 ground state formation of Ru_2O_9 dimers proposed here.

7.5. Conclusion

It has been shown in this section that $Ba_3ARu_2O_9$ (A = Y, La) undergo AFM ordering transitions below 26 K. The magnetic ordering implies that the ground state structures should have a space ground no higher than Cmcm. The breaking of the hexagonal symmetry has remained unobserved by high resolution neutron powder diffraction down to 2 K. The magnetic structures reveal that the exchange mechanism within the Ru_2O_9 dimers must be due to FM double exchange of the minority spin of the partial field t_{2g} orbitals ($t_{2g}^{\uparrow:3} t_{2g}^{\downarrow:0.5} eg^0$). Long range AFM ordering has been shown to be correlated with the ionic radii of A^{3+}, and superexchange A–O–Ru pathways are suggested as being responsible for the long range magnetic ordering.

In A = Nd the phase transition occurring at 90 – 120 K is shown to be driven by the crystal field effect of the Nd^{3+}. The FM ordering transition (T_1) at 25 K which results in an ordering of Nd moments, appears to result in a reduction of this effect, and the lattice responds by attempting to regain hexagonal symmetry. The return towards metric hexagonal symmetry appears to favour an AFM interaction resulting in a canting of the Nd moments at T_2 which is accompanied by an AFM ordering of Ru moments. The character and ordering temperature of these interactions at T_2 are in line with what is expected of the rest of the A = RE^{3+} series, suggesting that the crystal field effects of Nd^{3+} have become less pronounced.

Singlet ground state formation of the Ru_2O_9 dimers has been observed in $Ba_3CaRu_2O_9$ as evident from the neutron powder diffraction. This is accompanied by a significant decrease in $D_{Ru\text{-}Ru}$ resulting in an increase in microstrain. Magnetic susceptibility measurements support the S=0 ground state formation.

8. Conclusions and further work

Two different types of highly constrained systems have been examined in this thesis, Fe_3O_4 which have FeO_6 octahedra which are in infinite edge-sharing chains, and the 6H-perovskites system $Ba_3ARu_2O_9$ which have RuO_6 octahedra in face-sharing (Ru_2O_9) dimers which are separated by corner-sharing AO_6 octahedra.

In Fe_3O_4 the low temperature Verwey structure has been solved and shown to be charge ordered to a useful first approximation. However, the close proximity of Fe centres means that complete charge ordering is not realised, and instead the minority spin is delocalised over three sites (trimeron) with its wave function centred on a Fe state with formal 2+ valence. Trimerons explain the rather continuous distribution of valence states which has caused much controversy, in particular in the interpretation of resonant x-ray scattering result.[113-116] Trimerons also explain the large off-centre distortions observe in the Verwey structure which account for its acentricity and ferroelectricity. No normal mode(s) of the lattice appear(s) to act as an order parameter for the transition, and it is likely that the trimeron is the local order parameter. Diffuse scattering observed above the transition could hence be a result of dynamic trimeron fluctuations, which would explain the lower than expected change in entropy at the transition.

NMR results[109] show that there is some rearrangement of the structure in the region 120 – 90 K, and further single crystal diffraction studies should involve studying the structure at temperatures immediately below the temperature. Modelling of the diffuse scattering above T_v would also give insight as to whether the trimerons are the true order parameter for the transition.

The electronic structure calculations present here have been performed on the experimental coordinates only, and although the partial forces calculated from the electronic structure are small indicating that the experimental structure is close to equilibrium, it would nevertheless be insightful to perform a structure optimisation to verify that the proposed structure is stable under the DFT+U approximation. This may help to resolve some discrepancy between the experimental structure and previously published optimisations.[124, 125]

$Ba_3ARu_2O_9$ shows a host of different ordering phenomena. Tuning the charge of A and hence the oxidation state of $Ru^{n+}{}_2O_9$ changes the magnetic exchange interactions within the dimers from AFM for $n \geq 5$ to FM for $n \leq 4.5$. Charge ordering observed for A = Na, n =5.5 is suppressed in n = 4.5 and also appears to be very sensitive to the nature of the exchange paths between the dimers. Further work should involve extending the investigation in n to n = 4 for A = Ce^{4+} and Pr^{4+}. Anion doping (N^{3-} or F^- for O^{2-}) should also provide further means to extend the series allowing for a more systematic study of the effect of Ru oxidation state on magnetic exchange and charge ordering phenomena. The empirical trends derived for the $Ba_3ARu_2O_9$ series of compounds should aid to target the search for new $Ba_3AB_2O_9$ compounds which are thermodynamically feasible and are likely to exhibit interesting phenomena such as charge ordering.

For $Ba_3NdRu_2O_9$ the step in the hysteresis loop at 2 K at ~ 0.5 T should be investigated. In light of the complex magnetic ordering, and the spin reorientation observed at 18 K in this compound, it is likely that this step is also related to a spin reorientation transition. In situ magnetic field neutron powder diffraction studies should help to resolve the nature of this transition.

Overarching conclusion in both of these systems are that single ion effects resulting in charge and orbital ordering are not the sole driving force for the observed transitions, but instead it is more insightful to think of ordered units, or molecules within the crystal structure. For Fe_3O_4 these are three site units with a wave function which share a single electron across three sites. For $Ba_3NaRu_2O_9$ it is the ordering of Ru_2O_9 dimers which stabilises the unusual charge ordering of the 4d transition metal.

Experimentally it has been shown that the use of high resolution powder diffraction data coupled with single crystal diffraction is a very powerful method for accurate structure determination in materials which undergo a phase transition. The prior method enables the correct unit cell and symmetry to be determined so that the twinning may be correctly modelled in the latter. Careful analysis of both micro and macrostrain derived from Rietveld refinements has also been shown to be very valuable in identifying transitions and trends. Even background scattering has been shown to give valuable information about the electronic state in $Ba_3CaRu_2O_9$.

Bibliography

1 E. Wigner, Trans. Faraday Soc. **34**, 678 (1938).
2 E. J. W. Verwey, Nature **144**, 327 (1939).
3 D. E. Cox and A. W. Sleight, Acta Crystallogr., Sect. B: Struct. Sci. **35**, 1 (1979).
4 I. Yamada, et al., Angewandte Chemie International Edition **47**, 7032 (2008).
5 J. P. Attfield, Solid State Sci. **8**, 861 (2006).
6 K. E. Stitzer, M. D. Smith, W. R. Gemmill, and H. C. zur Loye, J. Am. Chem. Soc. **124**, 13877 (2002).
7 A. J. Williams and J. P. Attfield, Phys. Rev. B **66**, 220405 (2002).
8 A. J. Williams and J. P. Attfield, Phys. Rev. B **72**, 024436 (2005).
9 P. Karen, P. M. Woodward, J. Linden, T. Vogt, A. Studer, and P. Fischer, Phys. Rev. B **64** (2001).
10 T. Vogt, P. M. Woodward, P. Karen, B. A. Hunter, P. Henning, and A. R. Moodenbaugh, Phys. Rev. Lett. **84**, 2969 (2000).
11 E. Castillo-Martinez, A. J. Williams, and J. P. Attfield, J. Solid State Chem. **179**, 3505 (2006).
12 H. Sawa, et al., J. Phys. Soc. Jpn. **71**, 385 (2002).
13 J. Paul Attfield, J. F. Clarke, and D. A. Perkins, Physica B **180-181**, 581 (1992).
14 M. Angst, et al., Phys. Rev. Lett. **99**, 086403 (2007).
15 S. R. Bland, et al., Phys. Rev. B **82**, 115110 (2010).
16 Y. Yamada, S. Nohdo, and N. Ikeda, J. Phys. Soc. Jpn. **66**, 3733 (1997).
17 Y. Yamada, K. Kitsuda, S. Nohdo, and N. Ikeda, Phys. Rev. B **62**, 12167 (2000).
18 Y. Zhang, et al., Phys. Rev. B **76**, 184105 (2007).
19 N. Ikeda, et al., Nature **436**, 1136 (2005).
20 M. Angst, et al., Phys. Rev. Lett. **101**, 227601 (2008).
21 H. A. Jahn and E. Teller, Proc. R. Soc. Lond. A **161**, 220 (1937).
22 S. Blundell, *Magnetism in Condensed Matter* (Oxford University Press, Oxford, 2001).
23 R. L. Carlin, *Magnetochemsitry* (Springer-Verlag, Berlin, 1986).
24 J. B. Goodenough, Phys. Rev. **100**, 564 (1955).
25 J. B. Goodenough and A. L. Loeb, Phys. Rev. **98**, 391 (1955).
26 C. Hammmond, *The Basics of Crystallography and Diffraction* (Oxford University Press, Oxford, 2001).
27 http://reference.iucr.org/dictionary/Neumann's_principle.
28 M. T. Dove, *Structure and Dynamics, An atomic view of materials* (Oxford University Press, Oxford, 2003).
29 P. G. Radaelli, *Magnetic Structure Determination from Neutron Powder Diffraction Data* (Notes from course given at Consener's House, Abingdon, 2002).
30 D. Khomskii, Physics **2**, 20 (2009).
31 A. Wills, J. Phys. IV **11**, 133 (2001).
32 J. Rodriguez-Carvajal, Physica B **55**, 192 (1993).
33 B. J. Campbell, H. T. Stokes, D. E. Tanner, and D. M. Hatch, J. Appl. Crystallogr. **39**, 607 (2006).
34 S. Kerman, B. J. Campbell, K. K. Satyavarapu, H. T. Stokes, F. Perselli, and J. S. O. Evans, Acta Crystallogr., Sect. A **68**, 222 (2012).
35 Topas v3.0: General Profile and Structure Analysis Software for Powder
36 A. J. Balke, et al., *Crystal Structure Analysis Principles and Practice* (Oxford Science Publications, Oxford, 2009).

[37] J. Schlessman and D. B. Litvin, Acta Crystallogr., Sect. A **51**, 947 (1995).
[38] M. J. Cliffe and A. L. Goodwin, J. Appl. Crystallogr. **45**, 1321 (2012).
[39] P. W. Stephens, J. Appl. Crystallogr. **32**, 281 (1999).
[40] C. Giacovazzo, et al., *Fundamentals of Crystallography* (IUCr, Oxford University Press, Oxford, 1992).
[41] V. F. Sears, Neutron News **3**, 26 (1992).
[42] R. J. Harrison, Rev. Mineral. Geochem. **63**, 113 (2006).
[43] T. Hahn, *International Tables for Crystallography* (Kluwer Academic Publishers, Dordrecht, 2002).
[44] H. M. Rietveld, J. Appl. Crystallogr. **2**, 65 (1969).
[45] R. A. Young, *The Rietveld Method* (Oxford University Press, Oxford, 1995).
[46] L. Pauling, J. Am. Chem. Soc. **69**, 542 (1947).
[47] N. E. Brese and M. O'Keeffe, Acta Crystallogr., Sect. B: Struct. Sci. **47**, 192 (1991).
[48] http://www.isis.stfc.ac.uk/instruments/wish/wish-6465.html.
[49] http://www.isis.stfc.ac.uk/instruments/hrpd/.
[50] http://www.esrf.eu/UsersAndScience/Experiments/StructMaterials/ID11.
[51] http://www.esrf.eu/UsersAndScience/Experiments/StructMaterials/ID31.
[52] http://www.spring8.or.jp/wkg/BL19B2/instrument/lang-en/INS-0000000300.
[53] S. Cottenier, *Density Functional Theory and the family of (L)APW-methods: a step-by-step introduction* (Instituut voor Kern- en Stralingsfysica, K.U.Leuven, Belgium, 2002).
[54] M. Born and R. Oppenheimer, Ann. Phys.-Berlin **84**, 0457 (1927).
[55] P. Hohenberg and W. Kohn, Phys. Rev. B **136**, B864 (1964).
[56] W. Kohn and L. J. Sham, Phys. Rev. **140**, 1133 (1965).
[57] J. P. Perdew, K. Burke, and M. Ernzerhof, Phys. Rev. Lett. **77**, 3865 (1996).
[58] P. A. Cox, *Transition Metal Oxides* (Clarendon Press, Oxford, 1992).
[59] R. M. Martin, *Electronic Structure: Basic Theory and Practical Methods* (Cambridge University Press, 2004).
[60] W. H. Bragg, Nature **95**, 561 (1915).
[61] D. Jarosch, Mineral. Petrol. **37**, 15 (1987).
[62] W. L. Roth, J. Phys. Chem. Solids **25**, 1 (1964).
[63] S. Diaz, S. de Brion, M. Holzapfel, G. Chouteau, and P. Strobel, Physica B **346**, 146 (2004).
[64] L. Ortega-San-Martin, A. J. Williams, C. D. Gordon, S. Klemme, and J. P. Attfield, J. Phys.: Condens. Matter **20**, 104238 (2008).
[65] O. Tchernyshyov, R. Moessner, and S. L. Sondhi, Phys. Rev. B **66**, 064403 (2002).
[66] P. G. Radaelli, New Journal of Physics **7**, 53 (2005).
[67] M. Schmidt, W. Ratcliff, P. G. Radaelli, K. Refson, N. M. Harrison, and S. W. Cheong, Phys. Rev. Lett. **92**, 056402 (2004).
[68] J. Rodriguez-Carvajal, G. Rousse, C. Masquelier, and M. Hervieu, Phys. Rev. Lett. **81**, 4660 (1998).
[69] M. Reehuis, A. Krimmel, N. Buttgen, A. Loidl, and A. Prokofiev, European Physical Journal B **35**, 311 (2003).
[70] S. H. Lee, et al., Phys. Rev. Lett. **93**, 156407 (2004).
[71] S. H. Baek, et al., Phys. Rev. B **80**, 140406 (2009).
[72] S. Sarkar, T. Maitra, R. Valenti, and T. Saha-Dasgupta, Phys. Rev. Lett. **102**, 216405 (2009).
[73] H. Mamiya, M. Onoda, T. Furubayashi, J. Tang, and I. Nakatani, J. Appl. Phys. **81**, 5289 (1997).
[74] E. M. Wheeler, et al., Phys. Rev. B **82**, 140406 (2010).
[75] K. Matsuno, et al., J. Phys. Soc. Jpn. **70**, 1456 (2001).
[76] Y. Horibe, et al., Phys. Rev. Lett. **96**, 086406 (2006).

77 K. Matsuda, N. Furukawa, and Y. Motome, J. Phys. Soc. Jpn. **75**, 124716 (2006).
78 P. G. Radaelli, et al., Nature **416**, 155 (2002).
79 http://galileoandeinstein.physics.virginia.edu/more_stuff/E&M_Hist.html.
80 W. Gilbert, *De Magnete* (Dover (reprint), London, 1600).
81 L. Neel, Annales De Physique **3**, 137 (1948).
82 C. G. Shull, E. O. Wollan, and W. C. Koehler, Phys. Rev. **84**, 912 (1951).
83 G. S. Parks and K. K. Kelley, J. Phys. Chem. **30**, 47 (1926).
84 H. B. Bull, B. S. Ellefson, and N. W. Taylor, J. Phys. Chem. **38**, 401 (1934).
85 E. J. W. Verwey and J. H. De Boer, Recueil Des Travaux Chimiques Des Pays-Bas **55**, 531 (1936).
86 E. J. Verwey, P. W. Haayman, and F. C. Romeijn, J. Chem. Phys. **15**, 181 (1947).
87 N. C. Tombs and H. P. Rooksby, Acta Crystallogr. **4**, 474 (1951).
88 S. C. Abrahams and B. A. Calhoun, Acta Crystallogr. **6**, 105 (1953).
89 W. C. Hamilton, Phys. Rev. **110**, 1050 (1958).
90 S. C. Abrahams and B. A. Calhoun, Acta Crystallogr. **8**, 257 (1955).
91 E. J. Samuelse, E. J. Bleeker, L. Dobrzyns, and T. Riste, J. Appl. Phys. **39**, 1114 (1968).
92 G. Shirane, S. Chikazumi, J. Akimitsu, K. Chiba, M. Matsui, and Y. Fujii, J. Phys. Soc. Jpn. **39**, 949 (1975).
93 J. Yoshida and S. Iida, J. Phys. Soc. Jpn. **42**, 230 (1977).
94 M. Iizumi, T. F. Koetzle, G. Shirane, S. Chikazumi, M. Matsui, and S. Todo, Acta Crystallogr., Sect. B: Struct. Sci. **38**, 2121 (1982).
95 J. P. Wright, J. P. Attfield, and P. G. Radaelli, Phys. Rev. Lett. **87**, 266401 (2001).
96 J. P. Wright, J. P. Attfield, and P. G. Radaelli, Phys. Rev. B **66**, 214422 (2002).
97 C. Medrano, M. Schlenker, J. Baruchel, J. Espeso, and Y. Miyamoto, Phys. Rev. B **59**, 1185 (1999).
98 Y. Miyamoto and M. Shindo, J. Phys. Soc. Jpn. **62**, 1423 (1993).
99 R. J. Goff, J. P. Wright, J. P. Attfield, and P. G. Radaelli, J. Phys.: Condens. Matter **17**, 7633 (2005).
100 J. M. Zuo, J. C. H. Spence, and W. Petuskey, Phys. Rev. B **42**, 8451 (1990).
101 L. V. Gasparov, D. B. Tanner, D. B. Romero, H. Berger, G. Margaritondo, and L. Forro, Phys. Rev. B **62**, 7939 (2000).
102 A. Pimenov, et al., Phys. Rev. B **72**, 035131 (2005).
103 D. Schrupp, et al., Europhys. Lett. **70**, 789 (2005).
104 L. V. Gasparov, A. Rush, G. Guntherodt, and H. Berger, Phys. Rev. B **79**, 144303 (2009).
105 H. Magnan, et al., Phys. Rev. B **81**, 085121 (2010).
106 P. Kuiper, B. G. Searle, L. C. Duda, R. M. Wolf, and P. J. vanderZaag, J. Electron Spectrosc. Relat. Phenom. **86**, 107 (1997).
107 J. Garcia, et al., Phys. Rev. Lett. **85**, 578 (2000).
108 G. Subias, J. Garcia, and J. Blasco, Phys. Rev. B **71**, 155103 (2005).
109 P. Novak, H. Stepankova, J. Englich, J. Kohout, and V. A. M. Brabers, Phys. Rev. B **61**, 1256 (2000).
110 M. Mizoguchi, J. Phys. Soc. Jpn. **70**, 2333 (2001).
111 M. Bimbi, G. Allodi, R. De Renzi, C. Mazzoli, and H. Berger, Phys. Rev. B **77**, 045115 (2008).
112 J. Stankowski, W. Kempinski, S. Los, W. Bednarski, S. Waplak, and R. Micnas, J. Magn. Magn. Mater. **301**, 88 (2006).
113 S. R. Bland, et al., J. Phys.: Condens. Matter **21**, 485601 (2009).
114 J. E. Lorenzo, et al., Phys. Rev. Lett. **101**, 226401 (2008).
115 J. Schlappa, et al., Phys. Rev. Lett. **100**, 026406 (2008).

116 Y. Joly, J. E. Lorenzo, E. Nazarenko, J. L. Hodeau, D. Mannix, and C. Marin, Phys. Rev. B **78**, 134110 (2008).

117 J. Blasco, J. Garcia, and G. Subias, Phys. Rev. B **83**, 104105 (2011).

118 V. I. Anisimov, I. S. Elfimov, N. Hamada, and K. Terakura, Phys. Rev. B **54**, 4387 (1996).

119 V. N. Antonov, B. N. Harmon, V. P. Antropov, A. Y. Perlov, and A. N. Yaresko, Phys. Rev. B **64**, 134410 (2001).

120 G. K. H. Madsen and P. Novak, Europhys. Lett. **69**, 777 (2005).

121 Z. Szotek, W. M. Temmerman, A. Svane, L. Petit, G. M. Stocks, and H. Winter, Phys. Rev. B **68**, 054415 (2003).

122 H. T. Jeng, G. Y. Guo, and D. J. Huang, Phys. Rev. Lett. **93**, 156403 (2004).

123 I. Leonov, A. N. Yaresko, V. N. Antonov, M. A. Korotin, and V. I. Anisimov, Phys. Rev. Lett. **93**, 146404 (2004).

124 H. T. Jeng, G. Y. Guo, and D. J. Huang, Phys. Rev. B **74**, 195115 (2006).

125 K. Yamauchi, T. Fukushima, and S. Picozzi, Phys. Rev. B **79**, 212404 (2009).

126 J. P. Wright, A. M. T. Bell, and J. P. Attfield, Solid State Sci. **2**, 747 (2000).

127 R. B. V. Dreele, M. R. Suchomel, and B. H. Toby, (Argonne National Laboratory, U.S. Department of Energy), 2010).

128 http://sourceforge.net/apps/trac/fable/wiki/imaged11.

129 L. P. Bouckaert, R. Smoluchowski, and E. Wigner, Phys. Rev. **50**, 58 (1936).

130 SAINT, (Bruker AXS Inc., Madison, Wisconsin,USA, 1998).

131 (Bruker, SADABS, Bruker AXS Inc, Madison, Wisconsin, USA, 2001).

132 http://www.hwi.buffalo.edu/SnB/DREARhelp/DREARdocs/sortav.use.

133 P. W. Betteridge, J. R. Carruthers, R. I. Cooper, K. Prout, and D. J. Watkin, J. Appl. Cryst. **36**, 1487 (2003).

134 R. I. Cooper, R. O. Gould, S. Parsons, and D. J. Watkin, J. Appl. Crystallogr. **35**, 168 (2002).

135 G. Wu, B. L. Rodrigues, and P. Coppens, J. Appl. Crystallogr. **35**, 356 (2002).

136 G. M. Sheldrick, Acta Crystallogr., Sect. A **64**, 112 (2008).

137 W. C. Hamilton, Acta Crystallogr. **18**, 502 (1965).

138 http://home.comcast.net/~sharov/PopEcol/tables/f0001.html.

139 T. A. O'Brien, F. Bridges, L. Downward, J. F. Mitchell, and H. Zheng, Phys. Rev. B **75**, 064417 (2007).

140 M. Alexe, et al., Adv. Mater. (Weinheim, Ger.) **21**, 4452 (2009).

141 J. van den Brink and D. I. Khomskii, J. Phys.: Condens. Matter **20**, 434217 (2008).

142 N. A. Spaldin, J. Solid State Chem. **195**, 2 (2012).

143 J. P. Shepherd, J. W. Koenitzer, R. AragÃ³n, C. J. Sandberg, and J. M. Honig, Phys. Rev. B **31**, 1107 (1985).

144 P. W. Anderson, Phys. Rev. **102**, 1008 (1956).

145 T. Fukushima, K. Yamauchi, and S. Picozzi, J. Phys. Soc. Jpn. **80**, 014709 (2011).

146 P. Blaha, K. Schwarz, G. K. H. Madsen, D. Kvasnicka, and J. Luitz, Wien2k, An Augmented Plane Wave + Local Orbitals Program for Calculating Crystal Properties (K. Schwarz, Techn. Universit¨at Wien, Austria, 2001).

147 V. I. Anisimov, I. V. Solovyev, M. A. Korotin, M. T. Czyzyk, and G. A. Sawatzky, Phys. Rev. B **48**, 16929 (1993).

148 K. Momma and F. Izumi, J. Appl. Crystallogr. **44**, 1272 (2011).

149 R. H. Mitchell, *Perovskites, Modern and Ancient* (Almaz Press, Thunder Bay, 2002).

150 J. J. Randall and R. Ward, J. Am. Chem. Soc. **81**, 2629 (1959).

151 J. A. Kafalas and J. M. Longo, Mater. Res. Bull. **5**, 193 (1970).

152 R. Greatrex, G. Hu, and D. C. Munro, Mater. Res. Bull. **21**, 797 (1986).

153 V. M. Goldschmidt, Naturwissenschaften **14**, 1477 (1926).

154 C. Q. Jin, et al., Proc. Natl. Acad. Sci. U. S. A. **105**, 7115 (2008).

[155] S.-T. Hong and A. W. Sleight, J. Solid State Chem. **128**, 251 (1997).
[156] R. J. Bouchard and J. L. Gillson, Mater. Res. Bull. **7**, 873 (1972).
[157] Mazin, II and D. J. Singh, Phys. Rev. B **56**, 2556 (1997).
[158] J. G. Zhao, et al., J. Solid State Chem. **180**, 2816 (2007).
[159] J. M. Longo, P. M. Raccah, and J. B. Goodenough, J. Appl. Phys. **39**, 1327 (1968).
[160] S. A. J. Kimber, et al., Phys. Rev. Lett. **102** (2009).
[161] J. G. Cheng, J. S. Zhou, and J. B. Goodenough, Phys. Rev. B **80** (2009).
[162] H. Nakatsugawa, E. Iguchi, and Y. Oohara, J. Phys.: Condens. Matter **14**, 415 (2002).
[163] Y. Doi and Y. Hinatsu, J. Phys.: Condens. Matter **11**, 4813 (1999).
[164] P. D. Battle, Mater. Res. Bull. **16**, 397 (1981).
[165] Y. Izumiyama, Y. Doi, M. Wakeshima, Y. Hinatsu, Y. Shimojo, and Y. Morii, J. Phys.: Condens. Matter **13**, 1303 (2001).
[166] Y. Izumiyama, et al., J. Mater. Chem. **10**, 2364 (2000).
[167] P. D. Battle and C. W. Jones, J. Solid State Chem. **78**, 108 (1989).
[168] Y. Izumiyama, Y. Doi, M. Wakeshima, Y. Hinatsu, A. Nakamura, and Y. Ishii, J. Solid State Chem. **169**, 125 (2002).
[169] Y. Hinatsu and Y. Doi, Bull. Chem. Soc. Jpn. **76**, 1093 (2003).
[170] J. T. Rijssenbeek, T. Saito, S. Malo, A. T. Masaki, M. Takano, and K. R. Poeppelmeier, J. Am. Chem. Soc. **127**, 675 (2005).
[171] K. J. Range and A. Atzesdorfer, Z. Naturforsch., B: Chem. Sci. **48**, 237 (1993).
[172] S.-J. Kim, M. D. Smith, J. Darriet, and H.-C. zur Loye, J. Solid State Chem. **177**, 1493 (2004).
[173] K. E. Stitzer, et al., Inorg. Chem. **42**, 947 (2003).
[174] J. Darriet, M. Drillon, G. Villeneuve, and P. Hagenmuller, J. Solid State Chem. **19**, 213 (1976).
[175] T. Sakamoto, Y. Doi, and Y. Hinatsu, J. Solid State Chem. **179**, 2595 (2006).
[176] U. Treiber and S. Kemmler-Sack, Z. Anorg. Allg. Chem. **487**, 161 (1982).
[177] B. Rowda, M. Avdeev, P. L. Lee, P. F. Henry, and C. D. Ling, Acta Crystallographica Section B **64**, 154 (2008).
[178] H. W. Zandbergen and D. J. W. Ijdo, Acta Crystallogr., Sect. C: Cryst. Struct. Commun. **40**, 919 (1984).
[179] D. Verdoes, H. W. Zandbergen, and D. J. W. Ijdo, Acta Crystallogr., Sect. C: Cryst. Struct. Commun. **41**, 170 (1985).
[180] J. T. Rijssenbeek, Q. Huang, R. W. Erwin, H. W. Zandbergen, and R. J. Cava, J. Solid State Chem. **146**, 65 (1999).
[181] P. Lightfoot and P. D. Battle, J. Solid State Chem. **89**, 174 (1990).
[182] Y. S. Doi, Y. Hinatsu, and K. Ohoyama, J. Phys.: Condens. Matter **16**, 8923 (2004).
[183] A. J. Jacobson and A. J. Calvert, J. inorg. nucl. Chem. **40**, 447 (1978).
[184] P. Køuhl, Z. Anorg. Allg. Chem. **442**, 280 (1978).
[185] B. Schüpp-Niewa, L. Shlyk, Y. Prots, R. Niewa, and G. Krabbes, Z. Anorg. Allg. Chem. **632**, 572 (2006).
[186] M. Shikano, O. Ishiyama, Y. Inaguma, T. Nakamura, and M. Itoh, J. Solid State Chem. **120**, 238 (1995).
[187] F. Seveque, P. Delamoye, P. Poix, and A. Michel, C. R. l'Academie. Sci., Ser. C **269**, 1536 (1969).
[188] D. Harari, P. Poix, and J. C. Bernier, Journal of Solid State Chemistry **11**, 330 (1974).
[189] J. Darriet, R. Bontchev, C. Dussarrat, F. Weill, and B. Darriet, Eur. J. Solid State Inorg. Chem. **30**, 273 (1993).
[190] C. D. Ling, B. J. Kennedy, Q. Zhou, J. R. Spencer, and M. Avdeev, J. Solid State Chem. **183**, 727 (2010).

[191] M. D. Harari, M. J. C. Bernier, and P. Poix, J. Solid State Chem. **5**, 382 (1972).
[192] Y. Doi and Y. Hinatsu, J. Solid State Chem. **177**, 3239 (2004).
[193] C. Rabbow and H. Mullerbuschbaum, Z.Naturforsch.(B) **49**, 1277 (1994).
[194] Y. Doi, Y. Hinatsu, Y. Shimojo, and Y. Ishii, J. Solid State Chem. **161**, 113 (2001).
[195] Y. Doi and Y. Hinatsu, J. Phys.: Condens. Matter **16**, 2849 (2004).
[196] W. Miiller, et al., Phys. Rev. B **84**, 220406(R) (2011).
[197] W. Miiller, et al., J. Am. Chem. Soc. **134**, 3265 (2012).
[198] H.-C. zur Loye, S.-J. Kim, R. Macquart, M. D. Smith, Y. Lee, and T. Vogt, Solid State Sci. **11**, 608 (2009).
[199] J. G. Cheng, et al., Phys. Rev. Lett. **107**, 197204 (2012).
[200] H. D. Zhou, et al., Phys. Rev. Lett. **106**, 147204 (2012).
[201] E. Quarez, M. Huve, F. Abraham, and O. Mentre, Solid State Sci. **5**, 951 (2003).
[202] H. K. Mao, J. Xu, and P. M. Bell, Journal of Geophysical Research-Solid Earth and Planets **91**, 4673 (1986).
[203] A. W. Hull and W. P. Davey, Phys. Rev. **17**, 549 (1921).
[204] Y. Doi, M. Wakeshima, Y. Hinatsu, A. Tobo, K. Ohoyama, and Y. Yamaguchi, J. Mater. Chem. **11**, 3135 (2001).
[205] R. D. Shannon, Acta Crystallogr., Sect. A **32**, 751 (1976).
[206] J. T. Rijssenbeek, P. Matl, B. Batlogg, N. P. Ong, and R. J. Cava, Phys. Rev. B **58**, 10315 (1998).
[207] Y. Doi, K. Matsuhira, and Y. Hinatsu, J. Solid State Chem. **165**, 317 (2002).
[208] J. J. Hamlin, et al., Phys. Rev. B **76**, 014432 (2007).
[209] H. D. Zhou, et al., Phys. Rev. B **85**, 041201 (2012).
[210] L. Shlyk, S. Kryukov, V. Durairaj, S. Parkin, G. Cao, and L. E. De Long, J. Magn. Magn. Mater. **319**, 64 (2007).
[211] A. S. Wills, *Magnetic Structure Determination from Neutron Powder Diffraction Data* (Notes from course given at Cosener's House, Abingdon, 2005).
[212] R. D. Shannon and C. T. Prewitt, Acta Crystallogr., Sect. B: Struct. Sci. **B 26**, 1046 (1970).

Appendices

Appendix A : Full details of structural refinement models for Fe_3O_4

Detail of the P2/c provisional data refinement:

Details of the refinement of the provisional data in the P2/c subcell are given below. The refinement was made again a data sets with 1 s exposure time and a phi rotation of 0.2 ° per frame. This data was integrated in SAINT on $a_c \times a_c \times 2a_c$ cell and merged in sadabs. The resulting hkl file was transformed to the subcell setting in the program EXPREP. The coordinates along with those refined in the previous powder diffraction studying in ref. [96] are given in the subsequent tables.

Crystal Data	Å
Chemical Formula	Fe_3O_4
Cell setting, Space group	P2/c
Temperature(K)	90.0(0.2)
a, b, c (Å)	5.9444(10), 5.9247(10), 16.7752(10)
β(°)	90.236(10)
Volume (Å^3)	590.80(15)
D_c(g cm^{-3})	5.21
X-ray wavelength (Å)	0.26471(1)
μ(mm^{-1})	14.35 mm^{-1}
Crystal form, colour	Pyramid
Crystal size(mm)	r = 0.20
Data Collection	
Diffractometer	ID11@ESRF, Huber phi axis
Data collection method	φ
Absorption correction	None
No. of symmetry unique reflections	48 589
θ_{max}(°)	28.26
R_{int}	0.0830
Range of h,k,l	-21 → h → 20
	-20 → k → 20
	-0 → l → 58

Refinement	
Refine on	F
$R(F^2)$, $wR(F^2)$, S	0.144,0.161, 1.02
Cutoff: I >σ	3.0
No. of reflections	31815
No. of parameters	43
Weighting scheme	$w = w' \times [1 - (\Delta Fobs / 6 \times \Delta Fest)^2]^2$ $w' = [P0T0'(x) + P1T1'(x) + ...Pn\text{-}1Tn\text{-}1'(x)]\text{-}1$, where Pi are the coefficients of a Chebychev series in $t_i(x)$, and x = Fcalc/Fcalcmax. P0 - Pn-1 = 2.79 2.34 1.71
(Δ/α)mean	0.001
(Δ/α)max	0.0009
Δρmax, Δρmin (e $Å^{-3}$)	12.81, -8.69
Twin law	2-fold about c^*: (-1 0 0),(0 -1 0),(0 0 1)
Twin fraction:	0.477(4)

Label	*x*	*y*	*z*	$U_{iso/equiv}$
A(1)	0.25151(11)	0.00483(3)	0.063903(14)	0.000950(17)
	0.250	0.0034(4)	0.06366(7)	0.00005(4)
A(2)	0.25395(10)	0.50617(3)	0.189018(14)	0.001034(17)
	0.250	0.5061(2)	0.18867(8)	0.00005(4)
B(1a)	0.0000	0.5000	0.0000	0.001607(17)
	0.0	0.5	0.0	0.00070(3)
B(1b)	0.5000	0.5000	0.0000	0.001222(17)
	0.5	0.5	0.0	0.00070(3)
B(2a)	0.0000	0.01045(17)	0.2500	0.003061(17)
	0.	0.0096(3)	0.250	0.00070(3)
B(2b)	0.5000	0.00987(15)	0.2500	0.002078(17)
	0.5	0.0096(3)	0.250	0.00070(3)
B(3)	0.25068(11)	0.26390(4)	0.378684(14)	0.002914(17)
	0.250	0.2659(2)	0.38010(9)	0.00070(3)
B(4)	0.24635(8)	0.75514(3)	0.374895(12)	0.001335(17)
	0.250	0.7520(2)	0.37659(9)	0.00070(3)
O(1)	0.2485(5)	0.26070(18)	0.00377(6)	0.00132(4)
	0.250	0.2637(7)	-0.0023(3)	0.00227(8)
O(2)	0.2500(5)	0.74760(17)	0.00253(6)	0.00132(4)
	0.250	0.7461(6)	-0.0029(3)	0.00227(8)
O(3)	0.2541(5)	0.24346(17)	0.25274(6)	0.00132(4)
	0.250	0.2447(8)	0.2542(3)	0.00227(8)

O(4)	0.2528(5)	0.76947(17)	0.25244(6)	0.00132(4)
	0.250	0.7738(8)	0.2525(3)	0.00227(8)
O(5a)	-0.0088(3)	0.0157(3)	0.12828(10)	0.00132(4)
	-0.0091(4)	0.0095(6)	0.1277(2)	0.00227(8)
O(5b)	0.4818(3)	0.0033(3)	0.36827(10)	0.00132(4)
	0.4909(4)	0.0095(6)	0.3723(2)	0.00227(8)
O(6a)	-0.0067(4)	0.5021(4)	0.12561(12)	0.00132(4)
	-0.0081(4)	0.5046(6)	0.1246(2)	0.00227(8)
O(6b)	0.4883(3)	0.5071(4)	0.37682(12)	0.00132(4)
	0.4919(4)	0.5046(6)	0.3754(2)	0.00227(8)

Cubic structure refinement details against Xtal6 data at 130 K:

Crystal Data	
Chemical Formula	Fe_3O_4
Cell setting, Space group	$Fd\bar{3}m$
Temperature(K)	130.0(0.2)
a (Å)	8.3939(2) [1]
Volume ($Å^3$)	591.41
D_c(g cm^{-3})	5.222
X-ray wavelength (Å)	0.16653(1)
μ(mm^{-1})	0.188 mm^{-1}
Crystal form, colour	Pyramid
Crystal size(mm)	r = 0.020
Data Collection	
Diffractometer	ID11@ESRF, Huber Omega and phi axis
Data collection method	ω
Absorption correction	none
T_{min}	0
T_{max}	0
No. of observed, symmetry unique reflections	42855, 638
$\theta_{max}(^o)$	16.11
R_{int}	0.0552
Range of h,k,l	-27 → h → 27

	-27 → k → 27
	-27 → l → 27
Refinement	
Refine on	F^2
$R(F^2)$,R[F^2 >4 sigma], $wR(F^2)$, S	0.0137, 0.0093, 0.0205, 1.013
Cutoff: I >σ	none
No. of reflections	638
No. of parameters	7
Weighting scheme	Weight = 1 / [$sigma^2(Fo^2)$ + $(0.0095*P)^2$] P = Max(0.33333*Fo^2, 0) + 0.66667*Fc^2
(Δ/α)mean	0.000
(Δ/α)max	0.000
Δρmax, Δρmin (e Å-3)	1.09, -0.47

Sites	Fractional coordinate			
	x	y	z	U_{eq} ($Å^2$)
A	0.12500	0.12500	0.12500	0.00274(1)
B	0.25000	0.25000	0.25000	0.00423(1)
O	0.25490(2)	0.25490 (2)	0.25490(2)	0.00438(2)

U_{ij}($Å^2$)	U_{11}	U_{22}	U_{33}	U_{23}	U_{13}	U_{12}
A	0.00274(1)	0.00274(1)	0.00274(1)	0.00000	0.00000	0.00000
B	0.00423(1)	0.00423(1)	0.00423(1)	-0.00112(1)	-0.00112(1)	0.00112(1)
O	0.00438(2)	0.00438(2)	0.00438(2)	-0.00023(3)	-0.00023(3)	-0.00023(3)

	Distance	**Angles**		
A				
O	1.8885(2)			
O	1.8885(2)	109.47		
O	1.8885(2)	109.47	109.47	
O	1.8885(2)	109.47	109.47	109.47

	Distance	**Angles**				
B						
O	2.0582(1)					
O	2.0582(1)	180.00				
O	2.0582(1)	87.69(1)	92.31(1)			
O	2.0582(1)	92.31(1)	87.69(1)	180.00		
O	2.0582(1)	87.69(1)	92.31(1)	87.69(1)	92.31(1)	
O	2.0582(1)	92.31(1)	87.69(1)	92.31(1)	87.69(1)	180

	Distance	**Angles**				
B						
B	2.9677(1)					
B	2.9677(1)	180.00				
B	2.9677(1)	60.00	120.00			
B	2.9677(1)	60.00	120.00	60.00		
B	2.9677(1)	120.00	60.00	120.00	180.00	
B	2.9677(1)	120.00	60.00	180.00	120.00	60.00

	Distance	**Angles**		
O				
A	1.8885(2)			
B	2.0582(1)	123.65(1)		
B	2.0582(1)	123.65(1)	92.27(1)	
B	2.0582(1)	123.65(1)	92.27(1)	92.27(1)

Bond valence sums (BVS): A site (tetrahedral Fe) = 2.78

B site (octahedral Fe) = 2.61

Cc refinement details against final Xtal6 data at 90 K of the Verwey structure of magnetite

Crystal Data	
Chemical Formula	Fe_3O_4
Cell setting, Space group	Cc
Temperature(K)	90.0(0.2)
a,b,c (Å)	11.88881(3), 11.84940(3), 16.77515(14) [1]
β(°)	90.2363(2) [1]
Volume (Å^3)	2363.18(2)
D_c(g cm^{-3})	5.207
X-ray wavelength (Å)	0.16653(1)
μ(mm^{-1})	0.188 mm^{-1}
Crystal form, colour	Pyramid
Crystal size(mm)	r = 0.020
Data Collection	
Diffractometer	ID11@ESRF, Huber Omega and phi axis
Data collection method	ω
Absorption correction	none
T_{min}	0
T_{max}	0
No. of observed, symmetry unique reflections	595951, 91433
θ_{max}(°)	16.11
R_{int}	0.0842
Range of h,k,l	-39 → h → 39
	-39 → k → 39
	-55 → l → 55
Refinement	
Refine on	F^2
R(F^2),R[F^2 >4 sigma], wR(F^2), S	0.0518,0.0340, 0.0696, 1.001
Cutoff: I >σ	none
No. of reflections	91433
No. of parameters	506
Weighting scheme	Weight = [1.00 * exp (0.33*s^2)] / [sigma^2(Fo^2) + (0.0184*P)^2]

	where s = sin(theta)/lambda and P = Max(0.33333*Fo^2, 0) + 0.66667*Fc^2
(Δ/α)mean	0.001
(Δ/α)max	0.007
Δρmax, Δρmin (e $Å^{-3}$)	2.370, -3.820
Flack Parameter	-0.06(0.14)
Twin law	2-fold about c^*: (-1 0 0),(0 -1 0),(0 0 1)
Twin fraction:	0.1119(7)

Fractional coordinates:

Sites	x	y	z	U_{eq} ($Å^2$)
A11	0.87509(2)	0.75133(2)	0.065377(13)	0.00187(2)
A12	0.87814(2)	0.25204(2)	0.065046(13)	0.00172(2)
A13	0.62475(2)	0.75276(2)	0.437877(13)	0.00190(2)
A14	0.62660(2)	0.25398(2)	0.437830(13)	0.00186(2)
A21	0.874607(18)	0.50477(2)	0.190290(11)	0.00189(2)
A22	0.880722(18)	0.00074(2)	0.188506(11)	0.00184(2)
A23	0.625263(19)	0.50162(2)	0.31109(1)	0.00184(2)
A24	0.629229(18)	0.005024(19)	0.312775(11)	0.00179(2)
B1A1	0.75057(3)	-0.00212(3)	0.002273(14)	0.00232(1)
B1A2	0.75116(3)	0.49865(3)	0.001114(14)	0.00220(1)
B1B1	0.00187(3)	0.50050(3)	0.501700(15)	0.00240(1)
B1B2	-0.00257(2)	0.00076(2)	0.496931(13)	0.00206(1)
B2A1	0.74758(2)	0.756391(15)	0.252602(14)	0.00209(2)
B2A2	0.75929(2)	0.252197(16)	0.253673(13)	0.00186(2)
B2B1	0.00255(3)	0.74372(1)	0.751877(18)	0.00243(1)
B2B2	0.00214(3)	0.24588(1)	0.751910(17)	0.00194(1)
B31	0.87694(2)	0.879450(17)	0.379805(13)	0.00223(2)
B32	0.87644(2)	0.387473(16)	0.380749(13)	0.00191(2)
B33	0.62663(2)	0.886624(15)	0.121776(12)	0.00208(2)
B34	0.62878(2)	0.374621(18)	0.123112(13)	0.00197(2)
B41	0.87599(2)	0.62482(2)	0.376706(14)	0.00214(2)
B42	0.87543(2)	0.13087(2)	0.374365(15)	0.00243(2)
B43	0.62566(2)	0.62776(2)	0.125840(15)	0.00197(2)
B44	0.62788(3)	0.12601(3)	0.126517(16)	0.00228(2)

O11	0.87581(12)	0.88043(12)	0.00014(8)	0.00302(11)
O12	0.87607(12)	0.38072(11)	-0.00164(8)	0.00279(11)
O13	0.62691(13)	0.88186(11)	0.50500(8)	0.00326(11)
O14	0.62556(13)	0.38280(12)	0.50579(8)	0.00338(11)
O21	0.87636(13)	0.62353(12)	-0.00028(8)	0.00366(12)
O22	0.87698(13)	0.12378(13)	0.00003(9)	0.00401(13)
O23	0.62352(12)	0.62330(11)	0.50340(8)	0.00307(11)
O24	0.62575(13)	0.12474(11)	0.50178(8)	0.00303(11)
O31	0.87780(12)	0.86966(10)	0.25268(8)	0.00321(11)
O32	0.87420(13)	0.37602(11)	0.25512(8)	0.00350(11)
O33	0.62942(12)	0.87691(11)	0.24574(7)	0.00305(11)
O34	0.62492(12)	0.36980(10)	0.24567(7)	0.00281(10)
O41	0.87732(11)	0.63749(10)	0.25476(8)	0.00295(10)
O42	0.87801(12)	0.13169(11)	0.25180(8)	0.00344(11)
O43	0.62938(13)	0.63216(11)	0.24681(8)	0.00369(11)
O44	0.62708(12)	0.13680(10)	0.24925(7)	0.00320(11)
O5A1	0.74350(12)	0.75050(11)	0.13030(7)	0.00307(10)
O5A2	0.74854(13)	0.25644(11)	0.13035(7)	0.00309(11)
O5A3	0.75271(13)	0.75518(12)	0.37224(8)	0.00361(12)
O5A4	0.75586(13)	0.25737(11)	0.37420(8)	0.00338(10)
O5B1	0.01006(12)	0.74793(11)	0.62909(8)	0.00316(11)
O5B2	0.00517(13)	0.24490(12)	0.63080(8)	0.00369(12)
O5B3	-0.00515(13)	0.74641(11)	0.87217(7)	0.00310(11)
O5B4	-0.00274(12)	0.24439(11)	0.87124(7)	0.00277(10)
O6A1	0.74315(11)	0.50275(11)	0.12581(7)	0.00329(11)
O6A2	0.75103(11)	-0.00040(12)	0.12476(7)	0.00318(10)
O6A3	0.75239(11)	0.50327(13)	0.37652(7)	0.00335(11)
O6A4	0.75962(11)	0.00477(11)	0.37670(6)	0.00301(10)
O6B1	0.01099(11)	-0.00229(12)	0.62372(7)	0.00369(10)
O6B2	0.00278(11)	0.49870(13)	0.62608(7)	0.00327(10)
O6B3	-0.00284(11)	-0.00223(13)	0.87629(7)	0.00332(9)
O6B4	0.00068(11)	0.49824(13)	0.87740(7)	0.00385(11)

Anisotropic thermal parameters:

$U_{ij}(Å^2)$	U_{11}	U_{22}	U_{33}	U_{23}	U_{13}	U_{12}
A11	0.00198(4)	0.00185(3)	0.00178(4)	0.00016(3)	-0.00002(3)	-0.00008(3)
A12	0.00165(4)	0.00181(3)	0.00170(4)	0.00012(3)	-0.00015(3)	-0.00002(3)
A13	0.00224(5)	0.00182(4)	0.00164(4)	0.00005(3)	0.00008(3)	0.00000(4)
A14	0.00205(4)	0.00170(3)	0.00183(4)	0.00004(3)	-0.00007(3)	-0.00010(3)
A21	0.00209(5)	0.00202(4)	0.00157(3)	-0.00021(3)	-0.00008(3)	-0.00022(4)
A22	0.00186(4)	0.00190(3)	0.00174(3)	0.00009(3)	0.00003(3)	-0.00009(3)
A23	0.00201(4)	0.00165(3)	0.00188(3)	0.00005(3)	-0.00004(3)	-0.00008(3)
A24	0.00170(5)	0.00170(4)	0.00197(3)	-0.00012(3)	-0.00011(3)	-0.00020(4)
B1A1	0.00261(3)	0.00208(3)	0.00228(2)	-0.00027(3)	-0.00030(2)	0.00012(3)
B1A2	0.00205(3)	0.00207(3)	0.00249(2)	-0.00038(3)	-0.00013(2)	0.00046(3)
B1B1	0.00256(3)	0.00229(2)	0.00234(3)	0.00045(2)	0.00040(2)	0.00037(2)
B1B2	0.00214(4)	0.00215(2)	0.00188(4)	0.00040(3)	-0.00005(3)	0.00022(2)
B2A1	0.00234(4)	0.00199(3)	0.00195(4)	-0.00008(3)	-0.00030(3)	0.00003(3)
B2A2	0.00192(4)	0.00202(3)	0.00165(4)	0.00002(2)	-0.00028(3)	0.00014(2)
B2B1	0.00328(3)	0.00212(2)	0.00188(2)	0.00029(4)	0.00012(2)	-0.00002(4)
B2B2	0.00196(2)	0.00208(2)	0.00179(2)	0.00006(4)	0.00005(2)	0.00013(4)
B31	0.00254(4)	0.00212(3)	0.00203(4)	0.00013(3)	0.00013(3)	0.00013(3)
B32	0.00197(4)	0.00190(3)	0.00185(3)	-0.00011(3)	-0.00012(3)	-0.00005(3)
B33	0.00230(4)	0.00210(3)	0.00183(4)	0.00003(3)	-0.00011(3)	-0.00007(4)
B34	0.00198(4)	0.00173(2)	0.00222(4)	0.00004(3)	0.00002(3)	0.00004(3)
B41	0.00221(4)	0.00240(4)	0.00182(4)	0.00036(3)	-0.00002(3)	-0.00007(4)
B42	0.00252(4)	0.00238(4)	0.00241(4)	-0.00036(3)	0.00042(3)	-0.00030(3)
B43	0.00234(4)	0.00166(3)	0.00190(4)	0.00001(2)	-0.00002(3)	0.00019(3)
B44	0.00215(4)	0.00271(3)	0.00199(3)	-0.00043(3)	-0.00002(3)	-0.00012(3)
O11	0.0032(2)	0.0026(2)	0.0033(2)	0.00102(16)	-0.00003(18)	0.00027(18)
O12	0.0032(3)	0.0019(2)	0.0032(2)	0.00038(17)	0.00016(18)	-0.0001(2)
O13	0.0041(3)	0.0032(2)	0.0025(2)	-0.00064(18)	-0.00019(19)	0.0003(2)
O14	0.0040(3)	0.0034(2)	0.0027(2)	-0.00075(16)	-0.00011(18)	0.0006(2)
O21	0.0047(3)	0.0034(2)	0.0030(2)	-0.00069(17)	-0.00030(19)	0.0004(2)
O22	0.0050(3)	0.0039(2)	0.0031(2)	-0.00054(18)	-0.00046(19)	0.0002(2)
O23	0.0032(2)	0.0026(2)	0.0034(2)	0.00100(17)	-0.00003(18)	0.00002(18)
O24	0.0035(2)	0.0026(2)	0.0030(2)	0.00068(16)	-0.00004(18)	0.00066(18)
O31	0.0035(2)	0.0031(2)	0.00299(19)	0.00067(14)	0.00066(17)	0.00041(18)
O32	0.0043(3)	0.0028(2)	0.0034(2)	0.00148(16)	-0.00016(18)	0.00019(19)
O33	0.0037(2)	0.0033(2)	0.00212(17)	0.00094(15)	0.00013(16)	0.00075(18)
O34	0.0037(2)	0.00265(19)	0.00213(17)	-0.00040(13)	-0.00042(15)	-0.00017(16)
O41	0.0026(2)	0.0028(2)	0.0035(2)	-0.00091(16)	0.00006(17)	-0.00025(17)

O42	0.0031(2)	0.0028(2)	0.0045(2)	0.00006(15)	-0.00006(17)	0.00021(16)
O43	0.0040(3)	0.0033(2)	0.0037(2)	0.00042(15)	0.00004(18)	0.00083(18)
O44	0.0039(3)	0.0031(2)	0.0027(2)	-0.00026(16)	0.00052(18)	0.00010(19)
O5A1	0.0036(2)	0.00276(17)	0.00280(19)	0.00024(14)	0.00011(16)	-0.00055(15)
O5A2	0.0026(2)	0.0034(2)	0.0033(2)	-0.00037(16)	0.00021(17)	0.00033(17)
O5A3	0.0030(3)	0.0047(2)	0.0031(2)	-0.00046(18)	0.00035(18)	0.0001(2)
O5A4	0.0029(2)	0.0036(2)	0.0036(2)	-0.00065(15)	0.00092(15)	-0.00030(16)
O5B1	0.0021(2)	0.0042(2)	0.0032(2)	0.00067(17)	0.00017(16)	-0.00003(18)
O5B2	0.0032(3)	0.0047(3)	0.0032(2)	-0.00018(18)	-0.00076(18)	0.0009(2)
O5B3	0.0030(2)	0.0035(2)	0.0028(2)	0.00036(16)	-0.00071(17)	0.00077(18)
O5B4	0.0034(2)	0.0030(2)	0.00194(19)	0.00018(15)	-0.00023(16)	0.00072(17)
O6A1	0.0033(2)	0.0032(2)	0.00344(19)	0.00067(18)	-0.00070(16)	-0.00120(19)
O6A2	0.0034(2)	0.0031(2)	0.00302(17)	0.00033(17)	-0.00069(15)	0.00060(18)
O6A3	0.0034(2)	0.0038(2)	0.00286(18)	0.00004(17)	-0.00067(16)	0.00064(19)
O6A4	0.0025(2)	0.0031(2)	0.00342(17)	0.00029(17)	-0.00017(15)	-0.00155(18)
O6B1	0.0040(2)	0.0036(2)	0.00347(17)	-0.00010(17)	0.00037(15)	0.00107(18)
O6B2	0.0025(2)	0.0044(2)	0.00294(16)	0.0013(2)	0.00076(15)	0.0000(2)
O6B3	0.00263(19)	0.0038(2)	0.00355(18)	0.00033(17)	0.00055(15)	0.00063(17)
O6B4	0.0036(2)	0.0042(2)	0.00379(18)	0.0014(2)	0.00013(16)	-0.0003(2)

A-O distance angle table:

Site	Distance	Angles		
A11				
O21	1.8726(14)			
O11	1.8810(13)	108.39(06)		
O5B2	1.8931(14)	110.58(07)	108.20(07)	
O5A1	1.9099(14)	109.87(07)	109.98(06)	109.80(06)
A12				
O22	1.8708(14)			
O12	1.8912(13)	108.06(06)		
O5A2	1.8950(15)	110.81(07)	108.13(06)	
O5B1	1.8974(14)	109.54(07)	110.09(07)	110.17(06)
A13				
O5A3	1.8818(15)			
O23	1.8872(13)	111.19(06)		

O5B3	1.8937(14)	108.58(06)	109.57(06)	
O13	1.8997(13)	109.00(07)	108.02(06)	110.47(07)
A14				
O24	1.8698(13)			
O5A4	1.8751(15)	110.52(07)		
O5B4	1.8970(13)	109.87(06)	109.20(06)	
O14	1.9053(13)	108.23(06)	109.32(06)	109.69(6)
A21				
O6B2	1.8702(12)			
O32	1.8736(13)	108.69(07)		
O6A1	1.8972(12)	110.04(05)	108.46(06)	
O41	1.9088(12)	109.42(06)	110.01(06)	110.20(06)
A22				
O6A2	1.8729(12)			
O42	1.8806(14)	108.20(6)		
O31	1.8902(13)	107.59(6)	110.86(6)	
O6B1	1.8958(13)	110.20(5)	109.37(7)	110.58(6)
A23				
O6A3	1.8643(12)			
O6B3	1.8788(13)	108.32(05)		
O43	1.8863(13)	107.76(07)	110.65(07)	
O34	1.9090(12)	110.29(06)	109.75(06)	110.0(05)
A24				
O6B4	1.8777(13)			
O6A4	1.8813(12)	109.97(05)		
O33	1.8892(14)	109.27(06)	109.57(06)	
O44	1.8905(12)	109.47(07)	109.38(06)	109.16(05)

B-O distance angle table:

Site	**Distance**	**Angles**				
B1A1						
O11	2.0384(15)					

O13	2.0482(15)	178.93(07)				
O6A2	2.0547(11)	91.46(05)	88.26(6)			
O24	2.0768(14)	92.54(06)	88.50(6)	90.57(06)		
O6A4	2.1100(11)	86.10(05)	94.14(5)	176.91(06)	91.43(05)	
O22	2.1180(16)	87.83(06)	91.13(6)	90.68(06)	178.69(07)	87.34(06)
B1A2						
O12	2.0398(14)					
O14	2.0518(15)	179.10(07)				
O6A3	2.0903(12)	87.81(06)	93.08(05)			
O6A1	2.0949(12)	94.28(05)	84.83(06)	177.68(07)		
O23	2.0959(14)	93.17(05)	86.80(06)	91.08(05)	87.81(05)	
O21	2.0990(16)	88.07(06)	91.95(06)	89.35(06)	91.71(05)	178.70(07)
B1B1						
O13	2.0465(15)					
O12	2.0545(14)	179.86(8)				
O24	2.0824(15)	88.39(6)	91.75(6)			
O6B4	2.0852(13)	91.95(6)	88.04(6)	89.85(06)		
O6B2	2.0865(12)	88.00(6)	92.01(6)	90.33(06)	179.80(09)	
O21	2.0946(15)	92.05(6)	87.81(6)	179.03(07)	89.27(06)	90.54(06)
B1B2						
O11	2.0190(15)					
O6B3	2.0238(12)	91.29(06)				
O22	2.0571(16)	90.04(06)	91.90(06)			
O14	2.0723(15)	174.12(07)	94.34(06)	91.49(06)		
O23	2.0895(14)	91.59(06)	92.53(06)	175.24(07)	86.45(05)	
O6B1	2.1327(12)	92.09(05)	175.73(07)	90.71(06)	82.21(05)	84.76(05)
B2A1						
O33	2.0062(14)					
O5A3	2.0077(14)	94.63(06)				
O43	2.0372(15)	91.66(06)	93.47(06)			
O31	2.0489(14)	93.59(05)	89.10(06)	173.95(05)		
O5A1	2.0532(13)	87.32(06)	177.61(04)	85.08(06)	92.16(05)	
O41	2.0892(13)	176.17(05)	87.62(06)	91.29(04)	83.34(05)	90.50(06)

B2A2						
O32	2.0049(15)					
O42	2.0081(14)	92.38(06)				
O5A4	2.0234(14)	88.99(06)	93.11(06)			
O5A2	2.0728(13)	91.92(06)	92.41(06)	174.36(06)		
O44	2.0844(14)	173.84(06)	93.61(04)	92.13(06)	86.39(05)	
O34	2.1237(14)	91.89(05)	173.82(05)	91.44(05)	82.98(05)	82.03(05)
B2B1						
O5B3	2.0207(13)					
O5B1	2.0627(13)	177.71(3)				
O33	2.0809(14)	95.51(5)	86.15(5)			
O32	2.0845(15)	87.05(6)	94.43(6)	93.70(3)		
O42	2.0909(14)	87.39(6)	90.91(6)	176.78(6)	87.83(6)	
O43	2.1083(15)	93.71(6)	84.77(6)	87.62(6)	178.41(6)	90.80(3)
B2B2						
O5B4	2.0029(12)					
O34	2.0055(13)	94.03(5)				
O31	2.0149(14)	87.90(6)	94.02(3)			
O41	2.0285(13)	87.61(5)	178.34(5)	85.75(6)		
O5B2	2.0322(13)	178.95(6)	85.87(5)	91.06(6)	92.49(5)	
O44	2.0352(14)	92.98(5)	86.23(6)	179.06(6)	93.97(2)	88.05(6)
B31						
O22	2.0171(14)					
O6A4	2.0379(14)	92.10(5)				
O6B3	2.0405(14)	92.59(6)	87.66(5)			
O5B4	2.0548(14)	93.39(5)	174.42(5)	91.10(6)		
O5A3	2.0891(16)	92.55(6)	91.63(6)	174.83(6)	89.12(5)	
O31	2.1358(13)	175.79(5)	91.15(5)	90.21(5)	83.41(5)	84.68(5)
B32						
O21	2.0000(14)					
O6B4	2.0050(15)	94.32(6)				
O6A3	2.0154(14)	94.37(5)	94.49(5)			

O5A4	2.1077(14)	90.07(6)	173.51(6)	89.92(6)		
O32	2.1119(13)	172.54(5)	91.24(5)	90.14(5)	83.99(6)	
O5B3	2.1263(15)	91.26(5)	90.80(6)	171.96(5)	84.32(5)	83.69(5)
B33						
O6A2	1.9953(14)					
O6B2	2.0052(14)	95.09(5)				
O24	2.0175(13)	94.05(5)	94.61(6)			
O33	2.0829(12)	90.19(5)	90.58(5)	172.98(6)		
O5B1	2.1164(14)	171.67(6)	91.57(6)	90.39(5)	84.73(5)	
O5A1	2.1333(14)	91.33(6)	171.16(6)	90.98(5)	83.32(5)	81.54(5)
B34						
O5A2	2.0004(14)					
O23	2.0090(13)	95.08(5)				
O6A1	2.0385(13)	92.61(6)	91.78(5)			
O5B2	2.0454(15)	91.31(6)	92.98(5)	173.54(6)		
O34	2.0574(12)	86.49(5)	176.81(7)	90.93(5)	84.19(5)	
O6B1	2.0616(15)	175.38(6)	88.71(5)	84.63(5)	91.12(6)	89.85(5)
B41						
O12	2.0418(13)					
O41	2.0513(13)	177.60(5)				
O6A3	2.0576(15)	88.65(5)	93.33(5)			
O6B4	2.0794(15)	88.54(5)	92.78(5)	91.05(5)		
O5B4	2.1190(13)	93.97(5)	83.99(5)	176.33(6)	91.59(6)	
O5A3	2.1304(15)	93.20(5)	85.41(5)	90.93(6)	177.39(6)	86.35(5)
B42						
O6A4	2.0324(12)					
O5B3	2.0327(14)	178.35(6)				
O42	2.0564(14)	92.04(5)	88.01(5)			
O5A4	2.0658(15)	93.85(6)	87.80(5)	90.48(6)		
O6B3	2.1021(15)	86.16(5)	92.19(6)	90.33(5)	179.19(6)	
O1	2.1141(14)	86.15(5)	93.72(5)	176.50(6)	92.63(5)	86.56(5)
B43						

O5B1	2.0154(15)					
O6B1	2.0173(14)	94.49(6)				
O14	2.0177(14)	94.29(6)	86.51(6)			
O5A1	2.0205(14)	86.89(6)	178.21(7)	94.54(5)		
O43	2.0302(14)	88.07(5)	92.78(5)	177.58(7)	86.12(6)	
O6A1	2.0360(14)	178.44(6)	85.84(5)	87.26(5)	92.76(6)	90.39(5)
B44						
O13	2.0405(14)					
O44	2.0630(12)	178.90(6)				
O6A2	2.0948(14)	87.38(5)	93.70(5)			
O6B2	2.0966(15)	87.89(5)	92.35(5)	89.53(5)		
O5A2	2.1094(14)	93.73(5)	85.99(5)	92.81(6)	177.21(6)	
O5B2	2.1152(16)	93.78(5)	85.14(5)	178.67(6)	91.17(6)	86.45(5)

B-B distance angle table:

Site	**Distance**	**Angles**				
B1A1						
B33	2.8200(04)					
B31	2.9354(04)	178.18(02)				
B1B2	2.9367(04)	123.33(01)	57.41(01)			
B1B1	2.9567(05)	58.66(01)	120.61(01)	177.95(01)		
B44	2.9668(04)	58.67(01)	119.52(01)	120.86(01)	60.29(01)	
B42	3.0268(04)	121.84(01)	59.97(01)	59.20(01)	119.63(01)	179.42(01)
B1A2						
B32	2.8532(04)					
B34	2.9137(04)	177.76(02)				
B41	2.9536(04)	57.93(01)	120.01(01)			
B1B1	2.9807(05)	58.39(01)	120.11(01)	59.91(01)		
B43	2.9950(04)	121.05(01)	61.01(01)	178.97(02)	119.80(01)	
B1B2	3.0170(04)	120.48(01)	61.02(01)	119.33(01)	178.81(01)	60.93(01)
B1B1						
B33	2.8322(04)					
B32	2.8477(04)	179.87(02)				
B1A1	2.9567(05)	58.25(01)	121.74(01)			

B41	2.9633(04)	122.00(01)	57.87(01)	120.08(01)		
B44	2.9749(04)	58.44(01)	121.68(01)	60.02(01)	179.55(02)	
B1A2	2.9807(05)	121.43(01)	58.57(01)	179.43(02)	59.59(01)	120.31(01)
B1B2						
B31	2.8206(03)					
B1A1	2.9367(04)	61.27(01)				
B42	2.9469(04)	62.19(01)	61.92(01)			
B34	3.0120(03)	178.69(01)	119.42(01)	119.08(01)		
B1A2	3.0170(04)	121.48(01)	176.88(01)	120.28(01)	57.80(01)	
B43	3.0483(04)	119.38(01)	118.56(01)	178.42(01)	59.34(01)	59.18(01)
B2A1						
B2B1	2.9131(05)					
B43	2.9868(04)	60.95(01)				
B31	3.0029(03)	120.82(01)	177.91(01)			
B41	3.0114(04)	120.44(01)	118.11(01)	60.23(01)		
B2B2	3.0265(05)	179.30(01)	118.37(01)	59.86(01)	59.60(01)	
B33	3.0397(03)	61.78(01)	61.20(01)	120.39(01)	177.32(01)	118.15(01)
B2A2						
B42	2.8372(03)					
B2B1	2.8928(05)	62.11(01)				
B32	3.0048(03)	62.69(01)	62.48(01)			
B44	3.0330(04)	119.99(01)	120.87(01)	176.23(01)		
B34	3.0464(03)	177.80(01)	119.39(01)	119.29(01)	57.98(01)	
B2B2	3.0573(05)	119.63(01)	178.20(01)	117.61(01)	58.98(01)	58.88(01)
B2B1						
B2A2	2.8928(05)					
B2A1	2.9132(05)	178.75(01)				
B42	2.9563(04)	58.02(01)	120.76(01)			
B43	2.9928(04)	119.39(01)	60.74(01)	119.22(01)		
B33	3.0580(04)	120.07(01)	61.15(01)	178.03(02)	60.93(01)	
B32	3.0602(04)	60.55(01)	119.32(01)	60.72(01)	179.93(02)	119.13(00)
B2B2						

B44	2.9983(04)					
B34	3.0002(04)	58.84(01)				
B41	3.0009(04)	118.88(00)	177.63(01)			
B31	3.0083(04)	178.99(01)	122.00(00)	60.29(01)		
B2A1	3.0265(05)	120.58(01)	120.22(01)	59.95(01)	59.68(01)	
B2A2	3.0573(05)	60.10(01)	60.38(01)	119.48(01)	119.63(01)	179.22(01)
B31						
B1B2	2.8205(03)					
B1A1	2.9354(04)	61.32(01)				
B42	2.9807(04)	60.98(01)	61.54(01)			
B2A1	3.0029(03)	178.39(01)	118.40(01)	117.42(01)		
B2B2	3.0083(04)	119.80(01)	178.76(01)	118.33(01)	60.46(01)	
B41	3.0176(04)	121.56(01)	120.35(01)	177.20(01)	60.02(01)	59.73(01)
B32						
B41	2.8133(03)					
B1B1	2.8478(04)	63.13(01)				
B1A2	2.8533(04)	62.83(01)	63.05(01)			
B2A2	3.0048(03)	121.02(01)	175.00(01)	120.83(01)		
B42	3.0425(04)	176.59(01)	119.80(01)	119.71(01)	55.96(01)	
B2B1	3.0602(04)	119.45(01)	119.05(01)	177.28(01)	56.97(01)	57.95(01)
B33						
B1A1	2.8199(04)					
B1B1	2.8322(04)	63.08(01)				
B44	2.8377(04)	63.25(01)	63.29(01)			
B2A1	3.0397(03)	120.24(01)	176.40(01)	119.00(01)		
B2B1	3.0580(04)	176.85(02)	119.56(01)	119.16(01)	57.08(01)	
B43	3.0681(04)	119.02(01)	119.07(01)	177.12(01)	58.55(01)	58.49(01)
B34						
B1A2	2.9137(04)					
B44	2.9465(03)	121.32(01)				
B2B2	3.0001(04)	178.07(01)	60.55(01)			
B43	3.0002(03)	60.83(01)	177.81(01)	117.29(01)		
B1B2	3.0121(03)	61.19(01)	120.12(01)	118.63(01)	60.93(01)	

B2A2	3.0464(03)	119.40(01)	60.78(01)	60.74(01)	118.13(01)	178.66(01)
B41						
B32	2.8133(03)					
B1A2	2.9537(04)	59.25(01)				
B1B1	2.9633(04)	59.01(01)	60.50(01)			
B2B2	3.0009(04)	121.76(01)	178.98(01)	119.67(01)		
B2A1	3.0114(04)	122.35(01)	119.35(01)	178.49(01)	60.45(01)	
B31	3.0176(04)	177.61(01)	119.01(01)	118.88(01)	59.98(01)	59.75(01)
B42						
B2A2	2.8372(03)					
B1B2	2.9468(04)	178.65(01)				
B2B1	2.9563(04)	59.87(01)	119.76(01)			
B31	2.9807(04)	122.08(01)	56.83(01)	121.38(01)		
B1A1	3.0268(04)	121.51(01)	58.88(01)	178.57(02)	58.50(01)	
B32	3.0425(04)	61.35(01)	119.77(01)	61.33(01)	176.19(01)	118.73(01)
B43						
B2A1	2.9868(04)					
B2B1	2.9928(04)	58.31(01)				
B1A2	2.9950(04)	121.09(01)	179.30(02)			
B34	3.0002(03)	121.00(01)	121.71(01)	58.16(01)		
B1B2	3.0483(04)	178.94(01)	120.72(01)	59.89(01)	59.73(01)	
B33	3.0681(04)	60.25(01)	60.59(01)	119.55(01)	177.66(01)	119.05(01)
B44						
B33	2.8378(04)					
B34	2.9465(03)	177.28(01)				
B1A1	2.9668(04)	58.08(01)	119.75(01)			
B1B1	2.9748(04)	58.26(01)	119.47(01)	59.69(01)		
B2B2	2.9983(04)	121.55(01)	60.61(01)	179.49(02)	119.85(01)	
B2A2	3.0330(04)	121.01(01)	61.24(01)	119.54(01)	179.09(02)	60.91(01)

O-A, B distance angle table:

Site	Distance	Angles		
O11				
A11	1.8810(13)			
B1B2	2.0190(15)	125.99(8)		
B1A1	2.0384(15)	122.68(8)	92.74(6)	
B42	2.1142(14)	121.95(8)	90.92(6)	93.57(6)
O12				
A12	1.8912(13)			
B1A2	2.0398(14)	123.14(7)		
B41	2.0419(13)	124.42(7)	92.71(5)	
B1B1	2.0544(14)	121.90(7)	93.44(5)	92.67(6)
O13				
A13	1.8997(13)			
B44	2.0406(14)	123.73(7)		
B1B1	2.0465(15)	121.95(7)	93.41(6)	
B1A1	2.0482(15)	123.71(8)	93.04(5)	92.45(6)
O14				
A14	1.9053(13)			
B43	2.0177(14)	123.20(8)		
B1A2	2.0519(15)	121.27(8)	94.77(6)	
B1B2	2.0723(15)	120.27(7)	96.36(6)	94.03(6)
O21				
A11	1.8726(14)			
B32	2.0001(14)	129.77(8)		
B1B1	2.0946(15)	124.44(8)	88.10(6)	
B1A2	2.0990(16)	123.79(8)	88.19(5)	90.59(6)
O22				
A12	1.8708(14)			
B31	2.0171(14)	126.75(8)		
B1B2	2.0571(16)	126.44(8)	87.62(6)	
B1A1	2.1180(16)	124.43(8)	90.41(6)	89.38(6)

O23				
A13	1.8872(13)			
B34	2.0090(13)	124.89(7)		
B1B2	2.0895(14)	122.81(7)	94.58(6)	
B1A2	2.0960(14)	122.84(8)	90.41(5)	92.25(5)
O24				
A14	1.8698(13)			
B33	2.0175(13)	128.83(7)		
B1A1	2.0768(14)	124.73(8)	87.05(5)	
B1B1	2.0823(15)	125.75(7)	87.37(6)	90.62(5)
O31				
A22	1.8901(13)			
B2B2	2.0149(14)	122.65(8)		
B2A1	2.0489(14)	123.61(7)	96.27(5)	
B31	2.1358(13)	121.61(6)	92.86(5)	91.69(5)
O32				
A21	1.8736(13)			
B2A2	2.0049(14)	126.32(8)		
B2B1	2.0846(15)	122.38(8)	90.02(5)	
B32	2.1119(13)	121.79(7)	93.72(6)	93.64(5)
O33				
A24	1.8892(14)			
B2A1	2.0062(14)	122.71(7)		
B2B1	2.0809(14)	121.32(7)	90.90(5)	
B33	2.0829(12)	123.35(6)	96.02(6)	94.52(5)
O34				
A23	1.9090(12)			
B2B2	2.0054(13)	121.95(7)		
B34	2.0574(12)	123.48(6)	95.19(5)	
B2A2	2.1237(14)	120.05(7)	95.49(5)	93.53(5)

O41				
A21	1.9088(12)			
B2B2	2.0286(13)	123.96(7)		
B41	2.0513(13)	120.30(6)	94.70(5)	
B2A1	2.0892(13)	122.35(7)	94.60(5)	93.32(5)
O42				
A22	1.8806(14)			
B2A2	2.0081(14)	127.53(8)		
B42	2.0564(14)	124.13(7)	88.53(6)	
B2B1	2.0909(14)	124.69(8)	89.76(5)	90.93(6)
O43				
A23	1.8863(13)			
B43	2.0302(14)	123.36(7)		
B2A1	2.0372(15)	125.79(8)	94.50(6)	
B2B1	2.1083(14)	121.92(8)	92.61(5)	89.27(5)
O44				
A24	1.8905(12)			
B2B2	2.0351(14)	124.06(7)		
B44	2.0630(12)	120.75(6)	94.04(5)	
B2A2	2.0844(14)	120.89(7)	95.82(5)	93.99(5)
O5A1				
A11	1.9099(14)			
B43	2.0205(14)	123.51(7)		
B2A1	2.0532(13)	123.61(8)	94.30(5)	
B33	2.1333(14)	119.51(6)	95.19(6)	93.09(5)
O5A2				
A12	1.8950(15)			
B34	2.0004(14)	124.36(7)		
B2A2	2.0728(13)	121.96(8)	96.81(6)	
B44	2.1094(14)	121.11(6)	91.56(6)	92.97(6)
O5A3				

A13	1.8818(15)			
B2A1	2.0077(14)	124.31(8)		
B31	2.0891(16)	123.25(7)	94.25(6)	
B41	2.1304(15)	121.74(7)	93.34(6)	91.31(6)
O5A4				
A14	1.8751(15)			
B2A2	2.0234(14)	126.02(8)		
B42	2.0658(15)	123.32(7)	87.86(5)	
B32	2.1077(14)	123.01(7)	93.31(6)	93.60(6)
O5B1				
A12	1.8974(14)			
B43	2.0154(15)	123.14(7)		
B2B1	2.0627(13)	121.76(8)	94.42(6)	
B33	2.1164(14)	120.48(7)	95.87(6)	94.06(5)
O5B2				
A11	1.8931(14)			
B2B2	2.0322(13)	124.16(8)		
B34	2.0454(14)	124.42(7)	94.74(5)	
B44	2.1152(16)	121.68(7)	92.57(6)	90.16(6)
O5B3				
A13	1.8937(13)			
B2B1	2.0207(13)	122.76(8)		
B42	2.0327(14)	123.63(7)	93.66(5)	
B32	2.1262(15)	120.21(6)	95.08(5)	94.01(6)
O5B4				
A14	1.8970(13)			
B2B2	2.0029(12)	124.17(8)		
B31	2.0548(14)	121.94(6)	95.69(5)	
B41	2.1189(13)	121.14(6)	93.40(5)	92.60(6)
O6A1				
A21	1.8972(12)			

B43	2.0360(14)	123.66(7)		
B34	2.0385(13)	124.74(6)	94.84(5)	
B1A2	2.0949(12)	121.93(7)	92.93(5)	89.64(5)
O6A2				
A22	1.8729(12)			
B33	1.9953(14)	128.87(7)		
B1A1	2.0547(11)	124.74(7)	88.24(5)	
B44	2.0948(14)	124.10(7)	87.83(5)	91.27(5)
O6A3				
A23	1.8643(12)			
B32	2.0154(14)	127.22(7)		
B41	2.0576(15)	125.83(7)	87.37(5)	
B1A2	2.0904(12)	125.42(7)	88.02(5)	90.80(5)
O6A4				
A24	1.8813(12)			
B42	2.0324(12)	123.00(6)		
B31	2.0379(14)	125.31(6)	94.16(5)	
B1A1	2.1100(11)	121.59(6)	93.87(5)	90.08(5)
O6B1				
A22	1.8958(13)			
B43	2.0173(14)	123.41(7)		
B34	2.0616(15)	123.52(7)	94.70(6)	
B1B2	2.1327(12)	120.86(7)	94.49(5)	91.78(5)
O6B2				
A21	1.8701(12)			
B33	2.0051(14)	129.48(8)		
B1B1	2.0865(12)	125.12(7)	87.58(5)	
B44	2.0966(15)	124.20(7)	87.52(5)	90.66(5)
O6B3				
A23	1.8787(13)			
B1B2	2.0238(12)	125.75(7)		

B31	2.0405(14)	125.71(7)	87.89(5)	
B42	2.1021(15)	123.61(7)	91.14(5)	92.02(6)
O6B4				
A24	1.8777(13)			
B32	2.0050(15)	129.16(7)		
B41	2.0794(15)	124.35(8)	87.05(5)	
B1B1	2.0853(13)	125.12(7)	88.23(6)	90.72(5)

A-Site <A-O> and BVS:

Site	<A-O>	BVS
A1_1	1.889	2.77
A1_2	1.889	2.78
A1_3	1.891	2.76
A1_4	1.887	2.80
A2_1	1.887	2.79
A2_2	1.885	2.81
A2_3	1.885	2.82
A2_4	1.885	2.81

O-site BVS:

Site	BVS	Site	BVS
O1_2	2.02242	O5A_1	1.930013
O1_2	2.03735	O5A_2	1.9849
O1_3	2.022276	O5A_3	1.961678
O1_4	2.006502	O5A_4	2.00245
O2_1	2.015525	O5B_1	1.964849
O2_2	2.018811	O5B_2	1.97299
O2_3	1.983644	O5B_3	1.991202
O2_4	2.035009	O5B_4	1.988909
O3_1	1.976581	O6A_1	1.989812
O3_2	2.004522	O6A_2	2.070355

O3_3	2.006888	O6A_3	2.061921
O3_4	1.95581	O6A_4	2.009648
O4_1	1.968415	O6B_1	1.950761
O4_2	2.04	O6B_2	2.024898
O4_3	2.005343	O6B_3	2.030468
O4_4	1.985627	O6B_4	2.029743

Appendix B : Details of the distortion mode analysis for the Verwey structure

Details of the basis and origin shifts of the space groups on the symmetry descent from $Fd\bar{3}m$ to Cc shown in Figure 3.22 are given below.

POP	**SG**	**Basis**	**Origin**	**SOP**
Γ2-(a)	F-43m	(1,0,0),(0,1,0),(0,0,1)	(-⅛,-⅛,-⅛)	Γ1
Γ3(a,0)	$I4_1/amd$	(-½,½,0),(-½,-½,0),(0,0,1)	(0, ½,-½)	Γ1
Γ3-(a,0)	$I\bar{4}m2$	(-½,½,0),(-½,-½,0),(0,0,1)	(-⅜,-⅜,⅛)	Γ1,Γ3, Γ2-
Γ4(a,-a,0)	C2/m	(½,½,1),(½,-½,0),(½,½,0)	(0,0,0)	Γ1,Γ3, Γ5
Γ4-(a,a,b)	Cm	(½,½,1),(½,-½,0),(½,½,0)	(0,0,0)	Γ1, Γ3, Γ4, Γ5, Γ2-, Γ3-, Γ5-
Γ4-(a,0,0)	$I4_1md$	(½,½,0),(-½,½,0),(0,0,1)	(0,¼,¼)	Γ1,Γ3
Γ5(a,b,b)	C2/m	(½,½,1),(½,-½,0),(½,½,0)	(0,0,0)	Γ1,Γ3, Γ4
Γ5(a,0,0)	Imma	(½,-½,0),(½,½,0),(0,0,1)		Γ1,Γ3,
Γ5-(0,a,-a)	Ima2	(½,-½,0), (0,0,-1),(½,½,0)	(0,¼,-¼)	Γ1,Γ3, Γ5(0,a,0),Γ4-(a,a,0)
Γ5-(a,0,0)	$I\bar{4}2d$	(-½,½,0),(-½,-½,0),(0,0,1)	(⅛,⅜,⅜)	Γ1,Γ3
Δ2,Δ4 (0,0,0,0,a,b)	Pcc2	(½,-½,0),(½,½,0),(0,0,2)	(⅛,⅛,0)	Γ1,Γ3, Γ5, Γ2-, Γ3-, Γ4-
Δ2, Δ4(a,0.414a,0,0,0,0)	Pcca	(½,0,½),(½,0,-½),(0,2,0)	(0,0,0)	Γ1,Γ3, Γ5
Δ5(..,a,b,-b,a)	$Pmc2_1$	(½,-½,0),(-½,½,0),(0,0,2)	(⅛,⅛,0)	Γ1,Γ3, Γ5, Γ2-, Γ4- Δ5(..,a,b,b,-a), X1(a,b,0,0,0,0)
Δ5(..,a, -√2a,a, √2a)	Pmca	(½,½,0),(- ½,½,0),(0,0,2),	(0,0,0)	Γ1,Γ3, Γ5,Δ5(..,a,√2a,-√2a,a), X1(0,a,0,0,0,0)
X1	Pmm2	(0,-½,½),(0,- ½,-½),(1,0,0)	(0,-⅛,-⅛)	Γ1,Γ3, Γ5, Γ2-, Γ3-, Γ4- (0,0,a),X1(a,b,0,0,0,0)
X1	Pmma	(½,½,0),(-½,½,0),(0,0,1)	(0,0,0)	Γ1,Γ3, Γ5,X1(0,a,0,0,0,0)
X2	Pnna	(½,-½,0),(½,½,0),(0,0,1)	(¼ ,0,¼)	Γ1,Γ3, Γ5, X3(a,0,0,0,0,0)
X3*	Pmna	(½,-½,0),(½,½,0),(0,0,1)	(0,0,0)	Γ1,Γ3, Γ5, X3(0,a,0,0,0,0)
X4*	Pnma	(½,½,0),(-½,½,0),(0,0,1)	(0,¼ ,¼)	Γ1,Γ3, Γ5, Γ5, ,X4(a,0,0,0,0,0)
W1,W2 (..,a,b,-a,-b), (..,a,b,a,b)	Cm	(1,1,0),(-1,1,0),(½,½,1)	(0,½,0)	Γ1,Γ3, Γ4, Γ5, Γ2-, Γ3-, Γ4-, Γ5-,X1*,X3*,X4*)

Appendix C : Details of single crystal and powder refinement for $Ba_3NaRu_2O_9$

ID31 refined coordinates ($P6_3/mmc$, 293 K):

Instrument			ID31	
Method			Powder, Debye-Scherrer	
Cell setting, space group			Hexagonal, $P6_3/mmc$	
Temperature (K)			293	
a,b,c (Å)			5.87689 (1), 5.87689 (1), 14.46747(2)	
V(Å^3)			432.7313 (14)	
Z			2	
Phase Density (g cm^{-3})			5.99472(2)	
Radiation wavelength (Å)			0.3999700	
Refinement				
Parameters			22	
wR_p			9.61	
R_p			7.24	
R_b			3.43	
χ^2			3.72	
	x	y	x	Temperature factor (B_{iso}) (Å^2)
Ba1	0	0	0.25	0.798(15)
Ba2	1/3	2/3	0.90770(5)	1.268(13)
Na1	0	0	0	0.19(8)
Ru1	1/3	2/3	0.15512(5)	0.388(11)
O1	0.4825(5)	0.9650(10)	0.25	0.60(9)
O2	0.1800(4)	0.3600(8)	0.4098(3)	0.93(7)

ID31 refined coordinates (P2/c, 110 K):

Instrument	ID31
Method	Powder, Debye-Scherrer
Cell setting, space group	Monoclinic, P2/c
Temperature (K)	110K
a,b,c (Å)	5.84001(2), 10.22197(4), 14.48497(6)
β (°)	90.26267(33)
V(Å^3)	864.6907(57)
Z	4

Phase Density (g cm^{-3})		6.00007(4)		
Radiation wavelength (Å)		0.3999700		
Refinement				
Parameters		55		
wR_p		10.80		
R_p		8.276		
R_b		3.18		
χ^2		1.94		
	x	y	x	B_{iso} ($Å^2$)
Ba1_1	0	-0.00765(18)	0.25	0.171(8)
Ba1_2	0.5	0.48258(18)	0.25	0.171(8)
Ba2_1	0.5033(3)	0.15766(13)	0.91778(9)	0.171(8)
Ba2_2	0.0025(3)	0.68586(13)	0.90137(9)	0.171(8)
Na1_1	0	0	0	0.171(8)
Na1_2	0.5	0.5	0	0.171(8)
Ru1_1	0.4974(5)	0.1612(2)	0.15831(12)	0.171(8)
Ru1_2	-0.0028(5)	0.65675(19)	0.15221(12)	0.171(8)
O1_1	0.733(3)	0.2427(14)	0.2527(11)	0.12(7)
O1_2	0	0.5055(17)	0.25	0.12(7)
O1_3	0.195(2)	0.7354(14)	0.2361(10)	0.12(7)
O1_4	0.5	0.0147(18)	0.25	0.12(7)
O2_1	0.272(3)	0.0792(18)	0.4125(12)	0.12(7)
O2_2	0.736(3)	0.0824(18)	0.4064(12)	0.12(7)
O2_3	0.017(3)	0.8122(12)	0.4159(10)	0.12(7)
O2_4	0.800(3)	0.5679(17)	0.4192(12)	0.12(7)
O2_5	0.270(3)	0.5979(16)	0.3917(11)	0.12(7)
O2_6	0.503(3)	0.3130(12)	0.4129(10)	0.12(7)

ID31 refined coordinates (C/c, 10 K):

Instrument	ID31
Method	Powder, Debye-Scherrer
Cell setting, space group	Monoclinic, C2/c
Temperature (K)	10K
a,b,c (Å)	5.84470(2), 10.17706(3), 14.45866(5)
β(^{o})	90.2151(3)
V($Å^3$)	860.022(5)
Z	4
Phase density (g cm^{-3})	6.00007(4)
Radiation wavelength (Å)	0.3999700
Refinement	

Parameters			35	
wRr_p			11.83	
R_p			9.46	
R_b			5.12	
χ^2			5.210	
	x	y	z	B_{iso} (Å^2)
Ba1	0.49538(18)	0.17129(11)	0.59088(5)	0.511(8)
Ba2	0	-0.00811(14)	0.25	0.511(8)
Na1	0	0	0	0.511(8)
Ru1	0.4959(2)	0.16134(13)	0.15557(6)	0.511(8)
O1_1	0.7141(17)	0.0796(10)	0.0840(7)	0.40(6)
O1_2	-0.0105(17)	0.8177(9)	0.0872(7)	0.40(6)
O1_3	0.2499(17)	0.9126(10)	0.5971(7)	0.40(6)
O2_1	0.2780(16)	0.2381(10)	0.2564(7)	0.40(6)
O2_2	0	0.5147(14)	0.25	0.40(6)

Single Crystal diffraction studies on $Ba_3NaRu_2O_9$ at ambient temperature:

X-ray Single Crystal Data	$Ba_3NaRu_2O_9$ at 293K
Crystal Data	
Chemical Formula	$Ba_3NaRu_2O_9$
Cell setting, Space group	Hexagonal, $P6_3/mmc$
Temperature(K)	293(2)
a,b,c (Å)	5.8756(5), 5.8756(5), 14.4619(11)
Volume (Å^3)	432.37(6)
D_c(mg m^{-3})	6.00
Radiation type	Mo-Kα
No. reflections for cell parameters	246
μ(mm^{-1})	16.948
Crystal form, colour	hexagonal plate, black
Crystal size(mm)	0.13x 0.45x 0.45
Data Collection	
Diffractometer	Bruker Apex2
Data collection method	ω+φ
Absorption correction	Face indexed numerical
T_{min}	0.0616
T_{max}	0.1174
No. of measured, independent and observed reflections	4039/390
θ_{max}(°)	30.63
R_{int}	0.1798

Range of h,k,l	$-8 \rightarrow h \rightarrow 8$
	$-7 \rightarrow k \rightarrow 8$
	$-22 \rightarrow l \rightarrow 20$
Refinement	
Refine on	F^2
R[F2 > 2_(F2)], wR(F2), S	0.023, 0.058, 0.96
Cutoff: I >	$3.00\sigma(I)$
No. of reflections	298
No. of parameters	22
Weighting scheme	$1/[\sigma^2(F_{obs}^2) + (0.000 \times P)^2 + 0.000 \times P + 0.000 + 0.000 \times \sin\theta]$, $P = 0.333 \times \max(F_{obs}^2,0) + 0.667 \times F_{calc}^2$
(Δ/α)max	0.0001
$\Delta\rho$max, $\Delta\rho$min (e $Å^{-3}$)	1.76, -2.09

Label	*x*	*y*	*z*	$U_{iso/equiv}$	Occupancy
Ba1	0	0	0.25	0.0128	1
Ba2	0.3333	0.6667	0.09234(4)	0.0188	1
Ru1	0.6667	0.3333	0.15510(4)	0.0098	1
Na1	0	0	0	0.0114	1
O1	0.9653(8)	0.4826(4)	0.25	0.0145	1
O2	0.8220(3)	0.6440(6)	0.0898(3)	0.0199	1

Label	U_{11}	U_{22}	U_{33}	U_{23}	U_{13}	U_{12}
Ba1	0.0120(2)	0.0120(2)	0.0143(3)	0	0	0.00601(11)
Ba2	0.0145(2)	0.0145(2)	0.0274(3)	0	0	0.00727(10)
Ru1	0.0082(2)	0.0082(2)	0.0130(3)	0	0	0.00408(11)
Na1	0.0127(11)	0.0127(11)	0.009(2)	0	0	0.0064(6)
O1	0.012(2)	0.0155(14)	0.0152(16)	0	0	0.0058(10)
O2	0.0193(12)	0.0133(14)	0.0249(15)	0.0106(14)	0.0053(7)	0.0066(7)

Single Crystal diffraction studies on $Ba_3NaRu_2O_9$ at 110 K:

X-ray Single Crystal Data	$Ba_3NaRu_2O_9$ at 110K
Crystal Data	
Chemical Formula	$Ba_3NaRu_2O_9$
Cell setting, Space group	Monoclinic, P 1 2/c 1
Temperature(K)	110K (2)
a,b,c (Å)	5.83387(9) , 10.21659(15) , 14.4585(2)
β(°)	89.9910(5)
Volume (Å$^{\wedge 3}$)	861.76(2)
D_c(mg m^{-3})	6.02
Radiation type	Mo-Kα
No. reflections for cell parameters	725
μ(mm^{-1})	16.948 mm^{-1}
Crystal form, colour	hexagonal plate, black
Crystal size(mm)	0.13x 0.45x 0.45
Data Collection	
Diffractometer	Bruker Apex2
Data collection method	ω+φ
Absorption correction	Spherical
T_{min}	0.0616
T_{max}	0.1174
No. of measured, independent and observed reflections	11855,2549
θ_{max}(°)	30.5293
R_{int}	0.067
Range of h,k,l	-8 → h → 8
	0 → k → 14
	0 → l → 20
Refinement	
Refine on	F
R, wR(F), S	0.028, 0.032, 1.01
Cutoff: I >	3.00σ (I)
No. of reflections	2651
No. of parameters	80
Weighting scheme	$w=w' \times [1 - (\Delta F_{obs} / 6 \times \Delta F_{est})^2]^2$ $w'=[P_0T_0'(x) + P_1T_1'(x) + ...P_{n-1}T_{n-1}'(x)]^{-1}$, where P_i are the coefficients of a Chebychev series in $t_i(x)$, and $x = F_{calc}/F_{calcmax}$
(Δ/α)max	0.0010
Δρmax, Δρmin (e Å-3)	1.97, -1.36

Label	*x*	*y*	*z*	$U_{iso/equiv}$	Occupancy
Na1	0	0	0	0.0044(5)	1
Na2	0.5	0.5	0	0.0052(5)	1
Ba1	0	0.00689(4)	0.25	0.0051	1
Ba3	0.5	0.48195(5)	0.25	0.0052	1
Ba2	0.50537(14)	0.15771(3)	0.91817(2)	0.0053	1
Ba4	0.00413(14)	0.68674(4)	0.90174(2)	0.0057	1
Ru1	0.49931(19)	0.16087(3)	0.15941(2)	0.00395(9)	1
Ru2	0.00241(19)	0.65572(4)	0.15151(3)	0.00426(9)	1
O1	0.7317(6)	0.2404(4)	0.2461(6)	0.0054(8)	1
O3	0.2065(7)	0.7367(4)	0.2361(3)	0.0040(8)	1
O4	0	0.4843(6)	0.75	0.0095(12)	1
O5	0.5	-0.0109(6)	0.75	0.0096(12)	1
O2	0.2694(14)	0.0793(9)	0.4087(5)	0.0128(19)	1
O6	0.8090(9)	0.5704(5)	0.4236(3)	0.0083(9)	1
O7	0.0074(15)	0.1905(4)	0.9177(3)	0.0045(7)	1
O8	0.4920(16)	0.6846(4)	0.9122(3)	0.0040(7)	1
O9	0.7365(10)	0.0857(7)	0.4108(4)	0.0025(14)	1
O10	0.2827(8)	0.6028(5)	0.3892(3)	0.0080(9)	1

ANIS of Ba only:

Label	U_{11}	U_{22}	U_{33}	U_{23}	U_{13}	U_{12}
Ba1	0.00599(19)	0.0050(2)	0.00442(15)	0	-0.0007(4)	0
Ba3	0.00631(19)	0.00520(18)	0.00398(15)	0	0.0003(4)	0
Ba2	0.00563(15)	0.00438(14)	0.00603(12)	0.00034(9)	-0.0017(4)	0.0000(3)
Ba4	0.00532(14)	0.00573(14)	0.00599(13)	0.00065(10)	-0.0001(3)	-0.0040(3)